

SOLUTION COMBUSTION PROCESSED HIGH ENTROPY OXIDE DIELECTRICS FOR MICROELECTRONIC APPLICATIONS

Thesis

Submitted in partial fulfillment of the requirements for the degree of

DOCTOR OF PHILOSOPHY

by

ASHRITHA SALIAN

(Registration No: 187076187MT001)

Under the guidance of

Dr. Saumen Mandal

Associate Professor



**DEPARTMENT OF METALLURGICAL AND MATERIALS
ENGINEERING**

**NATIONAL INSTITUTE OF TECHNOLOGY KARNATAKA
SURATHKAL, MANGALURU – 575025**

DECLARATION

I hereby *declare* that the Research Thesis entitled “**Solution combustion processed high entropy oxide dielectrics for microelectronic applications**” which is being submitted to the National Institute of Technology Karnataka, Surathkal in partial fulfillment of the requirements for the award of the Degree of **Doctor of Philosophy** in the **Department of Metallurgical and Materials Engineering**, is a *bonafide report of the research work carried out by me*. The material contained in this Research Thesis has not been submitted to any University or Institution for the award of any degree.



Name: ASHRITHA SALIAN

Registration Number: 187076187MT001

Department of Metallurgical and Materials Engineering

Place: NITK, Surathkal

Date: 19-10-2023

CERTIFICATE

This is to *certify* that the Research Thesis entitled “**Solution combustion processed high entropy oxide dielectrics for microelectronic applications**” submitted by Ms. Ashritha Salian (Registration Number: 187076187MT001) as the record of the research work carried out by her, is *accepted as the Research Thesis submission* in partial fulfillment of the requirements for the award of the degree of Doctor of Philosophy.

Research supervisor


Dr. Saumen Mandal

Associate Professor

Department of Metallurgical and Materials Engineering

NITK Surathkal



Chairman- DRPC

Chairman - DRPC
Dept. of Metallurgical and Materials Engineering
National Institute of Technology Karnataka, Surathkal
Post Srinivasnagar, Mangaluru - 575 025
Karnataka, India

**DEDICATED TO THE ALMIGHTY GOD
AND MY PARENTS**

ACKNOWLEDGEMENTS

I express my sincere thanks to the almighty whose divine intervention was instrumental in the proceedings of this work. The dissertation must surely bear the imprint of the prayers, sacrifices made, love, and affection showered on me by my parents. I express my sincere gratitude to my father Mr. Vasanth Salian and my mother Mrs. Parvathi, who supported me throughout my life and during my doctoral study.

My sincere, graceful acknowledgment to my research supervisor Dr. Saumen Mandal, Associate Professor, Department of Metallurgical and Materials Engineering, National Institute of Technology Karnataka, Surathkal, for his valuable guidance, support, and help throughout the research. It has been an honor to be his 1st women Ph.D. student. I heartily thank him for his kindness, help, valuable suggestions, and constant encouragement, which I received during tough times in the Ph.D. pursuit. His constant guidance, cooperation, and moral support have always kept me going ahead. The research work presented here would have been impossible without the support and guidance of my supervisor. I would also like to thank his family members Mrs. Debashmita Mandal and Ms. Rudrani Mandal for their relentless love, care, and support shown to me as part of their family. I will always cherish and thank the Dr. Saumen Mandal family for involving me in the creation of beautiful memories as a family. I am blessed and lucky to have him as my research supervisor and be a part of his family.

I would like to sincerely thank the Department of Metallurgical and Materials Engineering, National Institute of Technology Karnataka, Surathkal, for providing the labs and research facilities. I would like to thank Dr. Ravishankar K. S., Head of the Department, Metallurgical and Materials Engineering, National Institute of Technology Karnataka, Surathkal, for the constant encouragement and support. I would also like to thank Prof. Udaya Bhat K., Prof. Anandhan Srinivasan, and Prof. K Narayan Prabhu, Ex-Head of the Department, Metallurgical and Materials Engineering, National Institute of Technology Karnataka, Surathkal, who served from 2016-2020 for the constant

encouragement and support. I would like to take this opportunity to thank Prof. K Narayan Prabhu, Department of Metallurgical and Materials Engineering, National Institute of Technology Karnataka, Surathkal, for his constant support and help in the allotment of the quarters during COVID-19. I would like to take this opportunity to thank members of my research program assessment committee (RPAC), Dr. B Rajasekaran, Department of Metallurgical and Materials Engineering, and Dr. Krishnan C M C, Department of Electrical and Electronics Engineering, National Institute of Technology Karnataka, Surathkal for their valuable suggestions and comments during the proposal, progress and pre-synopsis seminars.

I am obliged to the Ministry of Human Resource Development (MHRD), Government of India, and the National Institute of Technology Karnataka, Surathkal, for their financial assistance in conducting my research work in the form of contingency and research fellowship. I would also like to thank the Department of Chemical Engineering and Department of Chemistry, National Institute of Technology Karnataka, Surathkal, for providing access to the TGA facility. I would like to thank the Central Instrumentation Facility, Innovation Centre, MIT Manipal, Centre for Nano Science and Engineering (CeNSE), Indian Institute of Science, Bengaluru, and Central Research Facility, National Institute of Technology Karnataka, Surathkal for providing research facilities.

I express my sincere thanks to Prof. Sunkook Kim, Sungkyunkwan Universty (SKKU), South Korea and Dr. Pavan Pujar, Indian Institute of Technology (BHU) Varanasi, India for providing me transistor fabrication and analysis facility. I would like to express deep and sincere thanks to past and present Ceramics & Thin Films Research Group Members Dr. Pavan Pujar, Dr. Komalakrushna Hadagalli, Dr. Manjunath G, Dr. Robbi Vivek Vardhan, Mr. Lakkmisetti Lakshmi Praveen, Mr. Perabathula Satish, Mr. Mahin Saif Nowl, Ms. Santhra Krishnan P, Mr. Akshay Prasad K, Mr. Mohaneesh Dewangan, Mr. Vishal Gautam, Mr. Shaik Akhil, Ms. Ambili. V, Ms. Ramya Athani, Ms. Suchitra Chavani, Mr. Sukrit Dass T M, and Ms. Srinithya Juvva for their constant support throughout my research work. I would like to thank Dr. Sawan Shetty, MIT Manipal, and

his wife Dr. Nisha Shetty, MCOODS Manipal, and my research colleagues Dr. Shamitha Das, Dr. Divya Bharathi, and Mr. Naveen Baradishettar for their constant support and help in research work.

I am thankful to all teaching and non-teaching staff of the Department of Metallurgical and Materials Engineering, National Institute of Technology Karnataka, Surathkal, for constant support and help in various aspects of my course. A very special thanks to Mrs. Sharmila Dinesh, and Mr. Sundar Shettigar for helping me with necessary documentation and instrumentation assistance, respectively, at various stages of my Ph.D. I would also like to thank the family members of Mrs. Sharmila Dinesh, her daughter Ms. Deeksha Dinesh, and her husband Mr. Dinesh for treating me like their own family member and helping me in all my work at every step. I would also like to thank Mrs. Hemalatha. K, telephone operator, main building, National Institute of Technology Karnataka, Surathkal, for treating me like her own daughter and providing me with constant support and motivation in my research. I would also like to thank Mr. Ashok Hebbar, Central Library, National Institute of Technology Karnataka, Surathkal, for helping me with transportation assistance whenever necessary. I would also like to thank Mrs. Vinaya Shettigar, Mrs. Asha, Mrs. Geetha, Mrs. Sumathi, Mrs. Vidya, and Mrs. Prathima for making me smile, helping and motivating me constantly in my research journey.

I am thankful to all my doctors, Dr. M. Ashok Bhat, Department of Nephrology, KMC, Jyothi, Mangalore, Dr. Vivek Pathak, Department of Nephrology, Dr. Devdas Madhavan and team, Department of Urology, Kovai Medical Center and Hospital, Coimbatore, Tamil Nadu, my dearest uncle Dr. Laxman Suvarna, Orthopedic surgeon, Unity Hospital, Mangalore and my aunty Dr. Pramoda Laxman, Clinical Head - Fertility Specialist, Oasis Fertility, AJ Hospital, Mangalore for taking care of me and providing me all the necessary medical help on time. I would also like to thank the staff of the Renal Dialysis Unit, Yenepoya Speciality Hospital, Mangalore, and Kovai Medical Center and Hospital, Coimbatore, Tamil Nadu, for taking the necessary care and help in various aspects of my course.

I am grateful to all my ancestors and my two beautiful family members (Lokayya Suvarna – K.L. Sundari family (Beer, Kotekar) and Ananda Karkera – Girija Salián family (Pallakere)) for their constant care, support and unconditional love. Finally, I thank all my friends, and well-wishers, for their love and regards, prayers, and wishes, that directly and indirectly helped me to complete this research work.

ASHRITHA SALIAN

Abstract

An investigation of dielectric constant on the sintered high entropy oxide capacitor composed of Co, Cu, Mg, Zn, Ni (i.e., (CoCuMgZnNi)O), Ce, La, Pr, Sm, Y (i.e., (CeLaPrSmY)O) and Co, Cr, Fe, Mn, Ni (i.e., (CoCrFeMnNi)O) developed using solution combustion synthesis is performed. Stabilization of phase in high entropy oxide is extremely important as it directly influences the properties. In order to explore phase stabilization, in-depth studies of thermal, structural, morphological, and compositional analyses are carried out. The precursors of (CoCuMgZnNi)O were found to combust at 270 °C and 400 °C was considered to be the formation temperature. The (CoCuMgZnNi)O fully stabilized at 1000 °C shows a single-phase, fcc rocksalt structure with an *Fm-3m* space group. (CoCuMgZnNi)O displays one of its parent oxide Mg-O structural properties. Dielectric measurements at room temperature showed high constant (κ) with magnitudes $\sim 1.9 \times 10^3$, 4.7×10^1 , and 0.9×10^1 at 100, 1 k, and 100 kHz. In addition, a low-temperature formation of (CeLaPrSmY)O was evidenced at 500 °C and fully stabilized at 1000 °C with a single-phase, fcc fluorite structure with an *Fm-3m* space group. The (CeLaPrSmY)O displays one of its parent oxide Ce-O structural properties. Dielectric measurements at room temperature showed dielectric constant (κ) $\approx 29 - 5.7$ from 100 Hz - 1 MHz. Simultaneously, the precursors of (CoCrFeMnNi)O undergo combustion at a low temperature below 250 °C. Upon crystallization at 500 °C, no secondary impurity oxides were detected and phase-stabilized to a spinel structure (*Fd-3m*). The spinel (CoCrFeMnNi)O exhibited high dielectric constant, with values approximately 1.2×10^3 , 7.3×10^2 , and 3.1×10^1 at 100, 1 k and 100 kHz. The optimized processing parameters are further implemented on depositing (CoCrFeMnNi)O dielectric thin film followed by a thin film transistor. The spinel (CoCrFeMnNi)O thin film exhibited high dielectric constant and low leakage current density, with values approximately 3×10^1 , measured at 1 kHz and $\sim 10^{-8}$ A.cm⁻². The (CoMnNiFeCr)O thin film was integrated into thin film transistors with a molybdenum disulfide channel. The transistor operated at low voltage ($< 5V$) and showed

a field effect mobility of $8.8 \text{ cm}^2 \text{ V}^{-1} \text{ s}^{-1}$, an on-off ratio of approximately 10^5 , a threshold voltage of -1.5 V , and a subthreshold swing of 0.38 V.dec^{-1} .

Keywords: *High entropy oxide, phase stabilization, rocksalt, spinel, fluorite, solution combustion; dielectric properties*

CONTENTS

LIST OF FIGURES	vii
LIST OF TABLES	xv
NOMENCLATURE	xix
LIST OF SYMBOLS	xxiii
CHAPTER 1	1
INTRODUCTION	1
CHAPTER 2	7
LITERATURE REVIEW	7
2.1 Introduction	7
2.2 High entropy materials	7
2.2.1 Alloys.....	8
2.2.2 Metallic glasses	9
2.2.3 Ceramics	9
2.2.3.1 Oxides.....	9
2.2.3.2 Diborides	11
2.2.3.3 Carbides.....	11
2.2.3.4 Nitrides	11
2.2.3.5 Silicides	12
2.2.3.6 Silicates	13
2.2.4 Polymers	14
2.2.5 Sulfides	14
2.2.6 Metal-organic frameworks.....	14
2.2.7 Hydroxides.....	15

2.2.8 Dichalcogenides	15
2.2.9 MXenes	15
2.3 Concept of entropy engineering	16
2.4 Primary effects in high entropy materials.....	19
2.4.1 Sluggish diffusion effect	19
2.4.2 High entropy effect	20
2.4.3 Cocktail effect.....	20
2.4.4 Severe lattice distortion effect	21
2.5 High entropy oxides.....	21
2.5.1 Criteria for the selection of candidates	22
2.5.2 Processing	23
2.5.3 Crystal structures	33
2.5.4 Properties explored in high entropy oxides	61
2.5.4.1 Electrochemical	61
2.5.4.2 Electrical.....	67
2.5.4.3 Dielectric	68
2.5.4.4 Magnetic.....	71
2.5.4.5 Optical	75
2.5.3.6 Thermal	76
2.5.4.7 Catalytic	79
2.5.4.8 Mechanical	80
2.6 Solution combustion synthesis	84
2.6.1 Solution combustion processed thin films	88
2.6.2 High entropy oxide thin films	91
2.7 Metal oxide dielectrics.....	92
2.7.1 High- κ metal oxide dielectrics	96

2.7.1.1 Basic criteria to choose high- κ	97
2.7.1.2 Solution combustion processed high- κ metal oxides	98
2.7.1.3 Role of high- κ in thin film transistors	100
2.7.1.4 Applications	103
2.8 Research gap.....	104
2.9 Objectives of the present study.....	106
CHAPTER 3.....	107
INVESTIGATION OF DIELECTRIC PROPERTIES ON THE PHASE STABILIZED SOLUTION COMBUSTION PROCESSED HIGH ENTROPY ROCKSALT OXIDE (CoCuMgZnNi)O	107
3.1 Introduction	107
3.2 Experimental procedure.....	107
3.2.1 Formulation of combustible precursor.....	107
3.2.2 Synthesis and characterization.....	108
3.2.3 Development of sintered (CoCuMgZnNi)O capacitors.....	109
3.3 Results and discussion	110
3.3.1 Thermal decomposition analysis.....	110
3.3.2 Structural, compositional, and morphological analysis	112
3.3.3 Dielectric constant of sintered (CoCuMgZnNi)O capacitor.....	129
3.4 Conclusion	132
CHAPTER 4.....	135
INVESTIGATION OF DIELECTRIC PROPERTIES ON THE PHASE STABILIZED SOLUTION COMBUSTION PROCESSED HIGH ENTROPY FLUORITE OXIDE (CeLaPrSmY)O	135
4.1 Introduction	135
4.2 Experimental procedure.....	135

4.2.1 Formulation of combustible precursor	135
4.2.2 Synthesis and characterization	136
4.2.3 Development of sintered (CeLaPrSmY)O capacitors.....	137
4.3 Results and discussion	138
4.3.1 Thermal decomposition analysis.....	138
4.3.2 Structural, compositional, and morphological analysis	141
4.3.3 Dielectric constant of sintered (CeLaPrSmY)O capacitor.....	152
4.4 Conclusion	155
CHAPTER 5	157
INVESTIGATION OF DIELECTRIC PROPERTIES ON THE PHASE STABILIZED SOLUTION COMBUSTION PROCESSED HIGH ENTROPY SPINEL OXIDE (CoMnNiFeCr)O.....	157
5.1 Introduction	157
5.2 Experimental procedure.....	157
5.2.1 Formulation of combustible precursor	157
5.2.2 Synthesis and characterization	157
5.2.3 Development of sintered (CoMnNiFeCr)O capacitors	159
5.3 Results and discussion	159
5.3.1 Thermal decomposition analysis.....	160
5.3.2 Structural, compositional, and morphological analysis	161
5.3.3 Dielectric constant of sintered (CoMnNiFeCr)O capacitor	174
5.4 Conclusion	177
CHAPTER 6	179
APPLICATION OF LOW-TEMPERATURE SOLUTION COMBUSTION PROCESSED HIGH ENTROPY SPINEL OXIDE (CoMnNiFeCr)O IN THIN FILM TRANSISTORS	179

6.1 Introduction	179
6.2 Experimental procedure.....	179
6.2.1 Formulation of combustible precursor.....	179
6.2.2 Deposition of HEO thin film and characterizations.....	180
6.2.3 Fabrication of HESO thin film MIM capacitor and thin film transistor	182
6.3 Results and discussion	182
6.3.1 Thermal decomposition analysis.....	182
6.3.2 Structural, compositional, and morphological analysis	184
6.3.3 Performance of HESO thin film MIM capacitor and transistor.....	190
6.4 Conclusions	193
CHAPTER 7.....	195
CONCLUSIONS	195
7.1 Scope for future work	197
APPENDIX.....	199
APPENDIX I	199
APPENDIX II.....	201
APPENDIX III	203
APPENDIX IV	206
REFERENCES.....	209
LIST OF PUBLICATIONS	257
PATENTS	257
PUBLICATIONS IN PEER-REVIEWED JOURNALS.....	257
LIST OF CONFERENCE PRESENTATIONS	259
BIODATA.....	261

Page left intentionally blank

LIST OF FIGURES

Fig. No.	Description	Page No.
2.1	Timeline depicting the era of high entropy materials (Salian et al. 2023b).	8
2.2	Classification of high entropy materials (Salian and Mandal 2022b).	8
2.3	Formation of a single-phase rocksalt crystal structure of HEO (MgCuCoNiZn)O (Zheng et al. 2019).	10
2.4	Classification of materials based on configurational entropy.	18
2.5	(a) Principal elements and (b) their mole fractions (i.e., component cations) as a function of configurational entropy. The composition with the maximum configurational entropy will have an equimolar ratio of its primary components (the compositions with bold dots show these compositions) (Anandkumar and Trofimov 2023).	18
2.6	Schematic representation of the primary effects in high entropy materials (Pikalova et al. 2022)	19
2.7	The number of articles searched on HEO with the title and abstract keywords such as “high entropy oxide” or “entropy stabilized oxides” in Web of Science.	22
2.8	List of high entropy oxide processing techniques.	24
2.9	Schematic depiction of preparation of high entropy oxides (a) $(Y_{0.2}Yb_{0.2}Lu_{0.2}Eu_{0.2}Er_{0.2})_3Al_5O_{12}$ by solid-state reaction process (Chen et al. 2020c), (b) flame spray pyrolysis (Wang et al. 2020b), (c) with rare earth and transition metal by nebulized spray pyrolysis (Sarkar et al. 2018a) and (d) $(Nd_{0.2}Sm_{0.2}Eu_{0.2}Y_{0.2}Yb_{0.2})_4Al_2O_9$ by chemical coprecipitation (Xiang et al. 2021b; Zhao et al. 2020d).	25
2.10	Schematic depiction of preparation of high entropy oxides (a) $(Co_{0.2}Cu_{0.2}Mg_{0.2}Ni_{0.2}Zn_{0.2})O$ via solution combustion synthesis (Mao et al. 2019c), (b) $(LaY)(Zr_{0.5}Ti_{0.5}Ce_{0.5}Hf_{0.5})O_7$ by sol-gel process (Tang et	29

	al. 2022), and (c) $(Y_{0.2}Yb_{0.2}Sm_{0.2}Eu_{0.2}Er_{0.2})_2O_3$ through electrospinning (Xing et al. 2022).	
2.11	Schematic of the (a) pulsed laser deposition, (b) magnetron sputtering deposition, and (c) plasma spraying method.	31
2.12	Timeline of the structures explored in HEOs since 2015.	33
2.13	(a) Ionic conductivity of Li doped sample at room temperature (Bérardan et al. 2016b), (b) charge and discharge profile with a photograph of LED powered by HEO fuel cell (Wang et al. 2019b), (c) long-term cycling performance of HEOs (Zheng et al. 2019) and, (d) Comparison of capacity retention of Li(HEO)F and LiNiOF (Wang et al. 2019c).	65
2.14	Room-temperature magnetic hysteresis loop for spinel-type HEOs (Mao et al. 2019a), (b) coercivity (H_c), magnetization (M), and lattice distortion against synthesis temperature for spinel-type HEOs (Mao et al. 2019a) and, (c) plot of DC magnetic susceptibility as a function of temperature (Zhang et al. 2019a).	73
2.15	The plot of indentation hardness and elastic modulus of $(Al_{0.19}Cr_{0.13}Nb_{0.19}Ta_{0.30}Ti_{0.19})O_2$ HEO thin film on sapphire substrates versus (a) oxygen flow rate ratios f_{O_2} from 30 % to 80 % and (b) annealing temperature (Kirnbauer et al. 2019).	83
2.16	Required components for combustion synthesis (Carlos et al. 2020).	86
2.17	A schematic representation of different solution-based methods of film deposition. (Pasquarelli et al. 2011)	90
2.18	(a) Change in dielectric constant (κ) and dielectric loss ($\tan \delta$) with respect to different polarizations and frequency, (b) pictorial representation of (b)electronic, (c) ionic, (d) orientation, (e) interfacial, and (f) electrode or EDL (electric double layer) polarization (Wang et al. 2018a).	93
2.19	(a) Pictorial representation of a metal-insulator-metal (MIM) parallel-plate capacitor, (b) comparative study of the frequency-dependent areal capacitance of high and low- κ dielectric films, (c) voltage-dependent	96

	areal capacitance and (d) change in current density with respect to the electric field for a typical high- κ zirconium self-assembled nanodielectric film on silicon.	
2.20	Periodic table for choosing high- κ oxide dielectric materials depending on different κ values (Liu et al. 2018).	98
2.21	(a) A typical n-channel (electron-transporting) TFT configuration, (b) the output and, (c) transfer characteristics of a standard TFT device (Hong and Liao 2020).	101
3.1	Schematic of synthesis of (CoCuMgZnNi)O powder	108
3.2	(a) The weight loss (TGA and DTG) and (b) heat flow (DSC) of HERO precursor gel and (c) TGA and DTG and (d) DSC of HERO-400.	111
3.3	X-ray diffraction patterns of (a) HERO-400 to HERO-1000, (b) zoomed X-ray diffraction patterns at 2θ equal to $35^\circ - 45^\circ$, (c) constancy of lattice parameter with an increase in temperature.	114
3.4	(a) X-ray diffraction patterns of individual parent metal oxides Co-Cu-Mg-Zn-Ni-O (HERO-1000), Co-O, Cu-O, Mg-O, Zn-O, and Ni-O, (b) zoomed XRD at 2θ $35^\circ - 45^\circ$ represent the major peak of the system, and (c) change in lattice parameter indicating the dependence of HERO with regard to parent metal oxide Co-O, Cu-O, Mg-O, Zn-O, and Ni-O.	120
3.5	(a) X-ray diffraction patterns of lower cation systems Co-Cu-Mg-Zn-Ni-O (HEO-1000), Co-Cu-Mg-Zn-O, Co-Cu-Mg-O, Co-Cu-O, and Co-O, (b) zoomed XRD at 2θ $35^\circ - 45^\circ$ represent the major peak of the system, and (c) change in lattice parameter indicating expansion of lattice with an increase in cations.	122
3.6	(a) Raman spectra of HERO-400 to HERO-1000, and (b) FTIR spectra of HERO-400 and HERO-1000.	124
3.7	(a-g) The surface morphology of HEO-400 to HEO-1000 displays a grain growth with temperature rise, (h) the pie chart indicating the elemental distribution of all five cations in HERO-1000 extracted from EDS, and (i) grain size distribution graph of grain size vs. temperature respectively.	126

3.8	High-resolution deconvoluted spectra of core level (a) Co 2p, (b) Cu 2p, (c) Mg 1s, (d) Zn 2p, (e) Ni 2p and (f) O 1s depicting their respective oxidation states.	128
3.9	(a) Schematic of the capacitor developed using (CoCuMgZnNi)O pellet sintered at 1000 °C, (b) the surface morphology of the (CoCuMgZnNi)O pellet sintered at 1000 °C and used for the development of capacitor, with admirable sinterability of the grain, and (c) the pie chart indicating the elemental distribution of all five cations in (CoCuMgZnNi)O pellet extracted from EDS, frequency dependence plots of the (d) dielectric constant (κ) and dielectric loss ($\tan \delta$), (e) real and imaginary part of the impedance (Z), (f) real and imaginary part of the electric modulus (M) measured at room temperature.	130
3.10	Schematic depicting the interfacial polarization which occurs due to various reasons such as vacancies, interstitials, dangling bonds, grain, grain boundaries, rotation of vacancy, electrodes, valence state transfer, the capture of space charge by the trap states, and dipole formation when an electric field is applied in HERO resulting in high dielectric constant.	132
4.1	Schematic of synthesis of (CeLaPrSmY)O powder.	136
4.2	The (a) weight loss (TGA and DTG) and (b) heat flow (DSC) of (CeLaPrSmY)O HEFO precursor gel and (c) TGA and DTG, and (d) DSC of HEO-500.	140
4.3	The Decomposition pathway of all (CeLaPrSmY)O metal nitrates with an increase in temperature towards the formation of stable oxides, respectively.	140
4.4	(a) X-ray diffraction patterns of HEO-500 to HEO-1000, (b) zoomed X-ray diffraction patterns at 2θ equal to $24^\circ - 40^\circ$, represent the major peak of the system, (c) constancy of lattice parameter with an increase in temperature.	143

4.5	Pictorial representation of phase stabilization of (CeLaPrSmY)O from precursor solution to the presence of secondary phase till the pure fluorite phase formation.	143
4.6	(a) X-ray diffraction patterns of individual parent metal oxides Ce-O, La-O, Pr-O, Sm-O, and Y-O, (b) zoomed XRD at 2θ $24^\circ - 40^\circ$ represent the major peak of the system, (c) change in lattice parameter.	144
4.7	(a) X-ray diffraction patterns of lower cation systems Ce-O, Ce-La-O, Ce-La-Pr-O, and Ce-La-Pr-Sm-O in comparison with Ce-La-Pr-Sm-Y-O (HEFO-1000), (b) zoomed XRD at 2θ $24^\circ - 40^\circ$ represent the major peak of the system, (c) change in lattice parameter indicating expansion of lattice with an increase in cations.	147
4.8	(a) Raman spectra, and (b) FTIR spectra of HEFO-500 and HEFO-1000.	149
4.9	(a-f) The surface morphology of HEFO-500 to HEFO-1000.	150
4.10	High-resolution deconvoluted spectra of core level (a) Ce 3d, (b) La 3d, (c) Pr 3d, (d) Sm 3d, (e) Y 3d, and (f) O 1s depicting their respective oxidation states,	152
4.11	(a) Schematic of the capacitor developed using (CeLaPrSmY)O pellet sintered at 1000°C , (b) the surface morphology of the (CeLaPrSmY)O pellet sintered at 1000°C and used for the development of capacitor, with admirable sinterability of the grain, and (c) the pie chart indicating the elemental distribution of all five cations in (CeLaPrSmY)O pellet extracted from EDS, frequency dependence plots of the (d) dielectric constant (κ) and dielectric loss ($\tan \delta$), (e) real and imaginary part of the impedance (Z), (f) real and imaginary part of the electric modulus (M) measured at room temperature	154
5.1	Schematic of the synthesis process of (CoMnNiFeCr)O powder.	158
5.2	The (a) weight loss (TGA and DTG) and (b) heat flow (DSC) of (CoMnNiFeCr)O precursor gel and (c) TGA and DTG and (d) DSC of HESO-400.	161

- 5.3 (a) X-ray diffraction patterns of HESO-400 to HESO-1000, (b) 163
corresponding zoomed X-ray diffraction patterns at 2θ equal to $35^\circ - 38^\circ$, (c) constancy of lattice parameter with an increase in temperature.
- 5.4 (a) X-ray diffraction patterns of respective parent metal oxides Co-Mn- 165
Ni-Fe-Cr-O (HESO-1000), Co-O, Mn-O, Ni-O, Fe-O, and Cr-O, (b)
zoomed XRD at 2θ $32^\circ - 38^\circ$ represent the major peak of the system,
(c) change in lattice parameter.
- 5.5 (a) X-ray diffraction patterns of lower cation systems Co-Mn-Ni-Fe-Cr- 168
O (HESO-1000), Co-Mn-Ni-Fe-O, Co-Mn-Ni-O, Co-Mn-O and Co-O,
(b) zoomed XRD at 2θ $35^\circ - 38^\circ$ represent the major peak of the system,
(c) change in lattice parameter.
- 5.6 (a) Raman spectra of HESO-400 to HEO-1000, and (b) FTIR spectra of 170
HESO-400 and HESO-1000.
- 5.7 (a-g) The surface morphology of HESO-400 to HESO-1000 displays a 171
grain growth with temperature rise, (h) the pie chart indicating the
elemental distribution of all five cations in HESO-1000 extracted from
EDS, and (i) grain size distribution graph of particle diameter vs.
temperature respectively.
- 5.8 Analysis of the chemical composition of the HESO-1000 using X-ray 173
photoelectron spectroscopy. High-resolution deconvoluted spectra of
core level (a) Co 2p, (b) Mn 2p, (c) Ni 2p, (d) Fe 2p, (e) Cr 2p and (f)
O 1s depicting their respective oxidation states.
- 5.9 (a) Schematic of the capacitor developed using (CoMnNiFeCr)O pellet 175
sintered at 1000°C , (b) the surface morphology of the (CoMnNiFeCr)O
pellet sintered at 1000°C and used for the development of capacitor,
with admirable sinterability of the grain, and (c) the pie chart indicating
the elemental distribution of all five cations in (CoMnNiFeCr)O pellet
extracted from EDS, frequency dependence plots of the (d) dielectric
constant (κ) and dielectric loss ($\tan \delta$), (e) real and imaginary part of the
impedance (Z), (f) real and imaginary part of the electric modulus (M)
measured at room temperature.

5.10	Schematic depicting the interfacial polarization which occurs due to various reasons such as vacancies, interstitials, dangling bonds, grain, grain boundaries, rotation of vacancy, electrodes, valence state transfer, the capture of space charge by the trap states, and dipole formation when an electric field is applied in (CoMnNiFeCr)O resulting in high dielectric constant.	176
6.1	Schematic of the synthesis process of (CoMnNiFeCr)O powder.	181
6.2	The thermal traces represent the weight loss (TGA and DTG) and heat flow (DSC) of HEO precursors.	183
6.3	GIXRD pattern with an increase in temperature of (a) HESOTF-5, (b) HESOTF-10, and (c) HESOTF-15 depicting the formation of a single-phase, face-centered cubic spinel structure with an $Fd-3m$ space group. With an increase in temperature, diffraction peaks started evolving, being narrower and more intense, signifying an increase in crystallinity.	185
6.4	(a) Raman spectrum of HESOTF-15 annealed at 300, 400, and 500 °C, (b-d) AFM image of HESOTF-15 annealed at 300, 400, and 500 °C, (e) surface morphology and (f) cross-sectional micrograph of HESOTF-15-500, and (g) pie chart displaying the elemental distribution respectively.	187
6.5	XPS analysis of HESOTF-15-500 with a corresponding high-resolution spectrum of (a) Co 2p, (b) Mn 2p, (c) Ni 2p, (d) Fe 2p, (e) Cr 2p, and (f) O 1s.	189
6.6	(a) The schematic architecture of metal insulator metal (MIM) capacitor with (CoCrFeMnNi)O acting as an insulating layer, (b) dielectric constant-frequency plot, (c) Plot of current density vs. applied voltage utilized in estimating the leakage current in HESOTF-15-500, (d) schematic architecture of bottom gate HEO based TFT, (e) I_{ds} - V_{ds} curves (output curves) of the (CoCrFeMnNi)O based TFT in the V_{gs} range from 1V – 5V, (f) transfer curve of (CoCrFeMnNi)O based TFT in the log scale.	192
6.7	The C-V response of the capacitor at 100, 1 k, and 10 kHz.	193

Page left intentionally blank

LIST OF TABLES

Table No.	Description	Page No.
2.1	List of published work on rocksalt-based high entropy oxides, their crystal structure, stabilization temperature, processing technique, and properties explored.	36
2.2	List of published work on spinel-based high entropy oxides, their crystal structure, stabilization temperature, processing technique and properties explored.	42
2.3	List of published work on fluorite-based high entropy oxides, their crystal structure, stabilization temperature, processing technique and properties explored.	46
2.4	List of published work on perovskite-based high entropy oxides, their crystal structure, stabilization temperature, processing technique, and properties explored.	49
2.5	List of published work on magnetoplumbite-based high entropy oxides, their crystal structure, stabilization temperature, processing technique and properties explored.	52
2.6	List of published work on monoclinic-based high entropy oxides, their crystal structure, stabilization temperature, processing technique and properties explored.	53
2.7	List of published work on rutile-based high entropy oxides, their crystal structure, stabilization temperature, processing technique and properties explored.	55
2.8	List of published work on pyrochlore-based high entropy oxides, their crystal structure, stabilization temperature, processing technique and properties explored.	56
2.9	List of published work on delafossite-based high entropy oxides, their crystal structure, stabilization temperature, processing technique and properties explored.	58

2.10	List of published work on garnet-based high entropy oxides, their crystal structure, stabilization temperature, processing technique and properties explored.	59
2.11	List of published work on ruddlesden popper-based high entropy oxides, their crystal structure, stabilization temperature, processing technique and properties explored.	60
2.12	The ionic conductivity, cyclic stability, and specific and discharge capacity of high entropy oxides.	64
2.13	Dielectric constant of high entropy oxides.	70
2.14	Thermal conductivity and elastic modulus of high entropy oxides.	78
2.15	Vickers hardness values of high entropy oxides.	84
3.1	Summary of thermal events in the (CoCuMgZnNi)O precursor gel and HERO-400 with an increase in temperature from TGA and DSC.	112
3.2	Summary of the lattice parameter of (CoCuMgZnNi)O with an increase in temperature.	115
3.3	A summary of all published work on solution-processed HERO having (Co, Cu, Mg, Zn, Ni)O composition compared with the present work.	116
3.4	Details of the diffraction peaks, standard ICDD file number, crystal structure, and lattice parameters corresponding to the individual oxides.	119
3.5	Summary of the lattice parameter of individual parent oxides and HEO-1000.	120
3.6	Summary of the lattice parameter of lower cation system and HEO-1000.	122
3.7	Summary of all the diffraction peaks and Raman modes present in XRD and Raman spectrum with an increase in temperature.	125
3.8	Summary of the percentage area contribution of deconvoluted peaks in cations.	129
4.1	Summary of thermal events in the (CeLaPrSmY)O precursor gel and HEFO-400 with an increase in temperature from TGA and DSC.	141

4.2	Summary of the lattice parameter of (CeLaPrSmY)O with an increase in temperature.	144
4.3	Details of the diffraction peaks, standard ICDD file number, crystal structure, and lattice parameters corresponding to the individual oxides.	145
4.4	Summary of the lattice parameter of individual parent oxides and HEO-1000.	146
4.5	Summary of the lattice parameter of lower cation system and HEFO-1000.	148
4.6	Summary of the percentage area contribution of deconvoluted peaks in cations.	151
5.1	Summary of thermal events in the (CoMnNiFeCr)O precursor gel and HESO-400 with an increase in temperature from TGA and DSC.	161
5.2	Summary of the lattice parameter of (CoMnNiFeCr)O with an increase in temperature.	163
5.3	Details of the diffraction peaks, standard ICDD file number, crystal structure, and lattice parameters corresponding to the individual oxides.	166
5.4	Summary of the lattice parameter of individual parent oxides and HESO-1000.	166
5.5	Summary of the lattice parameter of lower cation system and HESO-1000.	167
5.6	Summary of the percentage area contribution of deconvoluted peaks in cations.	174
6.1	Summary of thermal events in the (CoMnNiFeCr)O precursor gel with an increase in temperature from TGA and DSC.	183
6.2	Summary of the percentage area contribution of deconvoluted peaks in cations.	190
6.3	TFT Performance of oxide dielectrics.	193

Page left intentionally blank

NOMENCLATURE

AF	: Antiferromagnetic
AFM	: Atomic Force Microscopy
ALD	: Atomic Layer Deposition
BM	: Ball Milling
BGTC	: Bottom Gate Top Contact
CO	: Carbon Monoxide
CTE	: Coefficient Of Thermal Expansion
CDC	: Colossal Dielectric Constant
CMOS	: Complementary Metal Oxide Semiconductor
CP	: Co-Precipitation
D.I.	: Deionized
DLD	: Delay Line Detector
DTG	: Derivative Thermogravimetry
DSC	: Differential Scanning Calorimetry
DTA	: Differential Thermal Analysis
DCL	: Double-Ceramic-Layer
EDL	: Electric Double-Layer
EDS	: Energy Dispersive Spectroscopy
EBCs	: Environmental Barrier Coatings
FE-SEM	: Field Emission Scanning Electron Microscopy
FSP	: Flame Spray Pyrolysis
FTIR	: Fourier Transform Infrared
FDTR	: Frequency-Domain Thermoreflectance Technique
FM	: From Ferromagnetic
FWHM	: Full Width Half Maximum
GSD	: Grain Size Distribution
GI-XRD	: Grazing Incidence X-Ray Diffraction
HESOTF	: High Entropy Spinel Oxide Thin Film
HEAs	: High Entropy Alloys

HECs	: High Entropy Ceramics
HEFO	: High Entropy Fluorite Oxide
HEMs	: High Entropy Materials
HEOF	: High Entropy Oxide Film
HEOs	: High Entropy Oxides
HEPOF	: High Entropy Perovskite Oxide Film
HERO	: High Entropy Rocksalt Oxide
HESO	: High Entropy Spinel Oxide
HT	: Hydrothermal
HTT	: Hydrothermal Treatment
IGZO	: Indium Gallium Zinc Oxide
ITO	: Indium Oxide
IZO	: Indium Zinc Oxide
IR	: Infra-Red
ICSD	: Inorganic Crystal Structure Database
IC	: Integrated Circuit
ICDD	: International Centre For Diffraction Data
LDHs	: Layered Double Hydroxides
LED	: Light-Emitting Diode
LIPS	: Lithium Polysulfides
MS	: Magnetron Sputtering
MM	: Mechanical Mixing
M-OH	: Metal Hydroxide
MIM	: Metal Insulator Metal
MOSFET	: Metal Oxide Semiconductor Field Effect Transistor
M-O	: Metal-Oxygen
ME	: Methoxy Ethanol
ME-REOs	: Multi-component Equiatomic Rare Earth Oxides
NCs	: Nanocrystals
NSP	: Nebulized Spray Pyrolysis
OLEDs	: Organic Light-Emitting Diodes

PM	: Physical Mixing
PVD	: Physical Vapor Depositions
PCM	: Polymeric Complex Method
PS	: Polymeric Synthesis
PVP	: Polyvinylpyrrolidone
PLD	: Pulsed Laser Deposition
RF	: Radio Frequency
RFID	: Radio Frequency Identification
RFMS	: Radio-Frequency Magnetron Sputtering
RE	: Rare-Earth
REZ	: Rare-Earth Zirconate
RE-HEO	: Rare-Earth-Based HEO
RCP	: Reverse Co-Precipitation
RMS	: Root Mean Square
STEM-EDX	: Scanning Transmission Electron Microscopy – Energy-Dispersive X-Ray Spectroscopy
SWCNTs	: Single-Walled Carbon Nanotubes
SG	: Sol-Gel
SSR	: Solid State Reaction
SCS	: Solution Combustion Synthesis
SCBM	: Sono Chemical Based Method
SPS	: Spark Plasma Sintering
SS	: Subthreshold Swing
SAHM	: Surfactant-Assisted Hydrothermal Method
TBC	: Thermal Barrier Coating
TGA	: Thermogravimetric Analysis
TFT	: Thin Film Transistor
TDTR	: Time-Domain Thermoreflectance Technique
TMDs	: Transition Metal Dichalcogenides
TMC	: Transitional Metal Chalcogenide
TM	: Transition-Metal

TM-HEO	:	Transition-Metal High Entropy Oxide
TM-RE-HEO	:	Transition-Metal-Rare Earth High Entropy Oxide
TA	:	Transverse Acoustic
UV	:	Ultra Violet
UV-Vis	:	Ultraviolet-Visible
XAS	:	X-Ray Absorption Spectroscopy
XRD	:	X-Ray Diffractometer
XPS	:	X-Ray Photoelectron Spectroscopy
YIO	:	Yttrium-Doped In_2O_3
ZFCW	:	Zero Field Cooling
ZFCW	:	Zero-Field Cooling
ZTO	:	Zinc Tin Oxide

LIST OF SYMBOLS

A	: Area of the Parallel Plate Electrode
a and c	: Lattice Parameter
C_i	: Capacitance Per Unit Area
CMAS	: CaO-MgO-Al ₂ O ₃ -SiO ₂
d	: Distance Between the Parallel Plates
κ	: Dielectric Constant
k_B	: Boltzmann's Constant
MoSi ₂	: Molybdenum Disilicide
M ₂ SiO ₅	: Monosilicates
M ₂ Si ₂ O ₇	: Disilicates
R	: Universal Gas Constant
S	: Entropy
Si	: Silicon
ΔG_{mix}	: Free Energy of Mixing
ΔS_{mix}	: Entropy of Mixing
ΔH_{mix}	: Enthalpy of Mixing
ΔS_{config}	: Change in Configurational Entropy
v	: Metal Elements Oxidation State
φ	: Fuel-to-Oxidizer Ratio
ϵ_o	: Dielectric Constant of Free Space
θ	: Bragg Reflection Angle
λ	: Wavelength

Page left intentionally blank



CHAPTER 1

INTRODUCTION

Page left intentionally blank

CHAPTER 1

INTRODUCTION

In modern electrical and electronic power systems, energy storage dielectric capacitors are essential (Chu et al. 2006). These capacitors now face more demands due to rapid growth, including long cycle life and ultrafast charging/discharging speed (Wang et al. 2021a). Despite significant development, the relatively limited storage capacity compared to other electrochemical devices like batteries has been an obstacle in capacitors to miniaturization, integration, and cost-effectiveness (Chu et al. 2006; Li et al. 2020b; Wang et al. 2021a). Thus, high- κ oxide dielectrics serve as remedy in view of its high demand in the present digital world due to the requirements such as excellent stability, energy efficiency, high yield, economic processes, flexible wide-area manufacturing, and sustainable electronics (Robertson 2004). The solution-processed high- κ oxide dielectrics have shown remarkable progress in the field of sensors, microelectronics, and wearables due to its enhanced electronic properties. Solution-processed high- κ oxide dielectrics are known for their high mechanical tolerance, and excellent chemical and thermal stability, which play a crucial role in the performance of many electronic, energy storage, and memory devices. These characteristics lead to suppressed tunneling effect, easy miniaturization, and low input power operation (Liu et al. 2018).

Although SiO_2 is an industrial-grade dielectric, its low relative permittivity/dielectric constant ($\kappa \approx 3.9$) demands high operating voltage in thin film transistors (TFTs) (Moore 1998; Robertson and Wallace 2015). The thin SiO_2 (≈ 1.2 nm) faces a significant leakage current density of the order $> 1 \text{ A.cm}^{-2}$ at 1 V due to tunneling (Lo et al. 1997; Robertson and Wallace 2015). Thus, it imposes a substantial restriction on scaling. Hence, with the great demand for miniaturized electronics, large-scale integration requires a revisit to dielectric scaling. Further, high- κ metal oxides facilitate a thicker layer with the same capacitance, reducing leakage current as the probability of tunneling drops exponentially with thickness (Wong 2011). The outstanding dielectric is not just one with high dielectric constant; instead, a series of requirements, such as sufficient band offset ($> 5 \text{ eV}$), robust atomic-scale roughness,

and less prone to moisture adsorption, must be fulfilled to use it as a passive layer in the TFT stack (Liu et al. 2018). Besides these requirements, the deposition of dense metal oxides has always been a center of interest. In vapor-phase sputter deposition, the growth of thin films is relatively less cumbersome but needs capital-intensive deposition techniques. In contrast, with recent advancements in the field, atmospheric-pressure solution-phase deposition is more straightforward and can be fulfilled even on flexible polymeric substrates (Pasquarelli et al. 2011). As specific to the solution-processed thin films, the as-deposited films are thermally treated (or processed under photo-irradiation) at a temperature where the chemical ingredients undergo decomposition to form low-molecular-weight gaseous products, removal of which leaves a metal-oxygen-metal frame. Improving the overall properties of solution-processed high- κ oxide dielectrics can be challenging as ambient conditions like temperature and humidity affect the device's reproducibility, properties, and performance. This can be resolved by either doping or increasing the number of cations in the metal oxide (Wang et al. 2018a).

In this period of material growth, there is a perpetual and endless hunt for novel advanced materials having tailorable properties. Identifying and developing a new group of materials has always been a dynamic prospect for future technological advancements and discoveries. Innovations in materials lead to the discovery of new challenges and opportunities for researchers. Lately, configurational entropy-based concepts have drawn lot of attention, which can be used to design materials and methods for wide range of applications. In 2004, Yeh et al. (Yeh et al. 2004b) and Cantor et al. (Cantor et al. 2004) invented high entropy alloys (HEAs) with equimolar metallic composition, which offered the opportunity to influence the phase stability of solid solutions over a precise control of configurational entropy (Sarkar et al. 2019; Yeh et al. 2004a). HEAs have great recognition due to their unique compositions, microstructures, and adaptable properties in comparison with conventional alloys. Impelled from the exceptional hallmarks of HEAs, entropy engineering has flourished as an effective approach in non-metallic systems like high entropy ceramics (HECs). There have been several successful developments of novel HECs materials, including high entropy oxides (Bérardan et al. 2016a), high entropy carbides (Castle et al. 2018),

high entropy borides (Gild et al. 2016), high entropy silicides (Gild et al. 2019), and high entropy nitrides (Jin et al. 2018; Salian and Mandal 2022a; b). In 2015, Rost et al. (Rost et al. 2015) successfully explored the oxide system $(\text{Mg}_{0.2}\text{Zn}_{0.2}\text{Cu}_{0.2}\text{Co}_{0.2}\text{Ni}_{0.2})\text{O}$ which comprises five different cations in equiatomic ratios, results in a single-phase oxide system due to the entropy-driven structural stabilization effect with tailorable electrochemical properties. Thus, the authors coined a catchy new name, “entropy stabilized oxide” (Rost et al. 2015). Subsequently, Bérardan et al. reported a more generic terminology, “high-entropy oxides (HEOs)”, akin to “HEAs” and has been set up to categorize multi-cationic equiatomic oxide systems (Berardan et al. 2017; Bérardan et al. 2016a; b).

The basic perception of entropy stabilization is based upon the potential to sustain a single-phase crystal structure with an increase in the ΔS_{Config} of the system. Stabilization can be achieved by increasing the elements in the system, which are randomly distributed in a single lattice. From the fundamentals of Gibb’s phase rule, an increase in ΔS_{Config} higher than enthalpy conquers the enthalpy of mixing with a reduction in free energy, which results in stabilization into a single phase (Lei et al. 2019). But if the entropy is not able to counterbalance the enthalpy, then secondary phases will appear. Thus, the stabilization of phases may depend on various other factors that are yet to be investigated but are predicted to be mainly dependent on ΔS_{Config} . A few selection rules with regard to ionic radii, crystal structure, and miscibility of the elements have to be followed before selecting the candidates for HEO (Rost et al. 2015). Since the discovery of single-phase rocksalt type HEOs ($(\text{Mg}_{0.2}\text{Zn}_{0.2}\text{Cu}_{0.2}\text{Co}_{0.2}\text{Ni}_{0.2})\text{O}$) by Rost et al. (Rost et al. 2015), the composition has drawn more interest due to its dielectric and electrochemical properties (Berardan et al. 2017; Bérardan et al. 2016a; Sarkar et al. 2018b) and the study on HEOs is mainly concentrated on systems with single-phase rocksalt structures. But, with time, the broad array of HEOs has widened to comprise a single-phase spinel, fluorite, perovskite, magentopulmbite, and several other types (Salian and Mandal 2022a; b).

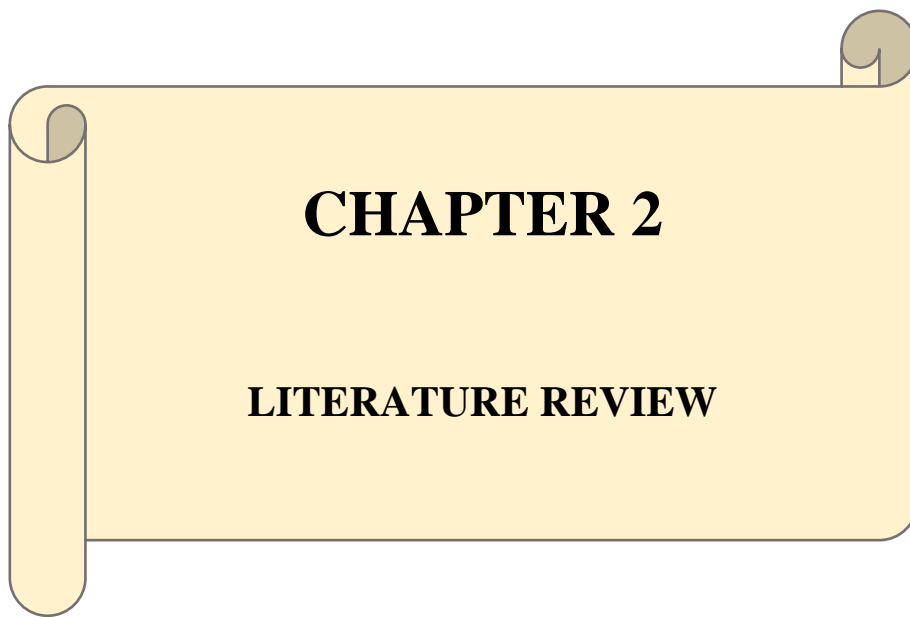
The HEOs showcase a homogeneous distribution of particles with appealing morphologies like spherical, cuboidal agglomerates and hexagonal-shaped crystals, etc, (Dąbrowa et al. 2018; Djenadic et al. 2017; Vinnik et al. 2019). HEOs are synthesized

via several techniques such as spray pyrolysis, sol-gel combustion, solid-state reaction, co-precipitation, and so on. Ultrafine nanocrystalline HEO films were grown on a variety of substrates with the help of radiofrequency (RF) magnetron sputtering (Bi et al. 2020; Nguyen et al. 2020b; Yang et al. 2019) and pulsed laser deposition (PLD) (Braun et al. 2018; Kotsonis et al. 2020; Rak et al. 2016; Sharma et al. 2018) etc. HEOs find applications in batteries, ferroelectrics, magnetic, catalytic, thermal barrier coatings, etc (Salian and Mandal 2022b). Moreover, the necessity for HEOs as a passive-dielectric in TFTs can be vital due to its structural stability of multi-cationic configuration, by maintenance of structural chaos at the atomic level (Salian and Mandal 2022a). The current thesis is not only restricted to the HEOs but also the fabrication of the same via a low-temperature aqueous combustion synthesis technique. Three systems of HEO powder are developed via solution combustion processing and employed the same as functional-dielectric. The first system with a rocksalt structure was based on Co, Cu, Mg, Zn, and Ni cations, the second system with a spinel structure was based on Co, Mn, Ni, Fe, and Cr cations and the third system with a fluorite structure comprised Ce, La, Pr, Sm, and Y cations. The phase-stabilization behavior of all the HEO systems with respect to temperature changes is briefly investigated. In addition, a systematic study of phase-stabilized HEO with their respective individual parent metal oxide and a lesser-cation system is provided. Further, a capacitor developed using HEO as a dielectric is demonstrated with the display of dielectric constant and loss, creating a new bridge between the HEO and electronics. Finally, the applications of the HEO in TFTs as a passive dielectric layer are analyzed. The subsequent paragraph describes the flow of the thesis.

CHAPTER 2 is devoted to the current literature in the existing area of research. **CHAPTER 3** is dedicated to the synthesis, characterization and investigation of dielectric properties on the phase-stabilized solution combustion processed high entropy rocksalt oxide (CoCuMgZnNi)O. **CHAPTER 4** is assigned to the synthesis, examination of dielectric properties on the phase-stabilized solution combustion processed high entropy spinel oxide (CoCrFeMnNi)O and their characterization studies. **CHAPTER 5** is allocated to the synthesis, characterization and study of dielectric properties on the phase-stabilized solution combustion processed high

entropy fluorite oxide (CeLaPrSmY)O. **CHAPTER 6** is allotted to the fabrication of low-temperature solution combustion processed high entropy spinel oxide (CoMnNiFeCr)O thin films, its characterization studies, and application in thin film transistors as a passive dielectric layer, respectively. Finally, **CHAPTER 7** is devoted to the conclusion and the future scope of the existing studies.

Page left intentionally blank



CHAPTER 2

LITERATURE REVIEW

The contents of this chapter have been published in the review articles:

Ashritha Salian, Saumen Mandal, **Crit. Rev. Solid State Mater. Sci.**, 47(2), 147-193, (2021).

Ashritha Salian, Saumen Mandal, **Bull. Mater. Sci.**, 45(1), 1-21, (2022).

Ashritha Salian, Pradyut Sengupta, Itesha VA, Avinash Gowda, Saumen Mandal, **Int. J. Appl. Ceram. Technol.**, 20(5), 2635-2660, (2023).

Page left intentionally blank

CHAPTER 2

LITERATURE REVIEW

2.1 Introduction

The development of novel research methods and the creation of materials with distinctive structural characteristics have typically been the two main ways that research in the field of materials has advanced. Based on the concepts mentioned earlier, a novel strategy known as "high-entropy" has become well-known. The high-entropy strategy provides an unparalleled opportunity to find and investigate formerly unattainable characteristics of materials throughout the whole periodic table and providing a room for advancements in materials research community. Combining five or more essential elements to create a single system is part of the high-entropy approach to material design. This differs from a doped system because the amount of the dopant is constrained and can become unstable when the concentration is above a particular threshold. On the contrary, high entropy materials enable higher concentrations of every essential element without destabilizing the structure due to their better elemental mixing abilities. The individual essential elements interact synergistically to result in a complex system that provides the high entropy materials with distinctive features, which have a significant impact on the performance of high entropy material.

2.2 High entropy materials

Materials where high configurational entropy is used as a driving force for stabilization of the phase are termed high entropy materials (HEMs). High entropy of mixing leads to the stabilization of disordered solid solution with single-phase crystal structure over intermetallic and multiphase microstructures (Cantor et al. 2004; Feuerbacher et al. 2015; Senkov et al. 2011a). Generally, HEMs are placed at the core of a multinary phase diagram which is often the least investigated domain of material compositions; thus, unpredicted behaviors can be anticipated (Bérardan et al. 2016a; b; Miracle and Senkov 2017; Murty et al. 2019; Ye et al. 2016). The discovery of high entropy materials started with a metal system, which with years, slowly moved to ceramic systems, as depicted in timeline Fig. 2.1. In addition, HEMs are classified

based on the design of advanced materials via entropy engineering, as shown in Fig. 2.2 (Lei et al. 2019).

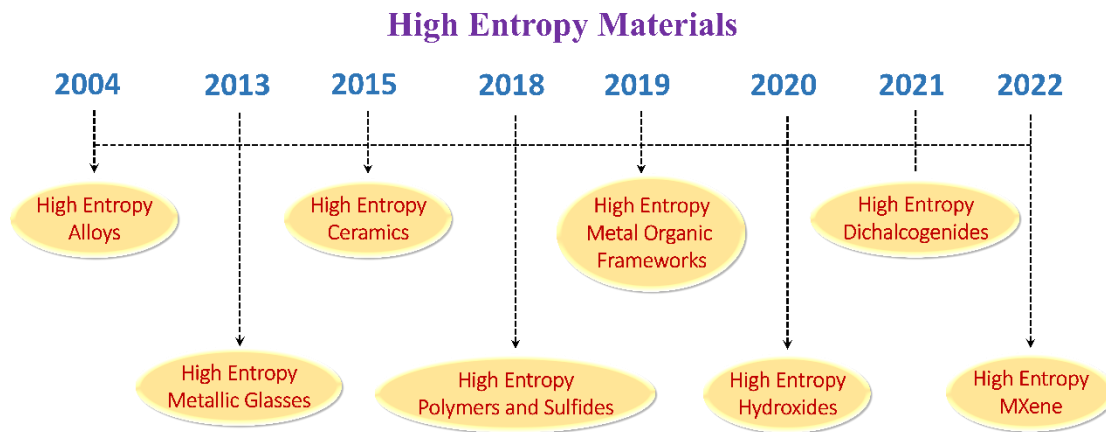


Fig. 2.1. Timeline depicting the era of high entropy materials (Salian et al. 2023b).

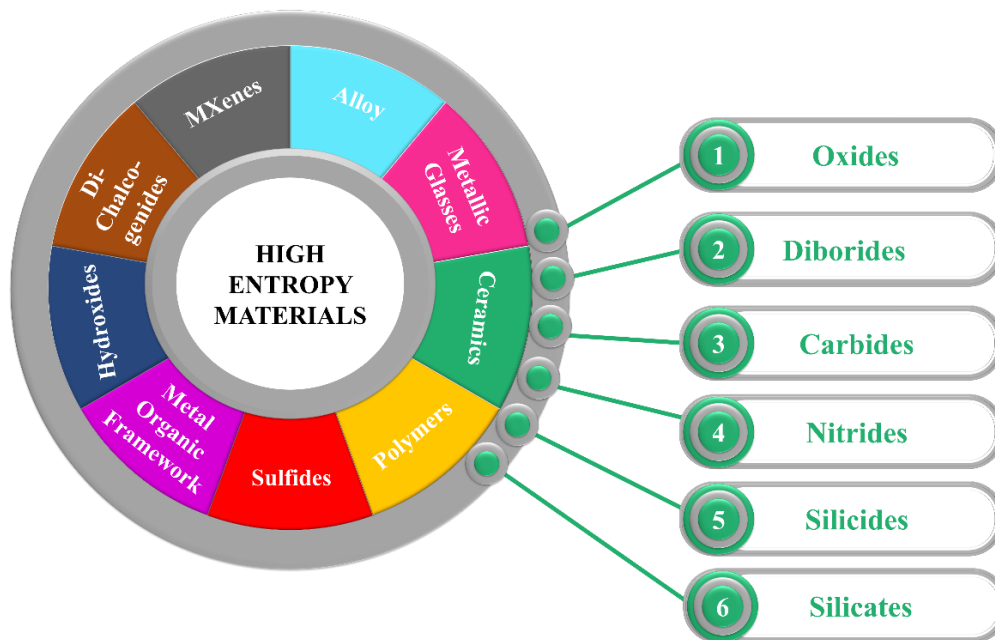


Fig. 2.2. Classification of high entropy materials (Salian and Mandal 2022b).

2.2.1 Alloys

HEAs are the first discovered material in the group of HEMs. The entropy engineering concept was initiated with phase stabilization of multiple metals. The incorporation of multiple (five or more) elemental species in equiatomic or nearly equiatomic portion into a single solid solution led to the discovery of CuCoNiCrAlFe and CuCoNiCrAlFeMoTiVZr HEAs (Yeh et al. 2004a). An increase in the number of

elements in the alloy increases the entropic contribution, which conquers the enthalpic contribution and hence stabilize the solid solution (George et al. 2019; Yeh et al. 2004a). HEAs can exhibit many new phenomena and properties similar to the components present or entirely different. Traditional alloys are based upon one and barely two elements with the incorporation of minor alloying, like nickel in superalloys, to obtain enhanced properties (Ye et al. 2016). In contrast to the same, the complex arbitrary arrangement of multiple elements and extraordinary chemical environment at the atomic level in HEAs like FeMnNiCoCr, VNbMoTaW, NbCrMoTaTiZr, TaNbHfZrTiMo, YGdTbDyLu, GdTbDbTmLu resulted in exceptional properties such as high thermal and phase stability, high hardness, high strength, excellent wear, corrosion, and fatigue resistance (Gludovatz et al. 2014; Hemphill et al. 2012; Juan et al. 2015; Li et al. 2016; Otto et al. 2013; Senkov et al. 2011b; a; Senkov and Woodward 2011; Shi et al. 2017; Takeuchi et al. 2014; Zou et al. 2015).

2.2.2 Metallic glasses

When metallic alloys are quickly quenched from the liquid state and still display an amorphous liquid structure at room temperature, they are termed metallic glasses (Wang 2014). Likewise, a class of amorphous alloys generally with three or more components but predicted on sole primary elements, Cu, Zr, Ce, and Fe, depict bulk metallic glasses. Therefore, utilizing the path used to develop HEAs, high entropy metallic glasses such as $\text{Sr}_{20}\text{Ca}_{20}\text{Yb}_{20}\text{Mg}_{20}\text{Zn}_{20}$, $\text{Er}_{20}\text{Tb}_{20}\text{Dy}_{20}\text{Ni}_{20}\text{Al}_{20}$, $\text{Zn}_{20}\text{Ca}_{20}\text{Sr}_{20}\text{Yb}_{20}(\text{Li}_{0.55}\text{Mg}_{0.45})_{20}$, $\text{Pd}_{20}\text{Pt}_{20}\text{Cu}_{20}\text{Ni}_{20}\text{P}_{20}$, $\text{Ti}_{20}\text{Zr}_{20}\text{Cu}_{20}\text{Ni}_{20}\text{Be}_{20}$, $\text{AlCoCrFeNiZr}_{0.6}$, $\text{Fe}_{20}\text{Si}_{20}\text{B}_{20}\text{Al}_{20}\text{Ni}_{20}$, $\text{CoCrCuFeNiZr}_{0.6}$, $\text{Fe}_{20}\text{Si}_{20}\text{B}_{20}\text{Al}_{20}\text{Nb}_{20}$, was developed with the superior glass-forming ability with excellent properties which include high strength, wear resistance, hardness, thermal stability, etc (Ding and Yao 2013; Gao et al. 2011; Guo et al. 2013; Lei et al. 2019; Ma et al. 2002; Takeuchi et al. 2011, 2016; Wang et al. 2014b; Zhao et al. 2011).

2.2.3 Ceramics

2.2.3.1 Oxides

The concept of entropy engineering led Rost et al. to discover a new class of oxide systems, “high entropy oxides” (HEOs) (Rost et al. 2015). HEOs are a class of

HECs and a field based on the generic concept of high entropy materials, i.e., to use multiple oxides (five or more) to acquire high configurational entropy of the system analogous to HEAs, which intensifies the formation of single-phase crystal structures (Rost et al. 2015). Rost et al. first-ever reported that the entropic contribution to Gibb's free energy can be utilized to stabilize a new oxide phase at higher temperatures (Rost et al. 2015).

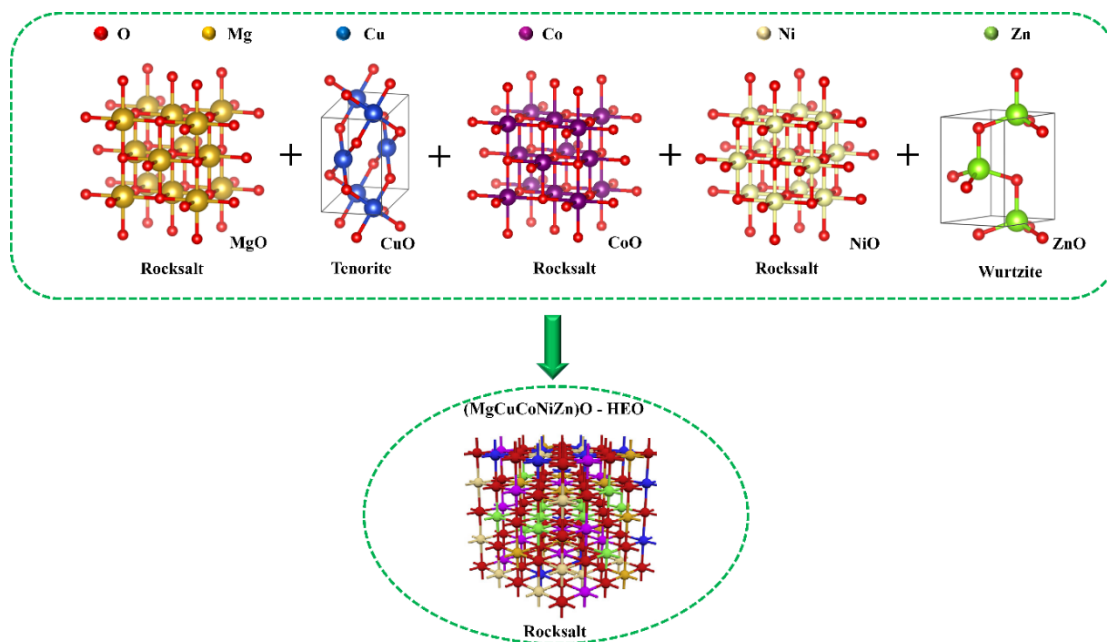


Fig. 2.3. Formation of a single-phase rocksalt crystal structure of HEO (MgCuCoNiZn)O (Zheng et al. 2019).

Fig. 2.3 represents a simulative crystal structure of HEO of composition (MgCoNiCuZn)O (Zheng et al. 2019), where inclusion of multiple cations with different crystal structures (rocksalt: MgO, CoO, NiO; Tenorite: CuO; Wurtzite: ZnO) stabilize into single-phase crystal structure HEOs (rocksalt: (MgCuCoNiZn)O). It led to novel and surprising properties because of the interaction between various metal cations. HEOs are classified based on the element used, such as transition-metal-based HEO (TM-HEO), for example (MgCuNiCoZn)O, (SnCeHfZrTi)_{0.2}O₂, (CoCrFeMnNi)₃O₄ (Bérardan et al. 2016a; b; Biesuz et al. 2018; Chen et al. 2018b; Dąbrowa et al. 2018; Dupuy et al. 2019; Hong et al. 2019; Kotsonis et al. 2018; Mao et al. 2019c; a; Meisenheimer et al. 2017; Qiu et al. 2019; Rost et al. 2015; Sarkar et al. 2017a, 2018b; Wang et al. 2019b), rare-earth-based HEO (RE-HEO) like

(Ce,Gd,La,Nd,Pr,Sm,Y)O (Jiang et al. 2018b; Sarkar et al. 2017b) and mixed HEO (TM-RE-HEO) as in $(\text{SmGdNdYLa})_{0.2}(\text{MnCoFeNiCr})_{0.2}\text{O}_3$ (Sarkar et al. 2018a; Witte et al. 2019).

2.2.3.2 Diborides

Borides of the groups IVB and VB transition metals, with boron (ZrB_2 , ReB_2 , WB_4 , CrB_4 , MnB_4), are an unique category of ultra-high temperature ceramics (Fahrenholtz and Wuchina 2014). These materials are among the appealing candidates for several applications, including microelectronics, cutting tools, and aerospace due to their high melting temperature, high-temperature strength, thermomechanical and chemical properties (Akopov et al. 2018; Holleck 1986; Matkovich 1977). Following the principle of HEAs, entropy engineering is applied to fabricate several high entropy diborides such as $(\text{Hf}_{0.2}\text{Zr}_{0.2}\text{Ta}_{0.2}\text{M}_{0.2}\text{Ti}_{0.2})\text{B}_2$ (M= Nb, Mo, Cr), $(\text{Hf}_{0.2}\text{Zr}_{0.2}\text{Ta}_{0.2}\text{Nb}_{0.2}\text{Ti}_{0.2})\text{B}_2$, $(\text{Hf}_{0.2}\text{Zr}_{0.2}\text{Mo}_{0.2}\text{Nb}_{0.2}\text{Ti}_{0.2})\text{B}_2$, $(\text{Hf}_{0.2}\text{Zr}_{0.2}\text{Ta}_{0.2}\text{Cr}_{0.2}\text{Ti}_{0.2})\text{B}_2$, $(\text{Hf}_{0.2}\text{Mo}_{0.2}\text{Ta}_{0.2}\text{Nb}_{0.2}\text{Ti}_{0.2})\text{B}_2$, $(\text{Ti}_{0.2}\text{Hf}_{0.2}\text{Zr}_{0.2}\text{Nb}_{0.2}\text{Ta}_{0.2})\text{B}_2$, which exhibits novel structural and mechanical properties (Gild et al. 2016; Liu et al. 2019; Mayrhofer et al. 2018; Moraes et al. 2018; Tallarita et al. 2019; Wang et al. 2018b; Zhang et al. 2019c).

2.2.3.3 Carbides

Analogous to borides, carbides are also one of the special class of ultra-high temperature ceramics, with potential applications in aerospace and nuclear energy due to their higher melting temperatures (Fahrenholtz and Wuchina 2014; Holleck 1986; Williams 1971). Akin to the ground-breaking studies presented in the alloy, oxide, and boride communities, high entropy carbides such as $(\text{Zr}_{0.25}\text{Nb}_{0.25}\text{Ti}_{0.25}\text{V}_{0.25})\text{C}$ (Ye et al. 2019), $(\text{Ti-Zr-Hf-V-Nb-Ta})\text{C}$ (Gorban' et al. 2017), $(\text{Ti-Zr-Hf-Nb-Ta})\text{C}$ (Vladescu et al. 2016), $(\text{Hf-Ta-Zr-Ni})\text{C}$ (Castle et al. 2018), $(\text{V}_{0.2}\text{Nb}_{0.2}\text{Ta}_{0.2}\text{Mo}_{0.2}\text{W}_{0.2})\text{C}$ (Harrington et al. 2019), $(\text{TiNbTaZrHf})\text{C}$ (Sure et al. 2020) exhibited excellent tribological behavior, high elastic modulus, and electrochemical performance (Castle et al. 2018; Sure et al. 2020).

2.2.3.4 Nitrides

Transitional metal nitrides are known for their excellent properties, such as high hardness, good adhesion to the substrate, good oxidation resistance, low friction, and

so on (Chauhan and Rawal 2014; Lai et al. 2006; Wang et al. 2018b). Exploration of multielement transitional metal nitrates system turned out to be of great interest as unique properties were explored. Interestingly, adopting the idea of entropy engineering, several research teams went beyond the traditional quaternary transitional metal nitrates system and synthesized several high entropy nitride systems such as (AlCrTaTiZr)N (Lai et al. 2006), (AlCrMoSiTi)N (Chang et al. 2008a; b), (AlMoNbSiTaTiVZr)₅₀N₅₀ (Tsai et al. 2008), (Ti-Hf-Zr-V-Nb)N (Pogrebnyak et al. 2014), (AlCrNbSiTiV)N (Huang and Yeh 2010), (AlCrMoTaTiZr)N (Cheng et al. 2011), (TiZrHfVNbTa)N (Pogrebnyak et al. 2016) with outstanding performance in comparison to the traditional transitional metal nitrates (Hsieh et al. 2013).

2.2.3.5 Silicides

Metal silicides are a compound of silicon (Si) known for high melting point, high fracture toughness, high hardness, high-temperature oxidation and creep resistance, excellent chemical stability, and low thermal and electrical conductivity, which directs its applications in high-temperature protective coatings and structural materials, heating elements and microelectronic devices (Petrovic and Vasudevan 1999; Zhang and Östling 2003). The most well-known material of silicides is undoubtedly molybdenum disilicide (MoSi₂) because of its combined attractive properties like relatively low density (6.23 g.cm⁻³), high melting point (2030 °C), and excellent high-temperature oxidation and corrosion resistance. For decades, MoSi₂ has been produced on a large scale and used extensively as resistive heating components up to 1800 °C in ambient conditions. But, fatal oxidation at low temperatures, inherent brittleness, and poor toughness of metal silicides hinders its use in vast engineering applications (Jeng and Lavernia 1994; McKamey et al. 1992). To tackle the drawbacks faced by the metal silicides, a variety of high entropy silicides and high entropy alumino silicides like (Mo_{0.2}Nb_{0.2}Ta_{0.2}Ti_{0.2}W_{0.2})Si₂ (Gild et al. 2019), (Ti_{0.2}Zr_{0.2}Nb_{0.2}Mo_{0.2}W_{0.2})Si₂ (Qin et al. 2019, 2020), (Mo_{0.2}W_{0.2}Cr_{0.2}Ta_{0.2}Nb_{0.2})Si₂ (Liu et al. 2020a; e), (Nb_{0.25}Ta_{0.25}Hf_{0.25}Ti_{0.25})Si₂ (Liu and Ning 2020), and (Mo_{0.25}Nb_{0.25}Ta_{0.25}V_{0.25})(Al_{0.5}Si_{0.5})₂ (Wen et al. 2020) have been developed. High entropy silicides displayed elevated properties than the traditional silicides, such as high melting point, high fracture toughness, high hardness, high-temperature oxidation,

corrosion and creep resistance, improved stiffness, excellent chemical stability, and low thermal and electrical conductivity. The above-mentioned properties could serve as a driving force towards design of the applications as insulation devices in the field of microelectronics, high-temperature oxidation resistance coatings for refractory alloys in jet engines and nuclear reactors, and structural materials for ultra-high temperature applications.

2.2.3.6 Silicates

A large part of the earth's crust is comprised of primitive oxide ceramics, like silica and silicate as natural minerals. Metal silicates are the compounds of Si with oxygen known for their high melting point, superior corrosion resistance in harsh environments, high-temperature durability and elasticity, excellent phase, thermal and chemical stability, low thermal conductivity, good thermal shock resistance, matched coefficient of thermal expansion (CTE) with Si-based substrates making them the most promising materials for environmental and thermal barrier coating applications (Turcer and Padture 2018). Metal silicates include monosilicates (M_2SiO_5) and disilicates ($M_2Si_2O_7$). The CTE of monosilicates is larger than disilicates and other SiC/SiC-based composites, which unfortunately leads to crack and peeling off and prevents its usage as an environmental coating for an extended lifetime. Meanwhile, the disilicates face instability in phase at high temperatures because of abundant phase transformation mechanisms, restricting their broad usage (Ren et al. 2019; Sun et al. 2020). To tackle the drawbacks faced by the metal silicates, high entropy silicates such as (Sc, Y, Nd, Dy, Er, Yb) $_2SiO_5$ (Ridley et al. 2020), (Lu $_{0.2}$ Yb $_{0.2}$ Er $_{0.2}$ Ho $_{0.2}$ Y $_{0.2}$) $_2SiO_5$ (Cao et al. 2021), and (Gd $_{1/6}$ Tb $_{1/6}$ Dy $_{1/6}$ Tm $_{1/6}$ Yb $_{1/6}$ Lu $_{1/6}$) $_2Si_2O_7$ (Sun et al. 2020), have been developed. The high entropy silicates showed improved properties than the traditional silicates like high melting point, superior corrosion resistance in harsh environments (from water vapor and low melting point oxide mixture CaO-MgO-Al $_2$ O $_3$ -SiO $_2$ (CMAS)), high-temperature durability and elasticity, excellent phase, thermal and chemical stability, low thermal conductivity, good thermal shock resistance, matched CTE with Si-based substrates. The catastrophe faced by the traditional silicates with regard to CTE and instability in phase at high temperatures, high entropy silicates displayed low CTE that matched with SiC/SiC-based composites and Si bond coat and also had excellent phase

stability at high temperatures (Abrar et al. 2023; Chen et al. 2022; He et al. 2023; Ren et al. 2019; Ridley et al. 2020).

2.2.4 Polymers

Organic materials are a large pool of carbon-based compounds, where co-crystallization of two dissimilar organic compounds is feasible. It widens the feature of organic crystals; hence, makes it a possible approach to develop high entropy polymers. Unlike metal alloys, the origin of entropy in organic co-crystals is from the acceptable change in molecular conformation as the spatial packing scheme of structural units is established through lattice interactions and the axial rotation of structural units within the crystalline lattice (Miranda L. Cheney et al. 2007; Oliveira et al. 2011). Moreover, the random incorporation of a variety of different structural units, such as trifluoro ethylene and vinylidene, within the lattice packing might result in high entropy polymers (Lei et al. 2019; Wu et al. 2018).

2.2.5 Sulfides

High entropy sulfides are materials consisting of multiple cations and sulfides acting as an anion. Cu-S are compounds with a diamond-like structure possess low thermal conductivity, is of low cost, and are eco-friendly materials (He et al. 2014; Kikuchi et al. 2016; Wang et al. 2016b). The anharmonic rattling mode in $\text{Cu}_{12}\text{Sb}_4\text{S}_{13}$ tetrahedrite containing five-atom atomic cage $\text{Sb}(\text{CuS}_3)\text{Sb}$ is considered to be key for discovering state-of-the-art thermoelectrics, where Cu-S acts as parent material (Lai et al. 2015; Vaqueiro et al. 2015). Considering this Cu-S system as a parent material, high entropy sulfides with multiple cations ($\text{Cu}_5\text{SnMgGeZnS}_9$, $\text{Cu}_3\text{SnMgInZnS}_7$) were fabricated (Lei et al. 2019; Zhang et al. 2018).

2.2.6 Metal-organic frameworks

Metal-organic frameworks are a sort of porous polymeric material comprised of metal ions interlinked by organic bridging ligands, which are applicable in a wide variety of fields, such as thin-film devices, catalysis, membranes, and biomedical imaging (Furukawa et al. 2010; James 2003; Rowsell and Yaghi 2004). Therefore, with the help of entropy engineering, the synthesis of high entropy metal-organic

frameworks with the incorporation of multiple metal ions appears to be highly possible (Lei et al. 2019; Zhao et al. 2019a).

2.2.7 Hydroxides

Layered double hydroxides (LDHs) are a form of ionic lamellar blends composed of positively charged brucite-like piles with a high capacity of anions and solvation molecules intercalation, finds its broad application in fields such as catalysis, magnetization, biomedical science, electrochemistry, environmental protection, and polymerization (Lei et al. 2019; Theiss et al. 2014; Wang and O'Hare 2012). The general layered sequence in LDHs is represented by the formula $[AcB Z AcB]_n$, where A and B denote the layers of hydroxide anions (HO^-), Z is the neutral molecules (such as water), and layers of other anions and c represents the layers of metal cations, whereas universally it is scripted as $[M^{2+}_{1-x}M^{3+}_x(OH)_2][A^{n-}]_{x/n} \cdot zH_2O$, where metal ion M^{3+} can substitute M^{2+} , and A^{n-} is an exchangeable ion, namely Cl^- , OH^- , CO_3^{2-} and NO_3^- (Wang and O'Hare 2012). There are several reports on various binary LDHs with no research on multicomponent (<3) LDHs. Therefore, by applying the entropy concepts with the addition of a multicomponent in the M^{2+} cation site, the techniques to synthesize high entropy hydroxides was made (Lei et al. 2019).

2.2.8 Dichalcogenides

Among the advanced materials, transition metal dichalcogenides are one class of layered materials, has very strong in-plane bonding and weaker bonding at the outer plane, thereby permits exfoliation in 2D layers of single unit cell thickness, therefore, enables it to be applicable in optical devices, electronics, catalysis, etc (Chhowalla et al. 2013; Lei et al. 2019; Lv et al. 2015; Wang et al. 2012). Henceforth, with the help of entropy engineering, it was highly possible to form layered structured high entropy dichalcogenides with unique properties (Cavin et al. 2021).

2.2.9 MXenes

The family of two-dimensional (2D) materials known as MXenes includes transition metal carbides and nitrides. The composition of MXenes 2D flakes is currently restricted to one or two transition metals and has $n+1$ ($n = 1-4$) atomic layers of transition metals interspersed by carbon/nitrogen layers. MXenes that have so far

been synthesized exhibit excellent catalytic and electrochemical activity (Lim et al. 2020), high in-plane mechanical stiffness (up to 386 ± 13 GPa for $\text{Nb}_4\text{C}_3\text{T}_x$) (Lipatov et al. 2020), and metallic electrical conductivity (up to $20,000 \text{ S}\cdot\text{cm}^{-1}$ for $\text{Ti}_3\text{C}_2\text{T}_x$) (Mathis et al. 2021). Therefore, with the help of entropy engineering, high entropy Mxenes with the multi-principal elements (TiVNbMoC_3) and (TiVCrMoC_3) were synthesized first by Nemani et al (Nemani et al. 2021).

2.3 Concept of entropy engineering

In the 1870s, Ludwig Boltzmann defined the term “entropy” during the evaluation of the analytical conduct of the microscopic components of the system (Gearhart 1990; Ruffa 1982). Following Boltzmann’s hypothesis on the relationship between the probability of the existence of the given state and the entropy of a system in a given state (Yeh et al. 2004a), entropy may be calculated from the following equation.

$$S = k_B \ln \omega \quad (2.1)$$

Where S is the entropy contribution to the system for the given state, k_B is Boltzmann’s constant ($1.3 \times 10^{-23} \text{ J}\cdot\text{K}^{-1}$), and ω is the probability of existence of the given state (Lei et al. 2019). An alloy can form a solid solution depending on the relative free energies (George et al. 2019). Hence, the reliance of the free energy of mixing (ΔG_{mix}) on the entropy of mixing (ΔS_{mix}) and enthalpy of mixing (ΔH_{mix}) is as follows.

$$\Delta G_{mix} = \Delta H_{mix} - T\Delta S_{mix} \quad (2.2)$$

From equation 2.2, we understand that higher entropy of mixing ΔS_{mix} would lead to a lower Gibb’s free energy of mixing (ΔG_{mix}), which decides the stability of the system provided if the enthalpy of mixing (ΔH_{mix}) remains same. In other words, by increasing the configurational entropy (ΔS_{config}) of the system, it is possible to stabilize a single-phase crystal structure, which can be achieved by increasing the number of elements in the system, which gets randomly distributed on the same lattice sites (Lei et al. 2019). In evidence of this statement, Rost et al. has proved that the addition of a greater number of elements (> 3) to a given system increases ΔS_{config} and attains a peak value when all elements are present in an equiatomic fraction (Rost et al. 2015). Therefore, configuration entropy can be evaluated using equation 2.3.

$$\Delta S_{Config} = -R \left[\left(\sum_{i=1}^N x_i \ln x_i \right)_{cation-site} + \left(\sum_{j=1}^M x_j \ln x_j \right)_{anion-site} \right] \quad (2.3)$$

Where R is the universal gas constant ($8.314 \text{ J.K}^{-1} \text{ mole}$), and x_i and x_j depict the mole fraction of the elements found in the cation and anion sites, respectively. The participation of the anion site is anticipated to have only a minor effect on the ΔS_{Config} when compare to the cation site as only one anion (oxygen) is present in the system of HEOs.

A high entropy system may be characterized in two different ways using its core components and configurational entropy (Miracle and Senkov 2017). The first definition states that a system has high entropy if it has at least five major elements and their atomic concentrations are in between 5 % and 35 %. The composition of any minor elements present in the same system must be less than 5 at. %. Likewise, based on materials configuration entropy, Murty et al. (Murty et al. 2019) classified the materials with $\Delta S_{Config} > 1.5R$ as “high entropy”, $1.5R > \Delta S_{Config} \geq 1R$ as “medium entropy”, and $\Delta S_{Config} < 1R$ as “low entropy” systems as shown in Fig. 2.4. As illustrated in Fig. 2.5, the configurational entropy of a system gradually increases with increase in number of major elements, taken in equimolar concentration. As a result, the ternary alloy configuration entropy is greater than $1R$ ($1.1R$), but the value for quinary alloys is higher than $1.5R$ ($1.61R$). In other words, single-phase can be achieved in high entropy systems when $\Delta S_{Config} > 1.5R$, i.e., from equation 2.2 it is understood when the $\Delta S_{Config} > 1.5R$ the term $T\Delta S_{mix}$ becomes very high such that it dominates the free energy landscape ΔG_{mix} and overcomes the ΔH_{mix} . Consequently, different entropy systems have been categorized using $1.5R$ as the threshold value. At high temperatures, it is anticipated that a system with a value of R greater than 1.5 will defeat the ordering effects. Thus, the truth is that high temperatures are advantageous in the formation of single-phase high entropy systems. However, several studies show that at room temperature, these criteria for the formation of a stable single phase are violated. At room temperature, the configuration entropy gain is insufficient to counterbalance the ΔH_{mix} , as a result of an intermediate product with a higher enthalpy of mixing (Miracle and Senkov 2017; Murty et al. 2019; Sarkar et al. 2019). Thus, pointing out that ΔS_{mix} cannot be the only parameter to design high entropy systems. Therefore, it can be

inferred from the literature, equation (2.3) for entropy of mixing may be applicable at only high temperatures, but not at low temperatures (Liu et al. 2020d; McCormack and Navrotsky 2021; Sarkar et al. 2020a; Takeuchi et al. 2013; Ye et al. 2015, 2016; Zhang et al. 2014).

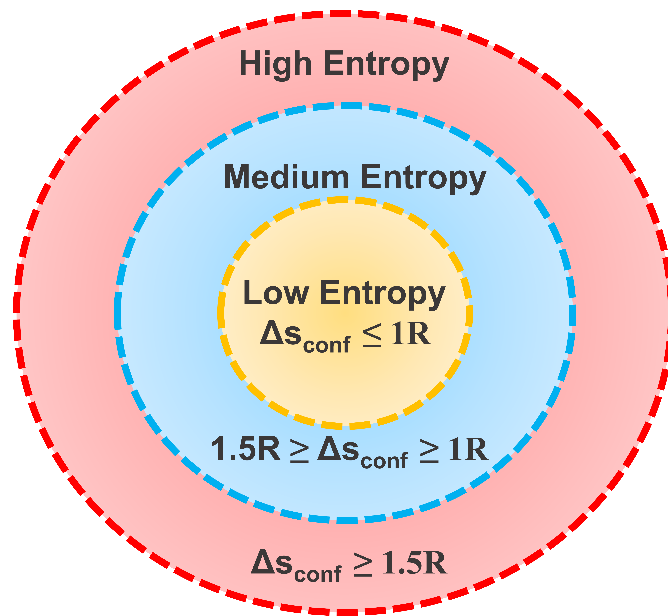


Fig. 2.4. Classification of materials based on configurational entropy.

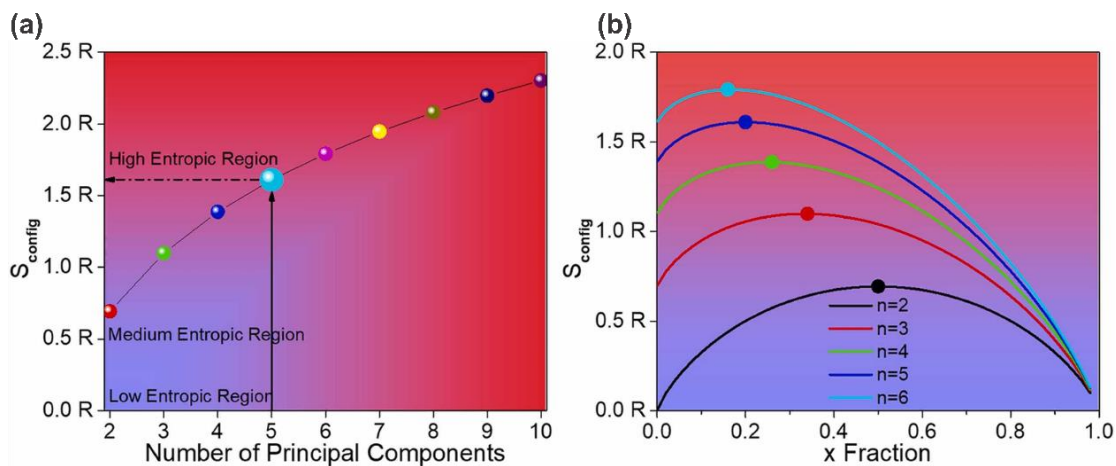


Fig. 2.5. (a) Principal elements and (b) their mole fractions (i.e., component cations) as a function of configurational entropy. The composition with the maximum configurational entropy will have an equimolar ratio of its primary components (the compositions with bold dots show these compositions) (Anandkumar and Trofimov 2023).

2.4 Primary effects in high entropy materials

High entropy materials show four main core effects as a result of their robust mixing nature: sluggish diffusion effect, high entropy effect, cocktail effect, and severe lattice distortion effect. Fig. 2.6 depicts the schematic representation of the primary effects in high entropy materials.

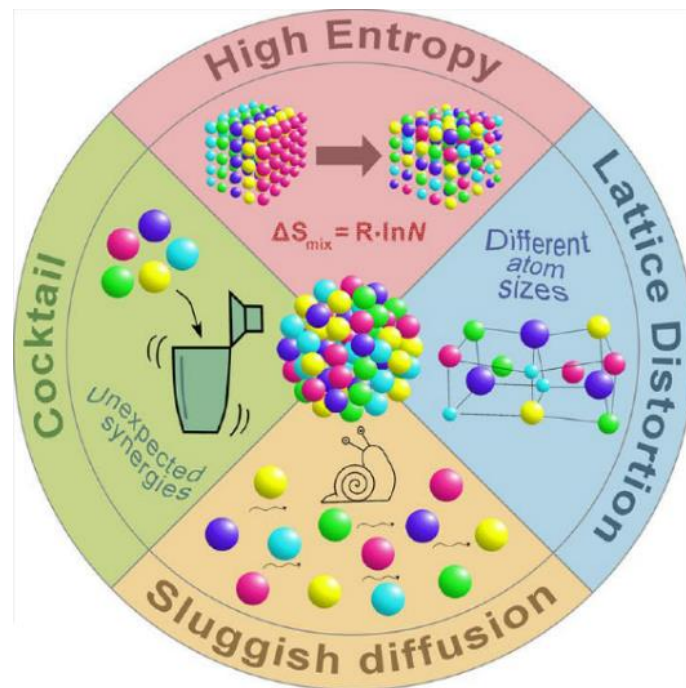


Fig. 2.6. Schematic representation of the primary effects in high entropy materials (Pikalova et al. 2022).

2.4.1 Sluggish diffusion effect

Compared to high-entropy systems, conventional systems have quicker diffusion and phase transition kinetics. High entropy systems which include cations of various sizes, results in sluggish diffusion and phase transition kinetics. Due to the multiple elements present in the HEMs crystal lattice, two adjacent atoms would rarely have comparable properties, which translates to a difference in the likelihood of neighbors during diffusion before and after an atom leap into a vacancy. Furthermore, by controlling the grain growth, the phase change is prevented because of distinct diffusion rates of the elements. The phase change requires rearrangement of individual components to produce a certain composition, which is difficult to achieve in high entropy systems. Therefore, in such cases, sluggish components function as restricting

components that stop phase transformation and maintain the equilibrium of the system. The structural stability of the active components and the durability of the electrodes in Li-ion batteries are explained by slow diffusion effect in the $\text{Mg}_{0.2}\text{Co}_{0.2}\text{Ni}_{0.2}\text{Cu}_{0.2}\text{Zn}_{0.2}\text{O}$ system (Qiu et al. 2019).

2.4.2 High entropy effect

Pure metals tend to melt because their liquid form has a higher entropy than their solid state. Similarly, phases of solid solutions in typical alloys have higher mixing entropies than intermetallic compounds. It is clearly understood that higher entropy of system will help in emergence of microstructure from its solid solutions easily. The second law of thermodynamics states that a system is in thermodynamic equilibrium when the Gibbs free energy is minimal at a specific temperature and pressure (equation 2.2). As a result of the enhanced solubility between individual components, there can be an apparent reduction in the number of phases in HEMs, which forms a pure single-phase structure. As mentioned previously, for example, the configuration entropy of an equimolar random solid solution with equal proportions of all 5 elements is $R = 1.61$. This means a perfectly ordered phase (where the entropy is zero) has 60 % less entropy than an equimolar quinary solid solution. Because the amount of ordering in HEMs decreases as temperature increases, the entropy effect stabilizes a phase with a higher entropy at adequately elevated temperatures. Regardless of this, an intermetallic complex will stay stable at high temperatures if its formation enthalpy is high enough to offset the effects of entropy. Therefore, a solid solution is not always the result of the entropy effect; rather, phase formation is controlled by its interaction with enthalpy. Rost et al. investigated the $(\text{MgCoNiZnCu})\text{O}$ system to show the entropy-dominated phase-stabilization impact in HEMs (Rost et al. 2015).

2.4.3 Cocktail effect

When compared to pure metal, multiple components provide a certain feature, which is nicely explained by Ranganathan in the 2003 article "Alloyed pleasures: multimetallic cocktails" (S Ranganathan 2003). The Cocktail effect, a multidimensional phenomenon spanning the atomic to the microscopic scale, is employed to demonstrate how a high-entropy system comprises at least five essential components that improve its characteristics which are influenced by the grain boundaries, grain-size distribution,

and characteristics of each phase. Moreover, the observed characteristics are cumulative from lattice distortion, interaction with other elements, and the rule of mixtures. High entropy components can be either single-phase, double-phase, or multiphase based on the processing circumstances and composition. The cocktail effect is demonstrated by Zhang et al., who synthesized a $\text{Ce}_{0.5}\text{Zn}_{0.1}\text{Co}_{0.1}\text{Mg}_{0.1}\text{Ni}_{0.1}\text{Cu}_{0.1}\text{O}_x$ solid solution by doping 50 mol % of divalent cations into the CeO_2 lattice. Both reactive oxygen species and a high number of oxygen vacancies were found in the resultant HEO. Volatile organic molecules in the HEO system are catalytically oxidized as a consequence of a cocktail effect (Shu et al. 2021).

2.4.4 Severe lattice distortion effect

Atoms in a system with a high degree of entropy have different atomic radii surrounding each one of them and the lattice under extreme stress, results in distortion in the lattice. Furthermore, nonsymmetric neighbours also contribute to distortions in the lattice due to different crystal structures and bond energies among the constituent elements. Consequently, specific characteristics will be impacted by the large lattice distortions. It has been observed that the deterioration of the lattice results in a decrease in the intensity of X-ray diffraction by a significant amount, and mass phonon scattering from the deformed lattice also reduces the thermal conductivity of HEMs (Murty et al. 2019). Lattice deformation was experienced in (MgCoNiCuZn)O-based high-entropy oxides, due to which X-ray intensity and broadened peak spectra are lowered (Berardan et al. 2017).

2.5 High entropy oxides

Motivated by HEAs, as mentioned above, Rost et al. (Rost et al. 2015) used the high entropy concept on ionic compounds by populating cation positions with several elements in equiatomic amounts which occupied the same lattice. These materials were named entropy-stabilized oxides and later turned into HEOs. To date, HEOs have been showing unexpected results and are attracting the research community to a great extent (Musicó et al. 2020; Salian and Mandal 2022b; Sarkar et al. 2019). Generally, binary or ternary systems are investigated based upon the corners of the phase diagram. It can be signified that, with the emergence of high entropy materials, the focal point has been displaced to the central region of the phase diagram, with anticipation of unexpected

behaviors and properties. The formation of multi-element (> 4), chemically complex, single-phase HEOs has inspired the exploration of vast compositional space (Sarkar et al. 2019; Ye et al. 2016; Zhang et al. 2014). HEOs are configurationally disordered and entropy-stabilized oxides with a maximum configurational entropy of mixing. HEOs consist of five or more metal ions that occupy the cation sublattice. Over the past few years, inspired by Rost et al. (Rost et al. 2015) work, research on HEOs has increased, extending from the initial rocksalt structure to spinel, perovskite, magneto-plumbite, fluorite, and several other types of HEOs. These oxides have superior properties like excellent electrochemical and catalytic behavior, high strength, increased electrical resistance, and good optical behavior (Musicó et al. 2020; Salián and Mandal 2022b; Sarkar et al. 2019). Fig. 2.7 depicts the number of articles searched on HEO with the title and abstract keywords such as “high entropy oxide” or “entropy stabilized oxides” in the Web of Science. Since the discovery of HEO, the volume of articles has grown significantly, which clearly demonstrates the interest in entropic materials and their potential significance.

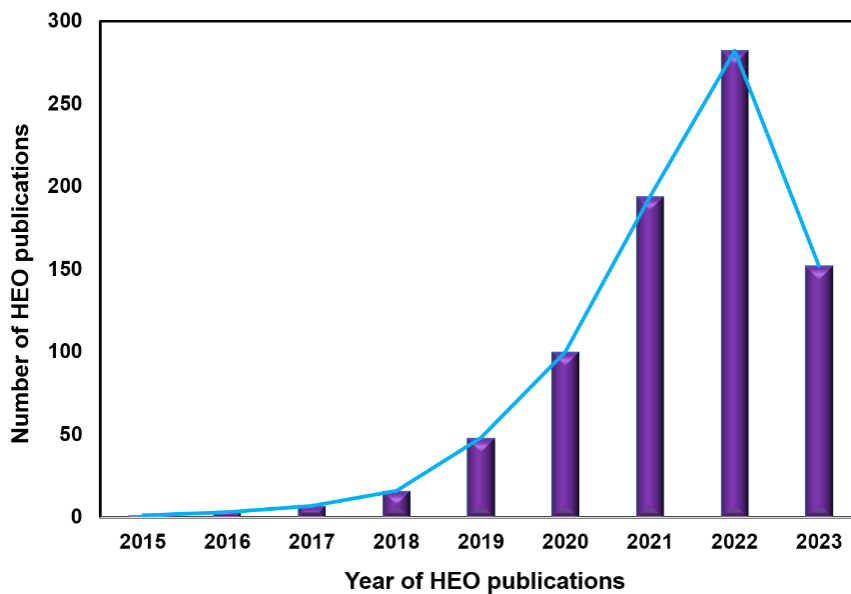


Fig. 2.7. The number of articles searched on HEO with the title and abstract keywords such as “high entropy oxide” or “entropy stabilized oxides” in Web of Science.

2.5.1 Criteria for the selection of candidates

Research group working in the field of HEOs, need to consider few selection rules for the choice of materials, which are as follows, (i) the group of binary oxides should not display a similar crystal structure, cation coordination or electronegativity, (ii)

binary oxides should exist in pairs (example: MgO-ZnO and CuO-NiO) and should not exhibit extensive miscibility based on oxide binary phase diagram, (iii) the cations should have alike ionic radii. Therefore, at least one of the cations crystal structure should be different and the overall system should have distinctive electronegativity. Intensive solubility of the components was also considered to be a selection rule. Also, as a minimum, one binary oxide system should not have a complete miscibility gap at 0.5 mole fraction. In summary, the geometric and electrical balance factors are critical factors for determining the constituents of the HEO systems where the uniformity of crystal structures, electro-negativities and coordination numbers is avoided while designing. Besides, the difference of the cationic radii of the components should be relatively small in order to have a single-phase oxide. To provide diversity in cationic radii and structure coordination, the cationic elements chosen for HEO system will be considered in an equiatomic or near equiatomic proportion within the mixture (Rost et al. 2015).

2.5.2 Processing

Presently, the processing routes of HEOs can be classified based on the precursors for oxide preparation. The techniques used to synthesize HEOs to date are solid-state reaction, co-precipitation, spray pyrolysis, sol-gel combustion, and so on. Fig. 2.8 depicts the flow chart of the processing techniques used to synthesize HEOs to date.

Solid-state reaction, which involves physical mixing of starting materials (respective individual oxides) is widely used to synthesize HEOs. The mixture of the starting materials is subjected to mechanical grinding or ball milling, pressed into required diameter pellets using a uniaxial hydraulic press (100 – 300 MPa), and sintered at considerably high temperature (>1000 °C) followed by air quenching as shown in Fig. 2.9 (a) (synthesis of phase-pure high-entropy $(Y_{0.2}Yb_{0.2}Lu_{0.2}Eu_{0.2}Er_{0.2})_3Al_5O_{12}$) (Biesuz et al. 2019; Chen et al. 2019a, 2018b; Dąbrowa et al. 2018; Dupuy et al. 2019; Gild et al. 2018; Grzesik et al. 2019; Hong et al. 2019; Jiang et al. 2018b; Jimenez-Segura et al. 2019; Osenciat et al. 2019; Qiu et al. 2019; Rost et al. 2015; Vinnik et al. 2019; Wang et al. 2019c). It is observed that entropy increases with the addition of new elements and reaches a maximum value when all elements have the same mole fraction. Single-phase structures occur at a temperature greater than 800 °C. Consequently,

calcination at low-temperature ($< 800\text{ }^{\circ}\text{C}$) will result in multiple phase formation from a single phase. In terms of mechanical grinding, the stoichiometric amount of HEOs, i.e., the individual metal oxides, were ground with agate balls in a vial (Berardan et al. 2017; Bérardan et al. 2016a; b). An increase in sintering temperature results in an increase in average grain size, thermal conductivity, and electrical resistance. Interestingly, tuning the disordering of the crystal structure by post-annealing treatment has an intense impact on the dielectric properties of the HEOs (MgCoNiCuZn)O (Berardan et al. 2017). The use of spark plasma sintering (SPS) for the post-annealing treatment substantially reduced the reaction time required for the conversion into a high entropy structure and drastically improved the densification process compared to conventional sintering (Biesuz et al. 2019).

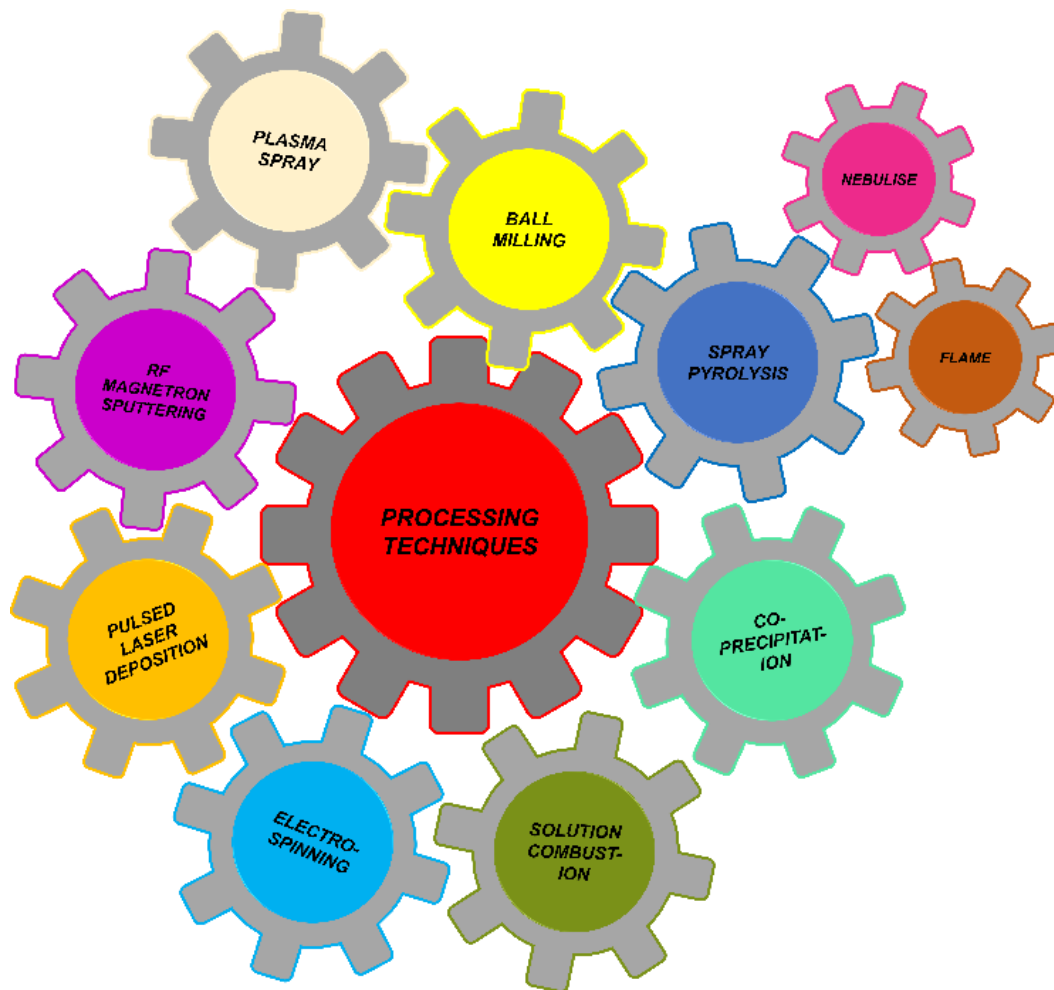


Fig. 2.8. List of high entropy oxide processing techniques.

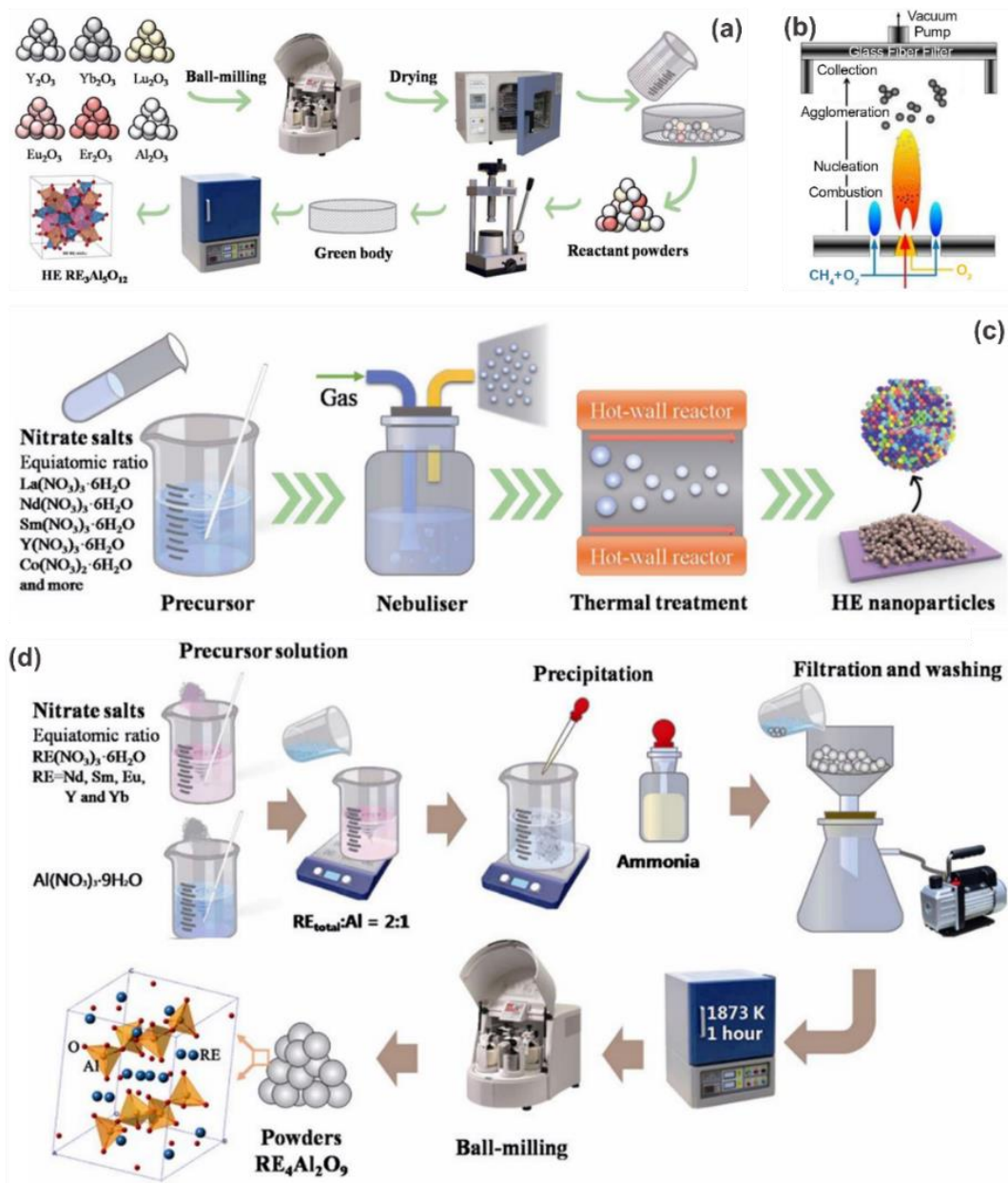


Fig. 2.9. Schematic depiction of preparation of high entropy oxides (a) (Y_{0.2}Yb_{0.2}Lu_{0.2}Eu_{0.2}Er_{0.2})₃Al₅O₁₂ by solid-state reaction process (Chen et al. 2020c), (b) flame spray pyrolysis (Wang et al. 2020b), (c) with rare earth and transition metal by nebulized spray pyrolysis (Sarkar et al. 2018a) and (d) (Nd_{0.2}Sm_{0.2}Eu_{0.2}Y_{0.2}Yb_{0.2})₄Al₂O₉ by chemical co-precipitation (Xiang et al. 2021b; Zhao et al. 2020d).

The spray pyrolysis technique is an aerosol process used to form a wide variety of materials in powder form and thin films of metals, metal oxides, and ceramics. Spray pyrolysis promotes better stoichiometric retention, thus particularly advantageous for the synthesis of metal oxides (Messing et al. 1993; Pratsinis and Vemury 1996). Using

a variety of spray pyrolysis techniques, HEO nanopowders ((Ce,Gd,La,Nd,Pr,Sm,Y)O, ((Ce Gd La Nd Pr Sm Y)O_{2.8})) were synthesized. In flame spray pyrolysis (FSP), the precursor solution containing metal salts of respective cation dissolved in a solvent is sprayed into a flame zone with the help of carrier gas, where the spray gets combusted and converts into nanosized metal/metal oxide powder as shown in Fig. 2.9 (b). In nebulized spray pyrolysis (NSP), the solution containing equiatomic cation combinations, i.e., includes nitrates/sulfates/chlorides of metals dissolved in a base solution (water), are continuously delivered into the piezo-driven nebulizer, which generates mist with fine droplets of precursor solution. It is then transported to the hot wall reactor (1150 °C, 900 mbar) along with flow of oxygen. The nanopowders are gathered using a filter-based collector and further calcined at 1000 °C, as shown in Fig. 2.9 (c) (Chellali et al. 2019; Djenadic et al. 2017; Sarkar et al. 2017b, 2018a; b; Wang et al. 2019b; Witte et al. 2019). It is noted that a higher concentration precursor solution is required for FSP because of the low production rate compared to NSP. The residence time of the particle formation is higher for FSP than NSP. In contrast to the solid-state reaction, there is a strong difference in powder behavior upon thermal treatment (Sarkar et al. 2017a). Apart from the high entropy effect, the choice of elements and the synthesis procedure employed for the multicomponent system, might impact the structure and phase stabilization (Sarkar et al. 2017b). Overall, NSP has many advantages in the preparation of HEO powders in comparison with FSP and solid-state reactions as they involve post-annealing treatment.

The co-precipitation technique is an excellent choice when high purity and better stoichiometric control are required. This technique is highlighted because of its ability of homogenous mixing at the atomic scale, scalability, simplicity, and tunability of particle morphology (Kolthoff 1932). To form precipitates, the reverse co-precipitation (RCP) process involves the addition of the precursor solution (contains nitrates/sulfates/chlorides of metals) into the base solution (precipitating agent) in a controlled fashion along with continuous stirring and maintaining the required pH level. The gelatinous precipitates are filtered, followed by grinding with agate motor or ball milling and calcination (>1000 °C) to obtain the desired crystalline oxide phase as shown in Fig. 2.9 (d) (Biesuz et al. 2018; Sarkar et al. 2017a). HEOs are also

synthesized by a combination of RCP and hydrothermal treatment (HTT), where the precursor and the base solution are mixed in a Teflon vessel under continuous stirring to form precipitate. After precipitation, the Teflon vessel is shut and placed in a stainless-steel pressure vessel for HTT (Biesuz et al. 2018). The main factors which affect the crystallite size, crystal structure, and morphology of HEO powder synthesized via RCP are the rate of addition of precursor solution into the base solution, pH, and temperature of calcination. Thus, post-annealing treatment of HEO powder synthesized using the RCP process yielded nanocrystalline single-phase (Sarkar et al. 2017a). In contrast, the powders prepared via a mixed mode of RCP and HTT do not undergo crystallization upon post-annealing-treatment as powders are already crystalline after the synthesis process.

Solution combustion synthesis (SCS) is the most broadly used approach, well known for its ability to successfully synthesize high-surface nanoscale materials, which includes composites, oxides, and sulfides. The advantage of SCS over the other processing techniques is its time and energy efficiency and results in the final product without the requirement of post-annealing treatment (Patil et al. 2002). Taking these into account, HEOs were synthesized via SCS (Mao et al. 2019c; a). In the SCS method, the precursor solution includes metal precursors (carbonates, nitrates, and sulfates, etc., as oxidizers) and fuel (starch, urea, sucrose, glycine, etc., as a reducing agent) are dissolved in the aqueous medium to assure molecular level homogenization, which then undergoes multiplication of self-sustained exothermic reactions upon heating, results in the direct end product as shown in Fig. 2.10 (a). It is noted that the SCS method can synthesize HEO nano-powder with very high crystallinity, where the lattice constant and crystallite size can be easily varied by controlling the synthesis temperature.

In addition, similar to SCS, the sol-gel technique is a flexible method that permits the creation of ceramic materials at lower temperatures with superior composition control as well as high purity levels. Sol-gel techniques are frequently employed in the production of ceramic materials such as metal oxides, nitrides, and carbides, etc., Low temperatures, excellent composition control, and ultra-high purity levels are some benefits of this method over conventional processing technologies. The hydrolysis and polycondensation reactions serve as the foundation for sol-gel operations.

$(\text{Sm}_{0.2}\text{Lu}_{0.2}\text{Yb}_{0.2}\text{Y}_{0.2}\text{Dy}_{0.2})_3\text{TaO}_7$ HEO nanoparticles were produced by Sang et al. (Sang et al. 2023) using an improved sol-gel technique followed by sintering. The corresponding metal oxides were dissolved in diluted nitric acid to produce a homogeneous solution of rare-earth nitrate. Then, a TaCl_5 -alcohol solution was treated with excessive citric acid to produce a polyester resin. After thoroughly combining the two solutions, the mixture was continually stirred at room temperature while ethylene glycol was added at a molar ratio of 4:3 with citric acid. The combined solution was allowed to become clear, and the majority of the ethanol and water were removed in a water bath. Until a sticky, moist solution was obtained, the solution was continually churned. The sol was dried in a drying oven at $260\text{ }^\circ\text{C}$ for six hours in order to create a black dry gel, which is followed by sintering to obtain HEO. The produced high-entropy ceramic oxide can be a good option for thermal barrier coatings due to its reduced Young's modulus, lower mean acoustic velocity, and higher Vickers microhardness. Through the use of the sol-gel process, Tang et al. (Tang et al. 2022) created pyrochlore oxide $(\text{LaY})(\text{Zr}_{0.5}\text{Ti}_{0.5}\text{Ce}_{0.5}\text{Hf}_{0.5})\text{O}_7$ as shown in Fig. 2.10 (b). The precursor solution containing metal nitrates is added to another solution (n-propanol and acetic acid taken in 4:1 weight-ratio) in 1:1 mass ratio to create a stable mixed solution, which was then agitated for three hours at ambient temperature and subsequently dried at $180\text{ }^\circ\text{C}$ for three hours in a vacuum drying oven. Further, it is sintered in a muffle furnace at a rate of $2\text{ }^\circ\text{C}\cdot\text{min}^{-1}$ to $800\text{ }^\circ\text{C}$ to produce high-entropy oxides of the pyrochlore type. It is demonstrated that the HEO used as an electrode in symmetrical supercapacitor device displayed a high capacitance of $128.5\text{ F}\cdot\text{g}^{-1}$ at a current density of $3\text{ A}\cdot\text{g}^{-1}$.

Ultrafine fibers may be produced quickly using the electrospinning process by using an electric field. The ability of electrospinning to create several kinds of ultrafine fibers has caught the interest of the scientific community. The electrospinning setup and process have undergone a number of improvements to regulate the fiber structure for practical purposes. The needle tip and the base of the collecting plate are typically connected to a high-voltage power source during an electrospinning procedure. Consequently, an electrostatic force generated between them reduces the liquid's surface tension and stretches or pulls the charged liquid, which creates an ultra-fine jet that lengthens, thins, and solidifies as it flows via the electric field across the collector,

as shown in Fig. 2.10 (c). Using an electrospinning approach, Xing et al. produced high-entropy ($\text{Y}_{0.2}\text{Yb}_{0.2}\text{Sm}_{0.2}\text{Eu}_{0.2}\text{Er}_{0.2}$) $_2\text{O}_3$ nanofibers (Xing et al. 2022). After dissolving various metal nitrates in an equal amount of ethanol and deionized water, the viscosity and spinnability were adjusted by adding polyvinylpyrrolidone (PVP). A homogenized and transparent precursor solution was produced after 5 hours of uninterrupted stirring at ambient temperature. Metal nitrates were distributed in a weight ratio of 0.8:1:5:5 with PVP, water, and ethanol. A peristaltic pump was used to deliver the precursor solution to a stainless-steel needle for electrospinning at a steady flow rate of 1 mL.h⁻¹. Under a high voltage of 12 kV, precursor fibers emerged from the needle and touched a grounded aluminum foil to create a nonwoven mat. Then, nanofibers were produced by the calcination of the acquired precursor nanofibers at 500 °C for two hours. The electrospun nanofibers remain continuous and have a smooth surface after calcination at 500 °C. Nevertheless, the diameter significantly decreases as a result of the degradation of the polymer skeleton and nitrate, which is a frequent occurrence in conventional electrospinning methods.

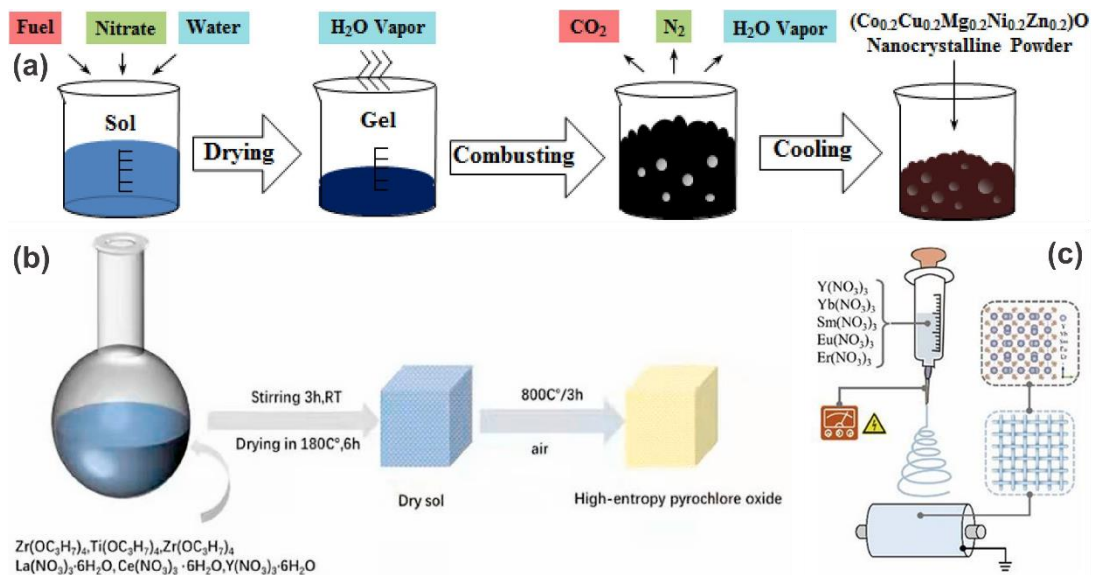


Fig. 2.10. Schematic depiction of preparation of high entropy oxides (a) $(\text{Co}_{0.2}\text{Cu}_{0.2}\text{Mg}_{0.2}\text{Ni}_{0.2}\text{Zn}_{0.2})\text{O}$ via solution combustion synthesis (Mao et al. 2019c), (b) $(\text{LaY})(\text{Zr}_{0.5}\text{Ti}_{0.5}\text{Ce}_{0.5}\text{Hf}_{0.5})\text{O}_7$ by sol-gel process (Tang et al. 2022), and (c) $(\text{Y}_{0.2}\text{Yb}_{0.2}\text{Sm}_{0.2}\text{Eu}_{0.2}\text{Er}_{0.2})_2\text{O}_3$ through electrospinning (Xing et al. 2022).

At present, the following methods of preparing high entropy oxide films (HEOFs) have been reported; pulsed-laser deposition (PLD), magnetron sputtering (MS), and

plasma spraying. In the past two decades, PLD has arisen as one of the most well-known and inherently simple techniques, used to deposit a range of new materials that are being investigated for future-generation applications (Lowndes et al. 1996; Mattox 2007). The fame of PLD is due to its intrinsic flexibility, versatility, and ability to produce high energy particles which results in high-quality film growth at low substrate temperature and less processing time. They are also known for producing multi-layered films of different materials by sequent ablation. PLD is one of the physical vapor depositions (PVD) processes conducted in a vacuum environment. A pulsed laser is emphasized on a target of HEOs to be deposited (Tudose et al. 2019). Usually, the selected elements (for example, binary elements such as cobalt oxide (CoO), nickel oxide (NiO), magnesium oxide (MgO), copper oxide (CuO), zinc oxide (ZnO), and more) are mixed, ground or milled and/or the composite powders are pressed into a pellet at 70,000 psi / 350 MPa, eventually are sintered at around 1000 °C – 1100 °C for 12 – 18 hours in an air atmosphere, leads to the development of an HEO target. To evaporate the HEOs from the target surface, high-power laser pulses are used and the supersonic jet of particles (plume) is directed towards the target. The plume stretches away from the target surface, and the ablated species gets condensed on the substrate, as shown in Fig. 2.11 (a). In order to deposit HEOs by the PLD technique, a Coherent UV excimer laser (KrF: $\lambda = 248$ nm) is used to ablate the HEO target in an oxygen environment. However, the properties of the grown HEOFs depend on various factors such as substrate temperature, ambient oxygen pressure, laser intensity, and many more (Eason 2006; Özgür et al. 2005). With the use of PLD, HEO thin films were grown on various substrates and their properties were varied by control of oxide composition (Kotsonis et al. 2018; Meisenheimer et al. 2017; Sharma et al. 2018). Targets for PLD were prepared by mixing and grinding the constituent elements (individual oxides like MgO, CoO, NiO, and CuO), which were further pressed and sintered at the required temperature (>1000 °C). Films were deposited by ablation from the laser. It was observed that the chemical and structural disorder of HEO can be used to engineer the exchange coupling by varying film thickness and concentration of magnetic ions. (Meisenheimer et al. 2017). The same formulation of HEO synthesized via PLD could not be stabilized as a single-phase structure using solid-state reactions. Overall growth

at low energy conditions produces phase separation, while growth at high energy conditions produces single-phase films.

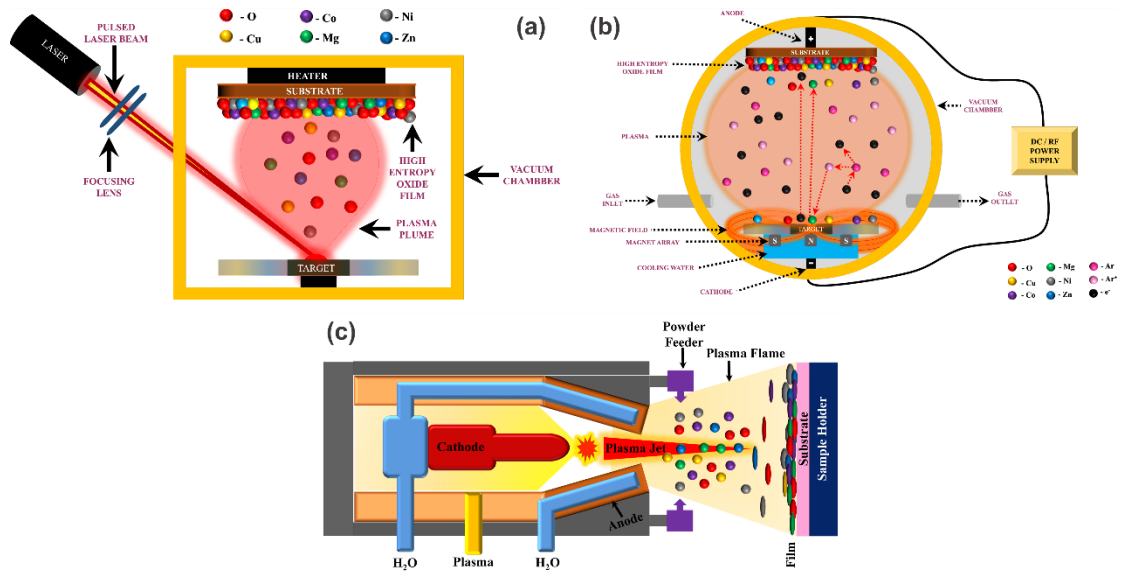


Fig. 2.11. Schematic of the (a) pulsed laser deposition, (b) magnetron sputtering deposition, and (c) plasma spraying method.

Radio-frequency magnetron sputtering (RFMS) is a superior physical vapor deposition (PVD) technique used to grow films by sputtering. In general working principle behind MS is as shown in Fig. 2.11 (b), the substrate to be coated is placed inside a high vacuum chamber. The chamber is purged with inert gas (usually Argon (Ar)). The negative potential is applied to the target, which releases free electrons from the target into the plasma environment. These free electrons collide with an outer shell of Ar. This collision changes Ar to positively charged ions, where they get attracted towards the negatively charged target at a very high velocity by an electric field. Due to the high velocity of attraction, a collision takes place at the target surface; atomic-size particles sputter from the target, and particles travel across the chamber and get condensed as thin films on the substrate. The sputtering of these particles is possible if the kinetic energy of bombarding particles is immensely higher than the thermal energy of the plasma. Since the bombarding particles are high-energy ions, the magnetic field is used to curb their behavior and velocity as well helps to generate plasma at very low pressure. Magnets are employed behind the negatively charged target to trap the electrons to avoid the bombardment of these electrons onto the substrates; hence, it

allows faster deposition rates, which restricts damage to the film texture. MS is known for its greater deposition rate, ease of automation, the comfort of sputtering any compound (metal, or alloy), exceptional homogeneity and density on large area substrates, high purity films, low substrate temperature, brilliant coverage of steps and minute features, comparatively inexpensive deposition method, great adhesion of films onto substrates, expandability to large areas, and so forth (Ellmer 2000; Lundin et al. 2019; Safi 2000; Tudose et al. 2019; Waits 1978). An enormous quantity of films can be prepared at relatively high purity and low cost (Mattox 2007). Hence, ultrafine nanocrystal HEO films are prepared using magnetron sputtering (Yang et al. 2019). The magnetron sputtering technique involves ejection of the material from the target onto a substrate and is observed that during deposition due to the greater ionization rate of oxygen, the preferred orientation of the HEO film becomes weak during the introduction of special species (He) into the film. Helium is known to sway the mechanical properties of the material, such as leads to embrittlement in the material, prevention of movement of dislocation, etc. In this case, the mechanical properties of the film were seen to deteriorate with the inclusion of special species, and RF-sputtered films were observed to be tender to the interplay between the species and defects (Yang et al. 2019). Various types of HEO thin films were explored using this technique (Kirnbauer et al. 2019).

Plasma spraying is well-known for its versatility and cost-efficiency. Fine metallic or non-metallic particles are injected into the plasma jet (RF/DC), and the plasma heat source activates with temperatures over 8000 K, which leads to melting or partially melting of the particles, as shown in Fig. 2.11 (c). The melted particles get flattened and solidified onto the substrates and forms layers of lamellae or splats, which forms the coating. Generally, plasma spraying is used in industries to spray high-added-value coatings like thermal barrier coatings, environmental barrier coating, and more (Fauchais 2004; Fauchais et al. 2001; Pawlowski 2008). Zhou et al. prepared a double-ceramic-layer (DCL) thermal barrier coating (TBC) of high entropy rare-earth zirconate (HE-REZ)($\text{La}_{0.2}\text{Nd}_{0.2}\text{Sm}_{0.2}\text{Eu}_{0.2}\text{Gd}_{0.2}$) $_2\text{Zr}_2\text{O}_7$) using atmospheric plasma spraying and examined its thermal stability (Zhou et al. 2020a). The HE-REZ powder was combined with gum Arabic through ball milling for 24 hrs. The ceramic and the bond coating

were sprayed onto the Ni-based superalloy. The substrate temperature was maintained at 200 °C, and the REZ powder was sprayed from a distance of 100 mm. The plasma was fired at 42 kW, and the primary gas (Ar), secondary gas (Hydrogen - H₂), and powder carrier gas (Nitrogen - N₂) had a flowrate of 35, 12, 2.8 standard liters per minute, respectively (Zhou et al. 2020a).

2.5.3 Crystal structures

As aforesaid, the fundamental thermodynamic studies involved in high entropy materials hypothesize that, in principle, the adequate temperature would promote a structure with a single sublattice with haphazard cation occupancy. The transition from multiphase to single-phase involves a change in chemical potential; in other words, the enthalpy penalty is associated with the structural transition (Rost et al. 2015). Hence, structural studies promote a basic understanding of the interaction of molecules or atoms at atomic, molecular, or supramolecular levels. Generally, X-ray diffraction is utilized to determine the structure and phase composition, and X-ray absorption fine structure (EXAFS) is used to analyze the structure on a local scale of the synthesized materials.

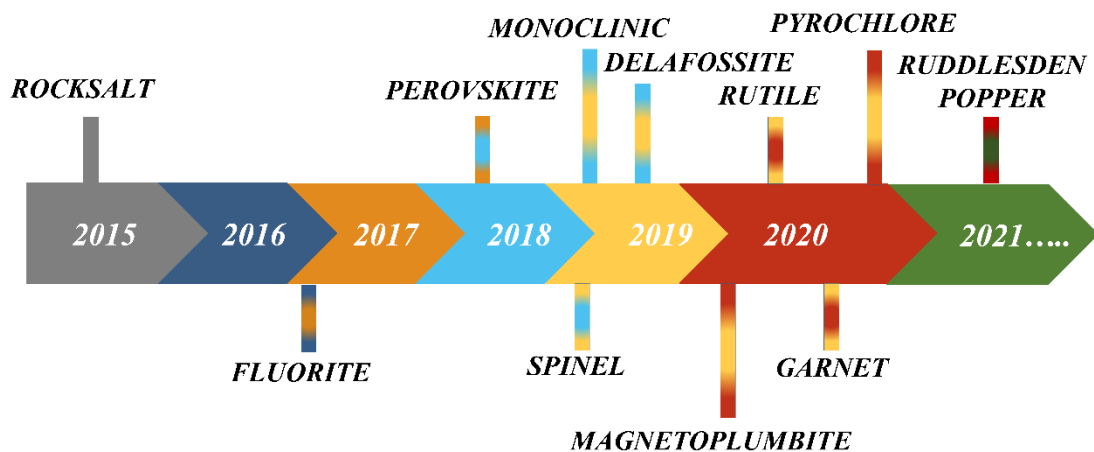


Fig. 2.12. Timeline of the structures explored in HEOs since 2015.

Fig. 2.12 shows the timeline of structure available in HEOs since 2015, with representative results of each structure detailed in table 2.1 – 2.11. Numerous oxides, including HEOs, exhibit the cubic rock-salt structure (AB; A - octahedral site and B - face centered cubic arrangement). The majority of HEOs with a rock-salt structure are centered on Mg-Co-Ni-Cu-Zn. Rocksalt-based HEOs prepared using different

synthesis techniques are listed in table 2.1 along with stabilization temperatures and resulted in outcomes. The rock-salt HEO ceramics are interesting from various perspectives, including Li conductivity, catalysis, structural, magnetic, mechanical, electrical, and thermal properties. The exceptionally high dielectric constants and superionic conductivity of the HEOs with the rock-salt structure make these materials desirable for use in the future as high- κ dielectrics and solid-state battery electrolytes. HEOs like $(\text{CoCrFeMnNi})_3\text{O}_4$ displayed spinel structure, first synthesized by Dabrowa et al., (Dąbrowa et al. 2018). Typical features of spinel-based HEO are listed in table 2.2. The typical formula of spinel-type oxides or ferrites is AB_2O_4 , in which the B cations are trivalent, while the A cations are divalent (Manikandan et al. 2014; Tian et al. 2015; Tomiyasu et al. 2004). Few HEOs, such as $(\text{Hf}_{0.2}\text{Zr}_{0.25}\text{Ce}_{0.25}\text{Y}_{0.25})\text{O}_{2-\delta}$, $(\text{Ce,Gd,La,Nd,Pr,Sm,Y})\text{O}$, etc., exhibited fluorite (AB_2 ; A - face centered cubic arrangement and B - tetrahedral interstitial sites) structure (Gild et al. 2018) with excellent mechanical and thermal properties which are summarized in table 2.3. HEOs namely $\text{Sr}(\text{Zr}_{0.2}\text{Sn}_{0.2}\text{Ti}_{0.2}\text{Hf}_{0.2}\text{Mn}_{0.2})\text{O}_3$, $\text{Sr}((\text{Zr}_{0.94}\text{Y}_{0.006})_{0.2}\text{Sn}_{0.2}\text{Ti}_{0.2}\text{Hf}_{0.2}\text{Mn}_{0.2})\text{O}_{3-x}$ etc, presented perovskite structure. These are known to have excellent and diverse physical properties, which are listed in table 2.4, along with stabilization temperatures and synthesis methods (Biesuz et al. 2019; Jiang et al. 2018b)(Sharma et al. 2018). These perovskites should have a minimum of 2 cation sublattices in an arrangement of ABO_3 , where A and B display two distinct kinds of cation groups and have either a cubic, orthorhombic, or hexagonal crystal structure. B-type cations are organized in a 6-fold coordination with an oxygen anion, where A-type cations are organized in a 12-fold coordination (Jiang et al. 2018b).

HEO $\text{Ba}(\text{Fe}_6\text{Ti}_{1.2}\text{Co}_{1.2}\text{In}_{1.2}\text{Ga}_{1.2}\text{Cr}_{1.2})\text{O}_{19}$ for the first time was synthesized by Vinnik et al., displaying a magnetoplumbite structure and HEO $(\text{Yb}_{0.25}\text{Yi}_{0.25}\text{Lu}_{0.25}\text{Er}_{0.25})_2\text{SiO}_5$ synthesized by Chen et al. showed monoclinic structure (Chen et al. 2019c; Vinnik et al. 2019). Table 2.5 and 2.6 provides a list of different HEOs which display magnetoplumbite and monoclinic structure along with their stabilization temperature, processing method used, and properties explored. Krinbauer et al. synthesized a new HEO thin film with a rutile structure with excellent mechanical properties (Krinbauer et al. 2019). The details of this film are displayed in Table 2.7. In recent, a new structure called pyrochlore and a mixture of defect fluorite and ordered

pyrochlore have been observed from HEO studies. Table 2.8 provides details of pyrochlore-based HEOs (Li et al. 2019). With two different kinds of A and B cations in the molecular structure of $A_2B_2O_7$, these oxides constitute a significant family of structural/functional ceramics. The general formulation of the pyrochlores may be represented as $(RE)_2(TM)_2O_7$ because A cations typically belong to rare-earth elements, and B cations belong to transition metals (TM). The pyrochlore structure of these oxides is characterized by a large atomic size A-type cation, which is coordinated with two 8b oxygen ions and six 48f oxygen ions. The smaller B-type cation is coordinated with six oxygen ions on 48f, with an oxygen vacancy at 8a surrounded by four B cations (Teng et al. 2020). One of the primary research objectives of pyrochlore HEOs is to reduce the thermal conductivity made of additional or different other rare-earth elements on the A/B site (Liu et al. 2009; Wan et al. 2009, 2010; Wang et al. 2013b). Delafossite, garnet, and ruddlesden popper are different other crystal structures reported in HEO, which are provided in Table 2.9, 2.10 and 2.11.

Table 2.1. List of published work on rocksalt-based high entropy oxides, their crystal structure, stabilization temperature, processing technique, and properties explored.

Composition of HEO	Crystal structure	Stabilization temperature (°C)	Processing technique	Properties explored	Ref.
(MgCoCuZnNi)O	Rocksalt	1150	BM	Effect of entropy on phase stabilization, structural and microstructural characterization	(Rost et al. 2015)
(Mg,Co,Ni,Cu,Zn)O, (Mg,Co,Ni,Cu,Zn) _{0.95} Li _{0.05} O, (Li, Mg,Co,Ni,Cu,Zn)O, (Mg,Co,Ni,Cu,Zn) _{0.8} (LiGa) _{0.2} O	Rocksalt	1000	MG	Effect of substituting aliovalent elements on dielectric properties	(Bérardan et al. 2016)
(Mg,Co,Ni,Cu,Zn) _{1-x} Li _x O, (Mg,Co,Ni,Cu,Zn) _{1-2x} Li _x Ga _x O	Rocksalt	1000	MG	Investigation on room temperature lithium superionic conductivity	(Bérardan et al. 2016)
(MgCoNiCuZn)O	Rocksalt	1000	MG	Impact of post-annealing treatments, stoichiometry, and synthesis conditions	(Berardan et al. 2017)
(Mg _{0.1} Co _{0.1} Cu _{0.1} Ni _{0.1} Zn _{0.1})O _{0.5} , M (Mg _{0.1} Co _{0.1} Cu _{0.1} Ni _{0.1} Zn _{0.1})O _{0.5} (M=Sc,Li)	Rocksalt	1000	MG and PLD	Study of charge compensation mechanism	(Rak et al. 2016)
(MgCoNiCuZn)O	Rocksalt	1000	BM	Study of charge compensation mechanism	(Osenciat et al. 2019)
(Co _{0.2} Cu _{0.2} Mg _{0.2} Ni _{0.2} Zn _{0.2})O	Rocksalt	1150	NSP	Study of anodic performance	(Wang et al. 2019)

$\text{Co}_{0.2}\text{Cu}_{0.2}\text{Mg}_{0.2}\text{Ni}_{0.2}\text{Zn}_{0.2}\text{O}$	Rocksalt	900	SCS	Study on chemical homogeneity and magnetic properties	(Mao et al. 2019)
$(\text{MgNiCuCoZn})\text{O}$	Rocksalt	1050	CP and HT	Sinterability and structural properties	(Biesuz et al. 2018)
$\text{Mg}_{0.2}\text{Ni}_{0.2}\text{Cu}_{0.2}\text{Co}_{0.2}\text{Zn}_{0.2}\text{O}$, $\text{M}(\text{Mg}_{0.167}\text{Ni}_{0.167}\text{Cu}_{0.167}\text{Co}_{0.167}\text{Zn}_{0.167}\text{O})$, ($\text{M} = \text{Sc}_{0.167}, \text{Sb}_{0.167}, \text{Sn}_{0.167}, \text{Cr}_{0.167}, \text{Ge}_{0.167}$)	Rocksalt	-	PLD	Effect of charge-induced disorder on thermal conductivity	(Braun et al. 2018)
$(\text{CoCuMgNiZn})\text{O}$	Rocksalt	1150 and 1250	FSP, RCP and NSP	Reversibility of phase transformations	(Sarkar et al. 2017a)
$(\text{CoCuMgNiZn})\text{O}$	Rocksalt	900	BM	Effect of average grain size on the phase spectrum behavior	(Dupuy et al. 2019)
$(\text{MgCoNiCuZn})\text{O}$	Rocksalt	1000	BM	Microstructural Evolution	(Hong et al. 2019)
$(\text{Mg}_{0.167}\text{Ni}_{0.167}\text{Co}_{0.167}\text{Cu}_{0.167}\text{Zn}_{0.167}\text{Sc}_{0.167})\text{O}$	Rocksalt	1000	BM and PLD	Effect of kinetic bombardment and growth conditions on the thin-film phase stabilization	(Kotsonis et al. 2018)
$(\text{Mg}_{0.2}\text{Co}_{0.2}\text{Ni}_{0.2}\text{Cu}_{0.2}\text{Zn}_{0.2})\text{O}$	Rocksalt	1150	NSP	Investigation of reversible lithium storage properties	(Sarkar et al. 2018b)
$(\text{Mg}_{0.25(1-x)}\text{Co}_x\text{Ni}_{0.25(1-x)}\text{Cu}_{0.25(1-x)}\text{Zn}_{0.25(1-x)})\text{O}$	Rocksalt	-	PLD	Tailoring of magnetic properties to increase exchange coupling	(Meisenheimer et al. 2017)
$(\text{Co}_{0.2}\text{Cu}_{0.2}\text{Mg}_{0.2}\text{Ni}_{0.2}\text{Zn}_{0.2})\text{O}$	Rocksalt	1150	NSP	Atomic-scale investigation of homogeneity	(Chellali et al. 2019)
$\text{Li}_x(\text{Co}_{0.2}\text{Cu}_{0.2}\text{Mg}_{0.2}\text{Ni}_{0.2}\text{Zn}_{0.2})\text{O}\text{F}_x$	Rocksalt	1250	BM	Effect of entropy on lithium storage performance	(Wang et al. 2019)

$(\text{Al}_{0.31}\text{Cr}_{0.20}\text{Fe}_{0.14}\text{Ni}_{0.35})\text{O}$	Rocksalt	-	RFMS	Effects of helium implantation on mechanical properties	(Yang et al. 2019)
$(\text{NiMgCuZnCo})\text{O}$	Rocksalt	1000	BM	Effect of entropy stabilization on lithium-sulfur battery performance	(Zheng et al. 2019)
$(\text{NiMgCuZnCo})\text{O}_x$	Rocksalt	900	MG	Effect of entropy maximization on catalytic performance	(Chen et al. 2019)
$(\text{Co, Cu, Mg, Ni, Zn})\text{O}$	Rocksalt	1000	BM	Defect Structure, chemical diffusion, and transport Property	(Grzesik et al. 2019)
$(\text{Mg}_{0.2}\text{Co}_{0.2}\text{Ni}_{0.2}\text{Cu}_{0.2}\text{Zn}_{0.2})\text{O}$	Rocksalt	1000	MM	Study on long-range magnetic ordering	(Jimenez-Segura et al. 2019)
$\text{M}(\text{MgCoNiCuZn})\text{O}_5$ (M= Li, Mn)	Rocksalt	1500	SSR	Study on stability, compressibility on cation-doped HEOs, and mechanical properties	(Chen et al. 2019)
$(\text{MgCoNiZn})_{1-x}\text{Li}_x\text{O}$ (x = 0.05, 0.15, 0.25, 0.35)	Rocksalt	1000	BM	Electrochemical performance in lithium-ion batteries	(Lökçü et al. 2020)
$\text{Mg}_{0.2}\text{Co}_{0.2}\text{Ni}_{0.2}\text{Cu}_{0.2}\text{Zn}_{0.2}\text{O}$	Rocksalt	900	SG	Effect of entropy stabilization during CO oxidation	(Fracchia et al. 2020a)
$(\text{Co}_{0.2}\text{Cu}_{0.2}\text{Mg}_{0.2}\text{Ni}_{0.2}\text{Zn}_{0.2})\text{O}$	Rocksalt	1150	NSP	Gassing behavior and cathode investigation	(Breitung et al. 2020)
$(\text{Co,Cu,Mg,Ni,Zn})\text{O}$	Rocksalt	900	BM	Study of catalytic stabilization through synergistic interfacial interaction	(Chen et al. 2020a)

					Effect of tuning	
$(\text{Mg}_{0.2}\text{Co}_{0.2}\text{Ni}_{0.2}\text{Cu}_{0.2}\text{Zn}_{0.2})\text{O}$	Rocksalt	1000	SSR		pseudocapacitive contribution	(Chen et al. 2019)
					on lithium storage	
$(\text{Mg}_{0.2}\text{Co}_{0.2}\text{Ni}_{0.2}\text{Cu}_{0.2}\text{Zn}_{0.2})\text{O}$	Rocksalt	500	PS		Study on sinterability	(Yoon et al. 2020)
$(\text{Mg},\text{Co},\text{Ni},\text{Cu},\text{Zn})\text{O}$	Rocksalt	900	SG		Investigation of phase evolution	(Sushil et al. 2020)
$(\text{Co}_{0.2}\text{Cu}_{0.2}\text{Mg}_{0.2}\text{Ni}_{0.2}\text{Zn}_{0.2})\text{O}$	Rocksalt	1150	NSP		Examination of lattice distortion and phase stability	(Cheng et al. 2020)
$\text{Au}(\text{Mg},\text{Co},\text{Ni},\text{Cu},\text{Zn})\text{O}$	Rocksalt	900	SSR		Effect of doping noble metal on catalytic performance	(Chen et al. 2020b)
$(\text{Mg}_{0.2}\text{Co}_{0.2}\text{Ni}_{0.2}\text{Cu}_{0.2}\text{Zn}_{0.2})\text{O}$	Rocksalt	1000	SSR		Investigation of the lithiation mechanism in the anode material	(Ghigna et al. 2020)
$(\text{Mg},\text{Co},\text{Ni},\text{Cu},\text{Zn})\text{O}$	Rocksalt	1000	SCS		Phase stability study and role of cationic stress on phases	(Bhaskar et al. 2020)
$(\text{Co}_{0.2}\text{Ni}_{0.2}\text{Cu}_{0.2}\text{Mg}_{0.2}\text{Zn}_{0.2})\text{O}$	Rocksalt	1000	Anchoring and merging process		Investigation on catalytic performance	(Feng et al. 2020)
$(\text{Mg}_{0.2}\text{Ni}_{0.2}\text{Co}_{0.2}\text{Cu}_{0.2}\text{Zn}_{0.2})\text{O}$	Rocksalt	200-600	PLD		Study on cation valence engineering and structural properties	(Kotsonis et al. 2020)

(Zn _{0.2} Ni _{0.2} Co _{0.2} Mn _{0.2} Cu _{0.2})O, (Zn _{0.2} Ni _{0.2} Co _{0.2} Mn _{0.2} Fe _{0.2})O, (Zn _{0.17} Ni _{0.17} Co _{0.17} Mn _{0.17} Fe _{0.17} Cu _{0.17})O, (Zn _{0.14} Ni _{0.14} Co _{0.14} Mn _{0.14} Fe _{0.14} Cu _{0.14})O, Li(Zn _{0.2} Ni _{0.2} Co _{0.2} Mn _{0.2} Cu _{0.2})O, Li(Zn _{0.2} Ni _{0.2} Co _{0.2} Mn _{0.2} Fe _{0.2})O, Li(Zn _{0.17} Ni _{0.17} Co _{0.17} Mn _{0.17} Fe _{0.17} Cu _{0.17})O, Li(Zn _{0.14} Ni _{0.14} Co _{0.14} Mn _{0.14} Fe _{0.14} Cu _{0.14})O,	Rocksalt	-	NSP	Structural investigation on phase stabilization and homogeneity	(Lin et al. 2020)
(Mg _{0.2} Ni _{0.2} Co _{0.2} Cu _{0.2} Zn _{0.2})O	Rocksalt	875	SSR	Sintering ability and phase stabilization study	(Sarkar et al. 2019)
(Mg _{0.2} Ni _{0.2} Co _{0.2} Cu _{0.2} Zn _{0.2})O	Rocksalt	1000	SSR	Multivariate curve resolution of operando XAS data for the investigation of lithiation mechanism	(Tavani et al. 2020)
(Mg,Co,Ni,Cu,Zn)O	Rocksalt	300	SCS	Thermodynamics and experimental evaluation	(Saghir et al. 2021)
(Mg,Co,Ni,Cu,Zn)O	Rocksalt	1100	SSR	Study on the elastic anisotropy properties	(Pitike et al. 2020)
(AlCrFeNiMn)O	Rocksalt	1200	RFMS	Investigation of microstructure, valence and magnetic properties	(Sun et al. 2021)
(Co _{0.2} Cu _{0.2} Mg _{0.2} Ni _{0.2} Zn _{0.2})O	Rocksalt	185 – 850	GGAC	Low-temperature synthesis of phase pure high entropy rock salt phase	(Gautam and Ahmad 2021)

(Mg, Cu, Ni, Co, Zn)O	Rocksalt	1000	MA	Synthesis of nanoparticles for Li-ion battery applications	(Kheradmandfard et al. 2021)
(Mg, Co, Ni, Cu, Zn)O	Rocksalt	600-1000	CGAC	The crystallographic phase evolution	(Sushil et al. 2021)
(Mg _{0.2} Fe _{0.2} Co _{0.2} Ni _{0.2} Cu _{0.2})O	Rocksalt	1000	HT	Effect of constituent cations on the electrocatalytic oxygen evolution reaction	(Kim and Choi 2022)
(Co,Cu,Mg,Ni,Zn)O	Rocksalt	1250, 950	NSP, RCP, FSP	Study of factors determining the band gap	(Usharani et al. 2022)
(MgCoNiCuZn)O	Rocksalt	800-900	SSR	Design and synthesis based on cluster-plus-glue-atom model	(Yu et al. 2022)
(CoCuMgZnNi)O	Rocksalt	1000	LTSC	Study of phase stabilization and dielectric measurements	(Salian et al. 2023b)
(Mg _{0.2} Co _{0.2} Ni _{0.2} Cu _{0.2} Zn _{0.2})O	Rocksalt	900	PAAGM	Study of electrochemical properties	(Ji et al. 2023)
Mg _{19.2} Co _{19.2} Ni _{19.2} Cu _{19.2} Zn _{19.2} Ti ₉₆ O ₂₈₈				Comparison of phase structure and optoelectrical properties	
Mg ₂₈ Co ₁₇ Ni ₁₉ Cu ₁₆ Zn ₁₆ Ti ₉₆ O ₂₈₈	Rocksalt	600–1400	CSSR		(Yu et al. 2023)

SSR - Solid-state reaction; **BM** - Ball milling; **MG** - Mechanical grinding; **MM** - Mechanical Mixing; **PLD** - Pulsed Laser Deposition; **NSP**- Nebulised Spray Pyrolysis; **FSP** - Flame spray pyrolysis; **SCS** - Solution Combustion Synthesis; **SG** – Sol-gel; **CP** - Co-Precipitation; **RCP** - reverse co-precipitation; **HT** - Hydrothermal; **RFMS** - Radio Frequency Magnetron Sputtering; **PS** - Polymeric synthesis; **LTSC** - Low temperature solution combustion; **PAAGM** -polyacrylamide gel method; **CSSR** - conventional solid-state reaction; **GGAC** - Glycine gel auto combustion; **MA** - Microwave assisted; **CGAC** - citrate gel auto-combustion.

Table 2.2. List of published work on spinel-based high entropy oxides, their crystal structure, stabilization temperature, processing technique and properties explored.

Composition of HEO	Crystal structure	Stabilization temperature (°C)	Processing technique	Properties explored	Ref.
$(\text{CoCrFeMnNi})_3\text{O}_4$	Spinel	1050	BM	Structural, microstructural, and characterization	(Dąbrowa et al. 2018)
$(\text{Cr}_{0.2}\text{Fe}_{0.2}\text{Mn}_{0.2}\text{Ni}_{0.2}\text{Zn}_{0.2})_3\text{O}_4$, $(\text{Cr}_{0.2}\text{Fe}_{0.2}\text{Mn}_{0.2}\text{Co}_{0.2}\text{Zn}_{0.2})_3\text{O}_4$	Spinel	650	SCS	Microstructural characterization and study on controllable magnetic properties	(Mao et al. 2020a)
$(\text{Co, Cr, Fe, Mn, Ni})_3\text{O}_4$, $(\text{Co, Cr, Fe, Mg, Mn})_3\text{O}_4$ and $(\text{Cr, Fe, Mg, Mn, Ni})_3\text{O}_4$	Spinel	1000	BM	Possibility of formation of quinary and senary HEOs and the effect of temperature on electrical conductivity	(Stygar et al. 2020)
$(\text{CoCrFeMnNi})_3\text{O}_4$	Spinel	1000	BM	Examination of defect structure and transport properties	(Grzesik et al. 2020)
$\text{Cu}_{0.05}\text{Ni}_{0.95}\text{Al}_{1.8}\text{Cr}_{0.2}\text{O}_4$	Spinel	900	PCM	An investigation of study on a possible alternative to platinum group metal three-way catalysts	(Hirakawa et al. 2019)
$(\text{Al}_{1/6}\text{Co}_{1/6}\text{Cr}_{1/6}\text{Fe}_{1/6}\text{Mn}_{1/6}\text{Ni}_{1/6})_3\text{O}_4$	Spinel	750	SCS	Study on phase purity and magnetic properties	(Mao et al. 2020b)
$(\text{Mg}_{0.2}\text{Co}_{0.2}\text{Ni}_{0.2}\text{Cu}_{0.2}\text{Zn}_{0.2})\text{Al}_2\text{O}_4$	Spinel	-	SSR	Structural and microstructural characterization and study on magnetic frustration	(Marik et al. 2020b)
$(\text{M31g}_{0.2}\text{Co}_{0.2}\text{Ni}_{0.2}\text{Cu}_{0.2}\text{Zn}_{0.2})\text{Cr}_2\text{O}_4$	Spinel	1100	SSR	Investigation of long-range magnetic ordering and magnetic-dielectric effect	(Marik et al. 2020a)

NiFe _{1.9} (DyErGdHoTb) _{0.02} O ₄ , (CoCrFeMnNi) _{0.2} Fe ₂ O ₄ , (CoCrFeMnNi) _{0.2} Fe _{1.9} (DyErGdHoTb) _{0.02} O ₄	Spinel	600	SG	Calculation of configurational entropy of mixing employing the sublattice model	(Parida et al. 2020)
(Al _{0.2} Cr _{0.2} Fe _{0.2} Ni _{0.2}) ₃ O ₄	Spinel	900	RFMS	Effects of surface irradiation on the indirect irradiation region	(Zhang et al. 2020a)
(Co _{0.2} Mn _{0.2} Ni _{0.2} Fe _{0.2} Zn _{0.2})Fe ₂ O ₄	Spinel	-	SSR	Stabilization of oxygen vacancy in HEO catalyst for Co-prosperity of efficiency and stability in an oxygen evolution reaction	(Zhang et al. 2020d)
Al ₂ O ₃ -BaO-CuO-Fe ₂ O ₃ -Mn ₂ O ₃ -NiO-SrO-TiO ₂ -ZnO, Al ₂ O ₃ -BaO-CuO-Fe ₂ O ₃ - NiO-SrO-TiO ₂ - WO ₃ -ZnO	Spinel	1400	SSR	Possibility of phase creation using SSR	(Zaitseva et al. 2020)
(Ni _{0.2} Co _{0.2} Mn _{0.2} Fe _{0.2} Ti _{0.2}) ₃ O ₄	Spinel	1350	SSR	In operando synchrotron X-ray studies for energy storage applications	(Chen et al. 2020d)
(Co,Mg,Mn,Ni,Zn)(Al,Co,Cr,Fe,Mn) ₂ O ₄	Spinel	1500	SSR	Examination of chemical homogeneity and phase purity with analysis of entropy effect	(Fracchia et al. 2020b)
(CrMnFeCoNi)O	Spinel	900	SAHM	Investigation of lithiation-delithiation performance	(Nguyen et al. 2020)
(FeCoNiCrMn) ₃ O ₄	Spinel	1000	SSR	Evaluation of anode performance for lithium-ion batteries	(Wang et al. 2020a)

Ni-Co-Cr-Fe-Mn-Tf	Spinel	400-1000	Sol gel	Sol-gel strategy for designing and synthesis of spherical mesoporous materials and their structural properties	(Wang et al. 2020b)
Li(NiCoMnAlZn) ₁ O ₂ , Li(NiCoMnAlFe) ₁ O ₂ , Li _{0.8} Na _{0.8} (NiCoMnAlFe) ₁ O ₂ ,	Spinel	900	NSP	Characterization of a series of Delafossite type HEOs and the role of entropy in structural stabilization	(Wang et al. 2020c)
(BeMgCaSrZnNi) ₃ O ₄	Spinel	1200	SSR	Electrochemical efficiency as an electrocatalyst for water and hydrazine hydrate oxidation	(Arshad et al. 2021)
CoMnFeZnYO ₇	Spinel	1050	SSR	Design of ultra-high stabilized two-phase multi-component oxide thermistor materials	(Wang et al. 2021)
(FeCoCrMnMg) ₃ O ₄	Spinel	900	SSR	Preparation and exploration of supercapacitive properties	(Wang et al. 2021b)
(Mg _{0.2} Ni _{0.2} Fe _{0.2} Co _{0.2} Cu _{0.2})Fe ₂ O ₄	Spinel	-	SSR	Magnetic texture of single crystal HEO spinel films	(Sharma et al. 2021)
(FeNiCrMnMgAl) ₃ O ₄	Spinel	780	SCS	Cycling stable anode material for Li-Ion battery with outstanding electrochemical performance	(Zheng et al. 2021a)
(Cr _{0.2} Mn _{0.2} Fe _{0.2} Co _{0.2} Ni _{0.2}) ₃ O ₄	Spinel	1000	Dip coating	Improved electrocatalytic water oxidation on high-surface-area spinel mesoporous HEO for electrode-based energy applications	(Einert et al. 2022)

$(\text{CoCrFeMnNi})_3\text{O}_4$	Spinel	750	RCP	HEO in electrocatalysis for methanol oxidation and oxygen evolution reactions	(Talluri et al. 2022)
$\text{Mn}_{1.56}\text{Co}_{0.96}\text{Ni}_{0.48}\text{O}_4$	Spinel	750	SSR	Synthesize of medium entropy thermosensitive films	(Wei et al. 2022)
$(\text{FeCoNiCrMn})_3\text{O}_4$	Spinel	500	STM	Synthesizing nanosized high-entropy nanoparticles for oxygen evolution reaction	(Duan et al. 2022)
$(\text{Mg}_{0.2}\text{Co}_{0.2}\text{Ni}_{0.2}\text{Cu}_{0.2}\text{Zn}_{0.2})\text{Fe}_2\text{O}_4$	Spinel	1000	SCS	High catalytic efficiency of high-entropy spinel ferrites	(Ai et al. 2023)
$(\text{Fe}_{0.2}\text{Mn}_{0.2}\text{Co}_{0.2}\text{Ni}_{0.2}\text{Zn}_{0.2})_3\text{O}_4$	Spinel	900	SCS	HEO with nanostructures as cathode material for solid oxide fuel cell	(Lin et al. 2023)
$(\text{MnCoFeNiCr})_3\text{O}_4$	Spinel	-	NSP	Structural characteristics and electrical conductivity of nanocrystalline high-entropy spinel oxide thin films	(Kamecki et al. 2023)
$(\text{CrFeMnNiCo}_x)_3\text{O}_4$	Spinel	900	SCS	Multifunctional high-entropy spinel oxides as promising LIB electrode materials with superior capacity, stability, and electronic conductivity.	(Liu et al. 2023a)
$(\text{CoCrFeMnNi})_3\text{O}_4$	Spinel	1400	SSR	Investigating Site Occupation, Structure, Stability, and Influence of oxygen partial pressure on spinel HEO	(He et al. 2023)

SSR - Solid-state reaction; **BM** - Ball milling; **SCS** - Solution Combustion Synthesis; **SG** – Sol-gel; **RFMS** - Radio Frequency Magnetron Sputtering; **PCM** - Polymeric complex method; **SAHM** - Surfactant assisted hydrothermal method, **RCP** - reverse co-precipitation; **STM**-Solvothermal Method; **NSP**- Nebulised Spray Pyrolysis

Table 2.3. List of published work on fluorite-based high entropy oxides, their crystal structure, stabilization temperature, processing technique and properties explored.

Composition of HEO	Crystal structure	Stabilization temperature (°C)	Processing technique	Properties explored	Ref.
(Ce,Gd,La,Nd,Pr,Sm,Y)O (Hf _x Zr _x Ce _x)(Y _y Yb _y)O _{2-δ} (x,y = 0.25, 0.125; 0.2, 0.2), (Hf _x Zr _x Ce _x)(Y _y Ca _y)O _{2-δ} (x,y = 0.25, 0.125), (Hf _x Zr _x Ce _x)(Y _y Gd _y)O _{2-δ} (x,y = 0.25, 0.125; 0.2, 0.2), (Hf _x Zr _x Ce _x)(Yb _y Gd _y)O _{2-δ} (x,y = 0.25, 0.125; 0.2)	Fluorite	1150	NSP	Factors affecting phase stability	(Djenadic et al. 2017)
	Fluorite	1500	BM	Role of entropy in structural stabilization and a comparison study on thermal, mechanical, and electrical properties	(Gild et al. 2018)
(Ce _{0.2} La _{0.2} Pr _{0.2} Sm _{0.2} Y _{0.2}) O _{2-δ}	Fluorite	1050	NSP	Investigation of defect structure and effect of bandgap	(Sarkar et al. 2017b)
(Ce _{0.2} La _{0.2} Pr _{0.2} Sm _{0.2} Y _{0.2}) O _{2-δ}	Fluorite	1150	NSP	Homogenous distribution of HEOs at the atomic scale	(Chellali et al. 2019)
(Ce _{0.2} La _{0.2} Pr _{0.2} Sm _{0.2} Y _{0.2}) O _{2-δ}	Fluorite	1000	NSP	Effect of pressure on lattice distortion	(Cheng et al. 2019)
(Ce _{0.2} Zr _{0.2} Y _{0.2} Gd _{0.2} La _{0.2}) O _{2-δ}	Fluorite	1500	HT	Role of entropy in structural stabilization	(Spiridigliozzi et al. 2020)
(Gd _{0.2} La _{0.2} Y _{0.2} Hf _{0.2} Zr _{0.2})O ₂	Fluorite	500	CP	Synthesis scalable approach and structural properties	(Anandkumar et al. 2019)

$(Y_{1/3}Yb_{1/3}Er_{1/3})_3TaO_7$, $(Y_{1/3}Yb_{1/3}Er_{1/3})_3NbO_7$, $(Sm_{1/6}Eu_{1/6}Y_{1/6}Yb_{1/6}Lu_{1/6}Er_{1/6})_3$ $(Nb_{1/2}Ta_{1/2})O_7$,	Fluorite	1450	SSR	Comparative study of hardness, phase stability, and chemical compatibility with Al_2O_3	(Zhao et al. 2020a)
$(CeZrHfTiLa)O$	Fluorite	900	MM	Entropy-driven strategy to stabilize Pd single atom	(Xu et al. 2020)
$(Hf_{(1-2x)/3}Zr_{(1-2x)/3}Ce_{(1-2x)/3}Y_xYb_x)O_{2-\delta}$ ($x=0.2,0.0074,0.029$)	Fluorite	1600	SSR	Examination of sand corrosion, thermal expansion, and ablation properties	(Wright et al. 2021)
$(Hf_{1/3}Zr_{1/3}Ce_{1/3})_{1-x}(Y_{1/2}X_{1/2})_xO_{2-\delta}$ ($x = Yb$, Ca and Gd and $x=0.4,0.148,0.058$)	Fluorite	1650	SSR	Investigation of phase stability, thermal conductivity, and mechanical properties	(Wright et al. 2020)
$Ce_{0.5}Zn_{0.1}Co_{0.1}Mg_{0.1}Ni_{0.1}Cu_{0.1}O_x$	Fluorite	900	SSR	Effect of high entropy on catalytic performance	(Shu et al. 2020)
$(CeGdLaNdPrSmY)O$	Fluorite	1000 – 1500	SSR	Effect of composition, sintering atmosphere, and the cooling rate on phase formation	(Pianassola et al. 2020)
$(Ti, Zr, Hf, Sn, Ge)O_2$, $(Ti, Zr, Hf, Sn, Pb)O_2$, $(Ti, Zr, Hf, Sn, Ce)O_2$	Fluorite	1500	SSR	Phase stability of entropy stabilized oxides with the α - PbO_2 structure	(Aamlid et al. 2023)
$(Zr_{0.2}Ce_{0.2}Hf_{0.2}Y_{0.2}Al_{0.2})O_{2-\delta}$	Fluorite	1500	Sol-gel	Analysis of atomic scale lattice distortions	(Wen and Liu 2023)
$(Ce_{0.2}La_{0.2}Pr_{0.2}Sm_{0.2}Y_{0.2})O_{1.6-\delta}$	Fluorite	1500	SCS	Dielectric properties	(Salian et al. 2023)

$(\text{RE}_3\text{NbO}_7, \text{RE} = \text{Dy}, \text{Y}, \text{Ho}, \text{Er}, \text{Yb})$	Fluorite	1650	SSR	Mechanical properties, thermal expansion coefficient	(Zhu et al. 2021)
$(\text{Zr}_{0.2}\text{Ce}_{0.2}\text{Hf}_{0.2}\text{Y}_{0.2}\text{Al}_{0.2})\text{O}_{2-\delta}$	Fluorite	1500	Sol-gel	Processing and microstructure	(Wen and Liu 2022)
$(\text{La}_{0.2}\text{Nd}_{0.2}\text{Yb}_{0.2}\text{Y}_{0.2}\text{Sm}_{0.2})_2\text{Ce}_2\text{O}_7$	Fluorite	1600	Sol-gel	Thermophysical and mechanical properties	(Tang et al. 2022)
$(\text{La}_{0.2}\text{Nd}_{0.2}\text{Yb}_{0.2}\text{Y}_{0.2}\text{Lu}_{0.2})_2\text{Ce}_2\text{O}_7$	Fluorite	1480	SSR	Thermal conductivity	(Xue et al. 2022)
$(\text{La}_{0.25}\text{Nd}_{0.25}\text{Sm}_{0.25}\text{Eu}_{0.25}\text{Gd}_{0.25})_2\text{Ce}_{2+x}\text{O}_{7+2x}$	Fluorite	1200	Sol-gel	Thermal and physical properties	(Lilin et al. 2022)
$(\text{Sm}_{0.2}\text{Lu}_{0.2}\text{Dy}_{0.2}\text{Yb}_{0.2}\text{Y}_{0.2})_3\text{TaO}_7$	Fluorite	1600	Sol-gel	Thermophysical and mechanical properties	(Sang et al. 2023)
$(\text{Zr}_{1/3}\text{Hf}_{1/3}\text{Ce}_{1/3})_{1-x}(\text{Y}_{1/2}\text{Gd}_{1/2})_x\text{O}_{2-\delta}$ ($\delta = 0.05-0.3$)	Fluorite	1600	SSR	wettability	(Li and Shen 2023)

SSR - Solid-state reaction; **BM** - Ball milling; **MM** - Mechanical Mixing; **NSP**- Nebulised Spray Pyrolysis; **CP** - Co-Precipitation; **HT** – Hydrothermal.

Table 2.4. List of published work on perovskite-based high entropy oxides, their crystal structure, stabilization temperature, processing technique, and properties explored.

Composition of HEO	Crystal structure	Stabilization temperature (°C)	Processing technique	Properties explored	Ref.
Sr (Zr _{0.2} Sn _{0.2} Ti _{0.2} Hf _{0.2} Mn _{0.2}) O ₃ , Sr (Zr _{0.2} Sn _{0.2} Ti _{0.2} Hf _{0.2} Nb _{0.2})O ₃ , Ba (Zr _{0.2} Sn _{0.2} Ti _{0.2} Hf _{0.2} Ce _{0.2})O ₃ , (Sr _{0.5} Ba _{0.5}) (Zr _{0.2} Sn _{0.2} Ti _{0.2} Hf _{0.2} Nb _{0.2})O ₃	Perovskite	1500	BM	Role of entropy in structural stabilization and tailoring of multiple physical properties	(Jiang et al. 2018)
(Gd _{0.2} La _{0.2} Nd _{0.2} Sm _{0.2} Y _{0.2}) (Co _{0.2} Cr _{0.2} Fe _{0.2} Mn _{0.2} Ni _{0.2})O ₃	Perovskite	1200	NSP	Role of entropy in structural stabilization	(Sarkar et al. 2018a)
(Gd _{0.2} La _{0.2} Nd _{0.2} Sm _{0.2} Y _{0.2}) (Co _{0.2} Cr _{0.2} Fe _{0.2} Mn _{0.2} Ni _{0.2})O ₃ , (Co _{0.2} Cr _{0.2} Fe _{0.2} Mn _{0.2} M Ni _{0.2})O ₃ , (M= Gd _{0.2} , La _{0.2} , Nd _{0.2})	Perovskite	1200	NSP	Investigation of magnetic properties and comprehensive study on AC and DC magnetometry	(Witte et al. 2019)
Sr((Zr _{0.94} Y _{0.006}) _{0.2} (Sn _{0.2} Ti _{0.2} Hf _{0.2} Mn _{0.2})O _{3-x}	Perovskite	1450	BM	Investigation of the application of spark plasma sintering on the structural properties	(Biesuz et al. 2019)
Ba (Zr _{0.2} Sn _{0.2} Ti _{0.2} Hf _{0.2} Nb _{0.2})O ₃	Perovskite	750	PLD	Study on phase stabilization of single-crystal epitaxial thin films	(Sharma et al. 2018)
Ba(TiSnZrHfNbGa) _{1/6} O ₃	Perovskite	1500	SSR	Phase evolution and dielectric properties	(Du et al. 2020)
(BaNaKBaCa) _{0.2} TiO ₃	Perovskite	840	BM	Dielectric characterization and energy storage efficiency	(Liu et al. 2020a)

BaSr(ZrHfTi)O ₃ , BaSrBi(ZrHfTiFe)O ₃ , Ru/BaSrBi(ZrHfTiFe)O ₃	Perovskite	1300	SCBM	The effect of room temperature synthesis via a sonochemical-based method on HEO nanoparticle catalyst	(Okejiri et al. 2020)
(LaPrNdSmEu) _{0.2} NiO ₃	Perovskite	735	PLD	Epitaxial stabilization and electrical performance	(Patel et al. 2020)
Na _{0.30} K _{0.07} Ca _{0.24} La _{0.18} Ce _{0.21} TiO ₃	Perovskite	1400	PM	Studying the possibility of obtaining perovskite phases and dielectric properties	(Vinnik et al. 2020b)
Ba (Zr _{0.2} Sn _{0.2} Ti _{0.2} Hf _{0.2} Me _{0.2})O ₃ (Me = Y, Nb, Ta)	Perovskite	1630	SSR	Microstructure analysis and dielectric properties	(Zhou et al. 2020)
BaZr _{0.2} Sn _{0.2} Ti _{0.2} Hf _{0.2} Ce _{0.2} O _{3-δ} , BaZr _{0.2} Sn _{0.2} Ti _{0.2} Hf _{0.2} Y _{0.2} O _{3-δ} , BaZr _{1/7} Sn _{1/7} Ti _{1/7} Hf _{1/7} Ce _{1/7} Nb _{1/7} Y _{1/7} O _{3-δ}	Perovskite	-	SSR	Possibility of proton conduction	(Gazda et al. 2020)
(Gd _{0.2} Nd _{0.2} La _{0.2} Sm _{0.2} Y _{0.2})CoO ₃	Perovskite	1200	CP-HT	Study on structural, magnetic, electrical	(Krawczyk et al. 2020)
Zn _{0.1} Ca _{0.1} Sr _{0.4} Ba _{0.4} ZrO ₃	Perovskite	1650	SSR	Study on phase stability, electronic structure, mechanical and thermal properties.	(Liu et al. 2020b)
La _{0.2} Pr _{0.2} Nd _{0.2} Sm _{0.2} Sr _{0.2} MnO _{3-δ}	Perovskite	1300	SG	Suppression of Sr segregation in cathodes	(Yang et al. 2021)
(Gd _{0.2} La _{0.2} Nd _{0.2} Sm _{0.2} Y _{0.2})CoO ₃ , (Gd _{0.2} La _{0.2} Nd _{0.2} Sm _{0.2} Y _{0.2})CrO ₃ , (Gd _{0.2} La _{0.2} Nd _{0.2} Sm _{0.2} Y _{0.2})FeO ₃	Perovskite	1200	NSP	A comprehensive study on magnetic properties	(Witte et al. 2020)

$(K_{0.5}Bi_{0.5})_{0.2}Ba_{0.2}Sr_{0.2}Ca_{0.2}Mg_{0.2}TiO_3$	Perovskite	-	SSR	Study of dielectric and ferroelectric properties.	(Ni et al. 2022)
$Ba(Ti_{0.2}Sn_{0.2}Zr_{0.2}Hf_{0.2}Nb_{0.2})O_3$	Perovskite	800	SSR	Designing high performance relaxor ferroelectric materials for piezoelectric, pyroelectric and electrocaloric applications.	(Sharma et al. 2022)
$Ba_7Nb_4MoO_{20}$. $Ba_7Nb_{3.9}Mo_{1.1}O_{20.05}$	Perovskite	900	SSR	Study on phase stability	(Yashima et al. 2021)
$Ba(Zr_{0.2}Sn_{0.2}Ti_{0.2}Hf_{0.2}Nb_{0.2})O_3$	Perovskite	600, 700 and 800	SG	Impact of annealing temperature on their electronic structure and charge transport properties	(Liang et al. 2021)
$La(CrMnFeCo_2Ni)O_3$	Perovskite	750	PRM	Synthesis and electrochemical properties were evaluated	(Nguyen et al. 2021)
$(Ca_{0.2}Sr_{0.2}Ba_{0.2}Pb_{0.2}La_{0.2})TiO_3$	Perovskite	1000	SSR	Study of thermoelectric oxides, thermal conductivity, electrical conductivity and oxygen vacancy	(Zheng et al. 2021b)
$(Na_{0.2}Bi_{0.2}Ba_{0.2}Sr_{0.2}Ca_{0.2})TiO_3$	Perovskite	900	SSR	Enhanced capacitive energy storage and dielectric temperature stability	(Ning et al. 2023)

SSR - Solid-state reaction; **BM** - Ball milling; **PM** - Physical Mixing; **PLD** - Pulsed Laser Deposition; **NSP**- Nebulised Spray Pyrolysis; **SG** – Sol-gel; **CP** - Co-Precipitation; **HT** - Hydrothermal; **SCBM** - Sonochemical based method; **PM** - Precipitation method

Table 2.5. List of published work on magnetoplumbite-based high entropy oxides, their crystal structure, stabilization temperature, processing technique and properties explored.

Composition of HEO	Crystal structure	Stabilization temperature (°C)	Processing technique	Properties explored	Ref.
Ba(Fe ₆ Cr _{1.2} Ti _{1.2} In _{1.2} Ga _{1.2} Co _{1.2})O ₁₉	Magnetoplumbite	1620 1400	SSR	Determination of optimum synthesis condition a homogeneity range	(Vinnik et al. 2019)
(Ba,Sr,Ca,La)Fe _{6-x} (Al,TiCr,Ga,In,Cu,W) _x O ₁₉	Magnetoplumbite	1350	SSR	Structure parameters and magnetic study	(Vinnik et al. 2020a)
(Ba,Sr,Ca,La)Fe _x (Ti,Al,Mn,Co,In,Ga,Cr) _{12-x} O ₁₉	Magnetoplumbite	1350	SSR	Exploration of crystal structure,	(Zhivulin et al. 2021)
Sr(CrMnFeCoNi) ₃ O ₄ Sr(MgAlTiCrFe) ₁₂ O ₁₉	Magnetoplumbite	1200	SSR	Investigation of crystal structure, phase formation, mechanical performance, and band gap engineering	(Gan et al. 2022)
BaFe _{12-x} (Ti, Mn, In, Ga) _x O ₁₉	Magnetoplumbite	1350	SR	Study of unique crystal shapes and ion incorporation behavior	(Cherkasova et al. 2023)
PbFe _{2.4} X _{2.4} Y _{2.4} Ga _{2.4} In _{2.4} O ₁₉	Magnetoplumbite	1150	SSR	Study of magnetic properties	(Zaitseva et al. 2023)
BaFe _{12-x} (Ti,Mn,In,Ga) _x O ₁₉	Magnetoplumbite	1400	SSR	Study on structural parameters.	(Vinnik et al. 2023)

SSR - Solid-state reaction. SR - Solvo-crystallization

Table 2.6. List of published work on monoclinic-based high entropy oxides, their crystal structure, stabilization temperature, processing technique and properties explored.

Composition of HEO	Crystal structure	Stabilization temperature (°C)	Processing technique	Properties explored	Ref.
(Yb _{0.25} Yi _{0.25} Lu _{0.25} Er _{0.25}) ₂ SiO ₅	Monoclinic	1200	SSR	Phase stability	(Chen et al. 2020c)
(Co,Cu,Mg,Ni,Zn)O	Monoclinic	900	FSP, NSP, RCP	Antiferromagnetism	(Usharani et al. 2020)
(La _{0.2} Ce _{0.2} Nd _{0.2} Sm _{0.2} Eu _{0.2})PO ₄	Monoclinic	1200	BM	Thermal conductivity	(Zhao et al. 2019)
(Nd _{0.2} Sm _{0.2} Eu _{0.2} Y _{0.2} Yb _{0.2}) ₄ Al ₂ O ₉	Monoclinic	RT to 1200	CP	Temperature stability, thermal conductivity, and anisotropy thermal expansivity	(Zhao et al. 2020b)
TiZrHfNbTaO _x	Monoclinic	1170	HPT + HT	Photocatalytic hydrogen evolution	(Edalati et al. 2020)
(Lu, Y, Ho, Nd, La) ₂ O ₃	Monoclinic	-	MPD	Tuning the melting point and phase stability	(Pianassola et al. 2022)
(Lu, Y, Gd, Nd, La) ₂ O ₃					
(Nd _{1/6} Sm _{1/6} Eu _{1/6} Gd _{1/6} Dy _{1/6} Ho _{1/6}) ₂ O ₃	Monoclinic	1250	SCS	Study of polymorphic transformation	(Zhuravlev et al. 2023)
(Lu _{0.2} Yb _{0.2} Er _{0.2} Tm _{0.2} Sc _{0.2}) ₂ Si ₂ O ₇	Monoclinic	1550	BM	Thermal conductivity	(Guo et al. 2022b)
Ho _{2-x} Sm _x CoMnO ₆ (0 ≤ x ≤ 1)	Monoclinic	1100	SSR	Magnetic and magnetocaloric properties	(El Oujih et al. 2022)

(MnNiCuZn)WO ₄ , (MnCoNiCuZn)WO ₄	Monoclinic	500	CP	Structural analysis of high-entropy tungstate using XRD and XAFS	(Bakradze et al. 2023)
(Lu, Y, Ho, Nd, La) ₂ O ₃ , (Gd, Eu, Sm, Nd, La) ₂ O ₃	Monoclinic B type	-	Wet chemical	In situ high-temperature structural analysis	(Pianassola et al. 2023a)
(Sm _{1/5} Dy _{1/5} Ho _{1/5} Er _{1/5} Yb _{1/5})NbO ₄ , (Sm _{1/6} Dy _{1/6} Ho _{1/6} Er _{1/6} Yb _{1/6} Lu _{1/6})NbO ₄ , (Sm _{1/7} Dy _{1/7} Ho _{1/7} Er _{1/7} Yb _{1/7} Lu _{1/7} Gd _{1/7})NbO ₄ , (Sm _{1/8} Dy _{1/8} Ho _{1/8} Er _{1/8} Yb _{1/8} Lu _{1/8} Gd _{1/8} Tm _{1/8}) NbO ₄	Monoclinic	-	SSR	Thermal conductivity Oxygen ion conductivity	(Lai et al. 2023)

SSR - Solid-state reaction; **BM** - Ball milling; **NSP**- Nebulised Spray Pyrolysis; **FSP** - Flame spray pyrolysis; **CP** - Co-Precipitation; **MPD** - micro-pulling-down.

Table 2.7. List of published work on rutile-based high entropy oxides, their crystal structure, stabilization temperature, processing technique and properties explored.

Composition of HEO	Crystal structure	Stabilization temperature (°C)	Processing technique	Properties explored	Ref.
$(Al_{0.19}Cr_{0.13}Nb_{0.19}Ta_{0.30}Ti_{0.19})O_2$	Rutile	1200	RFMS	Effect of oxygen flow ratio on the hardness of the film	(Kirnbauer et al. 2019)
$Ti_8Sn_8Nb_8Ta_8Me_{16}O_{96}$ (Me = Ga, Fe)	Rutile	1300	SSR	Exploration of optoelectrical properties	(Yu et al. 2022a)
Ti-Sn-Nb-Ta-Me-O (Me = Ga, Fe, Cr)	Rutile	1300	SSR	Investigation of their crystal structure, composition distribution, and stability	(Yu et al. 2022b)
$Fe_{0.25}Ni_{0.25}Co_{0.25}Cu_{0.25}SbO_x$, $Fe_{0.2}Ni_{0.2}Co_{0.2}Cu_{0.2}Zn_{0.2}SbO_x$, $Fe_{0.25}Ni_{0.25}Co_{0.25}Cu_{0.25}Sb_2O_x$, $Fe_{0.2}Ni_{0.2}Co_{0.2}Cu_{0.2}Zn_{0.2}Sb_2O_x$	Rutile	600	PM	Highly efficient, reusable multi-component metal oxide catalyst achieved at RT	(Soltani et al. 2023)
$(Ru_{0.2}Ir_{0.2}Cr_{0.2}W_{0.2}Cu_{0.2})O_2$	Rutile	-	SG	Water oxidation catalytic study	(Miao et al. 2023)

RFMS - Radio Frequency Magnetron Sputtering; **SG** - Sol-Gel; **SSR** - Solid-state reaction; **MS** - Magnetron Sputtering; **AO** – Alloy-oxidation;

RT - Room temperature; **PM** - Polyol method

Table 2.8. List of published work on pyrochlore-based high entropy oxides, their crystal structure, stabilization temperature, processing technique and properties explored.

Composition of HEO	Crystal structure	Stabilization temperature (°C)	Processing technique	Properties explored	Ref.
$\text{Gd}_2\text{Zr}_2\text{O}_7$, $(\text{Gd}_{1/7}\text{Eu}_{1/7})_2\text{Zr}_2\text{O}_7$, $(\text{Gd}_{1/7}\text{Eu}_{1/7}\text{Sm}_{1/7})_2\text{Zr}_2\text{O}_7$, $(\text{Gd}_{1/7}\text{Eu}_{1/7}\text{Sm}_{1/7}\text{Nd}_{1/7})_2\text{Zr}_2\text{O}_7$, $(\text{Gd}_{1/7}\text{Eu}_{1/7}\text{Sm}_{1/7}\text{Nd}_{1/7}\text{La}_{1/7})_2\text{Zr}_2\text{O}_7$, $(\text{Gd}_{1/7}\text{Eu}_{1/7}\text{Sm}_{1/7}\text{Nd}_{1/7}\text{La}_{1/7}\text{Dy}_{1/7})_2\text{Zr}_2\text{O}_7$, $(\text{Gd}_{1/7}\text{Eu}_{1/7}\text{Sm}_{1/7}\text{Nd}_{1/7}\text{La}_{1/7}\text{Dy}_{1/7}\text{Ho}_{1/7})_2\text{Zr}_2\text{O}_7$	Pyrochlore	1500	SSR	Structural investigation of the crystal structure	(Teng et al. 2020)
$(x\text{Nd}_{0.2}\text{Sm}_{0.2}\text{Eu}_{0.2}\text{Gd}_{0.2})_2\text{Zr}_2\text{O}_7$ ($x = \text{La}_{0.2}, \text{Y}_{0.2}$), $(x\text{La}_{0.2}\text{Y}_{0.2}\text{Eu}_{0.2}\text{Gd}_{0.2})_2\text{Zr}_2\text{O}_7$ ($x = \text{Sm}_{0.2}, \text{Nd}_{0.2}$), $(x\text{La}_{0.2}\text{Nd}_{0.2}\text{Sm}_{0.2}\text{Y}_{0.2})_2\text{Zr}_2\text{O}_7$ ($x = \text{Eu}_{0.2}, \text{Gd}_{0.2}$)	Pyrochlore	1000	SSR	Thermal conductivity	(Li et al. 2019)
$(\text{La}_{0.2}\text{Nd}_{0.2}\text{Sm}_{0.2}\text{Gd}_{0.2}\text{Yb}_{0.2})_2\text{Zr}_2\text{O}_7$	Pyrochlore	1200	SCS	Optical performance	(Zhang et al. 2020b)
$(\text{Yb}_{0.2}\text{Tb}_{0.2}\text{Gd}_{0.2}\text{Dy}_{0.2}\text{Er}_{0.2})_2\text{Ti}_2\text{O}_7$	Pyrochlore	1400	SSR	Characterization and Single-crystal growth study	(Kinsler-Fedon et al. 2020)
$(\text{La}_{0.2}\text{Nd}_{0.2}\text{Sm}_{0.2}\text{Eu}_{0.2}\text{Gd}_{0.2})_2\text{Zr}_2\text{O}_7$	Pyrochlore	1600	SSR	Microstructural evolution and aqueous durability	(Zhao et al. 2023b)
$(\text{Y}, \text{Dy}, \text{Ce}, \text{Nd}, \text{La})_2\text{Sn}_2\text{O}_7$	Pyrochlore	1300	SCS	Low discharge capacity in Li-ion batteries	(Jiang et al. 2023b)

$\text{La}_2(\text{Ti}_{0.25}\text{Zr}_{0.25}\text{Hf}_{0.25}\text{Ce}_{0.25})_2\text{O}_7$					
$\text{Nd}_2(\text{Ti}_{0.25}\text{Zr}_{0.25}\text{Hf}_{0.25}\text{Ce}_{0.25})_2\text{O}_7$					
$\text{Sm}_2(\text{Ti}_{0.25}\text{Zr}_{0.25}\text{Hf}_{0.25}\text{Ce}_{0.25})_2\text{O}_7$					
$\text{Eu}_2(\text{Ti}_{0.25}\text{Zr}_{0.25}\text{Hf}_{0.25}\text{Ce}_{0.25})_2\text{O}_7$	Pyrochlore	1500	SSR	Irradiation	(Wang et al. 2023b)
$\text{Gd}_2(\text{Ti}_{0.25}\text{Zr}_{0.25}\text{Hf}_{0.25}\text{Ce}_{0.25})_2\text{O}_7$					
$(\text{Sm}_{0.5}\text{Gd}_{0.5})_2(\text{Ti}_{0.25}\text{Zr}_{0.25}\text{Hf}_{0.25}\text{Ce}_{0.25})_2\text{O}_7$					
$(\text{Sm}_{0.2}\text{Eu}_{0.2}\text{Gd}_{0.2})_2(\text{Ti}_{0.25}\text{Zr}_{0.25}\text{Hf}_{0.25}\text{Ce}_{0.25})_2\text{O}_7$					
$(\text{La}_{0.2}\text{Nd}_{0.2}\text{Sm}_{0.2}\text{Eu}_{0.2}\text{Gd}_{0.2})_2(\text{Ti}_{0.25}\text{Zr}_{0.25}\text{Hf}_{0.25}\text{Ce}_{0.25})_2\text{O}_7$					
$\text{La}_2(\text{Zr}_{0.2}\text{Ce}_{0.2}\text{Hf}_{0.2}\text{Sn}_{0.2}\text{Ti}_{0.2})_2\text{O}_7$	Pyrochlore	1550	SSR	Thermal conductivity	(Zhang et al. 2022)
$(\text{Bi},\text{Li},\text{Na},\text{La},\text{Eu})_{1.9}(\text{Mg}_{0.5}\text{Nb}_{1.5})\text{O}_{7.8}$	Pyrochlore	1150	SCS	Optical and dielectric study	(Koroleva et al. 2023)

SSR - Solid-state reaction; **SCS** - Solution Combustion Synthesis; **FS** – Flash Synthesis; **RCP** - Reverse co-precipitation; **CP** - Co-precipitation;
SSP - Sol-spray pyrolysis; **PS** – Plasma spray; **SPS** – Spark-plasma sintering; **SG** - Spray granulation

Table 2.9. List of published work on delafossite-based high entropy oxides, their crystal structure, stabilization temperature, processing technique and properties explored.

Composition of HEO	Crystal structure	Stabilization temperature (°C)	Processing technique	Properties explored	Ref.
Li(NiCoMnAlZn) ₁ O ₂	Delafossite	900	NSP, SSR	Li-ion Batteries	(Wang et al. 2020d)
Li(NiCoMnAlFe) ₁ O ₂					
LiNa(NiCoMnAlFe) ₁ O ₂					
Li(Ni _{0.46} Co _{0.2} Mn _{0.2} Mg _{0.04} Al _{0.04} Cr _{0.015} Ti _{0.015} Zr _{0.015} Cu _{0.015}) ₁ O ₂					
Li(Ni _{0.47} Co _{0.2} Mn _{0.18} Mg _{0.04} Al _{0.04} Cr _{0.02} Ti _{0.02} V _{0.015} Cu _{0.015}) ₁ O ₂					

NSP - Nebulized spray pyrolysis; SSR - Solid state reaction

Table 2.10. List of published work on garnet-based high entropy oxides, their crystal structure, stabilization temperature, processing technique and properties explored.

Composition of HEO	Crystal structure	Stabilization temperature (°C)	Processing technique	Properties explored	Ref.
(Dy,Er,Gd,Ho,Y) ₃ Fe ₅ O ₁₂ (Dy,Gd,Ho,Sm,Y) ₃ Fe ₅ O ₁₂	Garnet	1300	MP	Temperature stability and moderate thermal expansion	(Dąbrowa et al. 2021)
(Y _{0.2} Eu _{0.2} Er _{0.2} Dy _{0.2} Lu _{0.2}) ₃ (Al _x Fe _{1-x}) ₅ O ₁₂ (x = 0.4–0.6))	Garnet	1650	SSR	Exploration of dielectric properties	(Liu et al. 2023b)
Ga _{0.2} Li _{5.75} La _{2.5} Nd _{0.5} Nb _{0.35} Ta _{0.3} Ce _{0.1} Zr _{0.75} Hf _{0.25} Ti _{0.25} O ₁₂	Garnet	950	SSR	Study on ionic conductivity	(Stockham et al. 2022)
Li _{6.2} La ₃ (Zr _{0.2} Hf _{0.2} Ti _{0.2} Nb _{0.2} Ta _{0.2}) ₂ O ₁₂	Garnet	1250	SSR	Study on ionic conductivity	(Han et al. 2023)
Li ₇ La ₃ Zr _{0.5} Hf _{0.5} Sc _{0.5} Nb _{0.5} O ₁₂ Li ₇ La ₃ Zr _{0.4} Hf _{0.4} Sn _{0.4} Sc _{0.4} Ta _{0.4} O ₁₂	Garnet	1200	SSR	Study on electrochemical properties	(Jung et al. 2022)

MP – Modified pechini; SSR -. Solid state reaction.

Table 2.11. List of published work on ruddlesden popper-based high entropy oxides, their crystal structure, stabilization temperature, processing technique and properties explored.

Composition of HEO	Crystal structure	Stabilization temperature (°C)	Processing technique	Properties explored	Ref.
$(\text{La}_{0.2}\text{Pr}_{0.2}\text{Nd}_{0.2}\text{Sm}_{0.2}\text{Eu}_{0.2})_2\text{CuO}_4$	Ruddlesden	-	PLD	Investigates configurational disorder	(Zhang et al. 2020c)
$(\text{La}_{0.2}\text{Nd}_{0.2}\text{Gd}_{0.2}\text{Tb}_{0.2}\text{Dy}_{0.2})_2\text{CuO}_4$, $(\text{La}_{0.2}\text{Pr}_{0.2}\text{Nd}_{0.2}\text{Sm}_{0.2}\text{Eu}_{0.2})_2\text{CuO}_4$	Ruddlesden	900	SSR & PSE	Study on phase transformation	(Musicó et al. 2021)
$(\text{La}_{0.2}\text{Pr}_{0.2}\text{Nd}_{0.2}\text{Sm}_{0.2}\text{Eu}_{0.2})_2\text{CuO}_4$	Ruddlesden	800	PLD	Study on insulating behavior	(Mazza et al. 2022)
$\text{LnSr}(\text{Co,Fe,Ga,Mn,Ni})\text{O}_4$, where (Ln = La, Pr, Nd, Sm, or Gd)	Ruddlesden	1200	Pechini SG	Investigation on crystal structure, thermal stability, and electrical conductivity	(Dąbrowa et al. 2022)

RFMS - Radio Frequency Magnetron Sputtering; **SSR** - Solid-state reaction; **PLD** - Pulsed Laser Deposition; **FD** – Freeze drying; **PSE** - Polymeric Steric Entrapment; **SG** – Sol-gel.

2.5.4 Properties explored in high entropy oxides

The ability to tailor the properties in HEOs is the main driving force for the increasing interest in this field, as it can be applied in many different areas of applications (Bérardan et al. 2016a; Braun et al. 2018; Chen et al. 2018a; Hong et al. 2019; Sarkar et al. 2017b).

2.5.4.1 Electrochemical

The most commonly used electrochemical energy storage device is the Li-ion solid-state battery due to its very high efficiency and reversibility. Nevertheless, the regular solid electrolytes are not adequately conductive for high-power applications to enable ultrafast charge/discharge rates. For example, the highest internal resistance in Li-ion batteries is seen to be offered from LiPON (Lithium Phosphorous Oxy-Nitride) solid electrolyte (Mizushima et al. 1980; Nagasubramanian and Doughty 2004; Nitta et al. 2015). Besides, commercial Li-ion batteries have a limited theoretical capacity of $(372 \text{ mAh g}^{-1})^{-1}$, which won't be enough to satisfy future energy demands (Cabana et al. 2010; Roy and Srivastava 2015). Hence, a hunt for fast ionic conductors at room temperature for high-power batteries is of essential interest. Therefore, HEOs entered this field to overcome the limitation of ionic conductivity and capacity barrier in commercial Li-ion batteries and flourished as the best solid-state electrolyte with superionic conductivity at room temperature and as a high energy density anode with exceptional cyclic and rate capability properties. Table 2.12 displays the electrochemical properties explored in HEOs, such as ionic conductivity, cyclic stability, specific capacity, and reverse specific capacity by various research groups worldwide.

Bérardan et al. (Bérardan et al. 2016b) reported on the colossal fraction of alkali ions (Na, Li, K) that can be integrated into the single-phase HEO lattice. This was possible due to the internal charge compensation and formation of internal defects (e.g., oxygen vacancies) within the system achieved through the oxidation of Co^{2+} to Co^{3+} (Bérardan et al. 2016b). It was also found that at room temperature, the HEO doped with alkali ions had high ion conductivity in the range from 10^{-6} to $10^{-3} \text{ S cm}^{-1}$, which increases with an increase in doping, as shown in Fig. 2.13 (a) and is comparatively higher than solid-state electrolytes. Besides, the material synthesis technique does not

prioritise the initial valence state of the cations, and results points toward the stabilization of HEOs (MgCoNiCuZn)O where good charge balance between cation and oxygen is required for the partial substitution of cations (Li and Ga) (Bérardan et al. 2016a). It is also observed that these HEOs (MgCoNiCuZn)_{1-x} Li_xO, (MgCoNiCuZn)_{1-x} Na_xO exhibited superionic Li⁺ and Na⁺ conductivity probably due to the oxygen vacancies. During oxidation, vacancies are created through charge compensation while a monovalent element is embodied in the pristine compound, thereby results in improved transport properties. The defects in HEOs provide the diffusion pathway for Li/Na ions through the crystal lattice, results in a high ionic conductivity ($> 10^{-3} \text{ Scm}^{-1}$) at room temperature. Adding on, the superionic conductivity offered by HEOs is 2 orders of magnitude larger than many of the existing solid electrolytes. Thus, HEOs proved to be a promising future candidate in all-solid-state electrolyte battery cells with negligible leakage current. The movement of dopants was through internal defects created in the lattice during the dopant incorporation (Bérardan et al. 2016b). Wang et al. examined the phase transformation from spinel to rocksalt with the addition of Li-ion during synthesis. Hence, transition could also be tailored by replacing multivalent elements. An increase in the redox activity was observed with the increase in Li content (Wang et al. 2020d). Zhao et al. developed HEO based Na-ion cathode (NaNi_{0.12}Cu_{0.12}Mg_{0.12}Fe_{0.15}Co_{0.15}Mn_{0.1}Ti_{0.1}Sn_{0.1}Sb_{0.1}O₂) for sodium (Na) ion batteries. HEO-based Na-ion cathode showcased longer cyclic stability and excellent rate capability. Over 83 % of the capacity was retained even after 500 cycles. Over 60 % of the total capacity was found to be stored in O3 type region (a region with a stack of alternate Na and HEO metal ions layers in an oxygen-ion framework where Na⁺ ions and metal ions occupy the octahedral sites of the respective layers, an ABCABC stacking) which resulted in a high reversible O3-P3 (P3 region is associated with gliding of metal ion layers and forms an ABBCA stack) phase transition behavior (Zhao et al. 2020a). Further investigation into the HEOs cathode and anode would give a ray of hope to stand out as excellent electrode material in rechargeable batteries.

Sarkar et al. reported that irrespective of the particle size (from a few nanometers to micrometers), HEOs ((Co_{0.2}Cu_{0.2}Mg_{0.2}Ni_{0.2}Zn_{0.2})O) electrodes show

promising coulombic efficiencies and long term cycling stability (Sarkar et al. 2018b). Besides this, Qiu et al. reported that the synthesized HEO ((Mg_{0.2}Co_{0.2}Ni_{0.2}Cu_{0.2}Zn_{0.2}O) nanoparticle, which was used as an anode material for Li-ion batteries, displayed a remarkable increase in specific capacity for more than 300 cycles and improved the performance (Qiu et al. 2019). Therefore, it can be observed that optimization the additional parameters such as binders, particle size, electrolyte, etc., could help in attaining superior specific capacities. The main reason behind such an excellent anode performance compared to the other binary oxides anode is the sluggish diffusion effect provided by the HEOs, which accounts for the structural stability and integrity of electrodes. Removal of a cation from the HEO system decreases the configurational entropy, which significantly alters the electrochemical characteristics, e.g., when Cu is removed, much low lithiation potential is noted. Over the first 100 cycles, HEOs displayed better capacity retention versus medium entropy oxides ((Cu_{0.2}Mg_{0.2}Ni_{0.2}Zn_{0.2})O, (Co_{0.2}Mg_{0.2}Ni_{0.2}Zn_{0.2})O, (Co_{0.2}Cu_{0.2}Mg_{0.2}Ni_{0.2})O), hence resulted in significant decay of performance when changing over to medium entropy oxides (Sarkar et al. 2018b). The presence of Co in the HEO system is a must, as its absence leads to the complete failure of cells within ten cycles. Simultaneously Qiu et al. also reported the significance of elements such as Co and Mg in the system (Qiu et al. 2019). Even after subsequent de-lithiation, the structure was noted to be preserved because of the unreduced cations, which allowed the reoccupation of reduced cations to their respective lattice sites during the oxidation reaction (Qiu et al. 2019). Although the deterioration of crystallinity upon cycling was observed in the HEO, traces of crystalline domains were noted after 300 cycles. Scanning transmission electron microscopy – Energy-dispersive X-ray spectroscopy (STEM-EDX) displayed the homogenous distribution of elements even after one complete cycle, thus indicates the preservation of the HEO host matrix throughout the conversion process, and provides reinsertion of metal cations in the de-lithiation cycle (Sarkar et al. 2018b). Qiu et al. presumed that the appearance of a stable host lattice and the slow diffusion effects was the cause of stable cycling performance and structural integrity. The slow diffusion, individual binary oxide formation, and prevention of element segregation are the cause of the preservation of the HEO crystal structure and display of superior electrochemical performance compared to other oxides (Qiu et al. 2019; Sarkar et al. 2018b).

Table 2.12. The ionic conductivity, cyclic stability, and specific and discharge capacity of high entropy oxides.

Composition of HEO	Ionic conductivity	Cyclic stability (cycles)	Specific capacity (mAh.g ⁻¹)	Discharge capacity (mAh.g ⁻¹)	Ref.
(Mg,Co,Ni,Cu,Zn) _{1-x} Li _x O, (Mg,Co,Ni,Cu,Zn) _{1-2x} Li _x Ga _x O	> 10 ⁻³ S.cm ⁻¹	-	-	-	(Bérardan et al. 2016b)
(Co _{0.2} Cu _{0.2} Mg _{0.2} Ni _{0.2} Zn _{0.2})O	-	up to 300	600	446	(Wang et al. 2019b)
(Mg _{0.2} Co _{0.2} Ni _{0.2} Cu _{0.2} Zn _{0.2})O	-	up to 300	1585	920	(Qiu et al. 2019)
(Mg Zn Ni Co Cu)O	-	up to 600	634 – 1148	479	(Zheng et al. 2019)
(Co _{0.2} Cu _{0.2} Mg _{0.2} Ni _{0.2} Zn _{0.2})O	-	up to 500	500-700	-	(Sarkar et al. 2018b)
(Li _x (CoCuMgNiZn) _{0.2} OF _x)	-	up to 300	222	120	(Wang et al. 2019c)
(MgCoNiZn) _{1-x} Li _x O (x = 0.35)	-	up to 130	-	500 – 925	(Lökçü et al. 2020)
(Co _{0.2} Cu _{0.2} Mg _{0.2} Ni _{0.2} Zn _{0.2})O	-	up to 600	>310	86	(Breitung et al. 2020)
(Mg _{0.2} Co _{0.2} Ni _{0.2} Cu _{0.2} Zn _{0.2})O	-	up to 150	-	408	(Chen et al. 2019b)
(Ni _{0.2} Co _{0.2} Mn _{0.2} Fe _{0.2} Ti _{0.2}) ₃ O ₄		up to 100	560	590	(Chen et al. 2020d)
(Mg _{0.2} Co _{0.2} Ni _{0.2} Cu _{0.2} Zn _{0.2})O		up to 900	600	190	(Ghigna et al. 2020)
(Co _{0.2} Mn _{0.2} Ni _{0.2} Fe _{0.2} Zn _{0.2})Fe ₂ O ₄					
(CrMnFeCoNi)O		up to 200	500	1235	(Nguyen et al. 2020a)
(FeCoNiCrMn) ₃ O ₄		up to 300	680	1034	(Wang et al. 2020a)

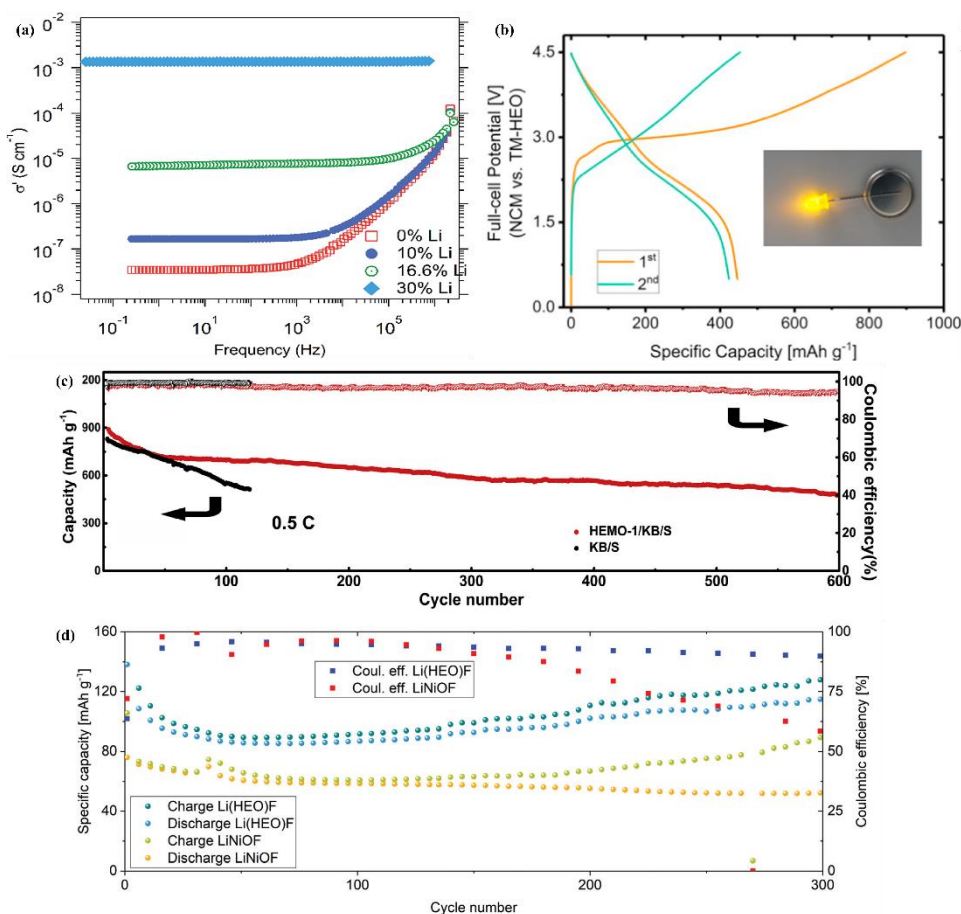


Fig. 2.13. (a) Ionic conductivity of Li doped sample at room temperature (Bérardan et al. 2016b), (b) charge and discharge profile with a photograph of LED powered by HEO fuel cell (Wang et al. 2019b), (c) long-term cycling performance of HEOs (Zheng et al. 2019) and, (d) Comparison of capacity retention of Li(HEO)F and LiNiOF (Wang et al. 2019c).

Furthermore, Wang et al. (Wang et al. 2019b) explored the ability of HEOs as an anode material for use in Li-ion batteries. Fuel cells with HEO ((Mg Zn Ni Co Cu)O) anode and $\text{LiNi}_{1/3}\text{Co}_{1/3}\text{Mn}_{1/3}\text{O}_2$ cathode were developed. As shown in Fig. 2.13 (b), these cells delivered a specific discharge capacity of 446 mAh g^{-1} in the first cycle and were maintained at 300 mAh g^{-1} and 256 mAh g^{-1} even after 50 and 100 cycles. Even at a high specific energy of 240 Wh kg^{-1} , specific currents of 1.6 A g^{-1} , and power densities of about 320 W kg^{-1} , these cells displayed stable cyclability. Additionally, these cells were used as a power source to supply electricity to 32 LED set up. Hence, these HEO anodes have the potential to be used as substitute electrode material for next-generation Li-ion batteries (Breitung et al. 2020; Chen et al. 2020d; Ghigna et al. 2020;

Lökçü et al. 2020; Nguyen et al. 2020a; Wang et al. 2020a; c, 2019b). An attraction to the field of electrochemistry for future studies was reported by Zheng et al. (Zheng et al. 2019) by devising a facile strategy where HEO ((Mg Zn Ni Co Cu)O) was used as an anchor to restrain lithium polysulfides (LIPS). It is observed that the HEOs retain the LIPS and assist the redox reaction in the cathode of Li-S batteries. A shuttle of LIPS between the anode and cathode is monitored to be eliminated due to the benefaction of S-Ni and Li-O from the interaction between HEOs and LIPs. These HEOs materials displayed competitive, reversible capacity, excellent cyclic stability, and low-capacity decay after 600 cycles, as shown in Fig. 2.13 (c). Thus, HEOs work as an excellent booster for polysulfide immobilizing in Li-S batteries and provide ample opportunity in energy conversion and storage fields (Zheng et al. 2019). Chen et al. investigated the electrochemical performance of (Mg_{0.2}Co_{0.2}Ni_{0.2}Cu_{0.2}Zn_{0.2})O HEO ultrafine nanofilm (3 – 5 nm) anode. Since the active material is in the nanoscale dimension, the pseudocapacitive effect is popped out. Hence, magnified interfacial lithium storage capacity was observed due to the enhancement in the pseudocapacitive effect. The anode delivered high specific charge and discharge capacities with long-term cyclic stability (Chen et al. 2019b). Wang et al. (Wang et al. 2019c) also developed a new multi cationic-multi anionic high entropy oxyfluoride compound (Li_x(Co_{0.2}Cu_{0.2}Mg_{0.2}Ni_{0.2}Zn_{0.2})OF_x -Li(HEO)F) and Na containing high entropy oxychloride (Na_x(Co_{0.2}Cu_{0.2}Mg_{0.2}Ni_{0.2}Zn_{0.2})OCl_x -Na(HEO)Cl) which acts as cathode active material with rocksalt structure for next-generation Li-ion battery applications. Herein, not only the cations but the anion can also be varied without hampering the single-phase rocksalt structure. These anion lattices contribute to the configuration entropy, results in additional structural stabilization gain, which enhances the Li-ion storage with high cyclability. In contrast to pure HEO, Li(HEO)F exhibited a working potential of 3.4 V vs. Li⁺/Li with the incorporation of fluorine into the HEO structure. The higher working potential of Li(HEO)F than pure HEO is due to the change in the entire (de)lithiation mechanism from conversion to insertion-type reaction. It is also observed that Li(HEO)F delivers a higher specific capacity than the conventional LiNiOF (Fig. 21 (d)) because the redox-active Nickel is replaced by other elements. Both cobalt and nickel are the only species prone to oxidation during delithiation. Specific capacity increased despite the decrease in redox-active ion fraction (Co and Ni

together amount to 0.4 instead of 1 in LiNiOF). Even after 150 cycles, the coulombic efficiency of Li(HEO)F is noted to be reasonably stable, while that of LiNiOF decreases to a considerable amount, as presented in Fig. 2.13 (d). The entropy stabilization appeared to play a vital role in maintaining high reversible capacities and stabilization of the coulombic efficiency. Thus the notion of multi-anionic and multi-cationic high entropy materials paves the way for future energy storage applications (Wang et al. 2019c). Recent work has shown that HEO can play a vital role in improving the performance of batteries. The flexibility of tuning the compositional space (both anion and cation site), disorder within the system, entropy stabilization, structure stability, and sluggish diffusion effect offered by HEOs results in superior electrochemical properties compared to conventional conversion or intercalation electrodes.

2.5.4.2 Electrical

As mentioned earlier, the unique mechanisms, such as charge compensation and defect formation, which take place within the HEO system, result in unpredictable electronic behavior. Hence based on the structural complexity and compositions, HEOs exhibit decent semiconducting, proton-conducting, and insulating properties, makes them exceptional from the traditional metal oxides. The electrical properties of HEOs were investigated by Bérardan et al. (Bérardan et al. 2016a). From the transport properties, the authors found that HEO ((Mg Co Ni Cu Zn)O) exhibited considerable electrical resistance (2 M Ω) at room temperature. In addition to this, HEOs also exhibited very high capacitance (1250 pF) with strong temperature and frequency dependency. In all HEO ((Mg Co Ni Cu Zn)O) samples substituted with Li, the authors observed an exponential change in the electrical resistance, behave like a semiconductor with an electrical bandgap of about 1 eV. These band gaps were observed to decline with Li substitution in the HEO system. Hence, a significant difference in the electrical resistance at room temperature in the HEOs (with and without Li substitution) was predicted due to the creation of electroactive defects correlated to the substitution of Li⁺. Furthermore, the charge compensation mechanism was assumed to hinder the HEO_xLi₅ ((Mg Co Ni Cu Zn)_{0.95}Li_{0.05}O) and HEO_x-Li₁₆ ((Li Mg Co Ni Cu Zn)O) samples from exhibiting a metallic behavior (p-type doping would entail a large concentration of carrier) (Bérardan et al. 2016a). Few spinel-based HEOs

like (Co, Cr, Fe, Mn, Ni)₃O₄, (Co, Cr, Fe, Mg, Mn)₃O₄, and (Cr, Fe, Mg, Mn, Ni)₃O₄ behaved like a semiconductor (Stygar et al. 2020), which is temperature dependent and electrons were attributed to be the primary charge carriers. Thus, the advantage of tailoring with compositional space and defect (by doping aliovalent or noble metals) offered by HEOs creates a pathway for future research in semiconducting HEOs.

Interestingly, Gazda et al. (Gazda et al. 2020) explored proton conduction in HEOs ($\text{BaZr}_{0.2}\text{Sn}_{0.2}\text{Ti}_{0.2}\text{Hf}_{0.2}\text{Ce}_{0.2}\text{O}_{3-\delta}$, $\text{BaZr}_{0.2}\text{Sn}_{0.2}\text{Ti}_{0.2}\text{Hf}_{0.2}\text{Y}_{0.2}\text{O}_{3-\delta}$, $\text{BaZr}_{1/7}\text{Sn}_{1/7}\text{Ti}_{1/7}\text{Hf}_{1/7}\text{Ce}_{1/7}\text{Nb}_{1/7}\text{Y}_{1/7}\text{O}_{3-\delta}$). The authors assign these perovskite HEOs as proton conductors due to the presence of protonic defects. Higher conductivity was observed in the humid atmosphere than in the dry, and typically represents a proton conductors isotope effect in HEOs. Besides, the mass of the material was enhanced during the shift from a dry to a humid atmosphere, which assured the inclusion of water into the structure. Moreover, the activation energy of the conductivity decreases in humid surroundings, and results in an increase in the proton conductivity. Accordingly, HEOs stepped into a new milestone with excellent proton conductivity. Overall, the convenience of engineering the structure, synthesis parameters, defect density, effect of entropy stabilization, and level of disorder provided by HEOs imply substantial opportunities to uncover highly efficient insulating, semiconducting, and proton conducting materials in HEOs.

2.5.4.3 Dielectric

In addition to the above properties, the display of colossal dielectric constant (CDC) by HEO_x-Li₅ ((Mg Co Ni Cu Zn)_{0.95}Li_{0.05}O), describes the ability of HEOs to store electrical energy in an electric field, which can be further modified by altering the fraction of constituent elements was reported by Bérardan et al. (Bérardan et al. 2016a). Large lattice disorder, complexity within the system, tunability, charge compensations, and creation of defects makes the HEOs an attractive candidate compared to regular metal oxides in dielectrics. Bérardan et al. were the first to report the CDC (2×10^5) for HEOs (substituted with Li) by considering a simple RC parallel circuit (Bérardan et al. 2016a). The sample was heated to a temperature of 700 °C for ten hours and then, it was cooled down slowly. During the cooling process, solid-solid transformation into a mixture of oxides took place, which resulted in a very low resistance (<30 kΩ at room

temperature) and zero capacitance value. Thus, certifying that CDC is not a general feature of oxides (MgO, CoO, NiO, CuO, ZnO) consisting of the divalent cations; instead, it is a characteristic of the HEO phase. In addition, Bérardan et al. also found that the dielectric constant decreases with increased frequency (2.3MHz – 100 Hz). The source of this high dielectric constant value is still a mystery. CDC behavior in oxides might be due to several effects, such as extraneous Maxwell-Wagner-type effects that arise from charge accumulation at interfaces, grain surfaces or grain boundaries (Lunkenheimer et al. 2002, 2009). Also, the samples with significant Li-ion content exhibited low bulk resistance, as substitution of Li led to disorder in the structure due to the defects arising from the substitution (Bérardan et al. 2016a). Hence, by varying the amount of Li added during synthesis, HEO materials could be effortlessly tailored. The lower the Li content in the HEO sample, the higher is the resistance and dielectric constant, which results in a smaller $\tan \delta$ value, i.e., the HEO sample has minimum dielectric loss, hence opens up a wide opportunity in the field of energy storage and electronics (Bérardan et al. 2016a). At the same time, Bérardan et al. also found that the disorder observed in the crystal structure has a substantial impact on the dielectric properties of the HEO (Berardan et al. 2017). The ability to substitute aliovalent elements into the HEO system through a charge compensation mechanism subsequently widened the phase space to a greater extent, which resulted in a larger number of vacancies with the formation of a percolating path. Thus, the advantage of tuning the defect concentration results in promising dielectric properties.

In addition to the above results, Bérardan and the team reported the influence of Cu concentration on the TM-HEOs ((MgCoNiCu)_{0.84}Zn_{0.16}O). As the presence of the precise concentration of Cu creates disorder/distortion in the crystal structure, it strongly influences the dielectric properties of the material. Both electrical resistivity and dielectric constant displayed powerful progress during the 35 days of measurement. The electrical resistivity tediously increased, and in parallel dielectric constant primarily heightened by about 20 % and then decreased asymptotically. A slight change in crystal structure was also observed during this measurement. Overall, the authors confidently stated that the development of dielectric properties in HEO was directly linked to the development of the crystal structure (Berardan et al. 2017). Besides, the

dielectric constant and loss tangent of high entropy perovskite ceramics $\text{Ba}(\text{TiSnZrHfNbGa})_{1/6}\text{O}_3$ displayed frequency dispersion (Du et al. 2020). Similarly, HEOs like $\text{Ba}(\text{Zr}_{0.2}\text{Ti}_{0.2}\text{Sn}_{0.2}\text{Hf}_{0.2}\text{Me}_{0.2})\text{O}_3$ (Zhou et al. 2020b) and $(\text{Na}_{0.2}\text{Bi}_{0.2}\text{Ba}_{0.2}\text{Sr}_{0.2}\text{Ca}_{0.2})\text{TiO}_3$ (Pu et al. 2019) displayed excellent dielectric properties with low dielectric loss due to the structural complexity and control of configurational entropy within HEOs. Table 2.13 displays the dielectric constant of HEOs explored by various research groups worldwide. Tailoring the ratio of ions and doping elements might enhance the dielectric constant of HEOs. Although HEOs exhibits impressive dielectric results in comparison to other binary oxides, an in-depth study on dielectric property in a variety of HEOs may be an achievable objective, and this ability of HEO to display dielectric behavior can be readily transferred to practical devices (Liu et al. 2020c).

Table 2.13. Dielectric constant of high entropy oxides.

Composition of HEO	Dielectric constant (κ)	Ref.
$(\text{Mg},\text{Co},\text{Ni},\text{Cu},\text{Zn})_{1-x}\text{Li}_x\text{O}$, $(\text{Mg},\text{Co},\text{Ni},\text{Cu},\text{Zn})_{1-2x}\text{Li}_x\text{Ga}_x\text{O}$	-	(Bérardan et al. 2016b)
$(\text{Co}_{0.2}\text{Cu}_{0.2}\text{Mg}_{0.2}\text{Ni}_{0.2}\text{Zn}_{0.2})\text{O}$	446	(Wang et al. 2019b)
$(\text{Mg}_{0.2}\text{Co}_{0.2}\text{Ni}_{0.2}\text{Cu}_{0.2}\text{Zn}_{0.2})\text{O}$	920	(Qiu et al. 2019)
$(\text{Mg Zn Ni Co Cu})\text{O}$	479	(Zheng et al. 2019)
$(\text{Co}_{0.2}\text{Cu}_{0.2}\text{Mg}_{0.2}\text{Ni}_{0.2}\text{Zn}_{0.2})\text{O}$	-	(Sarkar et al. 2018b)
$(\text{Li}_x(\text{CoCuMgNiZn})_{0.2}\text{OF}_x$	120	(Wang et al. 2019c)
$(\text{MgCoNiZn})_{1-x}\text{Li}_x\text{O}$ ($x = 0.35$)	500 – 925	(Lökçü et al. 2020)
$(\text{Co}_{0.2}\text{Cu}_{0.2}\text{Mg}_{0.2}\text{Ni}_{0.2}\text{Zn}_{0.2})\text{O}$	86	(Breitung et al. 2020)
$(\text{Mg}_{0.2}\text{Co}_{0.2}\text{Ni}_{0.2}\text{Cu}_{0.2}\text{Zn}_{0.2})\text{O}$	408	(Chen et al. 2019b)
$(\text{Ni}_{0.2}\text{Co}_{0.2}\text{Mn}_{0.2}\text{Fe}_{0.2}\text{Ti}_{0.2})_3\text{O}_4$	590	(Chen et al. 2020d)
$(\text{Mg}_{0.2}\text{Co}_{0.2}\text{Ni}_{0.2}\text{Cu}_{0.2}\text{Zn}_{0.2})\text{O}$	190	(Ghigna et al. 2020)
$(\text{Co}_{0.2}\text{Mn}_{0.2}\text{Ni}_{0.2}\text{Fe}_{0.2}\text{Zn}_{0.2})\text{Fe}_2\text{O}_4$		
$(\text{CrMnFeCoNi})\text{O}$	1235	(Nguyen et al. 2020a)
$(\text{FeCoNiCrMn})_3\text{O}_4$	1034	(Wang et al. 2020a)

2.5.4.4 Magnetic

Magnetic properties are an emerging arena in HEOs, which are yet to be well investigated. Lattice distortion, changes in electronegativity and phase transitions which arise due to high degree of disorder influence the magnetic behavior and exchange interaction in HEOs, makes them favorable terrain for tuning and uncovering fascinating and novel properties in contrast to conventional oxides (Musicó et al. 2020). The magnetic study by Meisenheimer et al. on the nature of magnetism in HEO hints at the role of composition and disorder on exchange anisotropy of HEO ($(\text{Mg}_{0.25(1-x)}\text{Co}_x\text{Ni}_{0.25(1-x)}\text{Cu}_{0.25(1-x)}\text{Zn}_{0.25(1-x)})\text{O}$) heterostructures (Meisenheimer et al. 2017). Meisenheimer et al. investigated the magnetic properties of HEO by examining the role of composition and disorder on exchange anisotropy of HEO ($(\text{Mg}_{0.25(1-x)}\text{Co}_x\text{Ni}_{0.25(1-x)}\text{Cu}_{0.25(1-x)}\text{Zn}_{0.25(1-x)})\text{O}$) heterostructures (Meisenheimer et al. 2017). The existence of anisotropic magnetic exchange and critical blocking temperature indicated antiferromagnetic to be the magnetic order for the above HEOs. Tailoring the composition of oxides, tunes the disorder, magnetic anisotropy, and exchange field. Therefore, Meisenheimer et al. utilized the property of tunability to strengthen the exchange field at low temperatures. Also, in the structural and magnetic parameters of the HEO, a substantial deviation from the rule of mixtures are detected, which signifies that the crystal is ruled by configurational entropy. Thus, the freedom of tuning the composition offered by HEOs allows for the improvement of the exchange field strength at low temperatures compared to the permalloy/CeO heterostructure. As a result, these HEO materials can be employed and customized to engineer magnetic functional phenomena in oxide thin films (Meisenheimer et al. 2017).

Mao et al. (Mao et al. 2019a) synthesized spinel-type HEO nanocrystalline powder ($(\text{CoCeFeMnNi})_3\text{O}_4$) through the solution combustion method at a temperature exceeding 623 K and explored its magnetic properties. These HEOs displayed a distinctive ferrimagnetic behavior at room temperature, with values of coercivity (H_c) and saturation magnetization (M) ranging from 176.55 – 21.39 Oe and 4.85 – 15.98 $\text{emu}\cdot\text{g}^{-1}$, respectively. Since these HEOs were annealed at different temperatures, there were tagged as S523, S623, S723, S823, S923, S1023, and S1123 respectively (Fig. 2.14 (a)). The numeric in the tag represents the annealing temperature (e.g., S523 –

sample annealed at 523 K). As evident from Fig. 2.14 (a), magnetic hysteresis loops indicated the presence of few magnetic moments, and no saturation of loops was observed at the highly applied magnetic field. The inset in Fig. 2.14 (a) shows the magnified display of the low-field region. The variation in values of M and H_c is predicted, which owns to the factors, namely crystallite size, crystallinity, the lattice constant, and lattice distortion, as shown in Fig. 2.14 (b). Mainly the rise in M with synthesis temperature was awarded to the enhanced exchange interaction and large crystallite size. In contrast, H_c is observed to be nearly varying with lattice distortion, and a change of H_c with crystallite size is assigned to the enhanced surface spins and their intense anisotropy. Therefore, by effectively altering the synthesis temperature, the magnetic properties of these spinel-type HEOs can be tailored easily, and makes them a potential candidate for magnetic recording, memory devices, and other particular applications (Mao et al. 2019a, 2020, Marik et al. 2020a; b). Along with spinel-type HEOs, Mao et al. (Mao et al. 2019c) explored the magnetic properties of rocksalt-type HEOs ((Mg Co Cu Zn Ni)O). These HEOs displayed long-range antiferromagnetic behavior below 160 K and paramagnetic conduct at room temperature, which was well understood by the super-exchange interactions, a strong antiferromagnetic coupling between next to nearest neighbor cations through a non-magnetic anion, in rocksalt HEOs. Mao et al. observed that the substitution of nonmagnetic ions such as Mg^{2+} and Zn^{2+} suppressed the antiferromagnetic order. Magnetization increased linearly with an increase in the magnetic field, thus, confirmed paramagnetic behavior in synthesized HEOs and M-H loops displayed weak ferromagnetic behavior at room temperature. Therefore, as a result, these HEOs can be used as promising materials in spintronics and random-access memories (Frandsen et al. 2020; Mao et al. 2019c; Usharani et al. 2020a). In comparison with other binary oxides, the benefit of increased solubility of elements, extremely high chemical and structural disorder within the HEOs, entropy stabilization, and ability to tune the temperature, composition, and defect concentration allow to engineer the HEOs when the magnetic properties are explored intelligently.

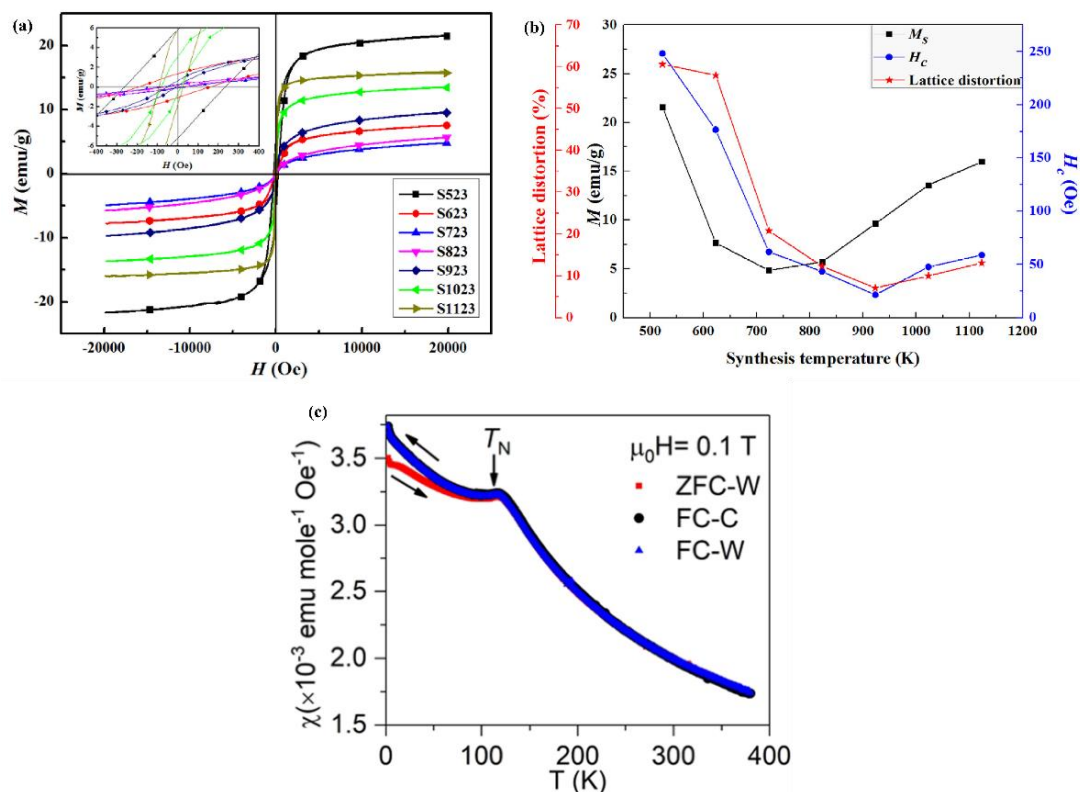


Fig. 2.14. Room-temperature magnetic hysteresis loop for spinel-type HEOs (Mao et al. 2019a), (b) coercivity (H_c), magnetization (M), and lattice distortion against synthesis temperature for spinel-type HEOs (Mao et al. 2019a) and, (c) plot of DC magnetic susceptibility as a function of temperature (Zhang et al. 2019a)

Witte et al. (Witte et al. 2019) performed a detailed study on the magnetic properties of RE and TM-based perovskite (ABO_3) type HEOs, which are compounds with combination of intermixed B site ($Co_{0.2}Cr_{0.2}Fe_{0.2}Mn_{0.2}Ni_{0.2}$) and single-A site (Gd La Nd Sm Y), and another combination of intermixed B site ($Gd_{0.2}La_{0.2}Nd_{0.2}Sm_{0.2}Y_{0.2}$) and single-A site (Co Cr Fe Mn Ni). To understand the interplay between a high degree of chemical disorder in the systems and magnetic exchange, an extensive study using AC and DC magnetometry combined with element-specific spectroscopy was reported. These materials displayed superior antiferromagnetic (AF) behavior with a small fraction of contribution from ferromagnetic (FM) behavior, due to the presence of an antiferromagnetic matrix or small ferromagnetic clusters, or a possible spin canting. A high degree of magnetic frustration was observed in the system due to competing FM and AF interactions and a large degree of disorder. They projected that the sign of magnetic exchange interactions domestically alternated, which led to small FM clusters

within the AF matrix. Thereby, this feature was considered responsible for the observed vertical exchange bias – a shift of the field-cooled magnetization loop of about 25 % of the remnant magnetization. Witte et al. also found that the magnetic ordering temperature of the HEOs was controlled by the size of the RE ions (Witte et al. 2019).

Zhang et al. made an in-depth study on the magnetic structure of HEO ($\text{Mg}_{0.2}\text{Co}_{0.2}\text{Ni}_{0.2}\text{Cu}_{0.2}\text{Zn}_{0.2}\text{O}$) using neutron powder diffraction (Zhang et al. 2019a). This HEO revealed sluggish magnetic transition but possessed a long-range ordered antiferromagnetic ground state, as shown in Fig. 2.14 (c) of DC magnetic susceptibility. DC magnetic susceptibility was measured as a function of temperature with the magnetic field of 0.1T on warming with the field (FC-W), cooling with the magnetic field (FC-C), and warming after zero-field cooling (ZFCW). The transition temperature (T_N) was found to be 113 K, and the magnetic susceptibility continued to increase below 113 K. Magnetic structure was found to consist of ferromagnetic sheets in the (111) planes with spins antiparallel between two neighboring planes. The ordered magnetic moment was found to be $1.4(1) \mu_B$ at 2 K, smaller than anticipated for the average pure spin moment. The reduction at the moment was understood due to the repression of ordering across the lattice on account of utmost chemical disorder and a considerable number of non-magnetic ions, magnetic fluctuations, covalency, or isolated or poorly connected magnetic ions that merely do not order. In addition, $(\text{Ba,Sr,Ca,La})\text{Fe}_{6-x}(\text{Al,Ti,Cr,Ga,In,Cu,W})_x\text{O}_{19}$ HEO with magnetoplumbite structure displayed ferromagnetic properties at low temperature (Vinnik et al. 2020). From the above notable superior magnetic properties of HEOs, Berlijn et al. made a theoretical investigation on the magnetic ground state and spin-wave excitations using linear spin-wave theory combined with supercell approximations to consider the high disorder in the system (Berlijn et al. 2020). Overall, HEOs do show excellent magnetic properties due to their inbuilt features such as a high degree of chemical and structural disorder, high level of entropy effect, tunability of compositional space, internal defect concentration, increased solubility, and many more, but further experimental trials on diverse compositions and assistance from the theoretical calculation in both bulk and films are required for an in-depth understanding in the concept of magnetism and to

enhance the strength of present contribution in HEOs (Krawczyk et al. 2020; Pitike et al. 2020; Rák and Brenner 2020; Witte et al. 2020; Zhang et al. 2019a)

2.5.4.5 Optical

As HEOs permit to play with its wide compositional space, its enables tuning with defects and crystal structure, imposes a strong influence on refractive indices when exposed to radiation, and exhibits different optical behaviors. Hence, Sarkar et al. (Sarkar et al. 2017b) synthesized a new multi-component equiatomic rare earth oxides (ME-REOs) ((Ce Gd La Nd Pr Sm Y)O_{2-δ}) also known as RE-HEOs comprising 3 – 7 rare earth elements (Ce, Gd, La, Nd, Pr, Sm, and Y) in equiatomic proportions and investigated the role of elements on the optical properties. Absorption spectrum was observed for the as-synthesized and calcined systems, and displayed strong absorption below 650 nm, which signified that the decline of the symmetry from fluorite (Fm $\bar{3}$ m) to bixbyite (Ia $\bar{3}$) type structure, as observed in these ME-REOs during calcination; the least influence was found on the optical properties of such systems. Numerous eminent absorption bands were identified at 750 nm, 815 nm, and 885 nm in the as-synthesized and calcined systems containing Sm and Nd. These were concerned with the transition from the 4f^N ground state to the excited state of the Nd³⁺ ion. In the infrared region, the absorption band is found at 108 nm, related to the transition of Sm³⁺ ions. Light absorption over the entire visible spectral range was enabled due to the display of narrow direct band gap energies in the range of 1.95 – 2.14 eV and indirect band gap energy in the range of 1.40 – 1.64 eV of ME-REOs, which could be of importance for practical applications. Interestingly, the bandgap values of this RE-HEOs system were found to be significantly low when compared to binary or doped RE oxides due to the presence of oxygen defects. Multivalent praseodymium (Pr^{3+/4+}) known to enhance the formation and migration of oxygen vacancies in the materials; whereas oxygen vacancies are often the reason for bandgap narrowing. Therefore, the presence of multivalent Pr are the reason behind the lowering of the value of bandgaps in the RE-HEO system. Primarily, the HEOs provides improved resilience for engineering the amount of defects and the ability to tune the properties without hampering the absorbing capability of visible light and phase purity.

Secondly, the most advantageous result of the HEO is the display of a low bandgap in comparison to the other binary oxides (Sarkar et al. 2017b, 2020b).

Zhang et al. synthesized a new HEO glass of composition $10\text{La}_2\text{O}_3\text{-}20\text{TiO}_2\text{-}10\text{Nb}_2\text{O}_5\text{-}20\text{WO}_3\text{-}20\text{ZrO}_2$ (LTNWZ) and explored its optical properties (Zhang et al. 2019b). This amorphous glass had a transmittance of ~62 % in the UV-Vis region with the UV absorption band edge at 354 nm. The IR transmission in LTNWZ widely ranged from 3.4 μm to 7.28 μm wavelength. The absorption band at ~3.4 μm was allotted to the free hydroxyl group, and the arrow mark indicated the absorption of ambient CO_2 . The glass was observed to be colorless and optically transparent in this area. The optical energy bandgap was about 3.18 eV, the Abbe number was 61 in the visible light, and the refractive index of LTNWZ at 587.6 nm was 2.22 higher than the optical glasses. Thus LTNWZ has potential optical applications from the visible to the infrared region (Zhang et al. 2019b). Besides, high entropy transparent ceramic $(\text{La}_{0.2}\text{Nd}_{0.2}\text{Sm}_{0.2}\text{Gd}_{0.2}\text{Yb}_{0.2})_2\text{Zr}_2\text{O}_7$ displayed in-line transmittance, which reached 69.06 % at 2108 nm and showed acceptable optical transparency with ~50 % in-line transmittance in the visible region (Zhang et al. 2020b). Due to the higher refractive index offered by HEOs than commercial optical glasses, it could lead to fascinating optical applications that require higher refractive indices and lower wavelength dispersions.

2.5.3.6 Thermal

From a thermal transport point of view, the unique advantage of HEOs over thermal conductivity is that the entropy stabilization of multiple principal elements and the local ionic charge disorder decreases the phonon scattering time and not velocity. A significant difference between elemental properties like interatomic force and mass reduces the rate at which phonons carry heat, thereby decreases the thermal conductivity of HEO (Musicó et al. 2020). Braun et al. synthesized single-crystal HEOs ($(\text{Mg Ni Co Cu Zn})_{x=0.2}\text{O}$ (J14), $(\text{Mg Ni Co Cu Zn Sc})_{x=0.167}\text{O}$ (J30), $(\text{Mg Ni Co Cu Zn Sb})_{x=0.167}\text{O}$ (J31), $(\text{Mg Ni Co Cu Zn Sn})_{x=0.167}\text{O}$ (J34), $(\text{Mg Ni Co Cu Zn Cr})_{x=0.167}\text{O}$ (J35), $(\text{Mg Ni Co Cu Zn Ge})_{x=0.167}\text{O}$ (J36)) and explored its thermal properties (Braun et al. 2018). They performed thermal characterization utilizing a combination of the time-domain thermoreflectance technique (TDTR) and frequency-domain

thermoreflectance technique (FDTR) by varying the pump heating event throughout frequencies to decouple the thermal diffusivity. They observed that the local ionic charge disorder without compromising mechanical stiffness can reduce the thermal conductivity of their systems. This reduction recommended an improved level of intrinsic phonon scattering in the synthesized HEOs. Overall, both simulation and experimental data revealed that these single-crystal HEOs pose low thermal conductivity with high elastic modulus due to charge disorder among ionic bonds, as shown in table 2.14. Comparative to other ceramics, the inbuilt feature of HEOs, such as high-temperature high entropy phase stabilization and extensive charge disorder, results in increased phonon scattering within the system, which makes these materials a potential candidate in thermoelectric and thermal barrier coating (Braun et al. 2018).

As mentioned before, Gild et al. (Gild et al. 2018) synthesized HEOs and explored their thermal behavior. In agreement with the observation made by Braun et al. (Braun et al. 2018), HEOs also displayed low thermal conductivity, as displayed in table 2.14, because of phonon scattering by a variety of masses and interatomic forces developed from multiple cations. Additionally, they reported that grain size and porosity can also affect thermal conductivity. Due to the large grain size of HEOs (1 – 3 μm), significant phonon scattering at the grain boundaries is not expected to be a major factor, and porosity results in less dense samples that reduce their thermal conductivities (Gild et al. 2018). Zhao et al. revealed low thermal conductivity behavior in $(\text{La}_{0.2}\text{Ce}_{0.2}\text{Nd}_{0.2}\text{Sm}_{0.2}\text{Eu}_{0.2})\text{PO}_4$ high entropy phosphate monazite. At room temperature, the thermal conductivity of $2.08 \text{ W}\cdot\text{m}^{-1}\text{K}^{-1}$ was revealed, which was about 42 % lesser than LaPO_4 , a widely studied thermal barrier coating material (Zhao et al. 2019b). Thus, the superior low thermal conductivity of HEOs is due to the benefit of increased phonon scattering, and the difference of the atomic mass in the crystal structure is extremely greater than the individual elements.

Table 2.14. Thermal conductivity and elastic modulus of high entropy oxides.

Compositions of HEOs	Thermal	Elastic	Ref.
	conductivity (κ) [W.m ⁻¹ .K ⁻¹]	modulus (E) [GPa]	
(Mg Ni Co Cu Zn) _{x=0.2} O	2.95 ± 0.25	152.0 ± 10.6	(Braun et al. 2018)
(Mg Ni Co Cu Zn Sc) _{x=0.167} O	1.68 ± 0.13	236.7 ± 15.9	(Braun et al. 2018)
(Mg Ni Co Cu Zn Sb) _{x=0.167} O	1.41 ± 0.17	158.4 ± 10.9	(Braun et al. 2018)
(Mg Ni Co Cu Zn Sn) _{x=0.167} O	1.44 ± 0.10	180.8 ± 17.9	(Braun et al. 2018)
(Mg Ni Co Cu Zn Cr) _{x=0.167} O	1.64 ± 0.24	151.0 ± 9.2	(Braun et al. 2018)
(Mg Ni Co Cu Zn Ge) _{x=0.167} O	1.60 ± 0.14	229.9 ± 21.2	(Braun et al. 2018)
Sr (Ti _{0.2} Fe _{0.2} Mo _{0.2} Nb _{0.2} Cr _{0.2}) O ₃	0.7	135.2 ± 12.7	(Banerjee et al. 2020)
Zn _{0.1} Ca _{0.1} Sr _{0.4} Ba _{0.4} ZrO ₃	1.45 – 1.87	213.8	(Liu et al. 2020f)
(Nd _{0.2} Sm _{0.2} Eu _{0.2} Y _{0.2} Yb _{0.2}) ₄ Al ₂ O ₉	1.5	-	(Zhao et al. 2020c)
(Hf Zr Ce Y) _{x=0.25} O _{2-δ}	1.74 ± 0.15	-	(Gild et al. 2018)
(Hf Zr Ce) _{x=0.25} (Y Yb) _{x=0.125} O _{2-δ}	1.55 ± 0.20	-	(Gild et al. 2018)
(Hf Zr Ce) _{x=0.2} (Y Yb) _{x=0.2} O _{2-δ}	1.29 ± 0.11	-	(Gild et al. 2018)
(Hf Zr Ce) _{x=0.25} (Y Ca) _{x=0.125} O _{2-δ}	1.1 ± 0.2	-	(Gild et al. 2018)
(Hf Zr Ce) _{x=0.25} (Y Gd) _{x=0.125} O _{2-δ}	1.17 ± 0.13	-	(Gild et al. 2018)
(Hf Zr Ce) _{x=0.2} (Y Gd) _{x=0.2} O _{2-δ}	1.61 ± 0.13	-	(Gild et al. 2018)
(Hf Zr Ce) _{x=0.25} (Yb Gd) _{x=0.125} O _{2-δ}	1.81 ± 0.14	-	(Gild et al. 2018)
(Hf Zr Ce) _{x=0.2} (Yb Gd) _{x=0.2} O _{2-δ}	1.62 ± 0.13	-	(Gild et al. 2018)

To overcome the phase transition issues at high temperatures faced by environmental barrier coatings (EBCs) and thermal barrier coatings (TBCs), Zhao et al. (Zhao et al. 2020c)(Zhao et al. 2020b) developed a coating of HEOs ((Nd_{0.2}Sm_{0.2}Eu_{0.2}Y_{0.2}Yb_{0.2})₄Al₂O₉) to subdue the phase transition and enhance phase stability. (Nd_{0.2}Sm_{0.2}Eu_{0.2}Y_{0.2}Yb_{0.2})₄Al₂O₉ displayed excellent temperature stability (300-1473K), low thermal conductivity (1.5 W.m⁻¹.K⁻¹), and anisotropic thermal expansion (6.96 × 10⁻⁶ K⁻¹ at 300 – 1473K) in comparison to that of Y₄Al₂O₉. The exhibition of low thermal conductivity was awarded to the mass difference of the constituent atoms, and lattice distortion and anisotropic thermal expansion were attributed to the anisotropic chemical bonding, which can be improved by the choosing large-sized cations. Besides, (Y_{1/3}Yb_{1/3}Er_{1/3})₃TaO₇, (Y_{1/3}Yb_{1/3}Er_{1/3})₃NbO₇, and (Sm_{1/6}Eu_{1/6}Y_{1/6}Yb_{1/6}Lu_{1/6}Er_{1/6})₃(Nb_{1/2}Ta_{1/2})O₇ displayed a coefficient of thermal

expansion of $7.96 \times 10^{-6} - 10.8 \times 10^{-6} \text{ }^\circ\text{C}^{-1}$ from room temperature to 1200°C (Zhao et al. 2020b) and HEO films ($\text{Hf}_{(1-2x)/3}\text{Zr}_{(1-2x)/3}\text{Ce}_{(1-2x)/3}\text{Y}_x\text{Yb}_x\text{O}_{2-\delta}$ ($x=0.2,0.0074,0.029$) developed by Wright et al. exhibited coefficient of thermal expansion of $11.4 \pm 0.5 \times 10^{-6} \text{ K}^{-1}$, $12.2 \pm 0.5 \times 10^{-6} \text{ K}^{-1}$ and $11.6 \pm 0.4 \times 10^{-6} \text{ K}^{-1}$ higher than 8YSZ ($11.4 \pm 0.5 \times 10^{-6} \text{ K}^{-1}$) respectively (Wright et al. 2020, 2021). Overall, in contrast to other ceramics, the inherent promising features of HEOs, like atomic mass difference, lattice vibrations, entropy effect, and charge disorder, makes it one of the best material to be applicable in applications that require low thermal conductivity, such as TBCs, EBCs, and turbine engines (Liu et al. 2020f).

2.5.4.7 Catalytic

Metal catalyst plays a pivotal role in the chemical industry and environmental mitigation, for example, activation of N_2 and CH_4 , automotive exhaust cleaning, CO oxidation, etc. (Bell 2003). The main problem faced in the design of the metal catalyst is to improve the cohesive energy that drives co-domain formation and sintering at high temperatures, and to design a catalyst with homogeneously dispersed metals as they enhance migration resulted in rapid sintering leads to minimum surface area for catalysis. As HEOs offer stabilization of homogeneously dispersed cations within the system and reduced particle surface area, they can enable migration and emerge as an excellent catalyst comparative to usual metal oxides (Li et al. 2020a). Thus, Chen et al. (Chen et al. 2018a, 2019a) designed and developed two systems, primarily a simple, low-cost entropy stabilized metal oxide catalyst made up of five metal cations ((NiMgCuZnCo) O_x)-HEOs with Pt) with intrinsic high-temperature (900°C) stabilities which used entropy maximization and secondarily, mechanochemical synthesis of HEOs ((NiMgCuZnCo) O_x)-HEOs with Pt/Ru) at low temperature (500°C). In the first approach, the use of these metal cations enabled the active sites to be strongly dispersed for high catalytic activity in CO oxidation and displayed intense thermal stability (900°C) as a result of high configurational entropy. A complete conversion of CO are observed at 155°C for reduced 0.3 wt % HEO with Pt (PtNiMgCuZnCo O_x), at 245°C for as-synthesized HEOs with Pt (PtNiMgCuZnCo O_x), and 305°C for HEOs (NiMgCuZnCo O_x); it can be conferred that Pt and Pt O_x plays a crucial role in CO oxidation. The reduced 0.3 wt % HEO with Pt displayed extreme stability for 40 h

reaction time during the catalytic oxidation of CO to CO₂ even at 135 °C. Thus, this HEO catalyst not only displayed high stability but also became support for Pt to form an efficient catalyst for CO oxidation (Chen et al. 2018a). Whereas in the second approach, the introduction of 5 wt % of precious metals Pt and Ru in HEOs ((NiMgCuZnCo)O_x), a single atom or cluster, displayed high catalytic activity in the hydrogenation of atmospheric CO₂ and CO. The motivation behind choosing Pt and Ru was their extensive use in industrial catalysis. Increase in the Ru and Pt catalyst loading in HEO from 2 to 5 wt % has shown a significant increment in the conversions of CO and CO₂, which displays an approach toward a low-temperature HEO stable catalyst (Chen et al. 2019a). At high temperatures, noble metal catalysts are known to aggregate and result in the deprivation of catalytic performance. Hence, Chen et al. also discovered the catalytic performance of HEOs with noble metal doping (Chen et al. 2020b). Incorporation of 1 wt % of the noble metals (Au, Pd, and Ru) within HEOs was allowed via entropy stabilization at 900 °C without aggregation, with good CO oxidation stability and catalytic performance. In contrast, Fracchia et al. worked on the stabilization of the Cu (II) active site during CO oxidation on Mg_{0.2}Co_{0.2}Ni_{0.2}Cu_{0.2}Zn_{0.2}O. Stabilization of this HEO resulted in the rocksalt phase, which allowed oxidation/reduction of Cu to be reversible, and the catalytic cycle to take place (Fracchia et al. 2020). Overall, the benefit of HEOs over the usual metal oxide catalyst is the entropy-driven effect which leads to high-temperature structure stabilization for CO oxidation activities. Indeed further research in the development of HEO as a catalyst will have a brilliant perspective in the catalysis area (Chen et al. 2020a; Feng et al. 2020; Hirakawa et al. 2019; Okejiri et al. 2020; Shu et al. 2020).

2.5.4.8 Mechanical

Motivated by the structural properties of HEAs and combining the concept of entropy in ceramics, the ability of non-metallics as a structural material was also investigated. The high degree of disorder and high intrinsic lattice strain involved in HEOs made it exclusive by displaying interesting and supreme mechanical properties compared to conventional oxides (Musicó et al. 2020). Fluorite oxides are known for their potential features, such as high hardness, high melting temperature, maximum strength, high elastic modulus, etc. Gild et al. (Gild et al. 2018) investigated the

mechanical property like hardness of synthesized HEOs ((Hf_{0.25}Zr_{0.25}Ce_{0.25})(Y_{0.125}Ti_{0.125})O_{2-δ}, (Hf_{0.25}Zr_{0.25}Ce_{0.25})(Y_{0.125}Ca_{0.125})O_{2-δ}, (Hf_{0.2}Zr_{0.2}Ce_{0.2})(Y_{0.25}Ca_{0.2})O_{2-δ}, (Hf_{0.25}Zr_{0.25}Ce_{0.25})(Y_{0.125}Gd_{0.125})O_{2-δ}, (Hf_{0.2}Zr_{0.2}Ce_{0.2})(Yb_{0.2}Gd_{0.2})O_{2-δ}, (Hf_{0.25}Zr_{0.25}Ce_{0.25})(Y_{0.125}Mg_{0.125})O_{2-δ}, (Hf_{0.25}Zr_{0.25}Ce_{0.25})(Y_{0.25})O_{2-δ}, (Hf_{0.25}Zr_{0.25}Ce_{0.25})(Y_{0.125}Yb_{0.125})O_{2-δ}, (Hf_{0.2}Zr_{0.2}Ce_{0.2})(Y_{0.2}Yb_{0.2})O_{2-δ}, (Hf_{0.25}Zr_{0.25}Ce_{0.25})(Y_{0.125}La_{0.125})O_{2-δ}, (Hf_{0.2}Zr_{0.2}Ce_{0.2})(Y_{0.2}Gd_{0.2})O_{2-δ}, (Hf_{0.25}Zr_{0.25}Ce_{0.25})(Yb_{0.125}Gd_{0.125})O_{2-δ}), Vicker's hardness measurement was used to explore the hardness of the synthesized single-phase HEOs, along with pure Y₂O₃, 8YSZ, and Yb₂O₃ samples being used as benchmarks. Pure Y₂O₃, 8YSZ, and Yb₂O₃ samples displayed hardness values of 6.9±0.3 GPa 13±0.5 GPa and 5.7±0.3 GPa. HEOs exhibited hardness values in the range of 12.3 to 13.6 GPa, as shown in table 2.15, comparable to that of 8YSZ, despite higher contents of softer components such as Y₂O₃ and Yb₂O₃ (Gild et al. 2018). Although, a large amount of softer components within it, the ability of HEOs to show comparable hardness makes it a prime competitor with commercially available fluorite oxides. Hong et al., (Hong et al. 2019) studied the mechanical properties of HEO ((Mg Co Cu Ni Zn)O) synthesized via field-assisted sintering technology. Maximum strength (323 MPa) and elastic modulus (108 GPa) after densification (relative density – 95.6 %) at 900 °C was obtained because of the trade-off between densification and grain growth. An increase in relative density, with an increase in sintering temperature from 800 °C to 900 °C resulted in an increment in the compressive strength and elastic modulus. At high sintering temperatures, the grain size was increased from 1 μm to 10 μm, which drastically reduced the strength of HEOs. Hence, it is suggested that the mechanical properties of HEOs processed at high temperatures may be controlled by the lattice distortion or defects caused by elemental agglomeration. Therefore, precise control over grain size and microstructure enhances the mechanical properties (Hong et al. 2019). Besides, the strain rate curves of the HEOs synthesized by Biesuz et al., (Biesuz et al. 2018) pointed out quite complicated dilatometric behavior, which was likely linked with the various phenomenon took place upon heating, such as densification, crystallization, and phase transitions. Interestingly, the HEO (LTNWZ) glass synthesized by Zhang et al. displayed an excellent hardness of 6.8 GPa, when compared to phosphate glass of composition Na₂O-BaO-CaO-P₂O₅ (3.35 – 4.09 GPa) and soda-lime-silica glass (5.5 GPa) (Zhang et al. 2019b).

Additionally, to overcome low Vickers hardness and toughness faced by thermal barrier coatings (TBCs), Zhao et al. developed a coating of HEOs ($(Y_{1/3}Yb_{1/3}Er_{1/3})_3TaO_7$, $(Y_{1/3}Yb_{1/3}Er_{1/3})_3NbO_7$, and $(Sm_{1/6}Eu_{1/6}Y_{1/6}Yb_{1/6}Lu_{1/6}Er_{1/6})_3(Nb_{1/2}Ta_{1/2})O_7$) to enhance the toughness and hardness (Zhao et al. 2020b). Surprisingly, the coatings displayed higher Vickers hardness values (10.9-12 GPa) than the principal elements RE_3TaO_7 and RE_3NbO_7 , with excellent phase stability and chemical compatibility. The benefit of high hardness and transparency in HEOs in comparison to other materials and glasses makes it a selective candidate in the development of hard coating, cutting tools, bulletproof glasses, and infrared windows.

Helium (He) bubbles are known to penetrate through the material via grain-boundaries and can prevent dislocations movement, which resulted in hardening and embrittlement of the material, thereby affects the mechanical properties in various ways. Hence, Yang et al. (Yang et al. 2019) took the initiative to explore the mechanical properties of ultrafine nanocrystal HEO ($(Al\ Cr\ Fe\ Ni)O$) film, which was implanted with He. Films were fabricated using a radio frequency (RF) magnetron sputtering system, and the effect of He bubbles on the mechanical properties of the films via nanoindentation measurement was examined. These HEO films had an average grain size ranging from 5.7 nm to 6.5 nm. Grain boundary cavities are observed to increase total strain and stress exponent, which intensifies the local stress transfer to the adjacent region. At the same time, cavities also accelerated the diffusion of vacancies or atoms by the creation of more internal surfaces. As a result, significant degradation of hardness, elastic modulus, and creep resistance of HEO films were observed due to the cavities induced by Helium at the grain boundary. Consequently, the mechanical properties of the He-induced HEO films not only depend upon the film properties, but also depend on the interplay between the He-bubbles and defects of the materials (Yang et al. 2019). A similar study was investigated by Zhang et al. on $(Al_{0.2}Cr_{0.2}Fe_{0.2}Ni_{0.2})_3O_4$ HEO. The damage induced by surface irradiation substantially extends to the indirect irradiation region of the film, where phase transformation, He bubbles dislocation, and nickel oxide segregation are found. Moreover, He vacancy played a significant role in the damage due to the stabilization of He on the vacancy. Therefore, the defects and cavities due to He bubbles within HEOs may not favor enhancement mechanical

properties of HEOs. Moreover, on a positive note, reduced He in the radiation may be a practical approach to design radiation tolerance materials (Zhang et al. 2020a). Kirnbauer et al. research displayed the effect of varying annealing temperature and oxygen flow rate on the indentation hardness and elastic modulus of HEO thin film $(\text{Al}_{0.19}\text{Cr}_{0.13}\text{Nb}_{0.19}\text{Ta}_{0.30}\text{Ti}_{0.19})\text{O}_2$ deposited on the sapphire substrate. With the magnification of the oxygen flow rate ratio, the hardness and elastic modulus slightly increased to 24 GPa and 400 GPa, as displayed in Fig. 2.15 (a). But, the change in the crystal orientation at 1000 °C annealing temperature led to a decline in hardness to 21 GPa and an increment in elastic modulus to 460 GPa, as displayed in Fig. 2.15 (b) (Kirnbauer et al. 2019). Overall, HEOs thin film strength must be further explored with precise understanding for a variety of applications. Thus, HEOs are an unpredictable material whose mechanical properties entirely depend on various factors such as entropy, enthalpy, temperature, morphology, compositions, and synthesis conditions.

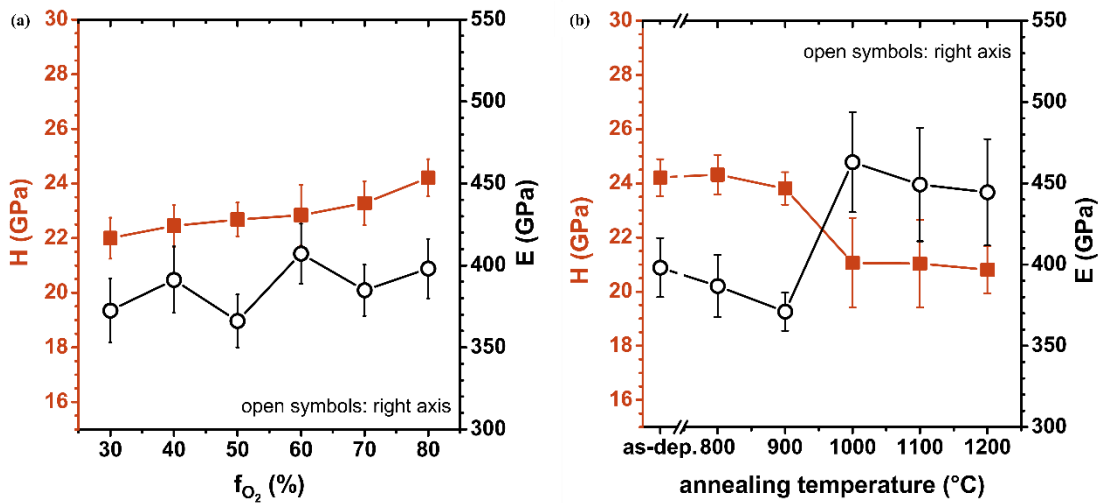


Fig. 2.15. The plot of indentation hardness and elastic modulus of $(\text{Al}_{0.19}\text{Cr}_{0.13}\text{Nb}_{0.19}\text{Ta}_{0.30}\text{Ti}_{0.19})\text{O}_2$ HEO thin film on sapphire substrates versus (a) oxygen flow rate ratios f_{O_2} from 30 % to 80 % and (b) annealing temperature (Kirnbauer et al. 2019).

Table 2.15. Vickers hardness values of high entropy oxides.

Compositions of HEOs	Vickers hardness (GPa)	Ref.
$(\text{Hf Zr Ce Y})_{x=0.25}\text{O}_{2-\delta}$	13.6 ± 0.5	(Gild et al. 2018)
$(\text{Hf Zr Ce})_{x=0.25}(\text{Y Yb})_{x=0.125}\text{O}_{2-\delta}$	12.7 ± 0.7	(Gild et al. 2018)
$(\text{Hf Zr Ce})_{x=0.2}(\text{Y Yb})_{x=0.2}\text{O}_{2-\delta}$	13.3 ± 0.6	(Gild et al. 2018)
$(\text{Hf Zr Ce})_{x=0.25}(\text{Y Ca})_{x=0.125}\text{O}_{2-\delta}$	13.3 ± 0.6	(Gild et al. 2018)
$(\text{Hf Zr Ce})_{x=0.25}(\text{Y Gd})_{x=0.125}\text{O}_{2-\delta}$	13.2 ± 0.5	(Gild et al. 2018)
$(\text{Hf Zr Ce})_{x=0.2}(\text{Y Gd})_{x=0.2}\text{O}_{2-\delta}$	13.1 ± 0.5	(Gild et al. 2018)
$(\text{Hf Zr Ce})_{x=0.25}(\text{Yb Gd})_{x=0.125}\text{O}_{2-\delta}$	12.6 ± 0.5	(Gild et al. 2018)
$(\text{Hf Zr Ce})_{x=0.2}(\text{Yb Gd})_{x=0.2}\text{O}_{2-\delta}$	12.3 ± 0.7	(Gild et al. 2018)
$(\text{Y}_{1/3}\text{Yb}_{1/3}\text{Er}_{1/3})_3\text{TaO}_7$, $(\text{Y}_{1/3}\text{Yb}_{1/3}\text{Er}_{1/3})_3\text{NbO}_7$, $(\text{Sm}_{1/6}\text{Eu}_{1/6}\text{Y}_{1/6}\text{Yb}_{1/6}\text{Lu}_{1/6}\text{Er}_{1/6})_3(\text{Nb}_{1/2}\text{Ta}_{1/2})\text{O}_7$	10.9-12	(Zhao et al. 2020b)

2.6 Solution combustion synthesis

Globally, the majority of primary energy is produced through combustion, which is a universal process. For combustion to take place, a fuel (such as coal, oil, nuclear energy, hydropower, renewable energy, and natural gas) is burned with an oxidizer, often air, to produce heat that is transferred down for various uses, including propulsion, heating, and energy generation (Carlos et al. 2020). Combustion may also be used to get rid of waste biomass and dangerous contaminants. A redox reaction, also known as an electron transfer process, that involves the oxidation of the fuel and the reduction of the oxidizer to produce an exothermic reaction is what defines combustion. Combustion processes that are widespread in society, such as those that occur in factories, wildfires, automobile exhaust, and power plants, are primarily characterized by high temperatures, which are frequently coupled with elevated pressures and transitory circumstances. Generally, products are often considered to be pollutants because they include noxious gases that are bad for the public's health, such as ammonia (NH_3), carbon dioxide (CO_2), sulfur dioxide (SO_2), nitrogen oxide (NO), carbon monoxide (CO), and nitrogen dioxide (NO_2) (Dmitrienko et al. 2018). But when combustion is used in synthesis, it enables the production of several inorganic compounds at low temperatures, like catalysts and ceramic powders (Chick et al. 1990; Merzhanov 2004). Fig. 2.16 shows the three essential components of combustion: an oxidizer, a fuel (reducer), and the required temperature. However, from ancient times, this synthesis

has been employed to create carbon black from flames for cave painting. Pechini carried out the first practical use of combustion synthesis in 1967. The Pechini technique uses precursor resins to produce oxides, which are then compacted into a thick ceramic to manufacture capacitors (Pechini P. Maggio 1967). In order to create refractory inorganic compounds, Merzhanov invented self-propagating high-temperature synthesis, also known as combustion synthesis, in the early 1970s (Merzhanov 2004). To generate non-oxide and oxide materials, the process needs high-purity fine precursors that burn at high temperatures ($> 1000\text{ }^{\circ}\text{C}$) and are very exothermic, reaches temperatures of $4000\text{ }^{\circ}\text{C}$. However, because of the solid-state reaction, it does not produce homogenous products; i.e., coarse particles with limited surface areas (Patil et al. 2008). The type of reactants, which may be gases, liquids, or solids, determines how the combustion synthesis process works. Due to this, combustion synthesis processes are categorized into three main classifications: gas phase combustion synthesis, solid phase combustion synthesis (which is further divided into self-propagating high-temperature synthesis and volume combustion synthesis), and solution combustion synthesis (Carlos et al. 2020). Gas phase combustion synthesis isn't simply a process in which each reactant is gaseous; it also includes combustion methods where the gas phase is involved in some way during the synthesis. It depends on a variety of variables, such as temperature, reactant concentration, and particle form (Brezinsky 1996). In solid-phase combustion synthesis, a powder mixture of solid reactants is compressed into a cylinder-shaped pellet and burnt using a laser, tungsten coil, or another appropriate energy source. The energy source works locally in self-propagating high-temperature synthesis and launches a highly exothermic reaction that spreads throughout the mixture (Merzhanov 2004). In the case of volume combustion synthesis, all of the volume of the sample with a mixture of powder undergoes heating evenly and controlled manner.

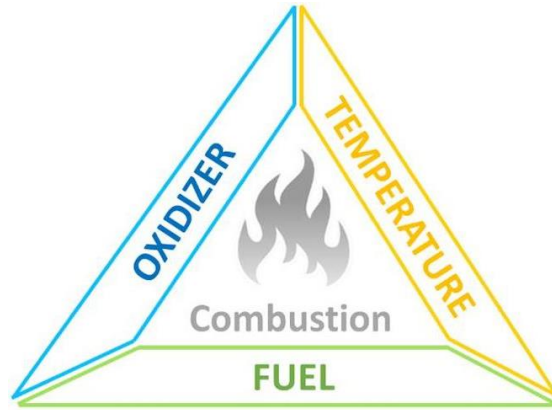
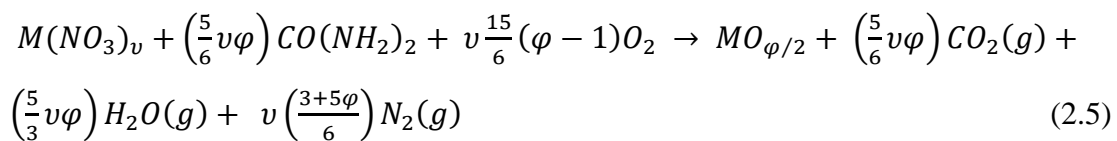


Fig. 2.16. Required components for combustion synthesis (Carlos et al. 2020).

Solution combustion synthesis (SCS) is the most broadly used approach, well known for its ability to successfully synthesize high-surface nanoscale materials, including composites, metal oxides, oxides, and sulfides (Kingsley and Patil 1988). The Jain technique was first used to accomplish SCS in 1981 (Jain et al. 1981). The technique relies on the stoichiometric ratio of the fuel and oxidizer (φ) and is expressed as follows

$$\varphi = \frac{\text{total valency of the fuel}}{\text{total valency of oxidizer}} \quad (2.4)$$

Consequently, the stoichiometric equilibrium combustion reaction can be written as follows, considering the reaction between the fuel, urea ($\text{CO}(\text{NH}_2)_2$), and metal nitrates ($\text{M}(\text{NO}_3)_v$)



Where v is the metal elements oxidation state. The mixture is "stoichiometric" when $\varphi = 1$, "fuel lean" when $\varphi > 1$, and "fuel rich" when $\varphi < 1$, according to equation (2.5). It means that when more fuel is added to the system, more oxygen is needed. But in an atmosphere without enough oxygen for the reaction to work correctly, it ends up with carbonaceous products. When less fuel is used, the combustion temperature gets lower, so it is essential to adjust the fuel amount to control the crystallinity and properties of the synthesized metal oxides.

SCS is the fastest, simplest, and most efficient process that is becoming increasingly popular around the world for the production of oxide materials with regulated characteristics (high purity and uniformity) for a broad range of applications, such as catalytic converters, solid fuel cells, and electronic devices (Carlos et al. 2020). The combustion synthesis of TiO_2 and ZrO_2 by the exothermic breakdown of the precursors was initially reported in 1993 by Sekar and Patil (Sekar and Patil 1993). In addition, the combustion synthesis of $\gamma\text{-Fe}_2\text{O}_3$ utilizing malonic acid dihydrazide as a fuel was also reported for the first time by Patil et al. (Suresh and Patil 1993). Deshpande et al. (Deshpande et al. 2005) and Mukasyan's et al., (Mukasyan and Dinka 2007) both described the creation of Fe_3O_4 powders, a major component of the clan of iron oxides, had a particular surface area of $50 \text{ m}^2.\text{g}^{-1}$ in an argon environment. Other energy-related compounds, such as ZnO (Nagaraja et al. 2011), WO_3 (Morales et al. 2008), SnO_2 (Fraigi et al. 2001), ZrO_2 (Deshpande et al. 2011), and Co_3O_4 (Ai and Jiang 2009), were also produced by SCS, demonstrates the broad applicability of this technique for making binary metal oxides. By using a combination of ethanol and ethylene glycol as solvents and tetra-n-butyl titanate as the source of titanium in the presence of trace quantities of metal ions such as Mn^{2+} , Cu^{2+} , Sn^{4+} , and Ce^{3+} , Ni et al. (Ni et al. 2011) reported the metal ion doping of TiO_2 nanoparticles by SCS. Additionally, it was discovered that a tiny quantity of Sn enhanced the percentage of oxygen vacancies and/or defects within the TiO_2 crystal, but the reverse effect was seen when other metal ions were used for doping. Doping frequently alters the morphology of materials. When co-doped ZnO was created, Ekambaram et al. (Ekambaram et al. 2007) discovered that the un-doped ZnO particles were interconnected in the manner of an enormous network structure with random pore sizes and shapes. Cobalt-doped ZnO , on the other hand, was found to have a flakes-like morphology. Using combinations of metal nitrates and tetra-formal trisazine, Manoharan and Patil (Manoharan and Patil 1993) documented the combustion synthesis of LnCrO_3 ($\text{Ln} = \text{La, Pr, Nd, Sm, Dy, Gd, and Y}$) and LaMO_3 ($\text{M} = \text{Mn, Co, and Ni}$). This study marked the beginning of the use of SCS for the preparation of complex compounds. Jiang et al. (Jiang et al. 2008) used citric acid and urea as co-fuels to manufacture spherical-shaped BiVO_4 photocatalysts by SCS, subsequently undergoing annealing at around $500 \text{ }^\circ\text{C}$ for various durations. There have been reports on the production of more complicated

ternary or quaternary oxides, like $\text{Bi}_4\text{TaO}_8\text{Cl}$ (Manikandan et al. 2011), Bi_2WO_6 (Zhang et al. 2010), $\text{K}_{0.80}\text{Ti}_{1.733}\text{Li}_{0.267}\text{O}_4$ (Yin et al. 2013), Li_4SiO_4 (Choudhary et al. 2014), $\text{Bi}_4\text{Ti}_3\text{O}_{12}$ (Subohi et al. 2012), and $\text{Bi}_2\text{Ce}_2\text{O}_7$ (Saha et al. 2012), which have small particle sizes, comparatively large specific surface areas, good crystallinity. The preparation of oxides with a more complicated structure often requires an elevated formation temperature and a more prolonged reaction time; as a result, the benefits of SCS are more apparent in the creation of these compounds.

2.6.1 Solution combustion processed thin films

Metal oxide thin films have been formed with vapour phase deposition methods for industrial applications, regardless of the functions. These widely used thin film deposition techniques have the advantage of being both mechanically and electrically robust (Fortunato et al. 2012; Pasquarelli et al. 2011). Thermal evaporation, sputtering, pulsed laser deposition, and atomic layer deposition are some of the vapour phase deposition processes. A good tuning of the oxygen content is necessary for the deposition of compositionally resistant metal oxides when using the thermal deposition method, which is frequently employed to deposit metalized products. Metal oxides are frequently deposited via sputtering. Sputtering creates durable metal oxide thin layers on plastic substrates even at room temperature, but the technique is expensive since it requires sophisticated targets and equipment. In the past two decades, pulsed laser deposition (PLD) has arisen as one of the most well-known and inherently simple techniques for depositing a whole range of new materials that are being investigated for future generation applications (Lowndes et al. 1996; Mattox 2007). The fame of PLD is due to its intrinsic flexibility, versatility and ability to produce high energy particles, which allows premium quality film growth at low substrate temperature. They are also known for producing multi-layered films of different materials by sequent ablation. PLD is one of the physical vapor depositions (PVD) processes, conducted in a vacuum environment. The metal oxide target is exposed to intense UV pulses that cause the metal oxide to vaporise into a plasma plume. Despite the fact that PLD can produce thin films with adequately controlled chemical compositions that are morphologically resilient, the technique is capital-demanding due to the sluggish deposition rates and tiny area deposition. In addition, the foundation of the atomic layer deposition (ALD)

approach is exposing the substrate to pulses of gaseous reagents. The self-limiting reactions of reagent gases enable the development of atomically thin films. The thin films produced by ALD deposition are durable and may be uniform across a vast region. Metal oxide dielectrics are often created using ALD procedures. ALD is a pricey and time-consuming method, nevertheless, because of the sluggish deposition rates. The vapour phase deposition techniques continue to be the best option for investigating novel material systems as they can produce thin films with benchmark characteristics that are morphologically resilient. In contrast, solution-based deposition approaches are an appealing and viable replacement for high-vacuum aided deposition techniques because of their scalability, simplicity of fabrication, and ability to reduce production costs (Pasquarelli et al. 2011).

When L. Gordon and his research partners noticed translucent layers preserved on the interior of the glass beaker during gravimetric analysis by the precipitation method, they realized that solution-based deposition was possible (Gordon 1952). The translucent layers provided a fresh perspective on how to comprehend the characteristics of these films and their effects. This unintentional finding gave rise to a brand-new branch of thin film deposition known as "solution processing." Solution-based deposition approaches, which may be divided into three primary categories: printing, spray coating, and spin coating, offer comparatively straightforward solutions to the inherent problems of different vacuum-based procedures. Printing is an additive deposition method that enables both deposition and patterning to occur simultaneously. Gravure, spray printing ink-jet, flexography, screen printing, and slot casting, are among the techniques of printing that are often utilized. For instance, metallic lines are frequently deposited for solar cells via screen printing. Furthermore, organic and organic-metal oxides have been effectively deposited via ink-jet printing. A nozzle-injected mist of atomized droplets is used for spray coating. For effective atomization, the process requires a volatile and low-viscosity solvent. Commercially, spray deposition is used to form thin coatings and to produce smooth thin films, it requires optimization. Additionally, the centrifugal force used in spin coating uniformly distributes the precursor solution over the substrate. The thickness of the film is affected by acceleration, the density of the solution, the volatility of solvent, and the

concentration of the solute (Pujar et al. 2020). Solution-based deposition methods are depicted in Fig. 2.17

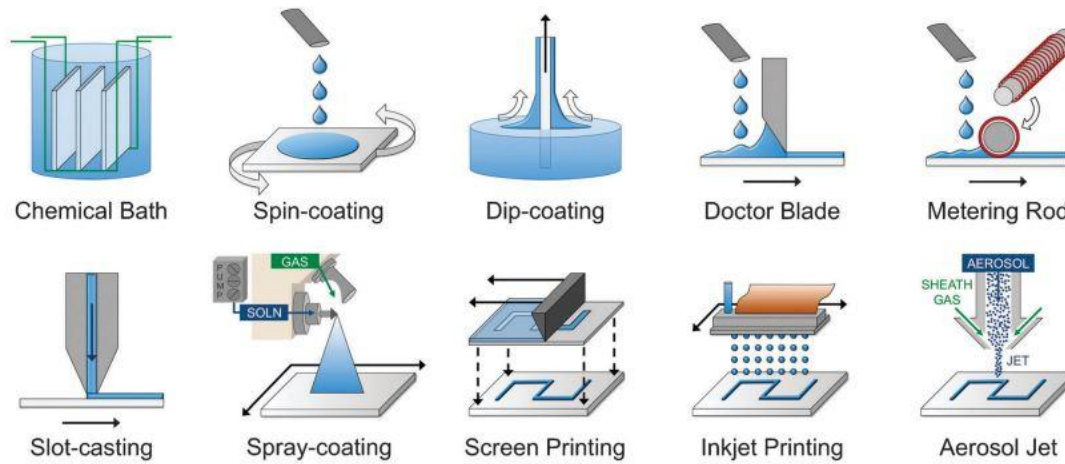


Fig. 2.17. A schematic representation of different solution-based methods of film deposition. (Pasquarelli et al. 2011)

The components of combustible precursors include metal nitrates and organic fuels (Varma et al. 2016). The metal oxide may develop with the least amount of external energy because of the high localized temperature created by the combustion process. In 2011, Kim et al. made the first mention of the usage of combustible precursors (Kim et al. 2011). Spin-coating and annealing at 200 °C were utilized to create functional metal oxide thin films of indium oxide (In_2O_3), indium zinc oxide (IZO), tin-doped indium oxide (ITO), and zinc tin oxide (ZTO) from the combustible precursor, which consisted of metal nitrates and fuel mixed in an organic solvent (2-methoxyethanol: 2-ME). All metal oxide thin films that had been deposited were uniformly smooth, and the In_2O_3 thin films were crystalline in nature. Thin films are more easily able to transport mass and heat because of their high surface-to-volume ratio. Pre-decomposition, sample size, and heating profile are important parameters that influence thin film combustion (Erri et al. 2004; Kim et al. 2012). The existence of fuel ligands does contribute to a reduction in the temperature of metal oxide formation, but the gradual reaction necessitates some degree of precursor pre-decomposition. In conventional bulk systems, enough heat may be persuaded by the exothermic reaction on to the surrounding materials to trigger a combustion reaction. In contrast, thin films require sufficient external heat to ignite combustion since the self-generated heat is

insufficient. Although the thin film has the necessary combustible elements, factors like the surface-to-volume ratio and the thermal conductivity of the substrate have a significant impact on the kinetics of reaction. Therefore, metal oxide formation in the thin film is a result of a combination of internal and exterior heating. In addition, novel multinary oxide systems, such as yttrium-doped In_2O_3 (IYO), indium gallium zinc oxide (IGZO), and $(\text{CoCrFeMnNi})\text{O}$ ((CCFMN)O)), are being developed by the combustion procedure. Since the first discovery, the low-temperature deposition of functional metal oxides has been extensively researched in several fabrication processes for electronic devices, such as gas sensors, solar cells, TFTs, and organic light-emitting diodes (OLEDs) and so on (Kim et al. 2012; Salian et al. 2023a; Sanchez-Rodriguez et al. 2013).

2.6.2 High entropy oxide thin films

Over the past few years, inspired by Rost et al. (Rost et al. 2015) work, research on HEOs has increased, which extends from the initial rocksalt structure to spinel, perovskite, magneto-plumbite, fluorite and several other types of HEOs. These oxides have shown superior properties like excellent electrochemical and catalytic behavior, high strength, increased electrical resistance, and good optical behavior (Musicó et al. 2020; Salian and Mandal 2022b; Sarkar et al. 2019). Since the discovery of HEOs, most of the works have been concentrated on bulk HEO systems, while investigation on thin film is rare. Post the discovery of HEAs, few groups worked on high entropy alloy oxide films which displayed excellent structure and increased electrical resistivity (Lin et al. 2010; Tsau et al. 2012, 2015). Impelled by these alloy oxide films and combining the concept of HEO, a few research groups have stepped forward and have performed an intense investigation on HEOFs (Rost 2016). Post the discovery of HEOs in 2015, HEOFs have been subsequently developed (Musicó et al. 2020; Rost et al. 2015). The composition design for the film is alike to that of HEOs. High entropy oxide film (HEOF) was first reported in 2016 when Rost et al. (Rost 2016) first, prepared entropy stabilized oxide film $(\text{MgZnNi})\text{OTiO}_2\text{Ga}_2\text{O}_3$, $(\text{MgCoCuNiZn})\text{OCaCO}_3$, $(\text{MgCoCuNiZn})\text{OSc}_2\text{O}_3$, $(\text{MgCoCuNiZn})\text{O}$, and MgCoCuNiZnXO ($\text{X}=\text{Ca},\text{Cr},\text{Sb},\text{Sn},\text{Ge}$) using pulsed laser deposition (PLD) and explored their behaviours, effect of processing parameters, structure, and stability. Rost et al. (Rost

2016) work created a gateway for further exploration of HEOFs. Meisenheimer et al. prepared permalloy/ $(\text{Mg}_{0.25(1-x)}\text{Co}_x\text{Ni}_{0.25(1-x)}\text{Cu}_{0.25(1-x)}\text{Zn}_{0.25(1-x)})\text{O}$ heterostructure film through PLD and studied the role of composition and disorder on exchange anisotropy (Meisenheimer et al. 2017). Later, Sharma et al. developed a single crystal epitaxial high entropy perovskite oxide film (HEPOF) $\text{Ba}(\text{ZrSnTiHfNb})_{0.2}\text{O}_3$ and examined its phase stability and phase structure (Sharma et al. 2018). With the ongoing progress, Kotsonis et al prepared $(\text{MgNiCoCuZnSc})_{0.167}\text{O}$ film and analyzed the effect of processing parameters like pressure, and kinetic energy on phase stabilization (Kotsonis et al. 2018, 2020), and Salian et al developed TFT using combustion derived $(\text{CoCrFeMnNi})\text{O}$ film. Processing routes reported so far in literature for the fabricating HEOFs are PLD, magnetron sputtering (MS), plasma spraying and solution combustion. HEOFs introduce a new path of developing advanced materials with unique properties. The display of promising properties is due to their ability to tune the features. The experimental results reported up to date have revealed that the HEOFs have major application potential in the magnetic, thermal, mechanical, optical and electrical fields (Ahn et al. 2021; Bi et al. 2020; Jacobson et al. 2021; Kirnbauer et al. 2019; Mazza et al. 2021; Meisenheimer et al. 2017; Patel et al. 2020; Sharma et al. 2018, 2020; Wang et al. 2021b; Witte et al. 2019; Yang et al. 2019; Zhou et al. 2020a). The microstructure of HEOFs can be controlled by various processing parameters such as cooling rate, substrate temperature, heat treatment and so on (Jacobson et al. 2021; Kotsonis et al. 2018, 2020). As HEOFs are in the cradle stage, a more extensive study should be carried out with the assistance of theoretical study and the development of new theories will give a better understanding of the functional behavior by providing a pathway to reach real-time use of HEOFs in various applications.

2.7 Metal oxide dielectrics

When an electric field is applied, a dielectric, which is an electrical insulator, can become polarized. When a dielectric is exposed to an electric field, electrical charges change from their typical equilibrium locations and leads to dielectric polarization. In order to minimize the total field within the dielectric itself, positive charges relocate in the direction of the field while negative charges relocate in the reverse direction (Wang et al. 2015a). A dielectric generally cannot instantly polarize when exposes to an

electric field. Dielectric relaxation, which results from a delay in polarization in response to a changing electric field in a dielectric material, indicates an irreversible loss of energy. The definition of the dielectric loss ($\tan \delta$), a metric for dielectric relaxation, is

$$\tan \delta = \frac{\kappa''}{\kappa'} \quad (2.6)$$

Where, κ and κ' are the real and imaginary parts of dielectric constant respectively. The dielectric materials with a minimal loss, often less than 0.01, are an intriguing class for TFT applications. Conventionally, the frequency-dependent electrical resistance and dielectric constant are characterized using dielectric spectroscopy, which investigates the relationship of the material being studied with a time-varying electric field (Wang et al. 2013a). The intensity and duration of charge density variations across the sample are characterized by the behavior of the frequency-dependent κ and $\tan \delta$ (Fig. 2.18 (a)). As shown in Fig. 2.18 (b-f), these variations are typically caused by electronic, ionic, molecular orientation, chain relaxation, free counterions polarization, space charges (interfacial) polarization, and electrode or electric double-layer (EDL) polarization (Wang et al. 2018a). As a result, the actual intensity of these polarizations variation in Fig. 2.18 (a) depends greatly on the kind of material used and not all polarization types react to the frequency of the time-varying electric field in the same way.

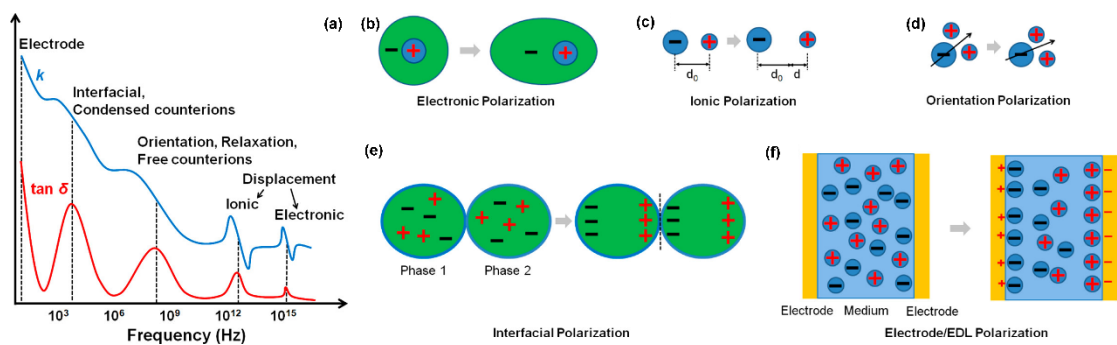


Fig. 2.18. (a) Change in dielectric constant (κ) and dielectric loss ($\tan \delta$) with respect to different polarizations and frequency, (b) pictorial representation of (b)electronic, (c) ionic, (d) orientation, (e) interfacial, and (f) electrode or EDL (electric double layer) polarization (Wang et al. 2018a).

When an electric field bends the negative electronic cloud close to a material's positive atomic nuclei in the direction counter to the field, it results in electronic

polarization (Fig. 2.18 (b)), which happens at frequencies up to $\approx 10^{15}$ Hz. Electronic polarization predominates in the dielectric characteristics of most atomic crystals because the atoms are tightly bound together in a lattice arrangement (Wang et al. 2014a). In ionic compounds, ionic polarization (Fig. 2.18 (c)) frequently takes place and reacts to field frequencies up to $\approx 10^{12}$ Hz. An induced polarization results from the displacement of the cations and anions in opposing directions when an external field is applied. Once a material has a permanent dipole moment that rearranges in response to the introduction of an electric field, orientational polarization (Fig. 2.18 (d)) results (Chernyak 2006). Polarization is caused by the dipolar moieties attached to polymers and permanent molecular dipole moments are being reoriented in the direction of the applied field. As a result, for the majority of polymeric dielectrics, chain relaxation and orientation polarization jointly dominate the dielectric behavior, and their relaxation frequencies fall within the range of intermediate frequencies ($\approx 10^8$ – 10^{10} Hz). Consequently, only at low frequencies $\approx 10^6$ and 10^3 Hz, respectively, interfacial and electrode polarization can contribute towards the dielectric response. When charge builds up at interfaces in a heterogeneous material made up of more than one phase, interfacial polarization (Fig. 2.18 (e)) takes place (Bécu et al. 2006). Both confined and free charges are affected by this kind of polarization. Interfacial polarization is hence typically seen in hybrid systems and polycrystalline materials. All electric/ionic conducting systems include free charges and/or ions, when moved towards the electrode/sample interface by an electric field, result in the production of electric/ionic double layers in those areas (Fig. 2.18 (f)). This phenomenon is known as electrode polarization (Bordi et al. 2004). The electrode polarization is influenced by a number of variables, such as the temperature, composition, conductivity, and physicochemical condition of the electrodes—more specifically, the physicochemical characteristics of the bulk phase (Ishai et al. 2013).

A parallel-plate metal-insulator-metal (MIM) capacitor is shown in Fig. 2.19 (a) and is used to gauge a dielectric characteristic of a material. The associated charge distribution is in equilibrium in the absence of an external voltage. When a voltage is applied to the electrodes, a net dipole moment seems to be averaged all over the volume, and this in return generates a surface charge density on the two sides of the material

that acts as a dielectric. The capacitance per unit area (C_i) is the figure-of-merit, or the capability of the capacitor to hold an electrical charge at a particular voltage, written using the following equation (Wang et al. 2016a)

$$C_i = \frac{\kappa \epsilon_0 A}{d} \quad (2.7)$$

Where, ϵ_0 is the dielectric constant of free space (8.854×10^{-12} F.m⁻¹), A is the area of the parallel plate electrode, and d is the distance between the parallel plates. Both a high- κ ($\kappa > 3.9$) and low- κ ($\kappa < 3.9$) dielectric are shown in Fig. 2.19 (b) as examples of frequency-dependent areal capacitance curves. At lower frequencies, the areal capacitance of high- κ materials of acceptable quality normally stays steady, while at higher frequencies it decreases noticeably. The explanation for this is that each polarization exhibits distinct behavior over a range of frequencies, and some polarizations in high- κ materials are unable to adapt to changes in a high-frequency electric field. Since electronic polarization makes up a large portion of κ in high-quality low- κ materials, the variation in areal capacitance is insignificant throughout the whole frequency range. In addition, variation in capacitance depletion and inversion identified by drop and rise in the capacitance respectively, is reflected in C_i - V plot for high- κ silicon dielectrics (Fig. 2.19 (c)). The occurrence of hysteresis in the C_i - V plots, a marker of charge trapping/de-trapping in the dielectric, is another crucial dielectric characteristic (Kim et al. 2001).

Simultaneously, dielectric films are designed to completely impede the flow of electric current; however, in reality, there is always some amount of leakage current, referred to as J_{leak} ; the amount of this current is usually dependent on the electrical field. An example of an electrical breakdown is an exponential increase in J_{leak} , which occurs when a part of the insulator is electrically conducted (see Fig. 2.19 (d)). This leads to permanent physical and chemical damage to dielectric films, and the most important parameters related to this process are V_b (breakage voltage) and E_b (breakage electric field). High breakdown strength dielectric films are necessary for the proper functioning of electronic devices. As a general rule of thumb, dielectric films with a thickness of less than 50 nm are expected to exhibit a low leakage current (below 1×10^{-7} A.cm⁻²) at a maximum operating voltage (2 MV.cm⁻¹). For dielectrics with a

thickness of 50 to 300 nm, a leakage current of less than $1 \times 10^{-6} \text{ A.cm}^{-2}$ at 2 MV.cm^{-1} is recommended. For dielectrics, such as most electrolytes and certain polymer dielectrics that require a film thickness of $>300 \text{ nm}$, a lower leakage current should be achieved at a maximum operating voltage. The breakdown voltage should be at least 1.5 – fold higher than the maximum operating voltage of the device.

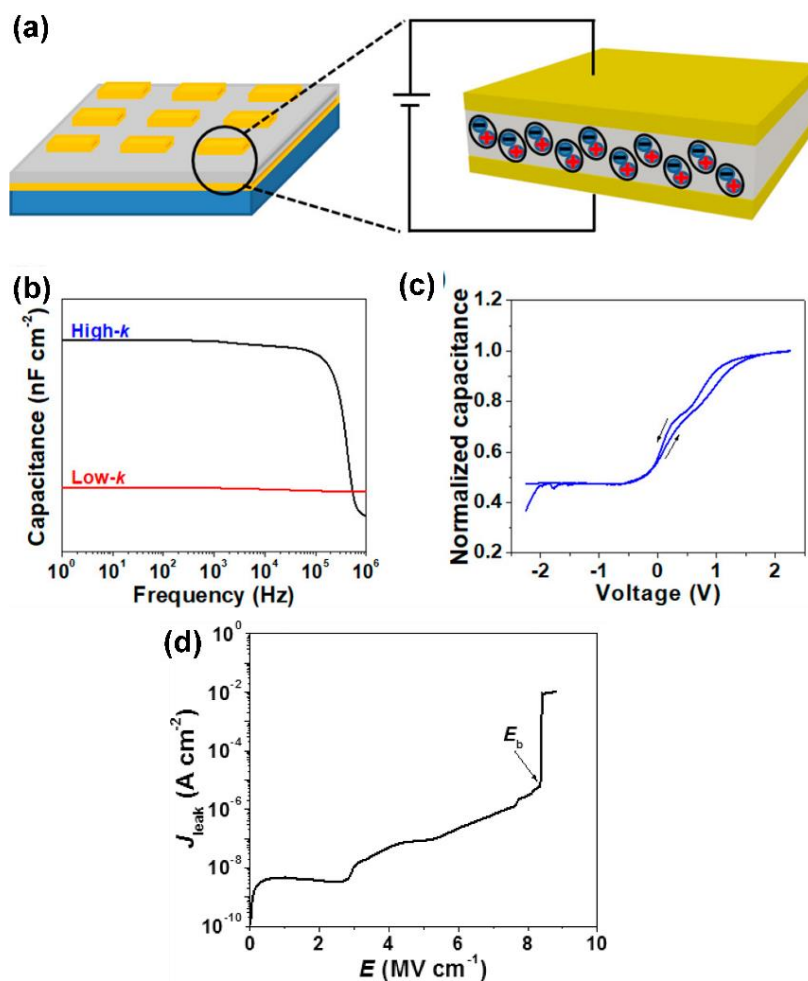


Fig. 2.19. (a) Pictorial representation of a metal-insulator-metal (MIM) parallel-plate capacitor, (b) comparative study of the frequency-dependent areal capacitance of high and low- κ dielectric films, (c) voltage-dependent areal capacitance and (d) change in current density with respect to the electric field for a typical high- κ zirconium self-assembled nanodielectric film on silicon.

2.7.1 High- κ metal oxide dielectrics

The most common form of silicon is silicon dioxide (SiO_2). Since silicon dioxide makes up around 28 % of the bulk of the crust of the earth, it makes up the second most prevalent chemical (Kaltenbrunner et al. 2013) and is frequently found in minerals,

sand, and dust. The SiO₂ is a well-known good insulator ($R = 10^{16} \Omega \cdot \text{cm}$), it has an impeccable track record when it comes to modern complementary metal oxide semiconductor (CMOS) technology. With Moore's law, which says that the number of electrical components in an electrical circuit can double every two years, the electronics industry has been working hard to reduce the size of electrical components, and silicon dioxide has been one of the key issues. Reducing dielectric layers of SiO₂ was at the top of the list, and the need for smaller, quicker and more cost-effective electronic circuits became increasingly important. The J_{leak} increases ($> 1 \text{ A} \cdot \text{cm}^{-2}$ at 1 V gate voltage) due to direct tunnelling when the SiO₂ layer thickness reaches the atomic scale, which poses major issues for idle power consumption and device stability. Even though the gate leakage issue has been solved since the end of the 90s (Lo et al. 1997), it is still not clear what kind of criteria are used to pick dielectric candidates. Finding a reliable dielectric has become one of the most significant and challenging issues for modern CMOS technology. Several engineers and scientists have worked extremely hard to develop a technology that can manufacture high-volume transistors with metal gates using high- κ dielectrics (Robertson and Wallace 2015). It was not until 2001 that this technological hurdle was overcome by substituting SiO₂ for HfO₂, which could be an alternative oxide material with high- κ value. Because tunnelling probability decreases exponentially with tunnelling distance, using high- κ dielectrics allows a thicker layer to provide the same capacitance, which helps to stop leakage current. This has encouraged in-depth study on high- κ dielectric materials across public and private sectors.

2.7.1.1 Basic criteria to choose high- κ

Apart from HfO₂, a range of other high- κ metal oxide dielectrics have been investigated such as TiO₂, Al₂O₃, ZrO₂ and many more as shown in Fig. 2.20. These candidates demonstrate higher κ values than traditional SiO₂, however, the selection of the "most suitable" high- κ dielectric is not straightforward and a number of factors must be taken into account. Dielectric constant is the primary prerequisite. The metal oxides κ value needs to be large enough to support an adequate amount of scaling nodes affordably. The metal oxide has to remain thermodynamically stable alongside the Si channel due to its proximity to one another. The band offset with neighbouring

a range of oxide high- κ metal oxide dielectrics, including HfO₂, Al₂O₃, TiO₂, ZrO₂, and rare-earth oxides. Marks et al. (Kim et al. 2011) were the ones who originally presented the combustion idea for producing solution-processed oxide TFTs. Al₂O₃ and ZrO₂ dielectric films produced from SCS and developed at 300 °C showed reduced J_{leak} (10^{-7} A.cm⁻² at 2 MV.cm⁻¹) and high C_i (> 600 nF.cm⁻²). Fully SCS IGZO TFTs with $I_{\text{on}}/I_{\text{off}}$ 10^5 and a remarkable average mobility of ≈ 5.3 cm².V⁻¹.s⁻¹ were built on ZrO₂ dielectric.

The spin coating process is a popular solution processing choice for the fabrication of oxide dielectric materials due to its cost-effectiveness and ease of processing. During this process, the pre-mixed precursor solution is applied to hydrophilic substrates and then accelerated to a high angular velocity in order to spin off the excess solution and form a thin and homogeneous film. Keszler and colleagues presented groundbreaking work in which sulfate/phosphate derivatives of AlPO, HfSO_x, and ZrSO_x dielectrics were integrated into TFTs with sputtered oxide semiconductors (Anderson et al. 2007). They found that the dielectric film was dense, had a moderate κ value (4.8 – 12), a low leakage current, and high breakdown voltages (> 6 MV.cm⁻¹). Kats et al. came up with a new type of sodium beta-alumina film (Nketia-Yawson et al. 2017). It had a special crystal structure, called a 2D layered crystal, and high ionic conductivity was achieved in the *ab* plan, which resulted in an ultrahigh- κ value of ≈ 170 . Furthermore, to the many uses for oxide TFTs, devices made of 2D transition metal dichalcogenides (TMDs), single-walled carbon nanotubes (SWCNTs), and semiconducting colloidal nanocrystals (NCs) (Kim et al. 2013a, 2014a; Rim et al. 2015; Talapin et al. 2010) are also made using spin-coated high- κ metal oxide dielectrics (Kwon et al. 2016). By substituting traditional SiO₂ with solution-processed high-ZrO_x dielectrics, Talapin and his team (Bong et al. 2010; Geng et al. 2014; Talapin et al. 2010) have achieved notable successes. They have created high-performance soldered CdSe NC transistors with a record maximum field effect mobility of 450 cm².V⁻¹.s⁻¹. This amount of field effect mobility is equivalent to MOSFETs made of crystalline silicon and is fourfold higher than that available in SiO₂ dielectric-based devices.

Spray pyrolysis, like spin coating, is another straightforward, low-cost solution-processed coating method. Spray pyrolysis is also suitable for large-scale deposition on a variety of substrates. The turning point in this area came with the publication of a series of papers on high-performance oxide TFTs & circuits using spray pyrolysis by the team of Antipoulou et al. (Adamopoulos et al. 2009, 2011; Bashir et al. 2009). At a substrate temperature of 400 °C and under natural conditions, they developed polycrystalline ZrO₂ dielectric thickness ($t = 100$ nm). The spray pyrolyzed ZrO₂ thin films that were produced had reduced surface roughness and excellent uniformity across vast regions. More notably, high- $\kappa = 14$, big $E_g = 5.9$ eV, low $J_{\text{leak}} \approx 0.5 \mu\text{A}\cdot\text{cm}^{-2}$ at 6 V, and break down voltage ≈ 1.6 MV.cm⁻¹ was exhibited by ZrO₂ dielectric. Nevertheless, one of the major issues with SCS is that the ferocious reaction might produce a lot of combustible gas, which may result in pinholes in the final films. Unwanted defects should be kept to a minimum in dielectric applications to prevent leakage current. As a result, TFTs based on solution combustion processed high- κ metal oxides often display high off-state current and low $I_{\text{on}}/I_{\text{off}}$. Despite the enormous advancements made so far, research on solution combustion processed high- κ metal oxide dielectrics has mostly been concentrated on the manufacturing of particular TFTs and has remained at the laboratory scale level. It is important to look into new application areas outside of CMOS ICs, such as memory, energy storage, as well as high-frequency modulation in telecom equipment.

2.7.1.3 Role of high- κ in thin film transistors

TFTs are electronic devices with three terminals whose primary purpose is electrical switching or signal strengthening. They're made up of three main parts: a semiconductor material that acts as a channel layer for transferring charge carriers (e.g., electrons or holes) laterally, a dielectric layer that acts as a capacitive coupling between a gate electrode and a semiconductor, and metal-based electrodes that inject and extract charge carriers (source/drain electrodes) and control charge conduction from the source to the drain electrodes (gate electrode). In a typical TFT, the dielectric is placed between semiconductors and the gate electrode. The flow of charge across the semiconductor channel between the two electrodes (source and drain) is controlled by the gate bias, which causes the dielectric to become polarized. A dielectric layer and its interface with

a semi-conductor must meet a number of criteria to achieve optimal TFT performance. First, the dielectric layer needs to be thinner and have a higher dielectric constant so it uses less power. Second, the film density needs to be high in order to minimize the leakage. Thirdly, a minimized number of defects, such as dangling bonds and interstitial or substitutional defects, can stop the polarization. Finally, the surface needs to be low in roughness resulting in a good surface energy balance between the dielectric and semi-conductor layers, to increase charge accumulation and reduce charge-trap sites. All of these things add up to good TFT performance and high charge carrier mobility (Hong and Liao 2020).

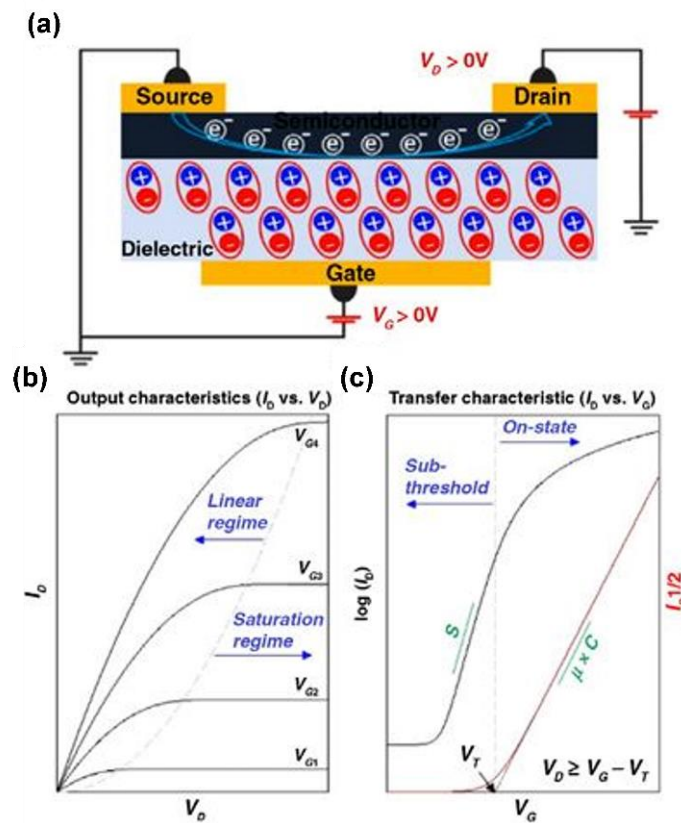


Fig. 2.21. (a) A typical n-channel (electron-transporting) TFT configuration, (b) the output and, (c) transfer characteristics of a standard TFT device (Hong and Liao 2020).

In the case of a semiconductor being n-type, a positive gate voltage of V_G cause the gate dielectric to be polarized, which generate electrons to build up at the semiconductor-dielectric interface, as illustrated in Fig. 2.21a. Applying drain voltage (V_D) maintains a drain current (I_D) at the "channel" across the metal-based source and

drain electrodes. If the $V_D < V_G - V_{T\text{T}}$ (threshold voltage), the drain current density is uniform, which is known as a linear-regime and is expressed as $I_{D,lin}$ (Kim et al. 2014b),

$$I_{D,lin} = \frac{W}{L} \mu C \left\{ (V_G - V_T) - \frac{V_D}{2} \right\} V_D \quad (2.8)$$

where W is the width of the channel, L is the length of the channel and μ is the mobility of the charge-carrier. When V_D goes above to $V_D \geq V_G - V_T$, the channel is narrowed at the drain, and the drain current in the saturation-region is represented as $I_{D,sat}$,

$$I_{D,sat} = \frac{W}{2L} \mu C (V_G - V_T)^2 \quad (2.9)$$

The change from linear to saturation region is shown by the output characteristics (I_D vs. V_D) with varying V_G levels, as illustrated in Fig. 2.21 (b). The crucial role that gate capacitance plays in determining TFT efficiency is well seen in a transfer characteristic in Fig. 2.21 (c). Theoretically, increased gate capacitance should draw more electrons at the same V_G . Consequently, in a TFT, an increased capacitance value allows for extremely steep switching in both sub- and above-threshold domains. Prior to the complete formation of the conduction channel, diffusion current caused by a concentration gradient induced by a V_D is thought to be responsible for conduction in the subthreshold domain (Hong and Liao 2020). Subthreshold swing (SS) is a parameter that is often used to control this current. The SS is equal to V_G range, which is needed to elevate I_D by $\log(I_D)$ of the plot Fig. 2.21 (c). Deep traps in the semiconductor band gap increase SS because it immobilizes part of the capacitively generated charge carriers. The formulation of this phenomenon is expressed as (Kim et al. 2013b)

$$SS = \frac{kT \ln 10}{q} \left(\frac{q^2 N_t}{C} + 1 \right) \quad (2.10)$$

Where k is Boltzmann's constant, T is the absolute temperature, q is the elementary charge and, N_t is the total trap density. In Fig. 2.21 (c), the red line represents the cubic root of I_D in the saturation region. This saturation region is often used to derive mobility from slope of I_D . It should be noted that the slope is essentially a function of capacitance and emphasises the necessity of a high capacitance in order to ensure a steep gate-modulation of I_D . Hence, the Fig. 2.21 (c) convincingly shows that use of a dielectric

with high capacitance is a good approach to efficiently raise the total current switching slope, and results in an indication of full on/off scanning throughout a relatively limited V_G range. Several metal oxides possess an intrinsically high κ , which is significantly higher than the standard amorphous SiO_2 ($\kappa = 3.9$). Furthermore, metal oxide insulator films are really strong and don't have too many flaws, which enables the ability to shrink the thickness of the material down to less than 100 nm without worrying about a gate leakage problem. These two features work together to lower the operating voltage of the TFTs, so are highly suited for making wearable electronic devices (Hong and Liao 2020).

2.7.1.4 Applications

Dielectrics with a high- κ value are extensively utilized in a variety of applications. Their primary use is as an insulating layer for transistors as mentioned in the earlier section, but they also play a fundamental role in the fabrication of memory, capacitor, energy storage and telecommunication devices with high-frequency modulation (Franklin 2015; Osada and Sasaki 2012; Vescio et al. 2017). A varistor is a resistor that changes its electrical resistance in response to applied voltage. Due to the barrier present in the diode junctions, only a very little current is seen at low voltage. The actions of thermionic emission and tunnelling cause the current to be significantly increased by many orders of magnitude when a voltage over the breakdown voltage is applied. Varistors can therefore be used as safeguards against high voltages. As varistor materials, metal oxides are frequently used. As a result of the grain boundary effect, several high- κ metal oxide materials have additionally been demonstrated to have nonlinear I-V characteristics. Electrically speaking, there are many grain boundaries with arbitrary orientations, which are comparable to a network of diodes connected back-to-back. Simultaneously, dielectric capacitors provide the better power density, maximum voltage of operation, and long operating lifespan, when compared to other energy storage technologies like supercapacitors and batteries. Due to its potential usage in current pulsed-power based electronic systems, such as hybrid automobiles, high-frequency conversion devices, and electrical weapons, the enormous needs of energy storage systems can be addressed. High- κ metal oxide materials have the potential to be a key contributor to the development of the next generation of advanced

printed electronic systems like disposable/paper electronic devices, radio frequency identification (RFID), smart labels and so on (Dang et al. 2013; Wang et al. 2019e).

2.8 Research gap

High- κ oxide dielectrics are in high demand in the present digital world due to the requirements such as excellent stability, energy efficiency, high yield, economic processes, flexible wide-area manufacturing, and sustainable electronics (Robertson 2004). The recent remarkable development enhances the field of sensors, microelectronics, and wearables in solution-processed high- κ oxide dielectrics. Solution-processed high- κ oxide dielectrics are known for their high dielectric constant, mechanical tolerance, and excellent chemical and thermal stability, which play a crucial role in the performance of many electronic, energy storage, and memory devices. These characteristics lead to suppressed tunnelling effect, easy miniaturization, and low input power operation (Liu et al. 2018). Improving the overall properties of solution-processed high- κ oxide dielectrics can be challenging as ambient conditions like temperature and humidity affect the device's reproducibility, properties, and performance. This can be solved by either doping or increasing the number of cations in the metal oxide (Wang et al. 2018a).

The metal oxide thin films are viable for various applications due to their versatile electrical functionality (Robertson 2006; Salian et al. 2019). Although SiO_2 is an industrial-grade dielectric, its low dielectric constant ($\kappa \sim 3.9$) demands high operating voltage in thin film transistors (TFTs) (Moore 1998; Robertson and Wallace 2015). The thin SiO_2 (~ 1.2 nm) faces a significant leakage current density of the order > 1 A/cm² at 1 V due to tunnelling (Lo et al. 1997; Robertson and Wallace 2015). Thus, it imposes a substantial restriction on scaling. Hence, with the great demand for miniaturized electronics, large-scale integration requires a revisit to dielectric scaling. Further, high- κ metal oxides facilitate a thicker layer with the same capacitance, reducing leakage current as the probability of tunnelling drops exponentially with tunnelling distance (Wong 2011). The outstanding dielectric is not just the one with high dielectric constant; instead, a series of requirements, such as sufficient band offset (> 5 eV), robust atomic-scale roughness, and less prone to moisture adsorption, must be fulfilled to use it as a passive layer in the TFT stack (Liu et al. 2018). Besides these requirements,

the deposition of dense metal oxides has always been a center of interest. In vapor-phase sputter deposition, the growth of thin films is relatively less cumbersome but needs capital-intensive deposition techniques. In contrast, with recent advancements in the field, atmospheric-pressure solution-phase deposition is more straightforward and can be fulfilled even on flexible polymeric substrates (Pasquarelli et al. 2011). As specific to the solution-processed thin films, the as-deposited films are thermally treated (or processed under photo-irradiation) at a temperature where the chemical ingredients undergo decomposition to form low-molecular-weight gaseous products, removal of which leaves a metal-oxygen-metal frame.

Inspired by the high entropy alloys in a metallic system, high entropy oxides (HEOs) have been proposed. HEOs are functional oxides composed of various cations in an equimolar stoichiometry (Rost et al. 2015). However, a handful of reports purely focus on the phase stabilization of the different combinations of cations, which ultimately requires stabilization of configurational entropy term in Gibb's free energy equation leading to a particular phase; various such combinations are proposed in the literature (Sarkar et al. 2019). To mention a few, the first discovered $(\text{Mg}_{0.2}\text{Ni}_{0.2}\text{Co}_{0.2}\text{Cu}_{0.2}\text{Zn}_{0.2})\text{O}$ and $(\text{CeZrHfTiLa})\text{O}$ stabilize as rocksalt at 875 °C and fluorite at 900 °C, respectively. Followed by, spinel structure in $(\text{CoCrFeMnNi})_3\text{O}_4$ is stabilized at 850 °C, and perovskite in the case of $(\text{Bi}_{0.2}\text{Na}_{0.2}\text{K}_{0.2}\text{Ba}_{0.2}\text{Ca}_{0.2})\text{TiO}_3$ at 840 °C (Liu et al. 2020b; c; Mao et al. 2019b; Xu et al. 2020). HEOs find applications in batteries, ferroelectrics, magnetic, catalytic, thermal barrier coatings, etc (Salian and Mandal 2022b). Moreover, the application as a passive-dielectric in TFTs demands HEOs, whose stabilization is comparatively effortless because of the unique multi-cationic configuration, which maintains the structural chaos at the atomic level (Salian and Mandal 2022a). So far, to the best of our knowledge, HEO materials are not implemented as a gate dielectric in TFT applications.

The bulk and thin films have a distinct mechanism of combustion. In bulk, combustion takes place in all directions, hence more mass gets combusted every time. However, on the contrary, in case thin films, combustion movement is not yet visually experienced. The kinetics of combustion is different in both case because of high surface to volume ratio in bulk results in easy removal of gases produced during

combustion in the nano scale level (Pujar et al. 2020; Varma et al. 2016). Hence, it is important to investigate the phase stabilization of HEO in both architecture, bulk as well as thin film. In the present thesis, we targeted both ways to understand how combustion takes place in them. Primarily, an investigation of dielectric constant on the sintered HEO capacitor composed of Mg, Co, Cu, Zn, Ni (i.e., (MgCoCuZnNi)O), Ce, La, Pr, Sm, Y (i.e., (CeLaPrSmY)O) and Co, Mn, Ni, Fe, Cr (i.e., (CoCrFeMnNi)O) developed using solution combustion synthesis. The three system were selected based on the initial discovery of HEO as mentioned in the above paragraph and its exploration as dielectrics creating a new bridge between the HEO and electronics.

2.9 Objectives of the present study

- To optimize and characterize the solution combustion processed phase-stable high entropy oxides powder containing metal oxides.
- Fabrication and characterization of solution combustion processed high entropy oxide-based sintered capacitors.
- To explore self-energy generating solution-combustion synthesis to deposit high entropy oxide films without any formation of the secondary phase.
- To fabricate and characterize high dielectric oxide-based thin films capacitor (MIM) and low voltage operation thin film transistors.

CHAPTER 3

INVESTIGATION OF DIELECTRIC PROPERTIES ON THE PHASE STABILIZED SOLUTION COMBUSTION PROCESSED HIGH ENTROPY ROCKSALT OXIDE (CoCuMgZnNi)O

The contents of this chapter have been published in the article:

Ashritha Salian, Lakkimsetti Lakshmi Praveen, Saumen Mandal, **Ceram. Int.**, 49(19),
31131-31143.

Page left intentionally blank

CHAPTER 3

INVESTIGATION OF DIELECTRIC PROPERTIES ON THE PHASE STABILIZED SOLUTION COMBUSTION PROCESSED HIGH ENTROPY ROCKSALT OXIDE (CoCuMgZnNi)O

3.1 Introduction

In the present chapter, high entropy rocksalt oxide (HERO) powder based on Co, Cu, Mg, Zn, and Ni cations ((Co_{0.2}Cu_{0.2}Mg_{0.2}Zn_{0.2}Ni_{0.2})O_{1- δ}) are developed via solution combustion processing and employed as functional-dielectric. A systematic derivation of the stoichiometric combustion reaction from sub-reactions of oxidation and reduction is depicted. Phase stabilization of the (CoCuMgZnNi)O with temperature is investigated. In addition, a systematic study of phase-stabilized (CoCuMgZnNi)O with individual parent metal oxide and a lesser-cation system is provided. Further, a capacitor developed using solution combustion processed rocksalt phase-stabilized (CoCuMgZnNi)O as a dielectric is demonstrated with the display of high- κ and low loss, which creates a new bridge between the HEO and electronics.

3.2 Experimental procedure

3.2.1 Formulation of combustible precursor

All the reagents were analytical-reagent quality and were employed directly without further purification. The individual metal nitrates, namely, cobalt nitrate [Co(NO₃)₂.6H₂O; (97.1 % purity)], copper nitrate [Cu(NO₃)₂.6H₂O; (99.5 % purity)], magnesium nitrate [Mg(NO₃)₂.6H₂O; (99 % purity)], nickel nitrate [Ni(NO₃)₂.6H₂O; (98 % purity)], and urea [CH₄N₂O; (99.5 % purity)] was procured from Molychem, India and zinc nitrate [Zn(NO₃)₂.6H₂O; (99.5 % purity)] was procured from SRL, India. Individually, each metal nitrate and urea was dissolved entirely in deionized water through a magnetic stirrer and stored in an airtight glass container maintained at room temperature.

3.2.2 Synthesis and characterization

The homogenous aqueous precursor solution was heated at 400 °C on a hot plate in the air atmosphere. The solution has undergone combustion by releasing a large amount of gaseous products. The as-combusted black powder was found at the bottom of the flask. The schematic of the synthesis process is displayed in Fig. 3.1. Subsequently, the as-combusted powder underwent analysis to assess phase stabilization. This analysis involved heating the powder in a tubular furnace over a range of temperatures, from 500 °C – 1000 °C. The as-combusted HERO powder obtained at 400 °C and the calcined HERO powder from 500 °C – 1000 °C were symbolically denoted as HERO-400, HERO-500, HERO-600, HERO-700, HERO-800, HERO-900, and HERO-1000.

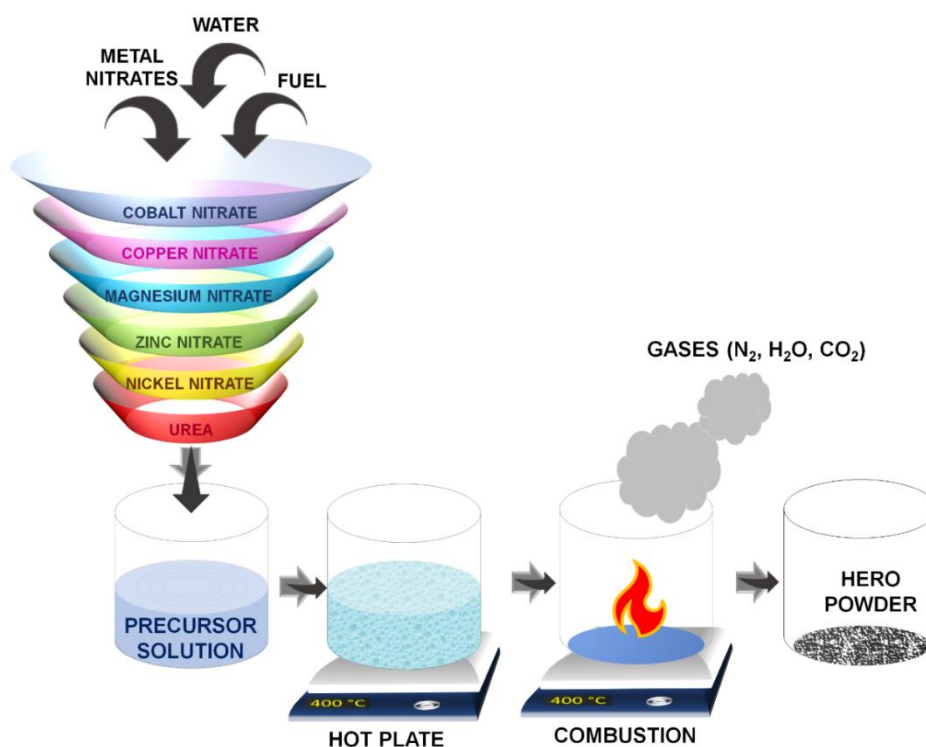


Fig. 3.1. Schematic of synthesis of (CoCuMgZnNi)O powder.

To gain insights into the thermal properties of precursor gel collected before the combustion process and the as-combusted powder was examined using a differential scanning calorimeter (DSC, NETZSCH DSC 404 F1) and thermogravimetric analyzer (TGA, Hitachi Exstar, TGA/DTA 6300). The heating rate used for analyses was 10 °C.min⁻¹. The phase purity and crystallinity of HERO were studied using a powder X-

ray diffractometer (XRD) (PANanalytical multipurpose high-resolution XRD). The XRD analysis utilized a Cu-K α radiation source (1.54 Å), and the step size was set at 0.02. Fourier Transform Infrared Spectroscopy (FTIR, Bruker Alpha 400) was conducted on HERO-400 and HERO-1000 using the KBr pellet technique. The FTIR spectra were recorded with a resolution of 2 cm⁻¹ and the range of 400 – 4000 cm⁻¹. A compact Raman spectrometer (Renishaw, UK) with 532 nm lasers was used to collect Raman spectra. Field-Emission Scanning Electron Microscopy (FE-SEM, Carl Zeiss AG model: GeminiSEM 300) attached with Energy Dispersive Spectroscopy (EDS) was employed to examine the morphology and elemental compositions. The FE-SEM analysis was conducted at an accelerating voltage of 20 kV. X-ray Photoelectron Spectroscopy (XPS, Kratos Axis Ultra DLD) was used to analyze the surface chemical compositions of HERO sintered at 1000 °C, which operated with an ultra-vacuum system maintained at a base pressure of 10⁻¹⁰ Torr. The XPS analysis employed an Al K α X-ray source, and the binding energy scale was referenced in 'eV'. The C-H peak of carbon, located at 284.6 eV, was used to calibrate the acquired XPS spectra. Peak fit analysis was performed on the cations (Co 2p, Cu 2p, Mg 2p, Zn 2p, and Ni 2p) and oxygen 1s (O 1s) peaks. Gaussian and Lorentzian functions were utilized for the peak fitting, with a fixed G/L (30 %) ratio. The software determined the full-width half-maxima (FWHM) of the synthetic peaks and was constrained to be the same to ensure consistency in the peak fitting analysis. The peak fit analysis was carried out using the CASAXPS 2.3.22PR1.0 software.

3.2.3 Development of sintered (CoCuMgZnNi)O capacitors

A high-temperature sintered HERO pellet is developed to analyze the dielectric performance. The as-combusted HERO powder was calcined at 600 °C for 3 hours to develop HERO pellets for the dielectric investigation. In a uniaxial hydraulic press (40 Ton), the calcined HERO powder was then compacted to form green compacts under a force of 12 kN. The compacts were sintered in the furnace at 1000 °C for 3 hours. Additionally, the pellet was coated on both sides with silver ink, and copper wire was soldered to the silver to create two electrodes for measuring the dielectric constant. Using an impedance analyzer (IM3536, Hioki, Japan), the dielectric constant, impedance, loss tangent, and electric modulus of the sintered pellet (HERO-1000) were

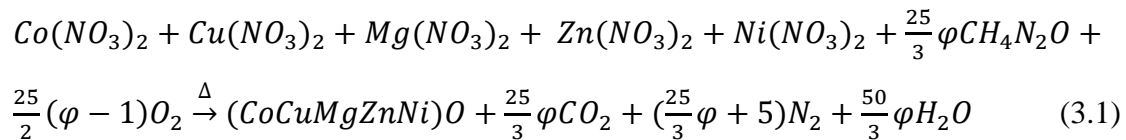
measured across the frequency range of 4 Hz to 1 MHz with bias voltage +1 V to – 1 V

3.3 Results and discussion

In order to characterize the efficacy of combustion in (CoCuMgZnNi)O powder, the systematic thermal, structural, and compositional study is performed as follows, and an investigation of dielectric constant on the sintered (CoCuMgZnNi)O capacitor is carried out.

3.3.1 Thermal decomposition analysis

The stoichiometric amount of all the five equimolar metal nitrates and the fuel were taken as per the balanced chemical stoichiometry equation (3.1), calculated using Jain's method (Patil et al. 2008).



Where the parameter φ denotes the fuel-to-oxidizer ratio. Here, $\varphi = 1$ represents stoichiometric oxygen concentration, implies that the oxidizers have a theoretically equal amount of oxygen to complete the reaction.

The ignition of the combustion process is necessary to convert the precursor into an HEO product. Combustion temperature is the temperature at which exothermic reactions occur in the combustible precursors to produce HEO. Fig. 3.2 portrays the TGA, derivative thermogravimetry (DTG), and DSC thermal events of the precursor gel (Fig. 3.2 (a and b)) and HERO-400 (Fig. 3.2 (c and d)). In Fig. 3.2 (a), at zone I (50 °C – 175 °C), a weight loss of 5 % at ≈ 110 °C is ascribed to the dehydration of the solvent. Consequently, at zone II (175 °C – 300 °C), the change in the weight loss of 27.3 % at ≈ 230 °C in TGA indicates the removal of hydrated water and ionization-complexation of the precursor mixture and simultaneously 18.5 % at 250 °C in TGA, accompanied with the sharp exothermic response at 270 °C in DSC as shown in Fig. 3.2 (b), are the evidence of destruction, combustion, and ignition of precursor gel. In Zone III (300 °C – 500 °C), a slight change in the weight loss of 9.3 % is observed, which represents the removal of the carbonaceous remnant (Hossain et al. 2019). On

the HERO-400, thermal analysis was carried out, as shown in Fig. 3.2 (c and d). The weight loss of 2.5 % at ≈ 110 °C in TGA and an endothermic response in DSC at ≈ 80 °C and 120 °C is dedicated to the removal of moisture adsorbed in zone I (50 – 200 °C), while in zone II (200 °C – 400 °C) an exothermic in DSC at ≈ 250 °C is attributed decomposition of hydroxides and basic carbonates with the release of crystallization water and carbon dioxide and the weight loss of 5.6 % at ≈ 300 °C in TGA and the endothermic response in DSC at ≈ 320 °C suggests the removal of $(OH)^-$ from $Cu(OH)_2$, $Zn(OH)_2$ and $Ni(OH)_2$. In zone III (400 °C – 600 °C), the weight change of 2.7 % in TGA at ≈ 470 °C indicates the formation of Co_3O_4 and MgO , while in zone IV (600 °C – 750 °C), the weight change of 0.3 % in TGA at ≈ 670 °C and an endothermic peak in DSC at ≈ 710 °C indicates the decomposition of residual Mg and Co hydroxides. Finally, in zone V (750 °C – 870 °C), the 1.1 % change in TGA and DSC at ≈ 850 °C is attributed to the partial dissolution towards solid solution formation of HERO (Biesuz et al. 2018; Yv et al. 2022). Table 3.1 summarizes all of the thermal events that occurred in the precursor gel and HERO-400 as a result of the TGA and DSC with an increase in temperature

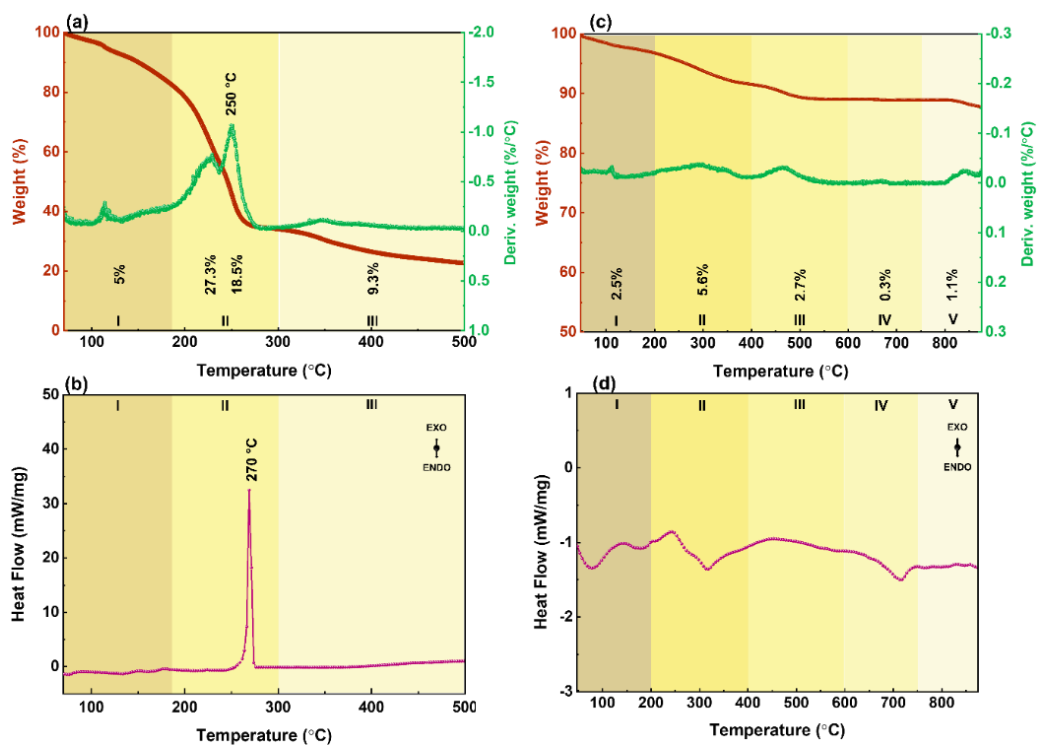


Fig. 3.2. (a) The weight loss (TGA and DTG) and (b) heat flow (DSC) of HERO precursor gel and (c) TGA and DTG and (d) DSC of HERO-400.

Table 3.1. Summary of thermal events in the (CoCuMgZnNi)O precursor gel and HERO-400 with an increase in temperature from TGA and DSC.

Materials	Zones	Temperature	Weight	Reasoning
		interval (°C)	loss (%)	
Precursor gel	I	50 – 175	5	Evaporation of solvent.
	II	175 – 240	27.3	Removal of hydrated water and ionization-complexation of the precursor mixture.
		240 – 300	18.5	Destruction, ignition, and combustion of precursor gel.
	III	300 – 500	9.3	Removal of residual carbon remnant.
HERO-400	I	50 – 200	2.5	Elimination of moisture adsorbed.
	II	200 – 400	5.6	Removal of (OH)- from Cu(OH) ₂ , Zn(OH) ₂ , and Ni(OH) ₂ and basic carbonates.
	III	400 – 600	2.7	Formation of Co ₃ O ₄ and MgO.
	IV	600 – 750	0.3	Decomposition of residual Mg and Co hydroxides.
	V	750 – 870	1.1	Partial dissolution towards solid solution formation of HEO

3.3.2 Structural, compositional, and morphological analysis

The phase formation of HERO powders (HERO-400 to HERO-1000) identified from XRD analysis is presented in Fig. 3.3 (a). The Bragg reflections noticed from the planes (111), (200), and (220) of HERO-400 correspond to the cubic rocksalt phase, with broadened noisy reflections, indicates the start of crystallization and direct the effective synthesis of HERO at a low temperature of 400 °C. A few minor reflections from planes (311) and (222) of the cubic rocksalt phase, which are not evident due to poor crystallinity, can be dedicated to inadequate thermal energy requirement to crystallize at ≤ 400 °C. The formation of HERO at 400 °C was because of the combustion redox reaction's exothermicity which may have helped in briefly attaining a considerably higher temperature for a short time, thereby favors the formation of incomplete and partial phases of the rocksalt-like HERO, with its residual oxides. With subsequent increases in temperature (500 °C – 1000 °C), the HERO planes began to evolve, and the diffraction peaks changed to show an improvement in crystallinity by becoming finer, narrower, and highly intense sharper peaks with low and flat

backgrounds. HERO shows a single-phase, face-centered cubic (fcc) rocksalt structure with a space group of $Fm-3m$. From HERO-400 to HERO-900, diffraction peaks pertaining to impurities are detectable. The secondary phases of Co_3O_4 (ICDD: 01–078–1969) and ZnO (ICDD: 01–073–8765) were noticeable upto 700 °C, while CuO (ICDD: 01–085–7520) were noticed up to a temperature of 900 °C as shown in Fig. 3.3 (a). Impurity-related diffraction peaks are not visible in HERO-1000. In general, the HEO phase is entropy stabilized when both the enthalpy (ΔH_f) and the entropy of formation (ΔS_f) are positive, and big enough to cause the Gibbs free energy of formation ($\Delta G_f = \Delta H_f - T\Delta S_f$) negative at a specific temperature (T) (McCormack and Navrotsky 2021). The higher configurational entropy in the equimolar concentration of cations in HEO exhibits a high entropy effect, which inhibits the formation of the complex phases and promotes single-phase solid solution formation (Ziehl et al. 2023). At high temperatures, the solubility between the individual cations increases, which reduces the number of phases, and forms a pure single-phase structure (Anandkumar and Trofimov 2023). Therefore, in HERO, the complex phases observed below 1000 °C indicate domination of enthalpy over the high entropy effect. But, at 1000 °C, the synergistic effect of high entropy and high temperature increases the solubility and assists in the dissolution of secondary phases (CuO , Co_3O_4 , and ZnO) into a stable single-phase rocksalt structure of HEO (Aamlid et al. 2022). Thus, the entropy phase stabilization of HERO is achieved with a combination of critical temperature (1000 °C in the present study) and high entropy effect. Simultaneously, Fig. 3.3 (b) displays magnified XRD patterns at 2θ equal to $35^\circ - 45^\circ$, which reflects the major planes (111) and (200) in HEO. Due to the tiny lattice expansion caused by a rise in temperature, an insignificant minor peak shift to the left is seen (Teng et al. 2021). Furthermore, as demonstrated in Fig. 3.3 (c), the low lattice expansion was further justified by the variation in lattice parameters with respect to temperature. Low thermal expansion is shown by the insignificant variation of the lattice parameter from 4.22 to 4.25 Å in $(\text{CoCuMgZnNi})\text{O}$, and the results are summarized in table 3.2.

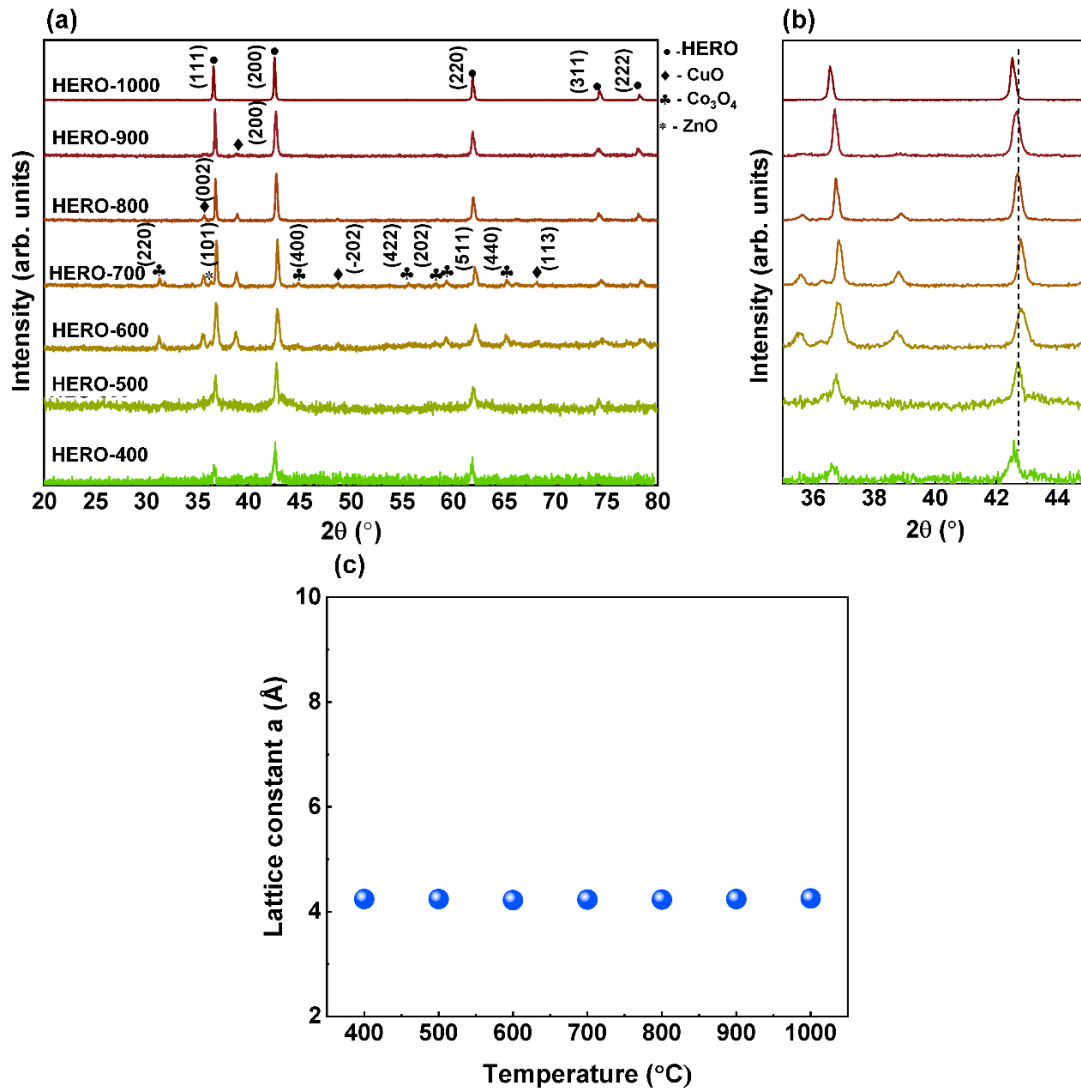


Fig. 3.3. X-ray diffraction patterns of (a) HERO-400 to HERO-1000, (b) zoomed X-ray diffraction patterns at 2θ equal to $35^\circ - 45^\circ$, (c) constancy of lattice parameter with an increase in temperature.

The lattice parameter ‘ a ’ for the cubic system is extracted from the XRD by calculating using equation (3.2) and Cohen’s method.

$$\frac{1}{d^2} = \frac{h^2+k^2+l^2}{a^2} \quad (3.2)$$

where $d = \lambda/2 \sin \theta$ and θ is the half of the Bragg reflection angle, $\lambda = 1.5406 \text{ \AA}$ is the wavelength for Cu-K $_{\alpha}$ radiations. Cohen’s method was used to calculate the more accurate lattice parameter ‘ a ’. The precise lattice parameter ‘ a ’ of HEO500 – HEO-1000 is calculated using the following relations:

$$A\Sigma\alpha^2 + B\Sigma\alpha\delta = \Sigma\alpha\text{Sin}^2\theta \quad (3.3)$$

$$A\Sigma\alpha\delta + B\Sigma\delta^2 = \Sigma\delta\text{Sin}^2\theta \quad (3.4)$$

where $A = \lambda^2/4a^2$, $B = D/10$, $\alpha = h^2 + k^2 + l^2$, and $\delta = 10\text{Sin}^2\theta$.

In comparison with the current work, table 3.3 summarizes all research on solution-processed HERO which have (Co, Cu, Mg, Zn, Ni)O composition that has been published. It is observed that HEO with a rocksalt structure displays secondary phases at low temperatures during formation, is process dependent, and requires high temperatures for stabilization. The present work has the lowest formation temperature among others as visible in table 3.3.

Table 3.2. Summary of the lattice parameter of (CoCuMgZnNi)O with an increase in temperature.

Temperature (°C)	$a = \frac{(h^2+k^2+l^2)^{1/2}}{a}$ (Å)	Cohen's method a (Å)
400	4.22	4.24
500	4.25	4.24
600	4.21	4.22
700	4.2	4.23
800	4.24	4.23
900	4.24	4.24
1000	4.21	4.25

Table 3.3. A summary of all published work on solution-processed HERO having (Co, Cu, Mg, Zn, Ni)O composition compared with the present work.

Synthesis technique	Lattice parameter, a (Å)	HERO structure	HERO formation temperature (°C)	HERO fully stabilized temperature (°C)	Ref.
Microwave Heating	-	MgO	650	850	(Lou et al. 2023)
SCS	4.2173	MgO	550	850	(Mao et al. 2019c)
CP	4.2442	MgO	450	1000	(Biesuz et al. 2018)
HT	4.2368	MgO	450	1000	(Biesuz et al. 2018)
NSP	4.23	NiO (ICSD – 61318)	-	1150	(Wang et al. 2019b)
FSP	4.2366	NiO (ICSD – 9866)	-	1000	(Sarkar et al. 2017a)
RCP	4.2346	NiO (ICSD – 9866)	-	1000	(Sarkar et al. 2017a)
NSP	4.2449	NiO (ICSD – 9866)	1150	1150	(Sarkar et al. 2017a)
NSP	-	NiO (ICSD – 61318)	1150	1150	(Sarkar et al. 2018b)
NSP	4.2354	MgO	1150	1150	(Chellali et al. 2019)
Sol-Gel	4.2366	-	-	900	(Fracchia et al. 2020)
NSP	-	NiO	1150	1150	(Breitung et al. 2020)

(ICSD – 61318)					
Polymeric Synthesis	4.233	MgO	550	550	(Yoon et al. 2020)
Low-temperature annealing strategy	-	MgO	450	850	(Raza et al. 2023)
SCS	4.25	MgO (ICDD: 00-004-0829)	400	1000	Present Work

SCS: Solution Combustion Synthesis; **CP:** Co-Precipitation; **HT:** Hydrothermal; **NSP:** Nebulised Spray Pyrolysis; **FSP:** Flame spray pyrolysis; **RCP:** reverse co-precipitation.

Additionally, the individual parent oxide systems, sintered at 1000 °C, are compared and examined with HERO-1000. Fig. 3.4 (a) shows the XRD analysis of the individual parent oxides. It is evident that the diffraction pattern of the individual parent oxides, Co-O, corresponds to the cubic spinel Co_3O_4 , while Cu-O has a mixture of cubic Cu_2O and monoclinic CuO, Mg-O has cubic MgO, Zn-O has hexagonal ZnO, and Ni-O has cubic NiO diffraction peaks, respectively. The details of the diffraction peaks, standard ICDD file number, crystal structure, and lattice parameters corresponding to the individual oxides are provided in table 3.4. The Mg-O and Ni-O are the parent metal oxides with a crystal structure identical to HERO-1000 (Maiyalagan et al. 2014). Among the two-parent metal oxide, Mg-O has a very close match with the diffraction peaks of the HERO system as observed in Fig. 3.4 (a). As a result, HERO derived its structure from the Mg-O parent oxide. Concurrently, Fig. 3.4 (b) displays the zoomed XRD patterns at 2θ equal to $35^\circ - 45^\circ$ and represents the primary peaks of each parent metal oxide. Compared to Mg-O parent oxide, the peak of HERO-1000 has a little leftward shift. This shift can be ascribed to the very minimal lattice expansion (Teng et al. 2021), variation in electronegativity and ionic radius of elements present (Pażik et al. 2015), cationic disorder, the interface between several defect-related dipoles (Tian et al. 2015) in HERO-1000. Furthermore, none of the parent oxides Co-O, Cu-O, and Zn-O could match even a single peak with HERO-1000, as observed in Fig. 3.4 (a) and (b). This proves HERO-1000 is a member of the same family of cubic rocksalt as Mg-O and exhibits a structural characteristic of its parent oxide. For further comparison, the information of lattice parameters ‘ a ’ and ‘ c ’ is extracted from the XRD using equation 3.2 for the cubic system, equation 3.5 for the hexagonal system, and Cohen’s method.

$$\frac{1}{d^2} = \left(\frac{4}{3}\right) \frac{h^2+k^2}{a^2} + \frac{l^2}{c^2} \quad (3.5)$$

where $d = \lambda/2 \sin \theta$ and θ is the half of the Bragg reflection angle, $\lambda = 1.5406 \text{ \AA}$ is the wavelength for Cu- K_α radiations. Cohen's method was used to calculate the more accurate lattice parameters ‘ a ’ and ‘ c ’. The dominating phase in every parent oxide is considered for the calculation of the lattice parameters. The precise lattice parameter ‘ a ’ of Co-O, Cu-O, Mg-O, and Ni-O is calculated using equations 3.3 and 3.4, while

precise lattice parameters ‘ a ’ and ‘ c ’ for hexagonal Zn-O is calculated using the following relations:

$$A\Sigma\alpha^2 + B\Sigma\alpha\gamma + C\Sigma\alpha\delta = \Sigma\alpha\sin^2\theta \quad (3.6)$$

$$A\Sigma\alpha\gamma + B\Sigma\gamma^2 + C\Sigma\gamma\delta = \Sigma\gamma\sin^2\theta \quad (3.7)$$

$$A\Sigma\alpha\delta + B\Sigma\gamma\delta + C\Sigma\delta^2 = \Sigma\delta\sin^2\theta \quad (3.8)$$

where $A = \lambda^2/3a^2$, $B = \lambda^2/4c^2$, $C = D/10$, $\alpha = h^2 + k^2$, $\gamma = l^2$, and $\delta = 10\sin^2\theta$ for hexagonal structure. Table 3.5 contains a summary of the findings. Fig. 3.4 (c) displays the individual parent oxide and HEO-1000 lattice parameter (Cohen’s data is used). As can be seen, Mg-O and Ni-O are the only parent oxides with lattice parameters that are slightly near HERO-1000, with Mg-O to be a very close match among the two (Maiyalagan et al. 2014).

Table 3.4. Details of the diffraction peaks, standard ICDD file number, crystal structure, and lattice parameters corresponding to the individual oxides.

System	Oxides	ICDD file	Crystal structure	Lattice parameter of major phases
Co-O	Co ₃ O ₄	01-078-1969	Cubic Fd-3m 227	$a = 8.08 \text{ \AA}$ (Cubic Fd-3m 227)
Cu-O	Cu ₂ O and CuO	00-005-0667 and 00-045-0937	Cubic Pn-3m 224 and Monoclinic C2c-15	$a = 4.27 \text{ \AA}$ (Cubic Pn-3m 224)
Mg-O	MgO	00-004-0829	Cubic Fm-3m 225	$a = 4.21 \text{ \AA}$ (Cubic Fm-3m 225)
Zn-O	ZnO	01-073-8765	Hexagonal P63mc-186	$a = 4.78 \text{ \AA}$ and $b = 5.26 \text{ \AA}$ (Hexagonal P63mc-186)
Ni-O	NiO	00-047-1049	Cubic Fm-3m 225	$a = 4.18 \text{ \AA}$ (Cubic Fm-3m 225)

Table 3.5. Summary of the lattice parameter of individual parent oxides and HEO-1000.

Temperature (°C)	a (Å)	c (Å)	Cohen's method	Cohen's method
			a (Å)	c (Å)
Co-O	8.08	8.08	8.08	8.08
Cu-O	4.27	4.27	4.27	4.27
Mg-O	4.21	4.21	4.21	4.21
Zn-O	2.9	5.2	4.78	5.26
Ni-O	4.18	4.18	4.18	4.18
Co-Mn-Ni-Fe-Cr-O	4.21	4.21	4.25	4.25

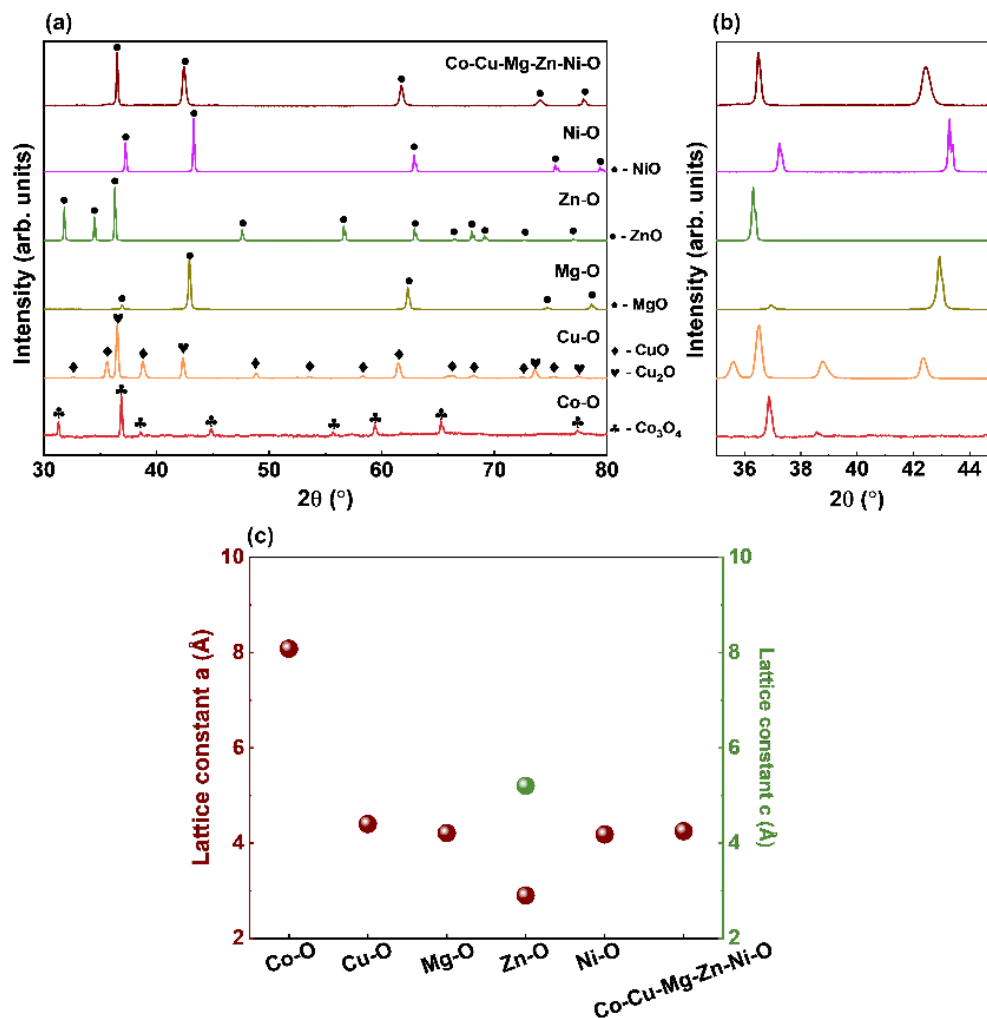


Fig. 3.4. (a) X-ray diffraction patterns of individual parent metal oxides Co-Cu-Mg-Zn-Ni-O (HERO-1000), Co-O, Cu-O, Mg-O, Zn-O, and Ni-O, (b) zoomed XRD at 2θ 35° - 45° represent the major peak of the system, and (c) change in lattice parameter indicating the dependence of HERO with regard to parent metal oxide Co-O, Cu-O, Mg-O, Zn-O, and Ni-O.

A similar study is carried out by decreasing from five cation systems to lower (1, 2, 3, and 4), and changes observed in the lattice constant ‘ a ’ are assessed. The XRD patterns of the HEO-1000 (Co-Cu-Mg-Zn-Ni-O) and lower cation system (Co-Cu-Mg-Zn-O, Co-Cu-Mg-O, Co-Cu-O, and Co-O) are presented in Fig. 3.5 (a). The diffraction peaks of 1 cation system Co-O attributes to the cubic spinel Co_3O_4 , similar to Fig. 3.4 (a). While the major diffraction peaks in the XRD of 2 cation system Co-Cu-O corresponds to Co_3O_4 01-078-1969 with the presence of CuO as secondary peaks. Furthermore, the major peaks in the XRD of the 3-cation system Co-Cu-Mg-O and the 4-cation system Co-Cu-Mg-Zn-O match the standard ICDD file of MgO 00-004-0829, similar to HEO-1000. But, the 3 and 4 cation systems have secondary Co_3O_4 , CoO, CuO, and Cu_2O peaks. Hence, the prominent peaks of the lower cation systems show a face-centered cubic (fcc) structure with an $Fd-3m$ (1 and 2 cation system) and $Fm-3m$ (3, 4, and 5 cation system) space group. The transition of crystal structure from cubic spinel to cubic rocksalt is evident with the addition of Mg-O. Therefore, Mg-O is the principal cation for the formation of the cubic rocksalt phase. The presence of an additional phase in the lesser cation system and the demonstration of single-phase in HEO-1000 point to the importance of configurational entropy in the process of phase stabilization. Concurrently, magnified XRD patterns at 2θ equal to $35^\circ - 45^\circ$, representing the major peaks of the system, are shown in Fig. 3.5 (b). The spinel to rock-salt phase transition was evident with the addition of Mg-O. Moreover, the transition and formation were further supported by the lattice parameter with respect to the number of cations in the system, as shown in Fig. 3.5 (c) (Cohen’s data is used). The information of lattice parameter ‘ a ’ for the cubic system is extracted from the XRD using equation 3.2 and Cohen’s method (equations 3.3 and 3.4). As shown in Fig. 3.5 (c), the lattice parameter changed from 8.08 to 4.25 Å with an increasing number of cations, and the results are summarized in table 3.6. This change is observed with the addition of Mg, which indicates the transition from cubic spinel to cubic rocksalt phase, and the transition can be ascribed to variation of ionic radius, cationic disorder, and electronegativity of elements present (Pażik et al. 2015), lattice expansion during the incorporation of cations (Teng et al. 2020, 2021).

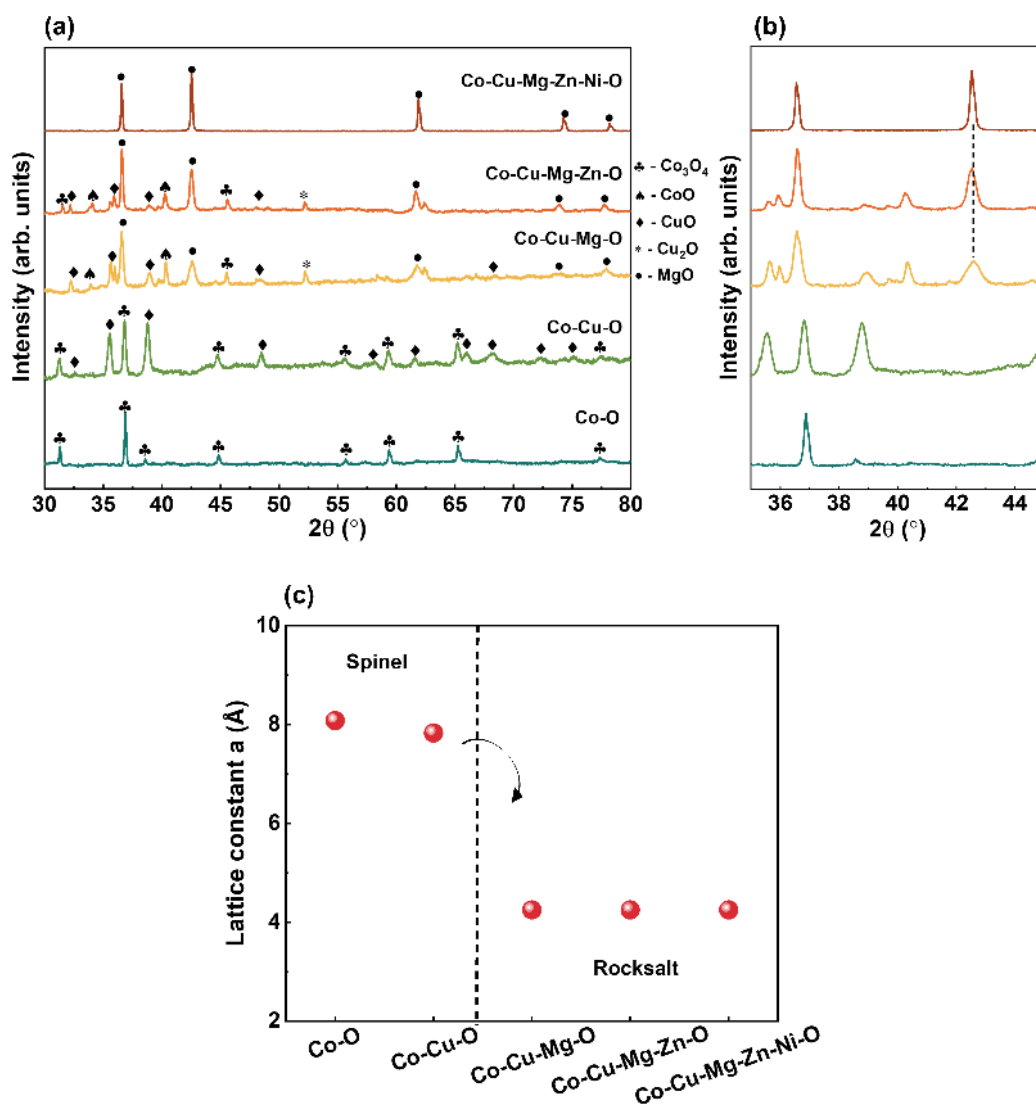


Fig. 3.5. (a) X-ray diffraction patterns of lower cation systems Co-Cu-Mg-Zn-Ni-O (HEO-1000), Co-Cu-Mg-Zn-O, Co-Cu-Mg-O, Co-Cu-O, and Co-O, (b) zoomed XRD at 2θ $35^\circ - 45^\circ$ represent the major peak of the system, and (c) change in lattice parameter indicating expansion of lattice with an increase in cations.

Table 3.6. Summary of the lattice parameter of lower cation system and HEO-1000.

Temperature (°C)	a (Å)	Cohen's method
		a (Å)
Co-O	8.08	8.08
Co-Cu-O	8.09	7.83
Co-Cu-Mg-O	4.25	4.25
Co-Cu-Mg-Zn-O	4.25	4.25
Co-Cu-Mg-Zn-Ni-O	4.21	4.25

Raman and FTIR spectroscopy were employed to comprehend the molecular vibration occurring within the HERO. For an ideal cubic rocksalt structure, no first-order Raman active modes are expected. However, disordered Raman active modes (stretching (A_{1g} and E_g) and bending (F_{2g})) are induced by the disordered cubic lattice of HERO due to randomly sited atoms. The Raman spectra of HERO powders (HERO-400 to HERO-1000) are shown in Fig. 3.6 (a). The HERO-400 to HERO-700 reveals six main Raman active modes with two E_g ($200 - 350 \text{ cm}^{-1}$ and $450 - 510 \text{ cm}^{-1}$) stretching modes, two A_{1g} ($600 - 650 \text{ cm}^{-1}$ and $690 - 720 \text{ cm}^{-1}$) stretching modes, and two F_{2g} ($100 - 200 \text{ cm}^{-1}$ and $510 - 550 \text{ cm}^{-1}$) bending mode. Furthermore, HERO-800 displays one E_g ($200 - 350 \text{ cm}^{-1}$) and one A_{1g} ($350 - 720 \text{ cm}^{-1}$) stretching mode, while the HERO-900 and HERO-1000 reveal only one A_{1g} ($350 - 720 \text{ cm}^{-1}$) stretching mode, respectively (Ravindra et al. 2014; Rivas-Murias and Salgueiriño 2017; Tang et al. 2008; Usharani et al. 2020b). As Raman active modes are related to the site symmetry of the cubic lattice, the presence of E_g and F_{2g} in HERO-400 to HERO-800 was clear evidence of distortion in the cubic lattice (Usharani et al. 2020b). The disappearance of the E_g and F_{2g} with temperature rise is possibly due to the presence of defects, symmetry disruption by the Jahn-Teller distortion by Cu cations, change in crystallite size, and disorder of cations in HERO (Cardoso et al. 2021; Dąbrowa et al. 2018; Sarkar et al. 2017b; Usharani et al. 2020a). Only one Raman mode A_{1g} is visible in HERO-900, and HERO-1000 indicates the stabilization and formation of cubic rocksalt structure with a disorder of cation sublattice in HERO (Dąbrowa et al. 2018; Lei et al. 2012; Sarkar et al. 2017b; Tang et al. 2008). A similar pattern is observed in the X-ray of HERO (Fig. 3.3 (a)) with the presence of secondary phases from HERO-400 to HERO-900 and a single phase at HERO-1000. The presence of lattice distortions and disorders in the cubic system and phase-stabilization of HERO is evident from Raman and XRD, as summarized in table 3.7. Raman spectra reveal the straightforward formation of phase-stabilized HERO with the disordered occupancy of different cations (Co, Cu, Mg, Zn, and Ni).

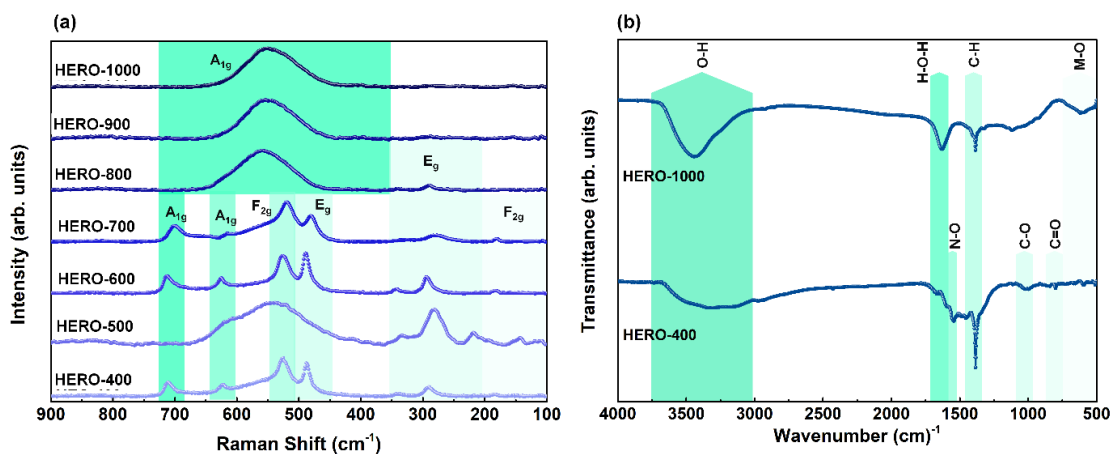


Fig. 3.6. (a) Raman spectra of HERO-400 to HERO-1000, and (b) FTIR spectra of HERO-400 and HERO-1000.

In parallel, the FTIR spectra of HERO-400 and HERO-1000 shown in Fig. 3.6 (b) show broad spectral absorption ranging from 3700 to 3000 cm^{-1} attributable to O-H bond stretching vibrations (Wei et al. 2009). The transmittance peak at 1380 cm^{-1} corresponds to the C-H symmetric bending, and the broad absorption ranges from 750 - 400 cm^{-1} is attributed to the metal-oxygen (M-O) (M = Co, Cu, Mg, Zn, Ni) stretching vibration mode (Wei et al. 2009). The transmittance peaks at 1680 cm^{-1} for HERO-400 and 1630 cm^{-1} for HERO-1000 represent the H-O-H bending modes of vibration (Wei et al. 2009). Three extra absorption peaks at 1550 cm^{-1} , 1012 cm^{-1} , and 796 cm^{-1} are assigned to N-O, C-O stretching vibrations, and C=O bending vibrations in HEO-400, respectively (Mihaylov et al. 2021; Wei et al. 2009). The vanishing of characteristic bands related to N-O, C-O, and C=O vibrations in HERO-1000 uncovered that they were from the nitrates and fuel urea consumed during the heat treatment at high temperature. Thus, the HERO formation is evident in both FTIR spectra of HERO-400 and HERO-1000, confirms a facile low-temperature solution-combustion synthesis of HERO at $400\text{ }^{\circ}\text{C}$, in addition to XRD and Raman results.

Table 3.7. Summary of all the diffraction peaks and Raman modes present in XRD and Raman spectrum with an increase in temperature.

Temperature (°C)	XRD phases and planes	Raman modes
400	HEO – (111), (200), (220)	A _{1g} , E _g , F _{2g}
	Co ₃ O ₄ – (220), (400), (511)	
	CuO – (002), (-202), (113)	
500	HEO – (111), (200), (220), (222)	A _{1g} , E _g , F _{2g}
	Co ₃ O ₄ – (220), (400), (511)	
	CuO – (002), (-202), (113)	
600	HEO – (111), (200), (220), (222)	A _{1g} , E _g , F _{2g}
	Co ₃ O ₄ – (220), (400), (422), (202), (511), (440)	
	CuO – (002), (200), (-202), (113)	
700	ZnO – (101)	A _{1g} , E _g , F _{2g}
	HEO – (111), (200), (220), (222)	
	Co ₃ O ₄ – (220), (400), (422), (202), (511), (440)	
800	CuO – (002), (200), (-202), (113)	A _{1g} , E _g
	ZnO – (101)	
	HEO – (111), (200), (220), (222)	
900	CuO – (002), and (200)	A _{1g}
	HEO – (111), (200), (220), (222)	
1000	CuO – (200)	A _{1g}
	HEO – (111), (200), (220), (222)	A _{1g}

The post-annealing treatments increase the grain size and lead to a small and fine grain boundary area. Therefore, it is essential to study the grain size distribution and morphology of the HERO, as it directly affects the leakage current behavior and dielectric nature. To show the morphologies and element composition of the developed HERO, FE-SEM is used. To comprehend the heat treatment effect, HERO powders heat treated from 400 °C to 1000 °C were evaluated, as shown in Fig. 3.7(a-g). Grain growth of HERO is observed with the temperature rise and displays excellent sinterability of the grain with an irregular shape. The elimination of carbonaceous impurities by heat treatment promotes the formation of a more prominent grain during the sintering process. The EDS of HERO-1000 (Fig. 3.7 (h)) displays a homogenous distribution of all five cations, with a near equiatomic percentage of all elements (Co –

6 %; Cu – 8 %, Mg – 6 %; Zn – 6 %; Ni – 8 %). The mapping of all the elements of HERO-1000 displays the distribution of elements and is provided in Appendix I (Fig. I). From 600 °C to 1000 °C, the average grain size was $0.15 \pm 0.004 \mu\text{m}$, $0.21 \pm 0.01 \mu\text{m}$, $0.46 \pm 0.02 \mu\text{m}$, $0.93 \pm 0.04 \mu\text{m}$, and $1.74 \pm 0.04 \mu\text{m}$. The grain boundary of the grains can be observed clearly from 800 °C to 1000 °C. The grain size of HERO powder (HERO-600 to HERO-1000) was estimated using ImageJ software. Fig. 3.7 (i) depicts the variation in the grain size distribution (GSD) with respect to temperature, respectively. The GSD curve for 600 °C, 700 °C, 800 °C, 900 °C, and 1000 °C follows the Gaussian fit, which is provided in Appendix I (Fig. II).

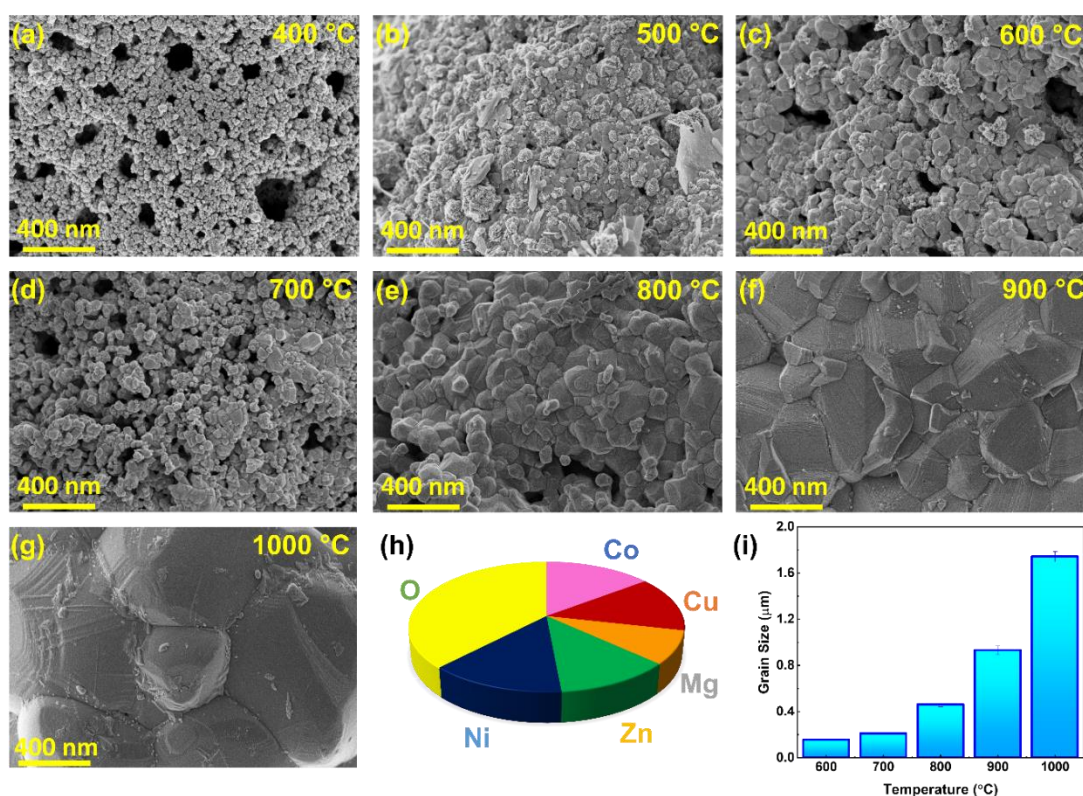


Fig. 3.7. (a-g) The surface morphology of HEO-400 to HEO-1000 displays a grain growth with temperature rise, (h) the pie chart indicating the elemental distribution of all five cations in HERO-1000 extracted from EDS, and (i) grain size distribution graph of grain size vs. temperature respectively.

To strengthen the analysis, the surface chemical compositions of HERO-1000 were investigated using XPS. The presence of the five cations Co, Cu, Mg, Zn, Ni, and other elements, including carbon (C) and oxygen (O), were detected by a survey scan covering an energy range of 0 – 1200 eV. The high-resolution spectra for each element

are depicted in Fig. 3.8. To accurately calibrate the HERO-1000 spectra, the carbon 1s (C 1s) spectrum, situated at 284.6 eV, was used as a reference. The survey scan and the C 1s spectrum are provided in Appendix I in Fig. III (a and b). The high-resolution scan of Co 2p of HERO-1000 is shown in Fig. 3.8 (a), where the peaks of Co 2p_{3/2} and Co 2p_{1/2} are positioned at around 779.77 eV and 795.39 eV and are attributed to Co³⁺ respectively; a satellite peak centered at 788.06 eV and 804.79 eV are attributed to Co³⁺ oxidation state. The fitted peak for Co 2p_{3/2} and Co 2p_{1/2} at 782.16 eV and 797.62 eV and a satellite peak centered at 785.28 eV and 802.25 eV are ascribed to the Co²⁺ oxidation state, respectively (Wang et al. 2020e; Xiang et al. 2021a). Despite the complex splitting observed, calculations based on the relative peak areas suggest that the Co ions are predominantly in the Co³⁺ state (Co²⁺/Co³⁺ = 0.29). Interestingly in the high-resolution scan Cu 2p spectra (Fig. 3.8 (b)), a higher Cu 2p_{3/2} peak located at 933.01 eV and a separate Cu 2p_{1/2} peak at 952.61 eV with three satellite peaks located at 940.52 eV, 943.06 eV, and 961.52 eV were observed. The fitted peak for Cu 2p_{3/2} and Cu 2p_{1/2} is assigned to Cu¹⁺ (933.01 eV and 952.61 eV), while the peaks centered at 934.94 eV and 954.66 eV are ascribed to Cu²⁺ respectively (Akgul et al. 2014; Wang et al. 2015b). However, calculations based on the synthetic peak areas indicate that the Cu ions are predominantly in the Cu¹⁺ state (Cu¹⁺/Cu²⁺ = 2.47). The high-resolution Mg 1s XPS spectra, as shown in Fig. 8 (c), exhibits one component at a binding energy of 1302.88 eV, corresponds to Mg²⁺ oxide (Aksoy et al. 2012). In Zn 2p XPS spectra (Fig. 3.8 (d)), Zn 2p_{3/2} and Zn 2p_{1/2} peaks are centered at 1021.05 eV and 1044.13 eV, respectively, which features spin-orbit coupling characteristics of Zn²⁺ (Aksoy et al. 2012). As shown in Fig. 3.8 (e), the Ni 2p spectra were reasonably deconvoluted into eight fitted peaks. The peaks positioned at 854.73 eV and 871.95 eV correspond to Ni²⁺ of Ni 2p_{3/2} and Ni 2p_{1/2} peaks, respectively. The peak at 857.44 eV and 874.25 eV of Ni 2p_{3/2} and Ni 2p_{1/2} is ascribed to Ni³⁺, respectively. The peaks at 861.07 eV, 864.49 eV, 877.70 eV, and 880.48 eV are shake-up satellite peaks of Ni, respectively (Nguyen et al. 2020a; Wang et al. 2020e). Calculating the area of the synthetic peaks revealed that, according to the current multiple splitting, the Ni ions were identified as Ni²⁺ (Ni²⁺/Ni³⁺ = 3.24), as shown in Fig. 3.8 (e). Fig. 3.8 (f) illustrates the contributions of different oxygen peaks in the O 1s region of HERO, where the peaks at 529.44 eV, 530.70 eV, 531.68 eV, 532.67 eV, and 533.8 eV correspond to lattice oxygen (O_{Latt}), oxygen

vacancy (O_v), surface metal hydroxide (M-OH), organic O, and chemisorbed oxygen (O_c), respectively (Lou et al. 2020; Nguyen et al. 2020a; Rojas et al. 2016). The contribution of oxygen vacancy is 13.5 % by calculating the synthetic peak area. Table 3.8 lists the dominant states in the system according to the XPS data, which are Co^{3+} , Cu^{1+} , Mg^{2+} , Zn^{2+} , and Ni^{2+} ions, respectively.

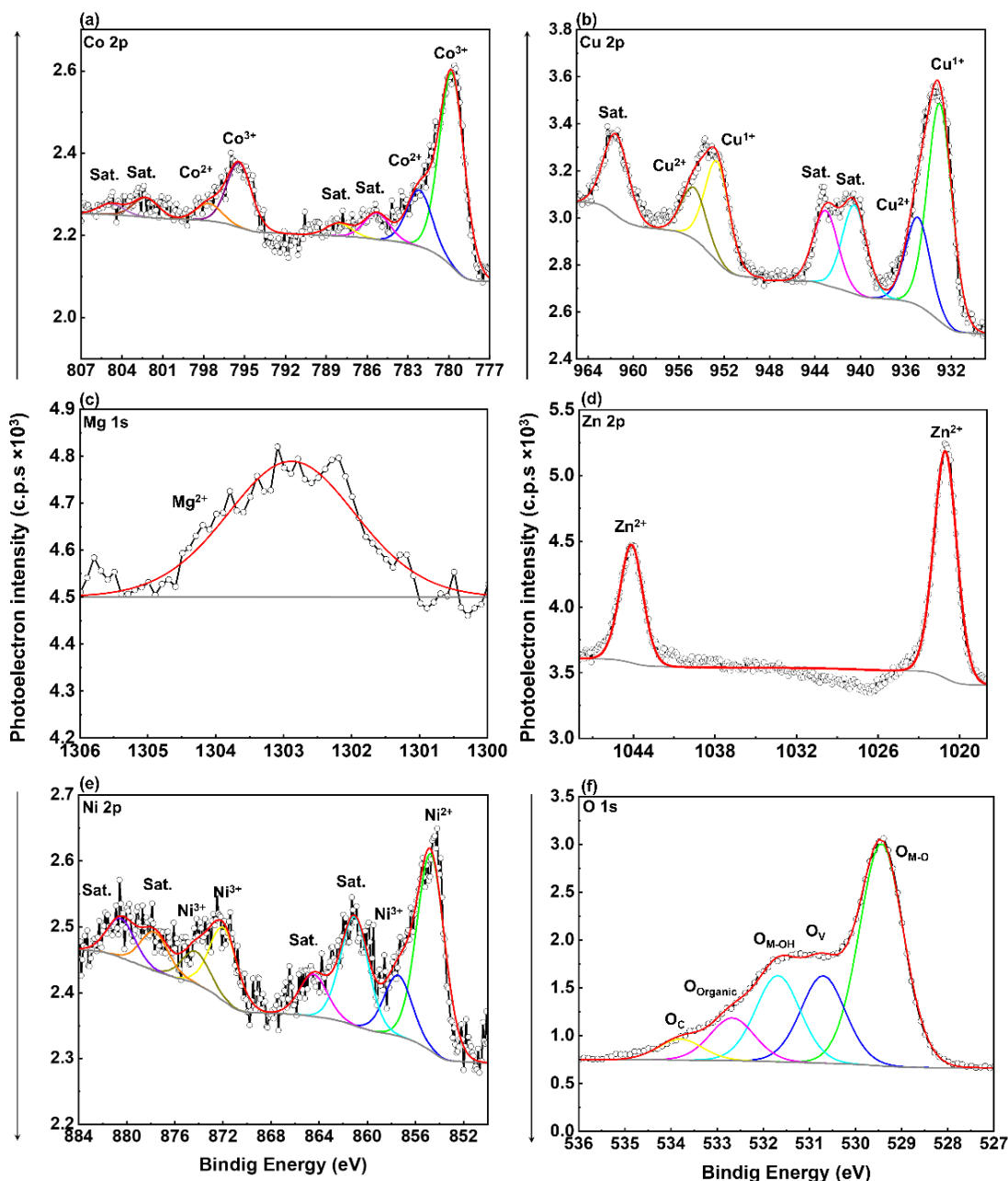


Fig. 3.8. High-resolution deconvoluted spectra of core level (a) Co 2p, (b) Cu 2p, (c) Mg 1s, (d) Zn 2p, (e) Ni 2p and (f) O 1s depicting their respective oxidation states.

Table 3.8. Summary of the percentage area contribution of deconvoluted peaks in cations.

Deconvoluted peak ratio	Area ratio
Co ²⁺ /Co ³⁺	0.29
Cu ¹⁺ /Cu ²⁺	2.47
Mg ²⁺	1
Zn ²⁺	1
Ni ²⁺ / Ni ³⁺	3.24

3.3.3 Dielectric constant of sintered (CoCuMgZnNi)O capacitor

The study focuses on the dielectric properties of a capacitor made from a HERO pellet, as illustrated in Fig. 3.9 (a). The pellet undergoes sintering at 1000 °C and results in a pore-free structure, as seen in Fig. 3.9 (b). In order to explore the elemental distribution, EDS analysis was performed, as depicted in Fig. 3.9 (c), which displayed a homogeneous distribution of the five cations with similar atomic percentages (Co – 3.8 %; Cu – 6.6 %, Mg – 9.6 %; Zn – 6.1 %; Ni – 5.5 %) as found in HERO-1000. The absence of pores and the presence of large grains due to successful sintering suggest that the HERO pellet may exhibit excellent dielectric performance with low leakage current. Fig. 3.9 (d) displays the dielectric constant (κ) and dielectric loss ($\tan \delta$) with respect to frequency, which is measured at room temperature. At a frequency of 20 Hz, κ reaches its peak value, $\approx 1.9 \times 10^3$. Moreover, within the frequency range of 1 kHz to 100 kHz, κ remains $\approx 10^1$, which is high dielectric constant relative to other metal oxide materials used in capacitors or transistors (Young and Frederikse 1973). The $\tan \delta$ remains minimal at low frequencies but gradually increases with frequency. Simultaneously, impedance analysis provides valuable insights into the dielectric behavior of HERO-1000 (Sen et al. 2013). Fig. 3.9 (e) illustrates the real (Z') and imaginary (Z'') parts of complex impedance (Z) with respect to frequency measured at room temperature. The decrease in Z' as frequency increases, suggests the presence of space charge effects at lower frequencies and shorter relaxation time for space charge at higher frequencies (Ali et al. 2015). In addition, the reduction in the magnitude of Z' is attributed to a lower density of trapped charges and improved immobile species at low frequencies (Sujatha et al. 2013). Two dispersions are observed in the spectra, one at lower frequencies (< 100 Hz) and another at a higher frequency range (> 1 KHz).

The dispersion at low frequencies indicates long-range mobility and delocalized relaxation mechanisms. In contrast, the dispersion at higher frequencies suggests a non-Debye type of relaxation involves short-range mobility within the material (Coşkun et al. 2018). In addition, the dispersions also indicate the contributions of grain and grain boundary effects, which become more significant at higher frequencies (Prado-Gonjal et al. 2017). The real (M') and imaginary (M'') parts of the electric modulus with respect to frequency measured at room temperature, where both exhibit similar trends. The near-zero value of M' at low frequencies is attributed to electrode polarization. A broad peak observed in M'' at higher frequency indicates a non-Debye type of relaxation behavior and a distribution of relaxation times, suggests the presence of a localized hopping mechanism instead of long-range charge carrier mobility (Padmasree et al. 2006).

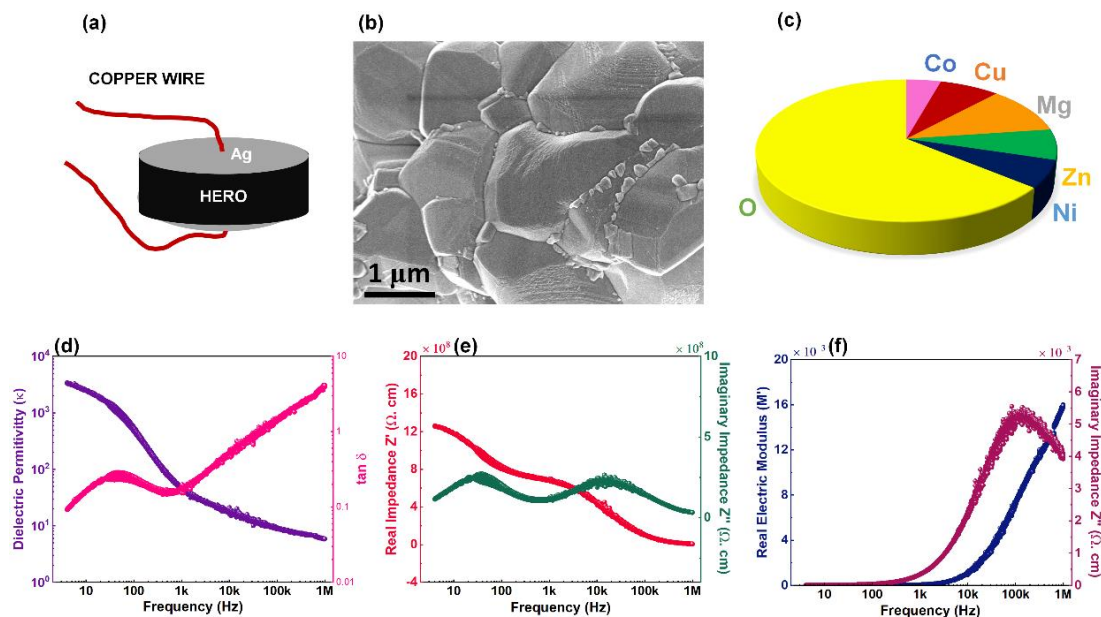


Fig. 3.9. (a) Schematic of the capacitor developed using (CoCuMgZnNi)O pellet sintered at 1000 °C, (b) the surface morphology of the (CoCuMgZnNi)O pellet sintered at 1000 °C and used for the development of capacitor, with admirable sinterability of the grain, and (c) the pie chart indicating the elemental distribution of all five cations in (CoCuMgZnNi)O pellet extracted from EDS, frequency dependence plots of the (d) dielectric constant (κ) and dielectric loss ($\tan \delta$), (e) real and imaginary part of the impedance (Z), (f) real and imaginary part of the electric modulus (M) measured at room temperature.

The observation of a high dielectric constant (κ) in HERO reveals a frequency-dependent trend. Fig. 3.10 provides a schematic explanation for the various factors which contribute to this high κ . As shown in Fig. 3.9 (d), an increase in frequency leads to a decrease in κ and an increase in $\tan \delta$ (dissipation factor), which can be ascribed to a reduction in space charge or the interfacial polarization (Du et al. 2020). The presence of structural inhomogeneity caused by the large surface-to-volume ratio of grains (Fig. 3.9 (b)) and defects like vacancies, micropores, and dangling bonds at grain boundaries allows charges to accumulate at interfaces, and results in interfacial polarization (Fig. 10) (Bérardan et al. 2016b; Du et al. 2020). In addition, when an electric field is applied, space charges in HERO move and are trapped by defects, which generates a dipole moment. Oxygen ion vacancies, detected in HERO-1000 via XPS (Fig. 3.8 (f)), act as positive charges and can create dipoles that align with the electric field when subjected to it, as shown in Fig. 3.10. Electrode polarization primarily influences high κ at low frequencies. The large number of space charges tends to accumulate at the interface between HERO and the electrode, which leads to a significant polarization, as depicted in Fig. 3.10 (Bérardan et al. 2016a; b). Furthermore, as the frequency increases, interfacial polarization relaxes due to high-energy electrons, shorter relaxation time, faster recombination of space charges, and instigating electronic and ionic polarization (Raymond et al. 2006b). The presence of larger radius ions in HERO (Co: 79 pm (+2) and 68.5 pm (+3), Cu 77 pm (+1) and 73 pm (+2), Mg: 72 pm (+2), Zn: 74 pm (+2), Ni: 83 pm (+2) and 70 pm (+3) and O: 126pm) facilitates easier electronic polarization compared to smaller ions (Bérardan et al. 2016b). Moreover, the varied cations in HERO contribute to a wide range of bond stiffness, and promotes ionic polarization. These factors collectively account for the observed high κ at higher frequencies. Hence, the high dielectric constant in HERO can arise from a combination of interface, orientation, ionic, and electronic polarization at low frequencies, while at higher frequencies, it results from a combination of ionic and electronic polarizations.

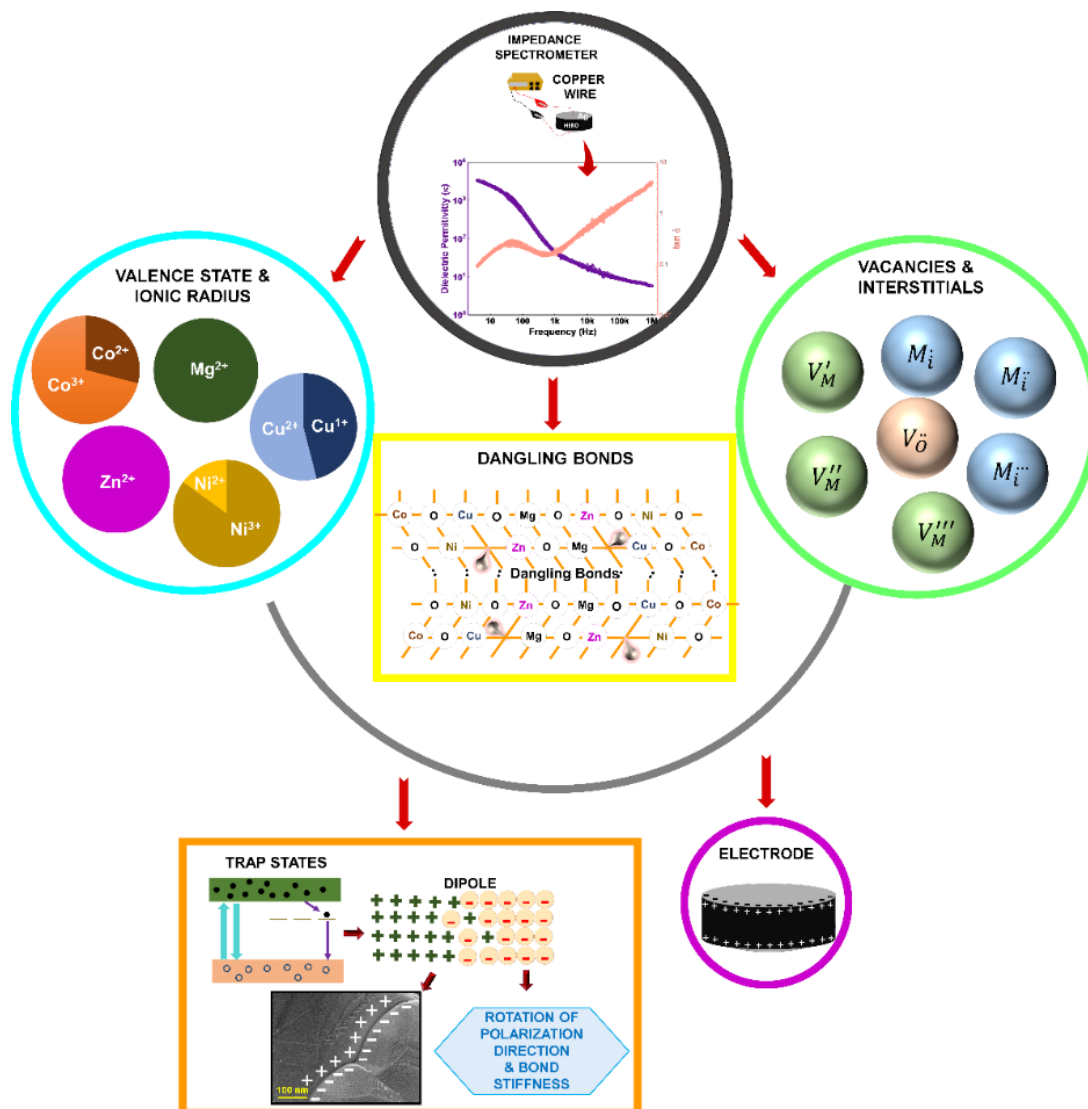


Fig. 3.10. Schematic depicting the interfacial polarization which occurs due to various reasons such as vacancies, interstitials, dangling bonds, grain, grain boundaries, rotation of vacancy, electrodes, valence state transfer, the capture of space charge by the trap states, and dipole formation when an electric field is applied in HERO resulting in high dielectric constant.

3.4 Conclusion

For the first time, at a low temperature (400 °C), solution combustion synthesis was successfully used to create high entropy rock salt oxide (CoCuMgZnNi)O, which was stabilized to single-phase rock salt structure at 1000 °C with high-κ property, and thus a bridge was built from HERO to capacitors. Thermal studies revealed that the precursor gel combusted at 240 °C. The HERO showed a single-phase, fcc rock salt structure with a space group of *Fm-3m*, while 400 °C and 1000 °C were considered to

be the HEROs synthesis and phase stabilization temperature. Since both HERO and Mg-O are members of the cubic family and have similar lattice constants, HERO exhibited one of the structural characteristics of its parent oxide, i.e., Mg-O. The XRD data of lower cation systems showed a transition from spinel to rocksalt structure with the addition of Mg-O. The secondary phases in the lower cation systems demonstrated the influence of configurational entropy on phase stabilization. The Raman spectrum and the XRD findings of HERO were perfectly in agreement, and it was clear that HERO formed at 400 °C and stabilized at 1000 °C. HERO powder had a morphology that was irregular in shape, and the average grain size enlarged with temperature from $0.15 \pm 0.004 \mu\text{m}$ to $1.74 \pm 0.04 \mu\text{m}$ with negligible porosity. The dielectric measurements display high dielectric constant (κ) $\sim 1.9 \times 10^3$, 4.7×10^1 , and 0.9×10^1 at 100, 1 k, and 100 kHz at room temperature, which is of noticeably higher dielectric constant values that are than those of other metal oxide materials, applicable in capacitors or transistors. The high- κ was attributed to a combination of the interface, orientation, ionic, and electronic polarization at low frequency, while at high frequency, a combination of ionic and electronic polarization. Therefore, the HERO mentioned in this chapter can be used in various devices, such as inverters, display back panels, integrated sensors, electronic circuits, logic devices, and many more. In order to fully realize the potential of HEO materials, more research needs to be done.

Page left intentionally blank

CHAPTER 4

INVESTIGATION OF DIELECTRIC PROPERTIES ON THE PHASE STABILIZED SOLUTION COMBUSTION PROCESSED HIGH ENTROPY FLUORITE OXIDE (CeLaPrSmY)O

The contents of this chapter have been published in the article:

Ashritha Salian, Akshay Prasad, Saumen Mandal, **J. Alloys Compd.**, 960, 170786, (2023).

Page left intentionally blank

CHAPTER 4

INVESTIGATION OF DIELECTRIC PROPERTIES ON THE PHASE STABILIZED SOLUTION COMBUSTION PROCESSED HIGH ENTROPY FLUORITE OXIDE (CeLaPrSmY)O

4.1 Introduction

This chapter deals with the development of high entropy fluorite oxide (HEFO) comprising Ce, La, Pr, Sm, and Y cations ((Ce_{0.2}La_{0.2}Pr_{0.2}Sm_{0.2}Y_{0.2})O_{1.6-δ}) via solution combustion processing and the HEFO is employed as functional dielectric. A stoichiometric combustion reaction is shown to be derivable from the sub-reactions of oxidation and reduction methodically. A comparative structural study on the (CeLaPrSmY)O with the rise in temperature, individual parent metal oxide, and lower cation systems is performed. In-depth thermal, structural, microstructural, and elemental analysis was made, which helped to draw a correlation with dielectric performances. Further, a capacitor with solution combustion processed fluorite phase-stabilized crystalline (CeLaPrSmY)O as a dielectric is demonstrated for the first time, which creates a new bridge between the HEFO and electronics.

4.2 Experimental procedure

4.2.1 Formulation of combustible precursor

All reagents were of analytical-reagent grade and used as received without purification. The respective metal nitrates, namely, cerium nitrate [Ce(NO₃)₃.6H₂O; (99.9 % purity)], lanthanum nitrate [La(NO₃)₃.6H₂O; (99 % purity)], and urea [CH₄N₂O; (99.5 % purity)] were purchased from Molychem, India; praseodymium nitrate [Pr(NO₃)₃.6H₂O; (99.9 % purity)], and samarium nitrate [Sm(NO₃)₃.6H₂O; (99 % purity)] from SRL, India; and yttrium nitrate [Y(NO₃)₃.6H₂O; (99.8 % purity)] from Sigma Aldrich, India. All the metal nitrates and urea, individually, were dissolved in deionized water and stored in an airtight glass container at room temperature. All solutions were mixed together with maintained molarity of 1, under stirring to obtain a clear aqueous combustible precursor.

4.2.2 Synthesis and characterization

The homogenous aqueous precursor solution was heated at 500 °C on a hot plate in the air atmosphere. The solution has undergone combustion by releasing a huge amount of gaseous products. The as-combusted black powder was found at the bottom of the flask. The schematic of the synthesis process is displayed in Fig. 4.1. Further, the as-combusted powder was analyzed for phase stabilization by heating the same in the tubular furnace at a varied temperature from 600 °C – 1000 °C. The as-combusted powder (500 °C) and the heat-treated powder from 600 °C – 1000 °C is symbolically represented as HEFO-500 (as-combusted) and HEFO-600, HEFO-700, HEFO-800, HEFO-900, and HEFO-1000, respectively.

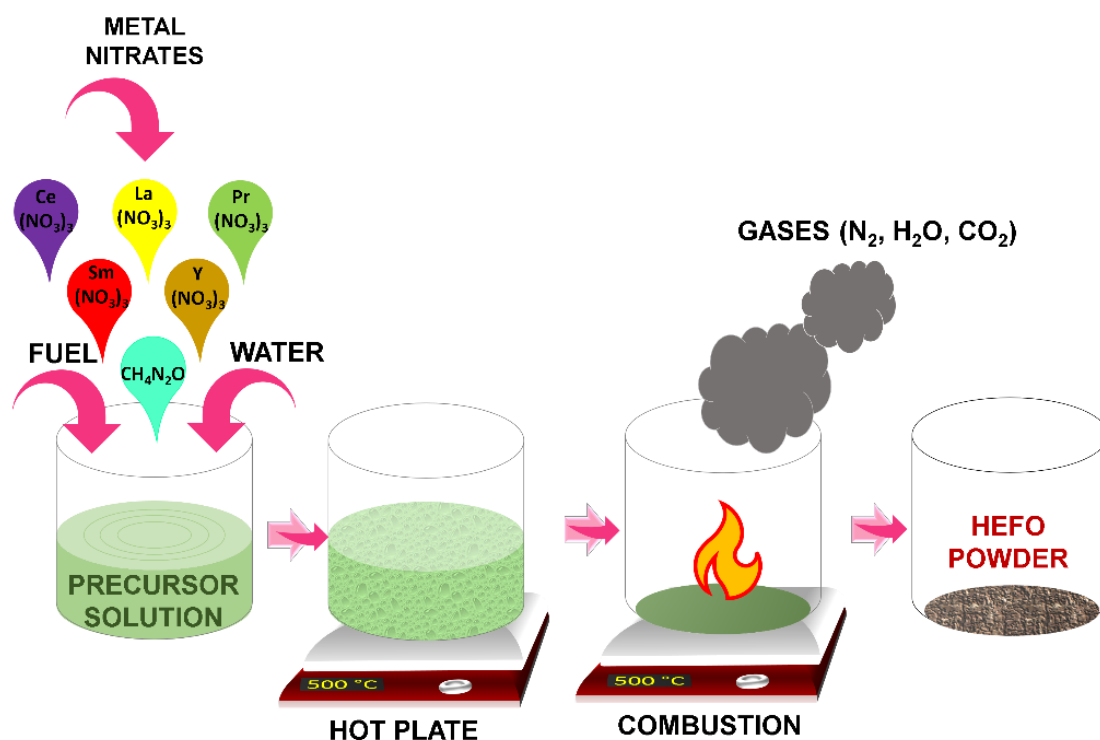


Fig. 4.1. Schematic of synthesis of (CeLaPrSmY)O powder.

To understand the combustion behavior, precursor gel was collected before combustion and was subjected to thermal analysis using TGA (Hitachi Exstar, TGA/DTA 6300) and DSC (NETZSCH DSC 404 F1) with a heating rate of 10 °Cmin⁻¹ in N₂ atmosphere. The phase purity and crystal structure were determined from powder XRD (PANalytical multipurpose high-resolution XRD) using a Cu-K α radiation source (1.54 Å) with a step size 0.02. To study the morphology and elemental

distribution, FE-SEM (Carl Zeiss AG model: GeminiSEM 300) coupled with EDS at an accelerating voltage of 20 kV was used. The FTIR (Bruker Alpha 400) was carried out for HEO-500 and HEO-1000 using the classic KBr pellet technique. The FTIR spectrum was at a scanning speed of 2 mm s^{-1} and resolution of 2 cm^{-1} with a range of 400 – 4000 cm^{-1} . The Raman spectra were recorded using the compact Raman spectrometer (Renishaw, UK) which consists of a laser that operates at 532 nm. Surface chemical compositions for HEO-1000 were analyzed using XPS (Kratos Axis Ultra DLD). The monochromatic Al K_{α} was used as the X-ray source for XPS. An ultra-vacuum system with a base pressure of $\sim 10^{-10}$ Torr is maintained. The binding energy scale was mentioned in 'eV'. The received spectra were calibrated using the C-H peak of the adventitious carbon positioned at 284.6 eV. The peak fit analysis of all five cations (Ce 3d, La 3d, Pr 3d, Sm 3d, and Y 3d) and oxygen 1s (O 1s) peaks were carried out using the product of Gaussian and Lorentzian functions with fixed G/L (30 %) ratio and FWHM of synthetic peaks fitted by the software (CASAXPS 2.3.22PR1.0). The FWHM of the synthetic peaks in the spectra of five metal cations and oxygen was constrained to be the same to avoid inconsistency in peak fitting. The peak fit analysis was performed using the CASAXPS 2.3.22PR1.0 software package.

4.2.3 Development of sintered (CeLaPrSmY)O capacitors

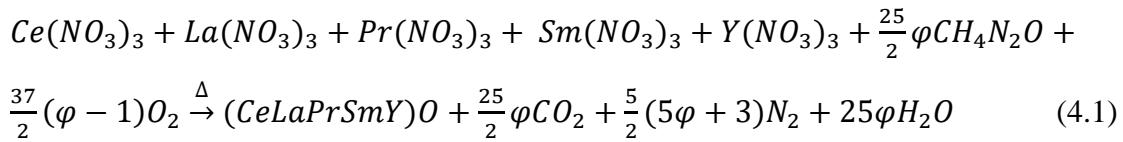
To study the dielectric performance, a dense body is required. Densification requires high-temperature sintering. Thus high-temperature sintered pellet of (CeLaPrSmY)O is prepared to investigate the dielectric performance. The fabrication of (CeLaPrSmY)O pellets for the dielectric study was prepared by calcining the as combusted (CeLaPrSmY)O powder at 600 °C for 3 h and then compressing the calcined (CeLaPrSmY)O powder under a load of 12 kN to obtain green compacts using a uniaxial hydraulic press (40 Ton). The compacts were sintered at 1000 °C for 3 h in the furnace. Further, silver ink was painted on both sides of the pellet, and copper wire was soldered onto the silver as two electrodes for dielectric measurement. The dielectric constant, loss tangent, impedance, and electric modulus of HEFO-1000 were determined at a frequency range from 100 Hz – 1 MHz with bias voltage +1 V to -1 V, using the impedance analyzer (IM3536, Hioki, Japan).

4.3 Results and discussion

In order to characterize the efficacy of combustion in (CeLaPrSmY)O powder, the systematic thermal, structural, and compositional study is performed as follows, and an investigation of dielectric constant on the sintered (CeLaPrSmY)O capacitor is carried out.

4.3.1 Thermal decomposition analysis

The stoichiometric amount of all the five equimolar metal nitrates and the fuel were taken as per the balanced chemical stoichiometry equation (4.1), calculated using Jain's method (Patil et al. 2008).



Where the parameter φ denotes the fuel-to-oxidizer ratio. Here, $\varphi = 1$ represents stoichiometric oxygen concentration, implies that the oxidizers have a theoretically equal amount of oxygen to complete the reaction.

The transformation of the precursor into a HEFO product requires the initiation of the combustion reaction. The temperature at which the combustible precursors undergo exothermic reaction and yield HEFO is termed as combustion temperature. Fig. 4.2 depicts the TGA, derivative thermogravimetry (DTG), and DSC thermal traces of precursor gel (Fig. 4.2 (a and b)) and HEO-500 (Fig. 4.2 (c and d)). The thermal events of all the metal nitrates incorporated in (CeLaPrSmY)O with an increase in temperature towards the formation of stable metal oxides are depicted in Fig. 4.3. In Fig. 4.2 (a and b), in zone I (50 °C – 190 °C), weight loss of 4.7 % in DTG (Fig. 4.2 (a)) at ≈ 110 °C is attributed to the evaporation of the solvent, and an endothermic response in DSC (Fig. 4.2 (b)) at ≈ 170 °C is due to the removal of bound water (Baqer et al. 2018). Consequently, in zone II (190 °C – 290 °C), the change in the weight loss profile of 20.1 % in DTG at ≈ 240 °C and simultaneously in DSC, multiple endothermic responses at ≈ 210 °C, 240 °C, and 260 °C indicates the dehydration of all metal nitrate species as seen in Fig. 4.3 (Kang et al. 2018; Mekhemer and Balboul 2001; Melnikov et al. 2013, 2014, 2018; Sotnikov et al. 2021). Furthermore, in Zone III (290 °C – 350

°C), the weight loss of 16.9 % in DTG at ≈ 320 °C and an exothermic peak at 320 °C in DSC is the evidence of destruction, ignition and combustion of precursor gel caused due to the reaction between the NO_2 and O_2 released by the metal nitrates and NH_3 and CO_2 . Post the combustion, an endothermic response in DSC at ≈ 345 °C is evident, which indicates the decomposition of Ce nitrate species with the formation of CeO_2 , dehydration of Pr and Y nitrate, and decomposition of hydroxides in Sm as shown in Fig. 4.3 (Kang et al. 2018; Melnikov et al. 2013, 2018; Sotnikov et al. 2021). In addition, in zone IV (350 °C – 430 °C), the weight loss of 15.2 % in DTG and endothermic response at ≈ 400 °C in DSC is due to the further decomposition in La hydroxides and Y (Mekhemer and Balboul 2001; Melnikov et al. 2013). Finally, in zone V (430 °C – 500 °C), the weight loss of 6.7 % in DTG and an endothermic response at ≈ 450 °C in DSC indicates the formation of LaONO_3 , $\text{Y}_4\text{O}_4(\text{NO}_3)_4$ and Pr_2O_3 . It is worth noting that the NO_3^- ions of La and Y do not decompose during combustion and require a higher temperature to decompose to form metal oxides (Mekhemer and Balboul 2001; Melnikov et al. 2013, 2018). Simultaneously, thermal analysis was performed on the HEO-500, as shown in Fig. 4.2 (c and d). In zone I (50 – 300 °C), the weight loss of 6.8 % at ≈ 110 °C in DTG (Fig. 4.2 (c)) and an endothermic response in DSC (Fig. 4.2 (d)) at ≈ 90 °C is dedicated to the elimination of moisture adsorbed, while in zone II (300 °C – 600 °C), a total weight loss of 21.7 % in TGA and an endothermic response at ≈ 450 °C in DSC is attributed incomplete decomposition from La, Sm, and Y and removal of carbon impurities (Mekhemer and Balboul 2001). Finally, in zone III (600 °C – 850 °C), a minimal weight loss of 3.3 % in TGA indicates further decompositions in La and Y and the formation of stable metal oxide, as observed in Fig. 4.3 and no such significant change in DSC is observed (Baquer et al. 2018; Mekhemer and Balboul 2001; Melnikov et al. 2013). The summary of all the thermal events in the precursor gel with an increase in temperature from TGA and DSC is summarised in table 4.1.

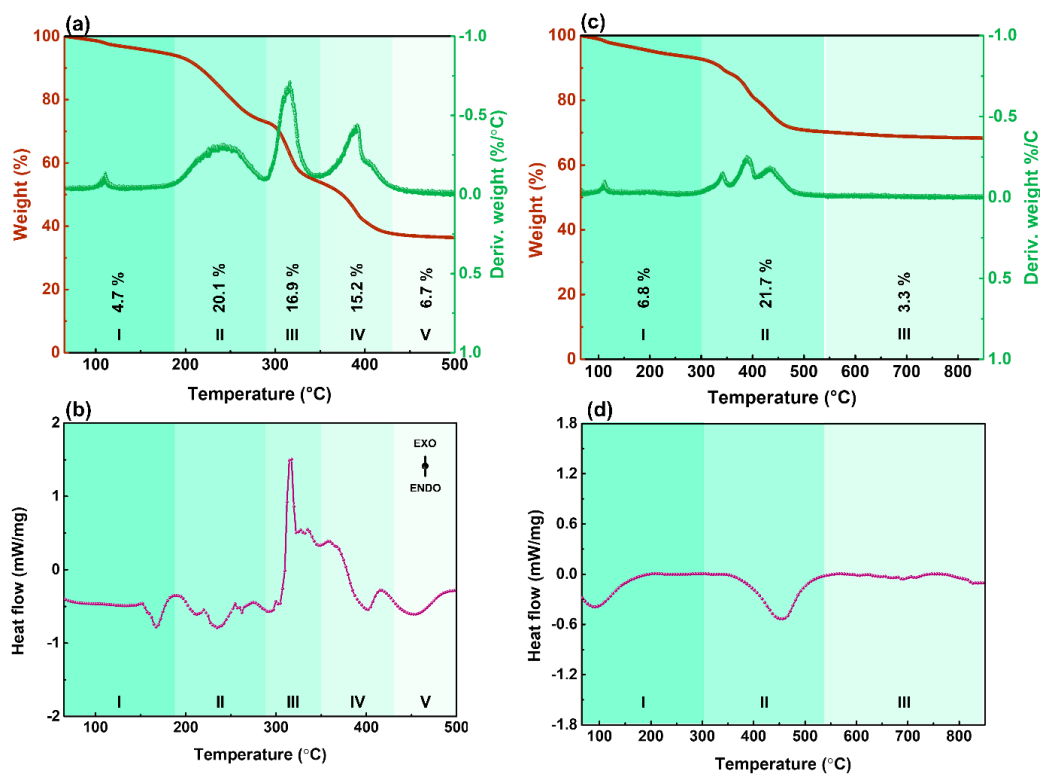


Fig. 4.2. The (a) weight loss (TGA and DTG) and (b) heat flow (DSC) of (CeLaPrSmY)O HEFO precursor gel and (c) TGA and DTG, and (d) DSC of HEO-500.

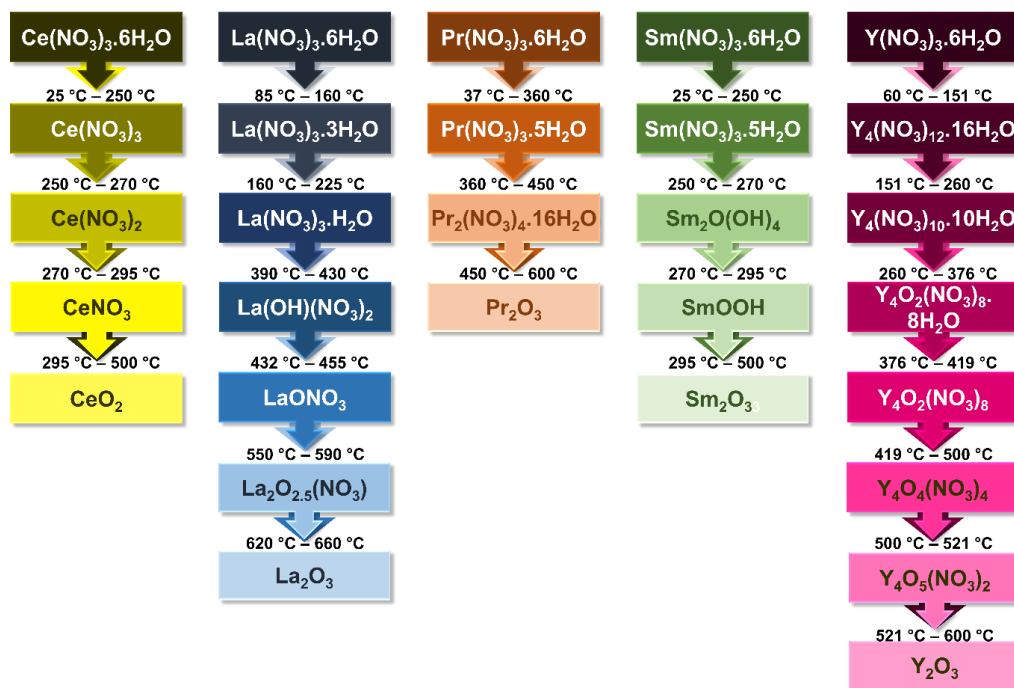


Fig. 4.3. The Decomposition pathway of all (CeLaPrSmY)O metal nitrates with an increase in temperature towards the formation of stable oxides, respectively.

Table 4.1. Summary of thermal events in the (CeLaPrSmY)O precursor gel and HEFO-400 with an increase in temperature from TGA and DSC.

Materials	Zones	Temperature interval (°C)	Weight loss (%)	Reason
Precursor gel	I	50 – 190	4.7	Evaporation of solvent and removal of bound water.
	II	190 – 290	20.1	The dehydration of all metal nitrate
	III	290 – 350	16.9	Combustion, dehydration of Ce, La, Pr, and Y nitrates, and decomposition of hydroxides in Sm
	IV	350 – 430	15.2	Formation of CeO ₂ , decomposition of La, Pr, and Y nitrates, and Sm hydroxide
	V	430 – 500	6.7	Decomposition of La, Pr, and Y nitrates and Sm hydroxide
HEFO-500	I	50 – 300	6.8	Elimination of moisture adsorbed
	II	300 – 600	21.7	Decomposition of incomplete from La, Pr, and Y nitrates and Sm hydroxide and removal of carbon impurities
	III	600 – 870	3.3	Decompositions of La and Y nitrates and formation of stable metal oxide

4.3.2 Structural, compositional, and morphological analysis

In order to identify the phase formed, (CeLaPrSmY)O powders (HEFO-500 to HEFO-1000) were subjected to XRD characterization. The XRD patterns of the (CeLaPrSmY)O powders, HEFO-500 to HEFO-1000, are presented in Fig. 4.4 (a). It is noticeable that the HEO-500 has diffraction peaks of planes (111), (200), (220), (311), and (400) that correspond to the cubic fluorite phase, with noisy and broadened reflections, indicates the beginning of crystallization, and directs the successful synthesis of (CeLaPrSmY)O at low temperature 500 °C. While a few diffraction peaks of the cubic fluorite phase with planes like (222), (331), (420), and (422) are not visible due to poor crystallinity, can be ascribed to the deficiency of adequate thermal energy to crystallize at ≤ 500 °C. Subsequently, with an increase in temperature (600 °C – 1000 °C), all planes started evolving, and the diffraction peaks became more fine, narrow,

intense, and sharper with low and flat backgrounds, signifies an enhancement in crystallinity. The diffraction peaks in the XRD pattern correspond to the standard ICDD file of CeO₂ (ICDD: 01-075-7757). The (CeLaPrSmY)O exhibits a single-phase, face-centered cubic (fcc) fluorite structure with an *Fm-3m* space group. Diffraction peaks concerning impurities are detectable from HEFO-500 to HEFO-900, and a pictorial representation is shown in Fig. 4.5. The secondary phases of Sm₂O₃ (ICDD: 01-078-4055) and Y₂O₃ (ICDD: 01-071-0049) were visible upto 500 °C, while La₂O₃ (ICDD: 01-083-1344) were detected up to 900 °C as shown in Fig. 4.4 (a). Diffraction peaks concerning impurities are not detectable HEFO-1000; thus, 1000 °C (HEFO-1000) is considered to be the phase stabilization temperature of the synthesized (CeLaPrSmY)O. Simultaneously, zoomed X-ray diffraction patterns at 2θ equal to 24° - 40°, which represent the major peaks (111) and (200) of the system, are shown in Fig. 4.4 (b). A non-significant slight peak shift towards the left is observed and is attributed to the minimal lattice expansion with an increase in temperature (Teng et al. 2021). Moreover, the low lattice expansion was further supported by the lattice parameter as a function of temperature, as shown in Fig. 4.4 (c). The lattice parameter non-significantly varies from 5.39 Å to 5.48 Å, indicates low thermal expansion in (CeLaPrSmY)O, and the results are summarized in table 4.2. The information of lattice parameter ‘*a*’ for the cubic system is extracted from the XRD using equation 3.2 and Cohen’s method (equations 3.3 and 3.4).

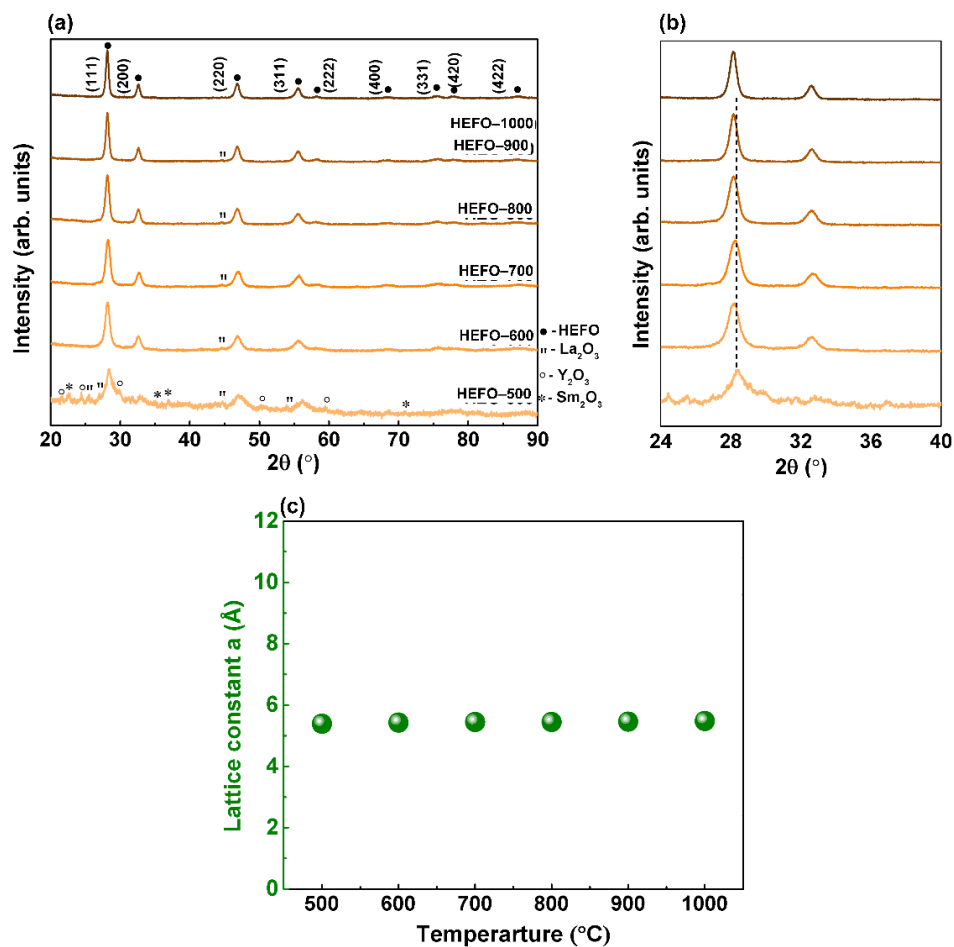


Fig. 4.4. (a) X-ray diffraction patterns of HEO-500 to HEO-1000, (b) zoomed X-ray diffraction patterns at 2θ equal to $24^\circ - 40^\circ$, represent the major peak of the system, (c) constancy of lattice parameter with an increase in temperature.

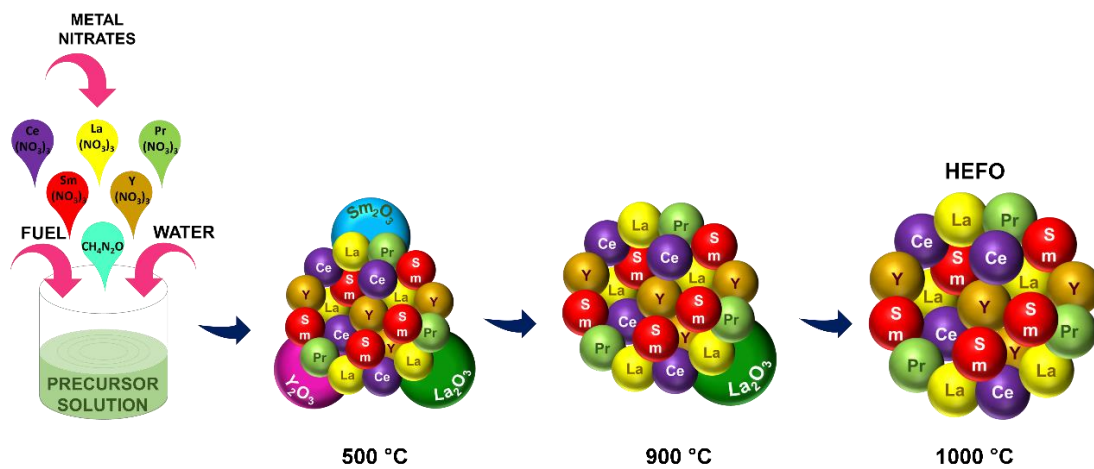


Fig. 4.5. Pictorial representation of phase stabilization of $(\text{CeLaPrSmY})\text{O}$ from precursor solution to the presence of secondary phase till the pure fluorite phase formation.

Table 4.2. Summary of the lattice parameter of (CeLaPrSmY)O with an increase in temperature.

Temperature (°C)	$a = \frac{(h^2+k^2+l^2)^{1/2}}{d}$ (Å)	Cohen's method a (Å)
500	5.44	5.39
600	5.48	5.43
700	5.48	5.45
800	5.49	5.45
900	5.49	5.46
1000	5.49	5.48

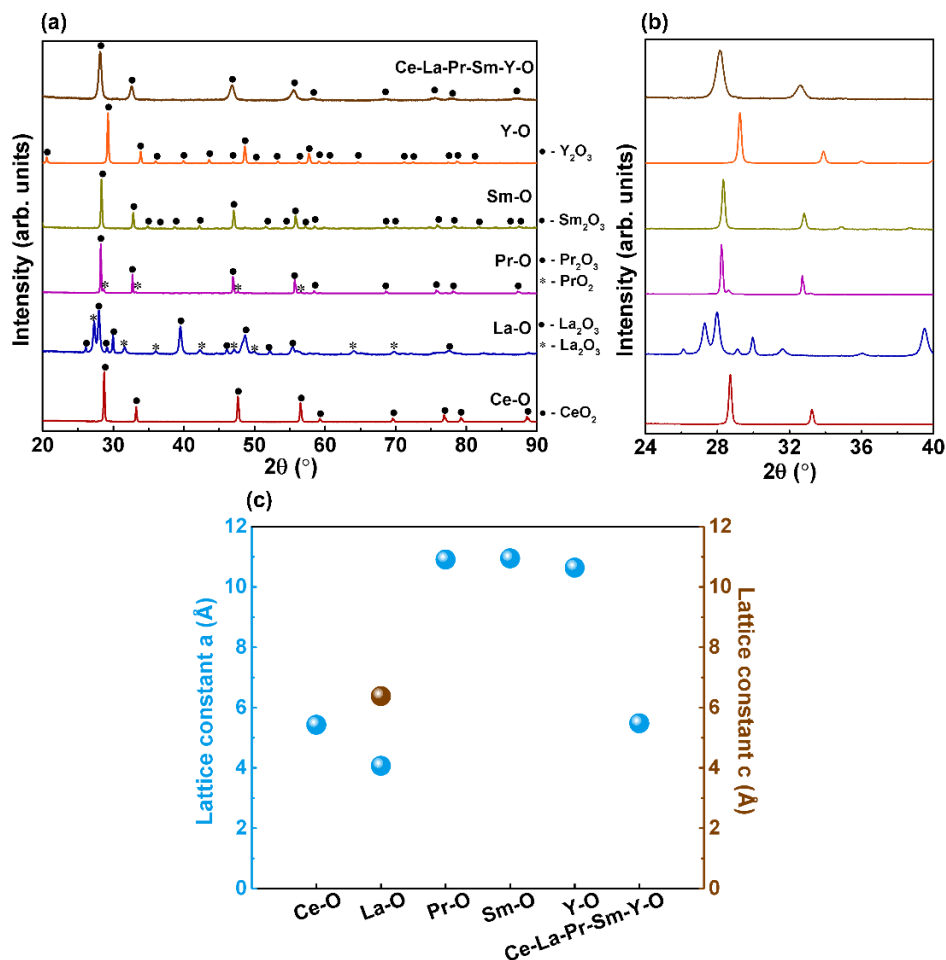


Fig. 4.6. (a) X-ray diffraction patterns of individual parent metal oxides Ce-O, La-O, Pr-O, Sm-O, and Y-O, (b) zoomed XRD at 2θ 24° – 40° represent the major peak of the system, (c) change in lattice parameter.

Furthermore, HEFO-1000 is compared and analyzed with individual parent oxide systems sintered at 1000 °C. The XRD patterns of the individual parent oxides are

presented in Fig. 4.6 (a). The details of the diffraction peaks, standard ICDD file number, crystal structure, and lattice parameters corresponding to the individual oxides are provided in table 4.3. The Ce-O is the only parent metal oxide with a crystal structure similar to HEFO-1000. Hence, (CeLaPrSmY)O incorporated its structure from the Ce-O parent oxide. Simultaneously, Fig. 4.6 (b) depicts the zoomed X-ray diffraction patterns at 2θ equal to $24^\circ - 40^\circ$, indicates similar diffraction patterns of HEFO-1000 and Ce-O, while the rest La-O, Pr-O, Sm-O, and Y-O have dissimilar patterns. This confirms that HEFO-1000 belongs to the cubic fluorite family as that of Ce-O and displays one of its parent oxide structural properties. For further comparison, the information of lattice parameters ‘ a and c ’ is extracted from the XRD using equations 3.2 – 3.4 for the cubic system and 3.5 – 3.8 for the hexagonal system. The dominating phase in every parent oxide is considered for the calculation of the lattice parameters, and the results are summarized in table 4.4. Fig. 4.6 (c) displays the lattice parameter of individual parent oxide and HEFO-1000 (here, Cohen’s data is used). As visible, Ce-O is the only parent oxide with a lattice parameter near HEFO-1000, with a difference of 0.05 \AA . As mentioned earlier, this can be attributed to the similar cubic fluorite structure of CeO_2 and HEFO-1000.

Table 4.3. Details of the diffraction peaks, standard ICDD file number, crystal structure, and lattice parameters corresponding to the individual oxides.

System	Oxides	ICDD file	Crystal structure	Lattice parameter of major phases
Ce-O	CeO_2	01-075-7757	Cubic Fm-3m 225	$a = 5.39 \text{ \AA}$ (Cubic Fm-3m 225)
La-O	La_2O_3 and La_2O_3	01-083-1344	Hexagonal P3m-1	$a = 3.94 \text{ \AA}$ and
		and 03-065-3185	164 and Cubic Ia-3 206	$c = 6.13 \text{ \AA}$ (Hexagonal P3m-1 164)
Pr-O	Pr_2O_3 and PrO_2	00-061-0049	Cubic Ia-3 206 and	$a = 10.94 \text{ \AA}$ (Cubic Ia-3
		and 00-024-1006	Cubic Fm-3m 225	206)
Sm-O	Sm_2O_3	00-078-4055,	Cubic Ia-3 206	$a = 10.92 \text{ \AA}$ (Cubic Ia-3 206)
Y-O	Y_2O_3	01-071-0049.	Cubic Ia-3 206	$a = 10.59 \text{ \AA}$ (Cubic Ia-3 206)

Table 4.4. Summary of the lattice parameter of individual parent oxides and HEO-1000.

Temperature (°C)	a (Å)	c (Å)	Cohen's method	Cohen's method
			a (Å)	c (Å)
Ce-O	5.39	5.39	5.43	5.43
La-O	3.94	6.132	4.07	6.38
Pr-O	10.94	10.94	10.91	10.91
Sm-O	10.92	10.92	10.95	10.95
Y-O	10.59	10.59	10.64	10.64
Ce-La-Pr-Sm-Y-O	5.49	5.49	5.48	5.48

A similar study is performed by reducing the number of cations from five to lower values (4, 3, 2, and 1) and estimating the variation in the lattice constant ' a '. The XRD patterns of the HEFO-1000 (Ce-La-Pr-Sm-Y-O) and lower cation system (Ce-La-Pr-Sm-O, Ce-La-Pr-O, Ce-La-O, and Ce-O) are presented in Fig. 4.7 (a). The diffraction peaks of 1 cation system Ce-O correspond to the cubic fluorite CeO₂, similar to as depicted in Fig. 4.6 (a). While the major diffraction peaks in the XRD of 2 and 3 cation system Ce-La-O and Ce-La-Pr-O corresponds to CeO₂ 01-075-7757 similar to HEFO-1000 with the presence of La₂O₃ (01-083-1344) as secondary peaks. Furthermore, the prominent diffraction peaks in the XRD of the 4-cation system Ce-La-Pr-Sm-O correspond to the standard ICDD file of CeO₂ 01-075-7757, similar to HEFO-1000. Hence, the major peaks of the lower cation systems also exhibit an fcc structure with an $Fm\bar{3}m$ space group. Therefore, it can be assumed that the presence of a secondary phase in the lower cation system and the display of single-phase in HEO-1000 indicates the role of configurational entropy in phase stabilization. Simultaneously, zoomed X-ray diffraction patterns at 2θ equal to $24^\circ - 40^\circ$, represents the major peaks (111) and (200) of the system, are shown in Fig. 4.7 (b). A non-significant slight peak shift towards the left is observed and is attributed to the minimal lattice expansion with an increase in temperature (Teng et al. 2021). Moreover, the low lattice expansion was further supported by the lattice parameter as a function of temperature, as shown in Fig. 4.7 (c) (here, Cohen's data is used). The information of lattice parameter ' a ' for the cubic system is extracted from the XRD using equation 3.2 and Cohen's method (equations 3.3 and 3.4) considering fluorite structure. As shown in Fig. 7c, the lattice parameter changed from 5.43 Å to 5.48 Å, with an increasing number of cations and

can be attributed to cationic disorder, variation of ionic radius, and electronegativity of elements present (Pażik et al. 2015), and lattice expansion with an increase in the number of cations (Teng et al. 2020, 2021) and the results are summarized in table 4.5. In addition, according to Bragg Law (Bragg et al. 1913), similar to HEFO-1000, a shift in peak to low angle and increase in lattice parameter indicates an effective entry of the solid solution atoms into the lattice to some extent.

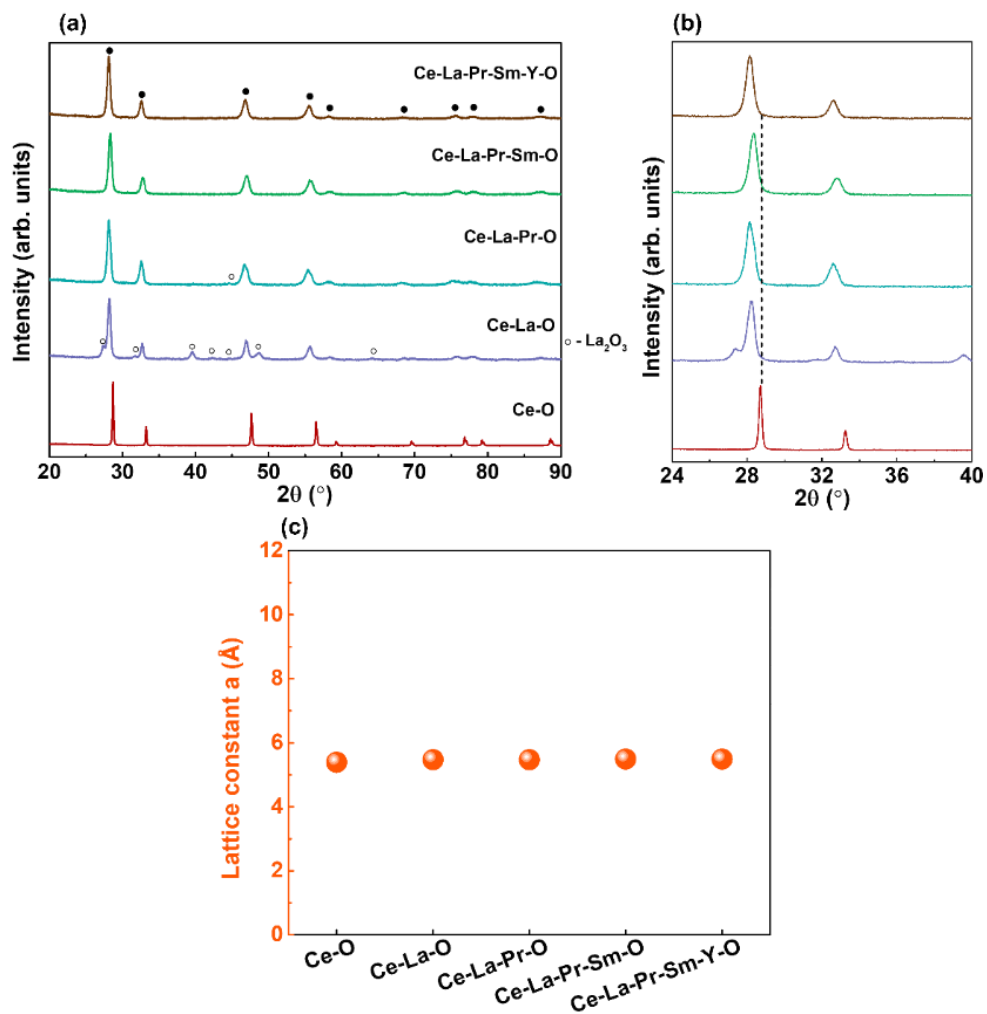


Fig. 4.7. (a) X-ray diffraction patterns of lower cation systems Ce-O, Ce-La-O, Ce-La-Pr-O, and Ce-La-Pr-Sm-O in comparison with Ce-La-Pr-Sm-Y-O (HEFO-1000), (b) zoomed XRD at 2θ $24^\circ - 40^\circ$ represent the major peak of the system, (c) change in lattice parameter indicating expansion of lattice with an increase in cations.

Table 4.5. Summary of the lattice parameter of lower cation system and HEFO-1000.

Temperature (°C)	$a = \frac{(h^2+k^2+l^2)^{1/2}}{a}$ (Å)	Cohen's method a (Å)
Ce-O	5.39	5.43
Ce-La-O	5.47	5.5
Ce-La-Pr-O	5.47	5.5
Ce-La-Pr-Sm-O	5.49	5.5
Ce-La-Pr-Sm-Y-O	5.49	5.48

To understand the molecular vibration happening within the (CeLaPrSmY)O, Raman and FTIR spectroscopy were used. For a perfect cubic CeO₂ fluorite structure, only the Raman band associated with the triple degenerate F_{2g} symmetric vibration mode of the Ce-O bond in eightfold coordination should be seen at around 460 cm⁻¹. The shape and position of the band are affected by the development of oxygen vacancies and changes in the initial Ce-O bond length brought about by the addition of other rare earth atoms to the cerium site. The Raman spectra of HEFO-500 to HEFO-1000 are shown in Fig. 4.8 (a). The F_{2g} symmetric vibration mode in (CeLaPrSmY)O is located at a range from 400-500 cm⁻¹, which confirms the formation of fluorite structure and becomes barely visible with an increase in temperature. The weakening of the F_{2g} Raman peak from HEFO-500 to HEFO-1000 can be attributed to the symmetry breaking (severe lattice distortion) due to the chemical disorder and phase stability (Sarkar et al. 2017b). The peaks in the range 100 – 300 cm⁻¹, 500 – 800 cm⁻¹, and 920 – 1200 cm⁻¹ are caused by the second-order transverse acoustic (2TA) mode, the defect-induced mode (D), and second-order longitudinal-optical mode (2LO), respectively. The broad peaks of the 2TA, D, and 2LO are due to the presence of defects mainly due to the formation of oxygen vacancies and their related bonding with +3 and +4 cations. The asymmetrical broadening and reduction in the peak intensity are due to changes in interatomic force and oxygen vacancies (Guo et al. 2016; Sarkar et al. 2020b). Thus, formation, presence of distortion, and disorder occupancy of multiple cations (Ce, La, Pr, Sm, and Y) in cubic lattice and phase stabilization of (CeLaPrSmY)O with the presence of defects are evident from Raman spectroscopy. In contrast, the FTIR spectra of HEFO-500 and HEFO-1000 are illustrated in Fig. 4.8 (b). In both spectra HEFO-500 and HEFO-1000, the broad absorption ranges from 3700 –

3000 cm^{-1} are attributable to the stretching vibration of the O-H bond [42], 1650 – 1550 cm^{-1} were related to the H-O-H bending vibration modes, 1300 – 1500 cm^{-1} are assigned to C-H bending, and 800 – 500 cm^{-1} correspond to the metal-oxygen (M-O) (M = Ce, La, Pr, Sm, Y) stretching vibration mode, respectively (Ghalmi et al. 2019a; Pujar et al. 2018; Safat et al. 2021). The HEFO-500 has four extra absorption peaks at 2430 cm^{-1} , 1525 cm^{-1} , and 1160 – 1000 cm^{-1} are assigned to C-C, N-O, and C-O stretching vibrations, while 1000 – 800 cm^{-1} is assigned to C=O bending vibrations (Mihaylov et al. 2021; Pujar et al. 2018), respectively. The vanishing of characteristic bands related to C-C, N-O, C-O, and C=O vibrations in HEFO-1000 uncovered that they were from the nitrates and fuel urea consumed during the high-temperature treatment. Thus, the formation of (CeLaPrSmY)O is evident in both spectrums HEFO-500 and HEFO-1000, confirms the successful synthesis of low-temperature (500 °C) (CeLaPrSmY)O, in addition to the Raman and XRD results.

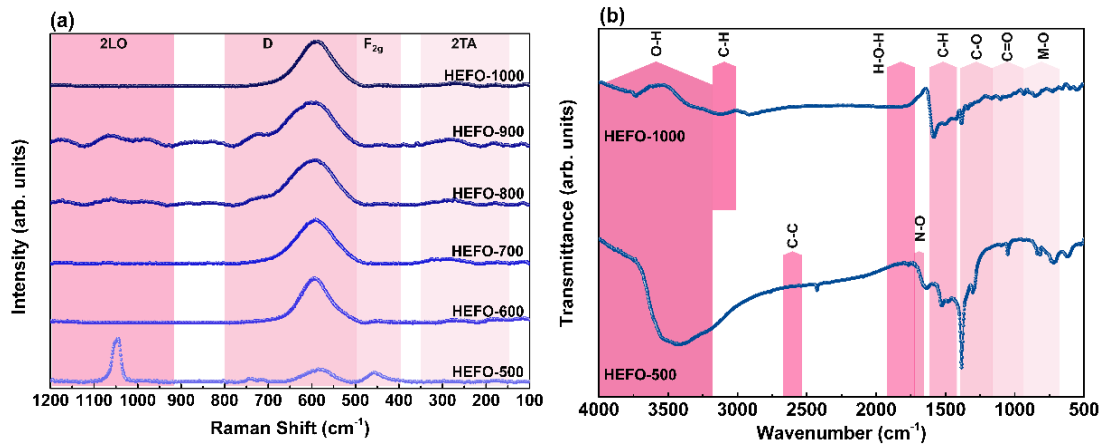


Fig. 4.8. (a) Raman spectra, and (b) FTIR spectra of HEFO-500 and HEFO-1000.

The heat treatment process exerts a change in morphology with regard to shape and size, which directly affects the dielectric nature and leakage current behavior. Thus, it is essential to know the (CeLaPrSmY)O morphology. Therefore, FE-SEM is used to reveal the morphologies and elemental distribution of the synthesized (CeLaPrSmY)O. To understand the effects of heat treatment, (CeLaPrSmY)O heat treated at all temperatures was examined, as evidenced in Fig. 4.9 (a-f). A flake morphology with nanogranular clusters on the surface was observed. The EDS of HEFO-1000 (Appendix II, Fig. I (a)) displays a homogenous distribution of all five cations, with the atomic percentage of the five elements being very close (Ce – 8 %; La – 8.5 %, Pr – 9.9 %; Sm

– 9.6 %; Y – 6.8 %). The mapping of all the elements of HEFO-1000 displays the distribution of elements without any segregation (Appendix II as Fig. I).

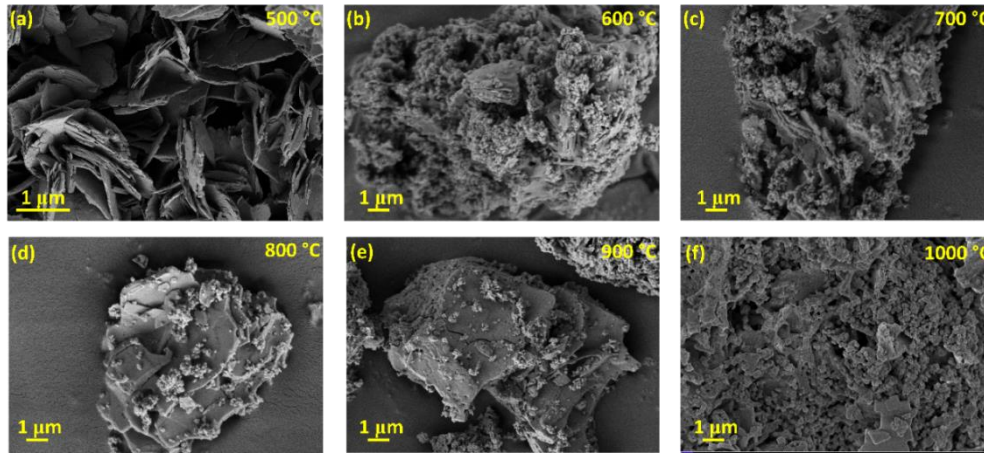
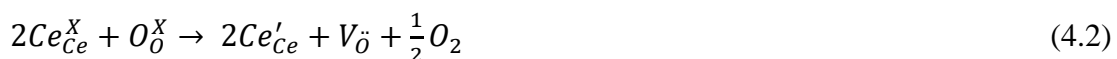


Fig. 4.9. (a-f) The surface morphology of HEFO-500 to HEFO-1000.

To strengthen the analysis, surface chemical compositions were analyzed using XPS on HEFO-1000. The five cations Ce, La, Pr, Sm, and Y, including other elements like C and O, were detected from the compositional analysis by XPS through a low-resolution survey scan in the range 0 – 1200 eV. The high-resolution spectra of all elements are displayed in Fig. 4.10; the spectra of HEFO-1000 are calibrated using the carbon 1s (C 1s) spectrum positioned at 284.6 eV. The low-resolution survey scan and the C 1s spectrum are provided in Appendix II as Fig. II (a and b). The fine scan of Ce 3d XPS spectra of HEO-1000 is given in Fig. 4.10 (a), in which the peaks of Ce 3d_{5/2} and Ce 3d_{3/2} are located at around 880.93 eV and 899.18 eV and are ascribed to Ce³⁺ respectively. The fitted peak for Ce 3d_{5/2} and Ce 3d_{3/2} at 885.97 eV and 901.28 eV is attributed to the Ce³⁺ oxidation state, while the peak at 883.71 eV, 888.11 eV, 896.61 eV, 904.49 eV, and 914.35 eV are of Ce⁴⁺ oxidation state, respectively. Thus, due to the splitting of the spin doublet, Ce 3d shows both oxidation states, Ce³⁺ and Ce⁴⁺. Nevertheless, according to the present multiple splitting, as shown in Fig. 4.10 (a), the Ce ions were identified mainly as Ce³⁺ by calculating the area of the synthetic peaks (Ce³⁺/Ce⁴⁺ = 1.96), indicates a partial valence reduction of Ce⁴⁺ using the lattice oxygen and releasing oxygen vacancies as shown in equation 4.2 (Bortamuly et al. 2020; Vinothkumar et al. 2018; Wen and Liu 2023).



Where, Ce_{Ce}^X is the Ce^{4+} , O_O^X represents the lattice oxygen, Ce'_{Ce} is the Ce^{3+} , V_O^{\cdot} is the oxygen vacancy and O_2 is the oxygen molecule. Interestingly in the fine scan La 3d XPS spectra (Fig. 4.10 (b)), a higher La 3d_{5/2} peak located at 836.79 eV and a separated La 3d_{3/2} peak at 852.82 eV are assigned to La³⁺, respectively (Uwamino et al. 1984). As shown in Fig. 4.10 (c), the Pr 3d spectra were reasonably deconvoluted into six fitted peaks. The peaks centered at 932.40 eV and 951.98 eV correspond to Pr³⁺ of Pr 3d_{5/2} and Pr 3d_{3/2} peaks. The fitted peak for Pr 3d_{5/2} and Pr 3d_{3/2} at 936.34 eV and 955.84 eV is attributed to Pr⁴⁺, respectively. The peaks at 928.29 eV and 947.77 eV are shake-up satellite peaks of Pr, respectively (Jiang et al. 2018a). According to the present multiple splitting, as shown in Fig. 4.10 (c), the Pr ions were recognized as Pr³⁺ in the majority by calculating the area of the synthetic peaks ($Pr^{3+}/Pr^{4+} = 2.36$). In a fine scan of Sm 3d XPS spectra (Fig. 4.10 (d)), Sm 3d_{5/2} and Sm 3d_{3/2} peaks are centered at 1081.89 eV and 1108.28 eV, respectively, which is the feature of spin-orbit coupling and characteristic of Sm³⁺ (Guo et al. 2011). The fine scan of Y 3d XPS spectra, as shown in Fig. 4.10 (e), exhibited three components, in which two at binding energies of 160.81 and 162.91 eV correspond to Y³⁺ of Y 3d_{5/2} and Y3d_{3/2} (Kaminaga et al. 2016). However, by calculating the area of the synthetic peaks ($Y^{2+}/Y^{3+} = 1.04$), the Y³⁺ is slightly higher in contribution than Y²⁺. Fig. 4.10 (f) shows four oxygen peak contributions of the O 1s region of the HEFO. The peaks at 532.51 eV and 535.67 eV are typical for a metal-oxygen peak $O_{Latt.}$ (lattice oxygen) and O_v (oxygen vacancy), respectively (Nguyen et al. 2020a). According to the results of XPS, it is found that the Ce^{3+} , La^{3+} , Pr^{3+} , Sm^{3+} , and Y^{3+} ions are the dominating states in the system, respectively, as tabulated in table 4.6.

Table 4.6. Summary of the percentage area contribution of deconvoluted peaks in cations.

Deconvoluted peak ratio	Area ratio
Ce^{3+}/Ce^{4+}	1.96
La^{3+}	1
Pr^{3+}/Pr^{4+}	2.36
Sm^{3+}	1
Y^{2+}/Y^{3+}	1

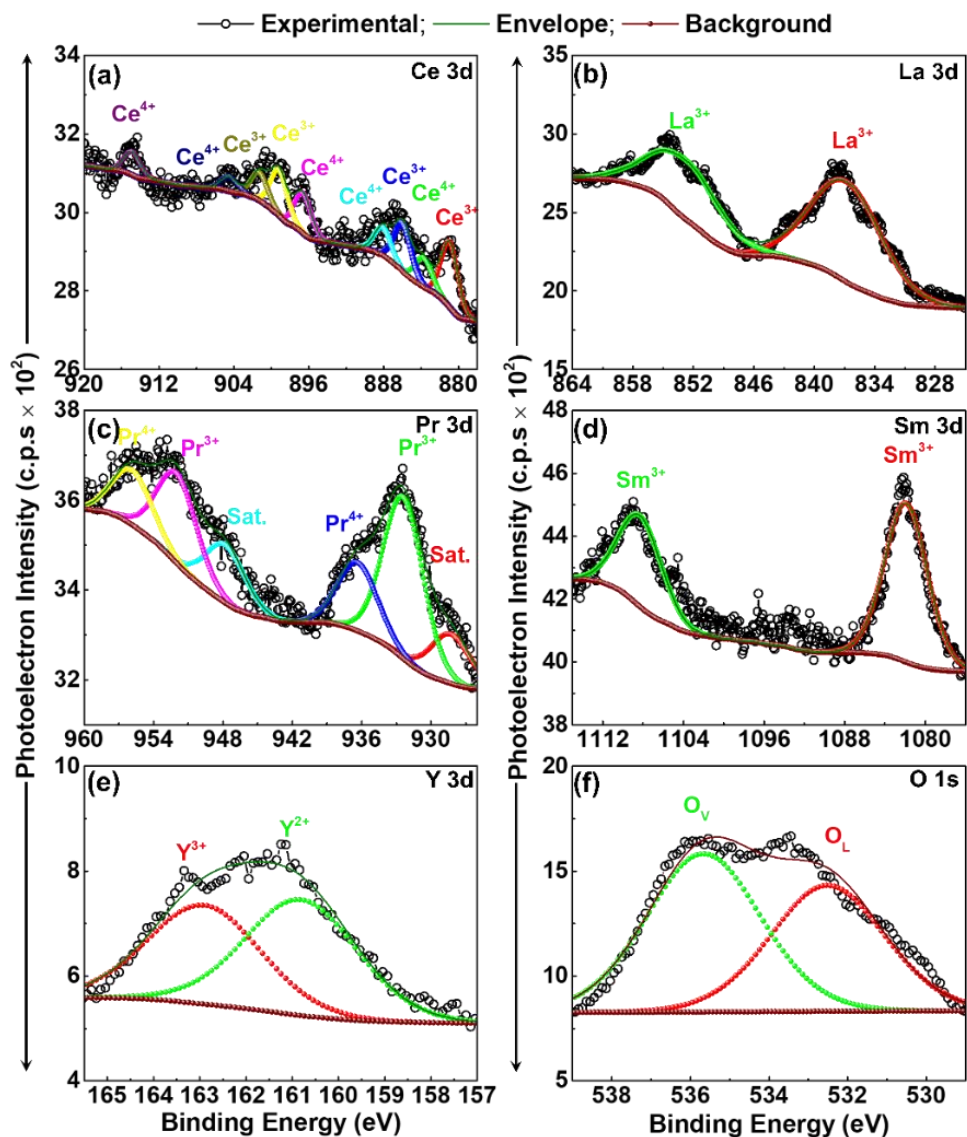


Fig. 4.10. High-resolution deconvoluted spectra of core level (a) Ce 3d, (b) La 3d, (c) Pr 3d, (d) Sm 3d, (e) Y 3d, and (f) O 1s depicting their respective oxidation states.

4.3.3 Dielectric constant of sintered (CeLaPrSmY)O capacitor

The dielectric study is performed on the capacitor developed using the (CeLaPrSmY)O pellet, as shown in Fig. 4.11 (a). The pellet is sintered at 1000 °C and displays compaction and sintering of flakes with porous structure, as observed in Fig. 4.11 (b). To further confirm the constituent elemental distribution in the (CeLaPrSmY)O pellet, an EDS was performed, as shown in Fig. 4.11 (c), which displayed the homogenous distribution of all five cations with the atomic percentage of the five elements being very nearby (Ce – 6.2 %; La – 6.2 %, Pr – 5.98 %; Sm – 6.2 %; Y – 3.9 %) as observed in HEFO-1000. Fig. 4.11 (d) depicts the room temperature

measured dielectric constant (κ) and dielectric loss ($\tan \delta$) throughout the frequency range of 100 Hz to 1 MHz. The κ measured is $\approx 29 - 5.7$ from 100 Hz – 1 MHz, which is of reasonably good dielectric constant value compared to SiO_2 (~ 3.5) applicable as a gate oxide in transistors or capacitors (Young and Frederikse 1973). In this frequency range, κ is observed to be flat or frequency independent, often known as the static value of dielectric constant. The amount of field lost as heat when an applied alternating electric field polarizes a material is known as the dielectric loss, also known as the tangent loss ($\tan \delta$). The $\tan \delta$ remains small at a low frequency and gradually increases with an increase in frequency. The $\tan \delta$ can be attributed to the increased space charge trapping by the inter-grain boundaries of the particles (Abbas et al. 2019). Fig. 4.11 (e) shows a plot of the real (Z') and imaginary (Z'') parts of complex impedance (Z) as a function of frequency measured at room temperature. The constant value of Z' and Z'' i.e., frequency independent, is attributed to the continual reduction in the barrier properties or release of space charge (Suman et al. 2006). The real (M') and imaginary (M'') part of the electric modulus as a function of frequency at room temperature is showcased in Fig. 4.11 (f), where both display similar behavior. The M' and M'' value is low at the lower frequency range and slightly rises with an increase in frequency. The near-zero value at a low frequency is caused by electrode polarization, and the change in the value with frequency can be ascribed to the non-Debye type of relaxation in the material and the distribution of relaxation time, where the short-range mobility of charge carriers replaces the long-range mobility of charge carriers (Gajula et al. 2020; Omri et al. 2020).

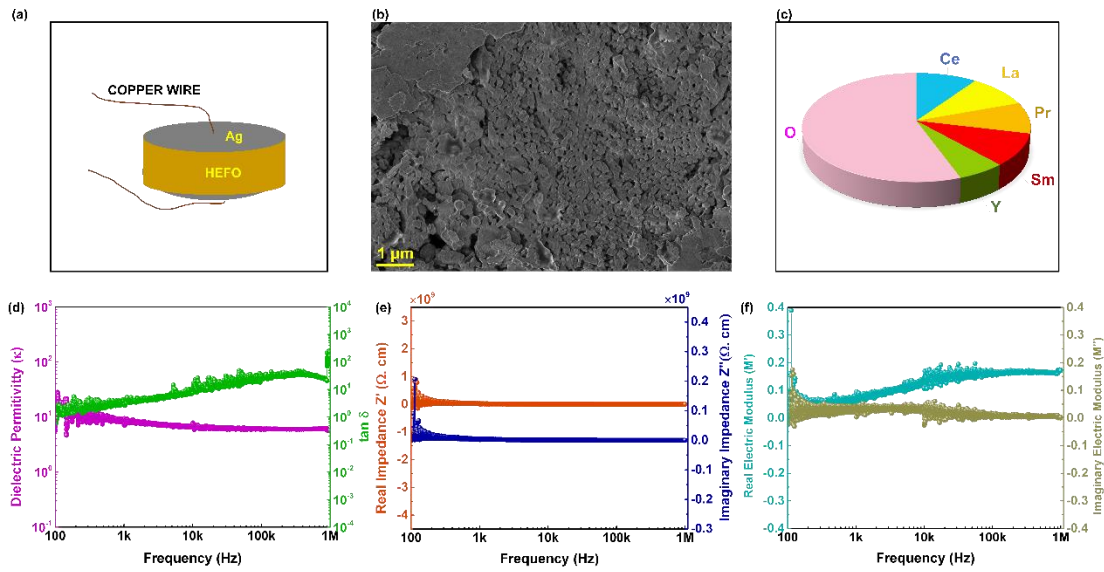


Fig. 4.11. (a) Schematic of the capacitor developed using (CeLaPrSmY)O pellet sintered at 1000 °C, (b) the surface morphology of the (CeLaPrSmY)O pellet sintered at 1000 °C and used for the development of capacitor, with admirable sinterability of the grain, and (c) the pie chart indicating the elemental distribution of all five cations in (CeLaPrSmY)O pellet extracted from EDS, frequency dependence plots of the (d) dielectric constant (κ) and dielectric loss ($\tan \delta$), (e) real and imaginary part of the impedance (Z), (f) real and imaginary part of the electric modulus (M) measured at room temperature.

In general, ionic, interfacial, or space charge, dipolar, and electronic polarization are among the polarization types that have been observed to affect the κ of metal oxides (Omri et al. 2020). The space charge or interfacial and dipolar polarization predominates in the low-frequency range as a result of the build-up of charges at grain boundaries. This adheres to the phenomenological theory of Koop (Kumari et al. 2014). When the frequency is low, dipoles have enough time to align with the applied field. Simultaneously, as the frequency rise, dipolar and space charge particles do not follow the alternating field and gradually lose their ability to contribute to the dielectric constant. According to Maxwell-Wagner theory, at a higher frequency, the electric dipole is unable to follow the rapidly changing alternating field, and increases the friction between them (Yager 1936). Hence, it is well known that ionic and electronic polarization play a prominent role in polarization in the high-frequency domain. As observed in Fig. 4.11 (d), the flat or frequency-independent nature in the κ with an increase in frequency can be attributed to the reduction of space charge or interfacial

polarization effect and dominance of ionic and electronic polarization. The main cause for the increase in frequency-dependent $\tan \delta$ is due to the defects, charge carriers, and imperfections or impurities in the crystal lattice, which causes the polarization to lag behind the alternating field (Hajra et al. 2019). Furthermore, according to Maxwell-Wagner and Koop's phenomenological theory, maximum energy is transferred to oscillating ions as a result of resonance phenomena, which occurs when jumping frequency equals the applied field and thereby creates a rapid increase in the $\tan \delta$ (Asif et al. 2021). Thus, the reason for the large κ in (CeLaPrSmY)O can be attributed to combined effects from electronic and ionic polarizations; the larger radii ions in (CeLaPrSmY)O (Ce: 115 pm (+3) and 101 pm (+4), La: 117.2 pm (+3), Pr: 113 pm (+3) and 99 pm (+4), Sm: 109.8 pm (+3), Y: 104 pm (+3) and O: 126pm) can be electronically polarized easily compared to the small radii ions (Bérardan et al. 2016b). However, the five distinct cations offer a large spectrum of bond stiffnesses, thus promotes ionic polarization. In addition, as HEFO-1000 possess oxygen ion vacancies, as seen in the XPS (Fig. 4.10 (f)), they may form dipoles as they are equivalent to positive charges. When exposed to an electric field, the dipole created by the oxygen vacancies may rotate, and give a resultant dipole moment (Maier et al. 1988). In addition, in comparison to other high- κ HEO (Bérardan et al. 2016a), the dielectric value of the present developed HEFO is less and can also be ascribed to the flake morphology and porous structure in the sintered body (Wang et al. 2019d). Hence, the dielectric performance of (CeLaPrSmY)O can be attributed to the combination of different polarization like space charge, ionic and electronic, and flake morphology and the porous structure.

4.4 Conclusion

For the first time, high entropy fluorite oxide (CeLaPrSmY)O was synthesized successfully at a low temperature (500 °C) using solution combustion synthesis, where phase was stabilized at 1000 °C with single-phase fluorite structure with a reasonably good dielectric performance. Thermal analysis displayed combustion of the precursor gel at 320 °C. The XRD patterns of the (CeLaPrSmY)O exhibited a low-temperature formation of HEFO at 500 °C. The presence of Sm_2O_3 and Y_2O_3 was visible upto 500 °C, while La_2O_3 was detected up to 900 °C and the (CeLaPrSmY)O fully got stabilized

at 1000 °C with a single-phase, fcc fluorite structure with an Fm-3m space group. (CeLaPrSmY)O displayed one of its parent oxide Ce-O structural properties as both belong to the fluorite family and had lattice parameters very close to each other. The presence of a secondary phase in the 2 and 3-cation systems and the display of a single phase in the 4 and 5-cation systems specified the role of configurational entropy in phase stabilization. The Raman spectrum was completely tallied with the XRD results of (CeLaPrSmY)O, and the formation of (CeLaPrSmY)O with fluorite structure was evident at 500 °C, the complete elimination of secondary phases at 1000 °C, and a fully disordered occupancy of various metal cations with severe lattice distortion. In contrast, the formation of (CeLaPrSmY)O was evident in both FTIR spectrums of HEFO-500 and HEFO-1000 from 800-500 cm⁻¹. A flake morphology with a nanogranular cluster on the surface was displayed. The dielectric measurements showed $\kappa \approx 29 - 5.7$ from 100 Hz – 1 MHz at room temperature. Therefore, the above character of (CeLaPrSmY)O can be applicable as a dielectric in devices like display back panels, inverters, integrated sensors, logic devices, electronic circuits, and many more.

CHAPTER 5

INVESTIGATION OF DIELECTRIC PROPERTIES ON THE PHASE STABILIZED SOLUTION COMBUSTION PROCESSED HIGH ENTROPY SPINEL OXIDE (CoMnNiFeCr)O

The contents of this chapter have been published in the article:

Ashritha Salian, Saumen Mandal, **Indian Patent**, Application No: **202141035822**, dated 09/08/2021 (Filed)

Ashritha Salian, Pavan Pujar, Robbi Vivek Vardhan, Haewon Cho, Sunkook Kim, Saumen Mandal, **ACS Appl. Electron. Mater.**, 5(5), 2608-2623, (2023).

Page left intentionally blank

CHAPTER 5

INVESTIGATION OF DIELECTRIC PROPERTIES ON THE PHASE STABILIZED SOLUTION COMBUSTION PROCESSED HIGH ENTROPY SPINEL OXIDE (CoMnNiFeCr)O

5.1 Introduction

This chapter deals with an investigation of dielectric constant on the sintered high entropy spinel oxide (HESO) capacitor composed of Co, Mn, Ni, Fe, Cr (i.e., $(\text{Co}_{0.2}\text{Mn}_{0.2}\text{Ni}_{0.2}\text{Fe}_{0.2}\text{Cr}_{0.2})\text{O}_{1.2-\delta}$) developed using solution combustion synthesis. A systematic derivation of the stoichiometric combustion reaction from sub-reactions of oxidation and reduction is depicted. In-depth thermal, structural, microstructural, and elemental analysis was made, which helped to draw a correlation between phase stabilization and dielectric performances.

5.2 Experimental procedure

5.2.1 Formulation of combustible precursor

All reagents were of analytical-reagent grade and used as received without purification. The respective metal nitrates, namely, cobalt nitrate [$\text{Co}(\text{NO}_3)_2 \cdot 6\text{H}_2\text{O}$; (99 % purity)], ferric nitrate [$\text{Fe}(\text{NO}_3)_3 \cdot 9\text{H}_2\text{O}$; (99 % purity)], nickel nitrate [$\text{Ni}(\text{NO}_3)_2 \cdot 6\text{H}_2\text{O}$; (98 % purity)], and urea [$\text{CH}_4\text{N}_2\text{O}$; (99.5 % purity)] were purchased from Molychem, India; chromium nitrate [$\text{Cr}(\text{NO}_3)_3 \cdot 9\text{H}_2\text{O}$; (99 % purity)] from Kemphasol, India; and manganese nitrate [$\text{Mn}(\text{NO}_3)_2 \cdot 4\text{H}_2\text{O}$; (99 % purity)] was obtained from Sigma Aldrich, India. All the metal nitrates and urea were individually dissolved in deionized water and kept in an airtight glass container at room temperature. All solutions were mixed together with maintained molarity of 1.5, under stirring to obtain a clear aqueous combustible precursor.

5.2.2 Synthesis and characterization

The synthesis process of (CoMnNiFeCr)O powder is depicted in Fig. 5.1. The homogenous aqueous precursor solution was heated at 400 °C on a hot plate in the air atmosphere. The solution has undergone combustion with the release of a large amount

of gaseous products. The as-combusted black powder was found at the bottom of the flask. Further, the as-combusted powder was analyzed for phase stabilization by heating the same in the tubular furnace at a varied temperature from 500 °C - 1000 °C. The as-combusted powder (400 °C) and the heat-treated powder from 500 °C - 1000 °C is symbolically represented as HESO-400 (as-combusted), and HESO-500, HESO-600, HESO-700, HESO-800, HESO-900, and HESO-1000, respectively.

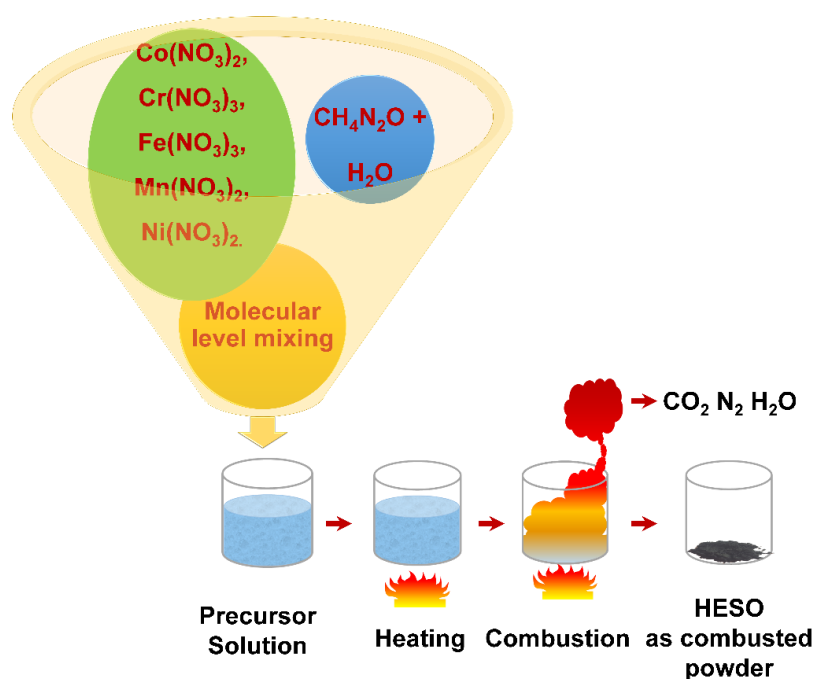


Fig. 5.1. Schematic of the synthesis process of (CoMnNiFeCr)O powder.

To understand the combustion behavior, precursor gel was collected during combustion and was subjected to thermal analysis using TGA (PerkinElmer, TGA 4000) and DSC (NETZSCH DSC 404 F1) with a heating rate of 10 °C min⁻¹. The phase purity and crystal structure of HESO powder was determined from powder XRD (PANalytical multipurpose high-resolution XRD) using a Cu-K α radiation source (1.54 Å) with a step size of 0.02. To study the morphology and elemental distribution, FE-SEM (Carl Zeiss AG model: GeminiSEM 300; JEOL: 7610FPLUS Japan) coupled with EDS at an accelerating voltage of 20 kV was used. The FTIR (PerkinElmer model: frontier MIR) was carried out for HESO-400 and HESO-1000 using the classic KBr pellet technique. The FTIR spectrum was at a scanning speed of 2 mms⁻¹ and resolution of 2 cm⁻¹ with a range of 400 – 4000 cm⁻¹. The Raman spectra were recorded using the

compact Raman spectrometer (Renishaw, UK) consists of a laser which operates at 532 nm. Surface chemical compositions for HESO-1000 powder were analyzed using XPS (Kratos Axis Ultra DLD). The monochromatic Al K_{α} was used as the X-ray source for XPS. An ultra-vacuum system with a base pressure of $\sim 10^{-10}$ Torr is maintained. The binding energy scale was mentioned in 'eV'. The received spectra were calibrated using the C-H peak of the adventitious carbon positioned at 284.6 eV and the peak fit analysis of all five cations (Co 2p, Mn 2p, Ni 2p, Fe 2p, and Cr 2p) and oxygen 1s (O 1s) peaks were carried out using the product of Gaussian and Lorentzian functions with fixed G/L (30 %) ratio and FWHM of synthetic peaks fitted by the software. The FWHM of the synthetic peaks in the spectra of five metal cations and oxygen was constrained to be the same to avoid inconsistency in peak fitting. The peak fit analysis was performed using the CASAXPS 2.3.22PR1.0 software package.

5.2.3 Development of sintered (CoMnNiFeCr)O capacitors

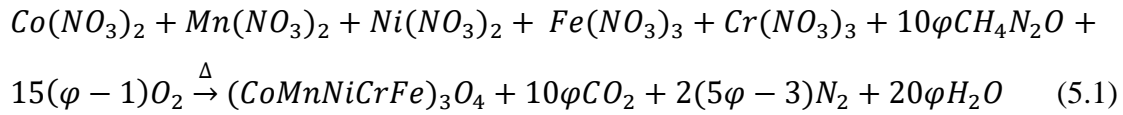
To study the dielectric performance of (CoMnNiFeCr)O, a dense body is required. Densification requires high-temperature sintering. Thus high-temperature sintered pellet of (CoMnNiFeCr)O was prepared to investigate the dielectric performance. In order to carry out the dielectric study, the (CoMnNiFeCr)O pellets were prepared by compaction of HESO-600 using a uniaxial hydraulic press under a load of 12 kN. The compacts were sintered at 1000 °C for 3 h in the furnace. Further, silver ink was painted on both sides of the pellet, and copper wire was soldered onto the silver as two electrodes for dielectric measurement. The dielectric constant, loss tangent, impedance, and electric modulus of HESO-1000 were determined at a different frequency range from 4 Hz – 1 MHz with bias voltage +1 V to -1 V, using the impedance analyzer (IM3536, Hioki, Japan).

5.3 Results and discussion

In order to characterize the efficacy of combustion in (CoMnNiFeCr)O powder, the systematic thermal, structural, and compositional study is performed as follows, and an investigation of dielectric constant on the sintered (CoMnNiFeCr)O capacitor is carried out.

5.3.1 Thermal decomposition analysis

The stoichiometric amount of all the five equimolar metal nitrates and the fuel were taken as per balanced chemical stoichiometry equation 5.1, calculated using Jain's method (Patil et al. 2008).



Where the parameter φ denotes the fuel-to-oxidizer ratio, and $\varphi = 1$ represents stoichiometric oxygen concentration, it implies that the oxidizers have a theoretically equal amount of oxygen to complete the reaction.

The transformation of the precursor into a useful HEO product requires the initiation of the combustion reaction. The temperature at which the combustible precursors undergo exothermic reaction and yield HEO is termed combustion temperature. Fig. 5.2 depicts the TGA, DTG, and DSC thermal traces of precursor gel and HESO-400. In Fig. 5.2 (a), at zone I, weight loss of $\approx 1.9\%$ in TGA and corresponding endothermic response in DSC at $\approx 70^\circ C$ are attributed to the evaporation of the solvent. Consequently, at zone II, considerable weight loss of $\approx 73\%$ in TGA, supplemented with the initiation of intense exothermic response at $240^\circ C$ in DSC, is the evidence of destruction, ignition, and combustion of precursor gel. In Zone III, no significant change is observed, which represents the stabilization of the system (Carp et al. 2003). Thermal analysis was performed on the HESO-400, as shown in Fig. 5.2 (b). In zone I, the weight loss of $\approx 2\%$ below $100^\circ C$ in TGA and an endothermic response in DSC at $\approx 74^\circ C$ are dedicated to the elimination of moisture, and $\approx 5\%$ below $250^\circ C$ is the removal of residual carbon products and adsorbed oxygen (Worku et al. 2021). No significant change is observed post- $300^\circ C$ in zone II, which indicates the stabilization of the system and can be further confirmed by structural analysis. The summary of all the thermal events in the precursor gel with an increase in temperature from TGA and DSC is summarised in table 5.1.

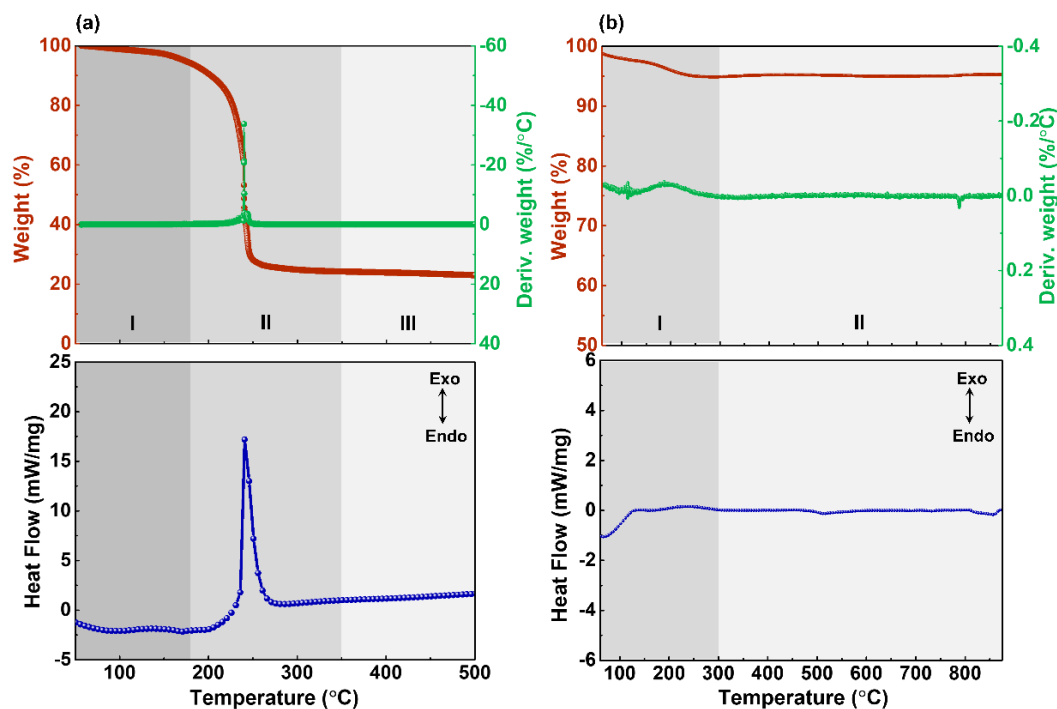


Fig. 5.2. The (a) weight loss (TGA and DTG) and (b) heat flow (DSC) of (CoMnNiFeCr)O precursor gel and (c) TGA and DTG and (d) DSC of HESO-400.

Table 5.1. Summary of thermal events in the (CoMnNiFeCr)O precursor gel and HESO-400 with an increase in temperature from TGA and DSC.

Materials	Zones	Temperature interval (°C)	Weight loss (%)	Reason
Precursor gel	I	30 – 175	1.9	Evaporation of solvent
	II	350 – 500	73	Destruction, ignition, and combustion of precursor gel.
	III	290 – 350	3	Removal of residual carbon remnant.
HESO-400	I	50 – 300	7	Elimination of moisture adsorbed and residual carbon remnant
	II	300 – 870	0.1	The stabilization of the system

5.3.2 Structural, compositional, and morphological analysis

Elevated properties result from diverse oxidation states of elements and the entropy stabilization effect of HESO. Therefore, a study on the phase stabilization of HEO is extremely important. In order to identify the phase formed, (CoMnNiFeCr)O powders (HESO-400 to HESO-1000) were subjected to XRD characterization. The XRD patterns of the synthesized (CoMnNiFeCr)O powders, HESO-400 to HESO-

1000, are presented in Fig. 5.3 (a). It is noticeable that the HESO-500 has diffraction peaks of planes (311) and (440) that correspond to the cubic spinel phase, with weak and broadened reflections indicates the beginning of crystallization. While few diffraction peaks of the cubic spinel phase with planes like (111), (220), (222), (400), (422), and (511) are not visible due to poor crystallinity, can be ascribed to the deficiency of adequate thermal energy to crystallize at ≤ 500 °C. Subsequently, with an increase in temperature (600 °C – 1000 °C), all planes started evolving, and the diffraction peaks became more fine, narrow, intense, and sharper with low and flat backgrounds, signifies an enhancement in crystallinity. The diffraction peaks in the XRD pattern correspond to the standard ICDD file of FeCr_2O_4 (ICDD: 00–034–0140) and exhibit a single-phase, face-centered cubic (fcc) spinel structure with an $Fd-3m$ space group. Thus, 500 °C (HESO-500) is considered to be the phase stabilization temperature of the synthesized HESO as the crystallization of the spinel phase is visible. Therefore, (CoMnNiFeCr)O powder stabilized at low temperature. Diffraction peaks concerning impurities or other phases are not detectable, specifies the high purity of the (CoMnNiFeCr)O. Simultaneously, zoomed X-ray diffraction patterns at 2θ equal to 35° - 38° , which represent the major peak of the system, are shown in Fig. 5.3 (b). A non-significant slight peak shift towards the left is observed and is attributed to the lattice expansion with an increase in temperature (Teng et al. 2021). Moreover, the lattice expansion was further supported by the lattice parameter as a function of temperature, as shown in Fig. 5.3 (c). The information of lattice parameter ‘ a ’ for the cubic system is extracted from the XRD using equation 3.2 and Cohen’s method (equations 3.3 and 3.4). The lattice parameter estimated from equations 3.2 – 3.4 equals ≈ 8.34 Å (HESO-1000). The lattice parameter slightly increases from 8.29 to 8.34 Å with an increase in temperature 500 °C – 1000 °C and can be attributed to cationic disorder, variation of ionic radius, and electronegativity of elements present (Pažik et al. 2015) and interaction between various defect-related dipoles (Teng et al. 2021; Tian et al. 2015).

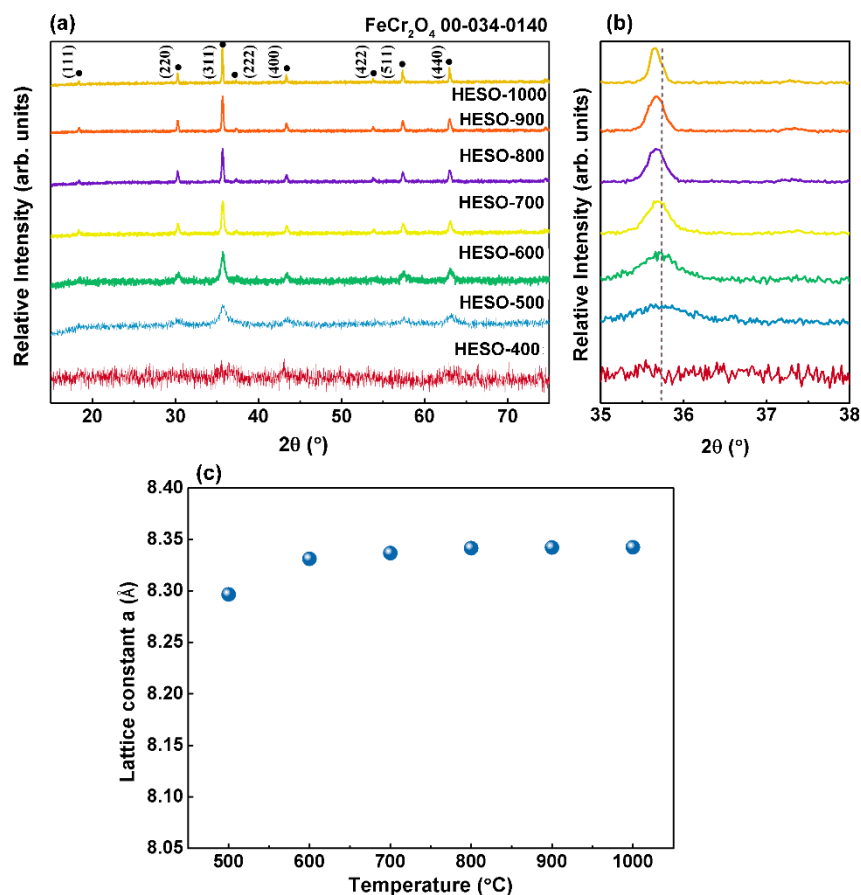


Fig. 5.3. (a) X-ray diffraction patterns of HESO-400 to HESO-1000, (b) corresponding zoomed X-ray diffraction patterns at 2θ equal to $35^\circ - 38^\circ$, (c) constancy of lattice parameter with an increase in temperature.

Table 5.2. Summary of the lattice parameter of $(\text{CoMnNiFeCr})\text{O}$ with an increase in temperature.

Temperature ($^\circ\text{C}$)	$a = \frac{(h^2+k^2+l^2)^{1/2}}{d}$ (\AA)	Cohen's method a (\AA)
500	8.27	8.29
600	8.28	8.33
700	8.305	8.34
800	8.305	8.34
900	8.32	8.34
1000	8.31	8.34

Furthermore, HESO-1000 is compared and analysed with individual parent oxide systems sintered at 1000°C . The XRD patterns of the individual parent oxides are presented in Fig. 5.4 (a). It is noticeable that the individual parent oxides Co-O, Mn-O,

Ni-O, Fe-O, and Cr-O have diffraction peaks that correspond to the cubic spinel Co_3O_4 , a mixture of tetragonal Mn_3O_4 and cubic Mn_2O_3 , cubic NiO, hexagonal Fe_2O_3 and hexagonal Cr_2O_3 . The details of the diffraction peaks, standard ICDD file number, crystal structure, and lattice parameters which correspond to the individual oxides are provided in table 5.3. Co-O is the only parent metal oxide with a crystal structure similar to HESO-1000 (Maiyalagan et al. 2014). Hence, $(\text{CoMnNiFeCr})\text{O}$ incorporated its structure from the Co-O parent oxide. Simultaneously, zoomed X-ray diffraction patterns at 2θ equal to $32^\circ - 38^\circ$ represent each system's major peak, as shown in Fig. 5.4 (b). A slight shift in the peak of HESO-1000 towards the left is observed compared to Co-O parent oxide (Co_3O_4). This shift can be attributed to the lattice expansion (Teng et al. 2021), cationic disorder, variation of ionic radius and electronegativity of elements present (Paçik et al. 2015), interaction between various defect-related dipoles (Tian et al. 2015) in HESO-1000. In addition, no single peak of other individual parent oxides Mn-O, Ni-O, Fe-O, and Cr-O matched with HESO-1000, as observed in Fig. 5.4 (a). This confirms that HESO-1000 belongs to the cubic spinel family as that of Co-O. For further comparison, the information of lattice parameters ' a and c ' is extracted from the XRD for the cubic system, tetragonal, and hexagonal systems. The information of lattice parameters ' a ' and ' c ' for the tetragonal is calculated as follows.

$$\frac{1}{d^2} = \frac{h^2+k^2}{a^2} + \frac{l^2}{c^2} \quad (5.2)$$

Where $d = \lambda/2 \sin \theta$, and θ is the half of the Bragg reflection angle, $\lambda = 1.5406 \text{ \AA}$ is the wavelength for Cu- K_α radiations. The information of lattice parameters ' a and c ' for the cubic and hexagonal systems is calculated using equations 3.2 and 3.5, respectively. Cohen's method was used to calculate the more accurate lattice parameters ' a ' and ' c '. The dominating phase in every parent oxide is considered for the calculation of the lattice parameters. The precise lattice parameter ' a ' of Co-O and Ni-O is calculated using equations 3.3 – 3.4, while precise lattice parameter ' a ' and ' c ' for hexagonal Fe-O and Cr-O is calculated using equations 3.6 – 3.8 and lattice parameter ' a ' and ' c ' for tetragonal Mn-O is calculated using the following relations:

$$A\Sigma\alpha^2 + B\Sigma\alpha\gamma + C\Sigma\alpha\delta = \Sigma\alpha\text{Sin}^2\theta \quad (5.3)$$

$$A\Sigma\alpha\gamma + B\Sigma\gamma^2 + C\Sigma\gamma\delta = \Sigma\gamma\sin^2\theta \quad (5.4)$$

$$A\Sigma\alpha\delta + B\Sigma\gamma\delta + C\Sigma\delta^2 = \Sigma\delta\sin^2\theta \quad (5.5)$$

where $A = \lambda^2/4a^2$, $B = \lambda^2/4c^2$, $C = D/10$, $\alpha = h^2 + k^2$, $\gamma = l^2$, and $\delta = 10\sin^2\theta$. The results are summarized in table 5.4. Fig. 5.4 (c) displays the lattice parameter of individual parent oxide and HESO-1000 (here, Cohen's data is used). As visible, Co-O is the only parent oxide that has a lattice parameter slightly near to HESO-1000 with a difference of 0.34 Å. As mentioned earlier, this can be attributed to the similar cubic spinel structure of Co_3O_4 and HESO-1000 (Maiyalagan et al. 2014).

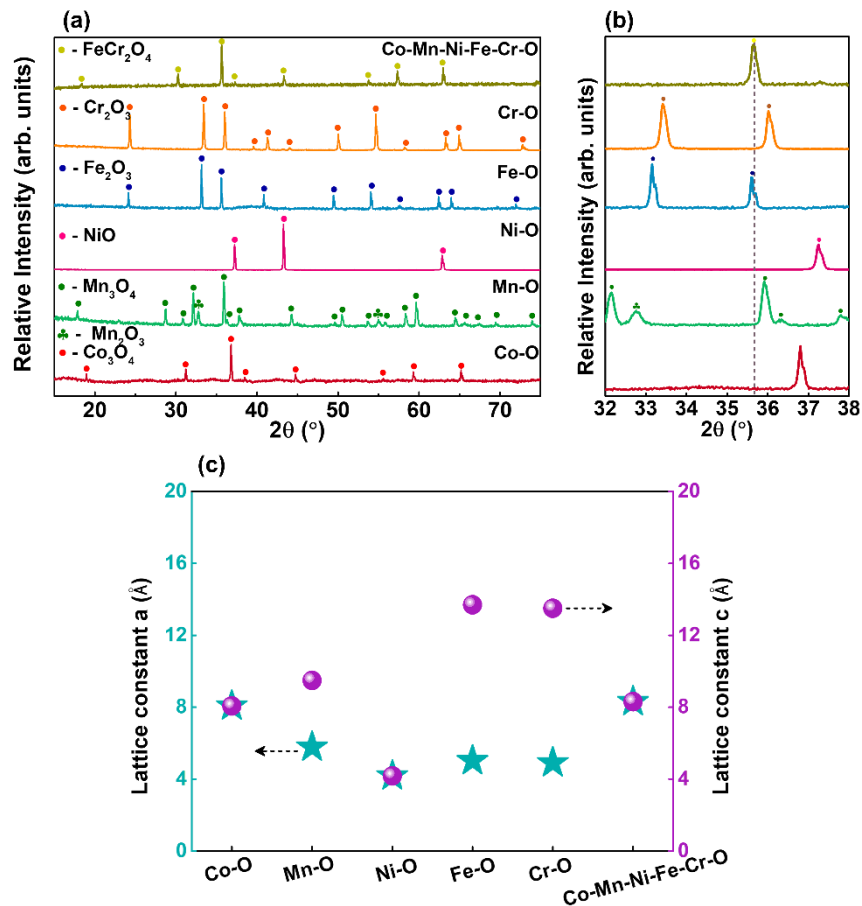


Fig. 5.4. (a) X-ray diffraction patterns of respective parent metal oxides Co-Mn-Ni-Fe-Cr-O (HESO-1000), Co-O, Mn-O, Ni-O, Fe-O, and Cr-O, (b) zoomed XRD at 2θ 32° - 38° represent the major peak of the system, (c) change in lattice parameter.

Table 5.3. Details of the diffraction peaks, standard ICDD file number, crystal structure, and lattice parameters corresponding to the individual oxides.

System	Oxides	ICDD file	Crystal structure	Lattice parameter of major phases
Co-O	Co ₃ O ₄	00-042-1467	Cubic Fd-3m 227	$a = 8.09 \text{ \AA}$ (Cubic Fd-3m 227)
Mn-O	Mn ₃ O ₄ and Mn ₂ O ₃	00-024-0734 and 00-041-1442	Tetragonal I41/amd and Cubic Ia-3 206	$a = 5.89 \text{ \AA}$ and $c = 9.71 \text{ \AA}$ (Tetragonal I41/amd)
Ni-O	NiO	00-047-1049	Cubic Fm-3m 225	$a = 4.18 \text{ \AA}$ (Cubic Fm-3m 225)
Fe-O	Fe ₂ O ₃	00-033-0664	Rhombohedral R-3c 167	$a = 5.02 \text{ \AA}$ and $c = 13.7 \text{ \AA}$ (Rhombohedral R-3c 167)
Cr-O	Cr ₂ O ₃	00-006-0504	Rhombohedral R-3c 167	$a = 4.9 \text{ \AA}$ and $c = 13.5 \text{ \AA}$ (Rhombohedral R-3c 167)

Table 5.4. Summary of the lattice parameter of individual parent oxides and HESO-1000.

Temperature (°C)	a (Å)	c (Å)	Cohen's method	
			a (Å)	c (Å)
Co-O	8.07	8.07	8.09	8.09
Mn-O	5.78	9.49	5.89	9.71
Ni-O	4.18	4.18	4.18	4.18
Fe-O	5.03	-	5.02	13.7
Cr-O	4.9	13.6	4.9	13.5
Co-Mn-Ni-Fe-Cr-O	8.31	8.31	8.34	8.34

A similar study is performed by reducing the number of cations from five to lower values (4, 3, 2, and 1) and estimating the variation in the lattice constant 'a'. The XRD patterns of the HESO-1000 (Co-Mn-Ni-Fe-Cr-O) and lower cation system (Co-Mn-Ni-Fe-O, Co-Mn-Ni-O, Co-Mn-O, and Co-O) are presented in Fig. 5.5 (a). The diffraction peaks in the XRD pattern of Co-Mn-Ni-Fe-O correspond to the standard ICDD file of FeCr₂O₄ 00-034-0140, similar to HESO-1000, whereas the XRD pattern of Co-Mn-Ni-O and Co-Mn-O correspond to MnCo₂O₄ 00-023-1237. The major peaks of the lower

cation systems also exhibit a single-phase, face-centered cubic (fcc) spinel structure with an $Fd-3m$ space group. Secondary phases were detected in all the lower cation systems Co-Mn-Ni-Fe-O, Co-Mn-Ni-O, and Co-Mn-O. Therefore, it can be assumed that the presence of a secondary phase in the lower cation system and the display of single-phase in HESO-1000, both indicates the role of configurational entropy in phase stabilization. Simultaneously, zoomed X-ray diffraction patterns at 2θ equal to $35^\circ - 38^\circ$, represents the major peak of the system, are shown in Fig. 5.5 (b). The peak shift toward the left is observed and is attributed to the lattice expansion with an increase in the number of cations (Teng et al. 2021). Moreover, the lattice expansion was further supported by the lattice parameter as a function of the number of cations in the system, as shown in Fig. 5.5 (c) (here, Cohen's data is used). The information of lattice parameter ' a ' for the cubic system is extracted from the XRD using equation 3.2 and Cohen's method (equations 3.4 – 3.3). The lattice parameter increased from 8.09 to 8.34 Å with an increased number of cations and can be attributed to cationic disorder, variation of ionic radius, and electronegativity of elements present (Pażik et al. 2015) and lattice expansion with an increase in the number of cations.(Teng et al. 2020, 2021) In addition, according to Bragg Law, (Bragg et al. 1913), similar to HESO-1000, a shift in peak to low angle and increase in lattice parameter indicates an effective entry of the solid solution atoms into the lattice to some extent.

Table 5.5. Summary of the lattice parameter of lower cation system and HESO-1000.

Temperature (°C)	$a = \frac{(h^2+k^2+l^2)^{1/2}}{d}$ (Å)	Cohen's method a (Å)
Co-O	8.07	8.09
Co-Mn-O	8.25	8.25
Co-Mn-Ni-O	8.26	8.31
Co-Mn-Ni-Fe-O	8.32	8.34
Co-Mn-Ni-Fe-Cr-O	8.31	8.34

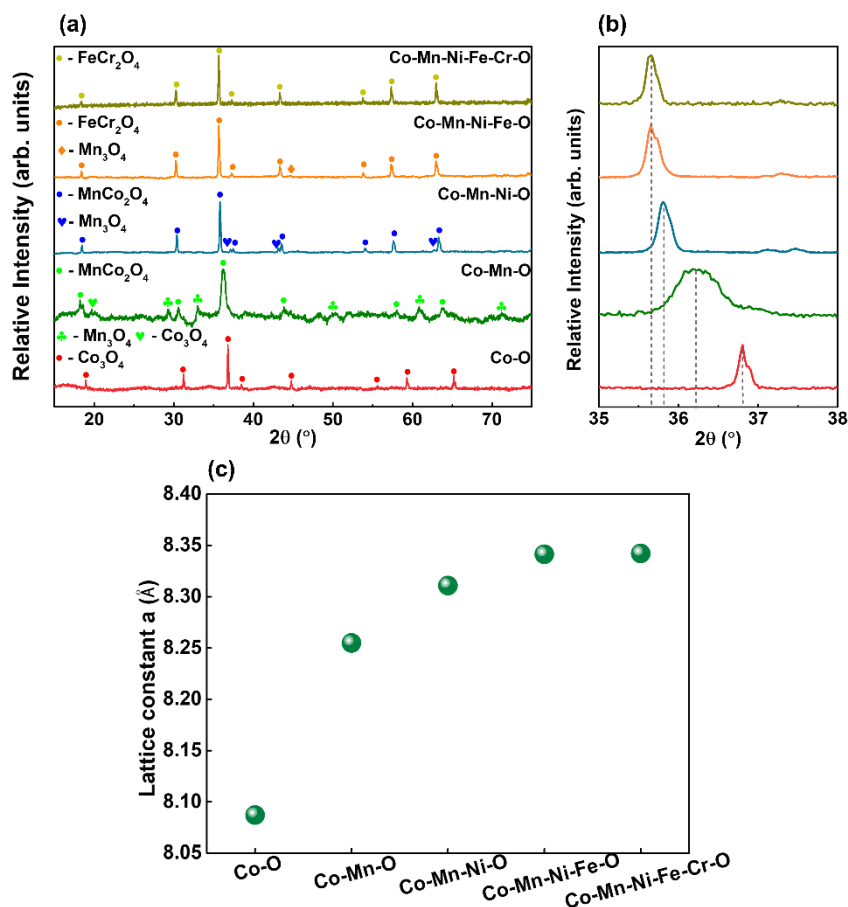


Fig. 5.5. (a) X-ray diffraction patterns of lower cation systems Co-Mn-Ni-Fe-Cr-O (HESO-1000), Co-Mn-Ni-Fe-O, Co-Mn-Ni-O, Co-Mn-O and Co-O, (b) zoomed XRD at 2θ $35^\circ - 38^\circ$ represent the major peak of the system, (c) change in lattice parameter.

To understand the molecular vibration happening within the HESO, Raman, and FTIR spectroscopy were used. The Raman spectra of HESO-400 to HESO-1000, as shown in Fig. 5.6 (a), reveal four main bands at 166, 300, 497, and 677 cm^{-1} . The bands are in good agreement with the reported Fe₃O₄ (Kumar et al. 2014), Co₃O₄ (Diallo et al. 2015), and chromites, ferrites, and other spinels (D’Ippolito et al. 2015). Based on the literature mentioned earlier, the bands at 166, 300, 497, and 677 cm^{-1} can be attributed to Raman active modes of F_{2g}(1), E_g, F_{2g}(2), and A_{1g}, respectively (Dąbrowa et al. 2018). A shoulder peak at 628 cm^{-1} is observed with respect to the A_{1g} active mode. Thus, the fingerprints of the Raman spectrum indicate the occupancy of metal cations with +2 (M²⁺) and +3 (M³⁺) oxidation likely to be in tetrahedral and octahedral sites. The F_{2g}(1) active mode at 166 cm^{-1} appeared due to the translation movement of the tetrahedral metal-oxygen bond, whereas the F_{2g}(2) at 497 cm^{-1} is ascribed to the

stretching vibration of octahedral sublattice (M^{3+} -O) and asymmetric stretching of the octahedral metal-oxygen bond. The E_g active mode at 300 cm^{-1} is attributed to the symmetric bending of oxygen in tetrahedral coordination with the divalent metal ion (M^{2+} -O). Finally, in spinel, the A_{1g} active mode at 677 cm^{-1} is ascribed to the local lattice effect observed in the sublattice of the tetrahedral site and symmetric stretching of metal-oxygen bond in tetrahedral coordination (M^{2+} -O), which affirms a complete disordered occupancy of various metal cations in the tetrahedral site (D'Ippolito et al. 2015; Phakatkar et al. 2021). A slight variation in the shape of all the Raman peaks with the temperature rise may be due to the optical phonon confinement in the case of nanomaterials, change in the grain size, variation in ionic radii, and states of multiple cations and lattice expansion as confirmed from XRD (Bhardwaj et al. 2022; D'Ippolito et al. 2015; Talluri et al. 2022; Teng et al. 2020). The successful synthesis of (CoMnNiFeCr)O with the disordered occupancy of multiple cations (Co, Mn, Ni, Cr, Fe, and Cr) in tetrahedral and octahedral sites of spinel structure is confirmed by the results of Raman spectroscopy. In contrast, the HESO-400 and HESO-1000 FTIR spectra are illustrated in Fig. 5.6 (b). In both spectra, the broad absorption ranges from $4000\text{-}3500\text{ cm}^{-1}$ correspond to the stretching vibration of the O-H bond (Ghalmi et al. 2019b; Wei et al. 2009). The band that appeared at 2885 cm^{-1} in HESO-400 and 2896 cm^{-1} in HESO-1000 correspond to the asymmetric and symmetric stretching C-H stretching vibrations due to the organic compounds, respectively (Coates 2006). The transmittance peaks at 1615 cm^{-1} for HESO-400 and 1600 cm^{-1} for HESO-1000 were related to the H-O-H bending vibration modes (Wei et al. 2009). In HESO-400, two extra absorption peaks at 1380 cm^{-1} and 923 cm^{-1} are evident, which are assigned to C-H symmetric bending and stretching vibration and carbon impurities in the sample (Ghalmi et al. 2019b; Rajith Kumar et al. 2020). The vanishing of characteristic bands related to C-H vibrations in HESO-1000 uncovered that they were from the fuel urea consumed during the heat treatment at high temperature. Finally, the broad absorption ranges from $750\text{ - }400\text{ cm}^{-1}$ in HESO-400 and HESO-1000 correspond to the metal-oxygen (M-O) ($M = \text{Co, Cr, Fe, Mn, Ni}$) stretching vibration mode. This broadening can be imputed to the presence of many cations in the lattice as each would arise in diverse relation behavior (Wei et al. 2009). Thus, the formation of (CoMnNiFeCr)O is

evident in both spectrums, confirms the successful synthesis of low-temperature (CoMnNiFeCr)O, in addition to the XRD results.

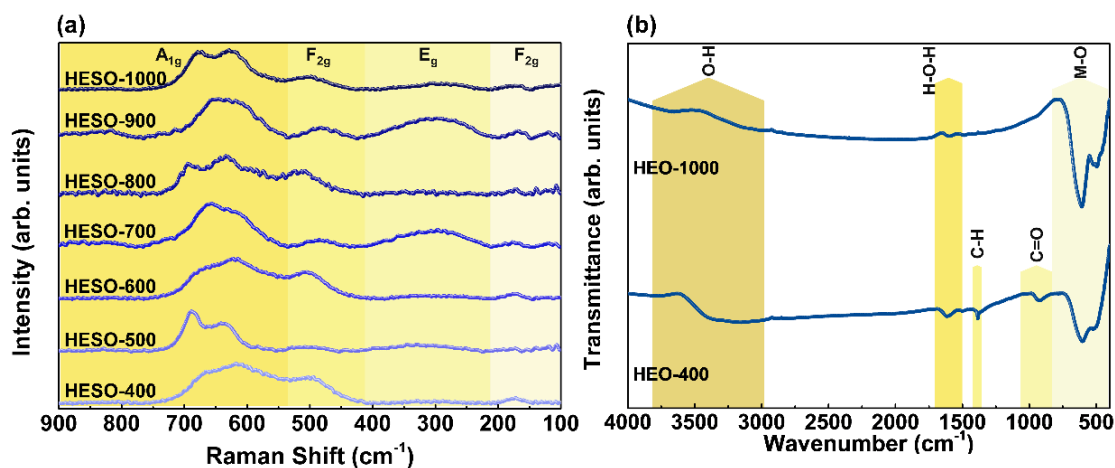


Fig. 5.6. (a) Raman spectra of HESO-400 to HESO-1000, and (b) FTIR spectra of HESO-400 and HESO-1000.

The heat treatment process increases the grain size. Hence, a larger grain size will lead to a smaller grain boundary area, which has a direct consequence in dielectric nature and leakage current behavior. Thus, it is essential to know (CoMnNiFeCr)O grain size distribution and morphology. Therefore, FE-SEM is utilized to reveal the morphologies and elemental distribution of the synthesized (CoMnNiFeCr)O. The (CoMnNiFeCr)O heat treated at all temperatures was examined to comprehend the effects of heat treatment, as evidenced in Fig. 5.7 (a-g). (CoMnNiFeCr)O displays excellent sinterability with the agglomerations of nano-sized particles which has irregularly shaped particles, and grain growth is observed with the increment in temperature (Dąbrowa et al. 2018). The heat treatment removes the carbonaceous impurities and promotes sintering which results in the formation of larger grain. Grain boundary can be observed clearly with minute traces of pores throughout HESO-700 to HESO-1000. Using ImageJ software, the average grain size of HESO-600 to HESO-1000 powders, is calculated and found to be increase from 9.25 ± 0.24 nm, 28.8 ± 11.42 nm, 55.05 ± 0.49 nm, 111.79 ± 4.35 nm to 142 ± 0.17 nm respectively. Fig. 5.7 (i) depicts the grain size distribution graph with temperature respectively. The distribution curve for 600 °C, 700 °C, 800 °C, 900 °C, and 1000 °C is provided in Appendix III (Fig. I), where the curve follows Gaussian fit. The EDS of HESO-1000 (Fig. 5.6 (h))

displays a homogenous distribution of all five cations, with a near-equiatomic percentage composition of the five elements (Co - 6 %; Mn - 8 %, Ni - 6 %; Fe - 6 %; Cr - 8 %), confirming the equimolar contribution of the cations in (CoMnNiFeCr)O. The mapping of all the elements of HESO-1000 displays the distribution of elements without any segregation and is provided in Appendix III in Fig. II.

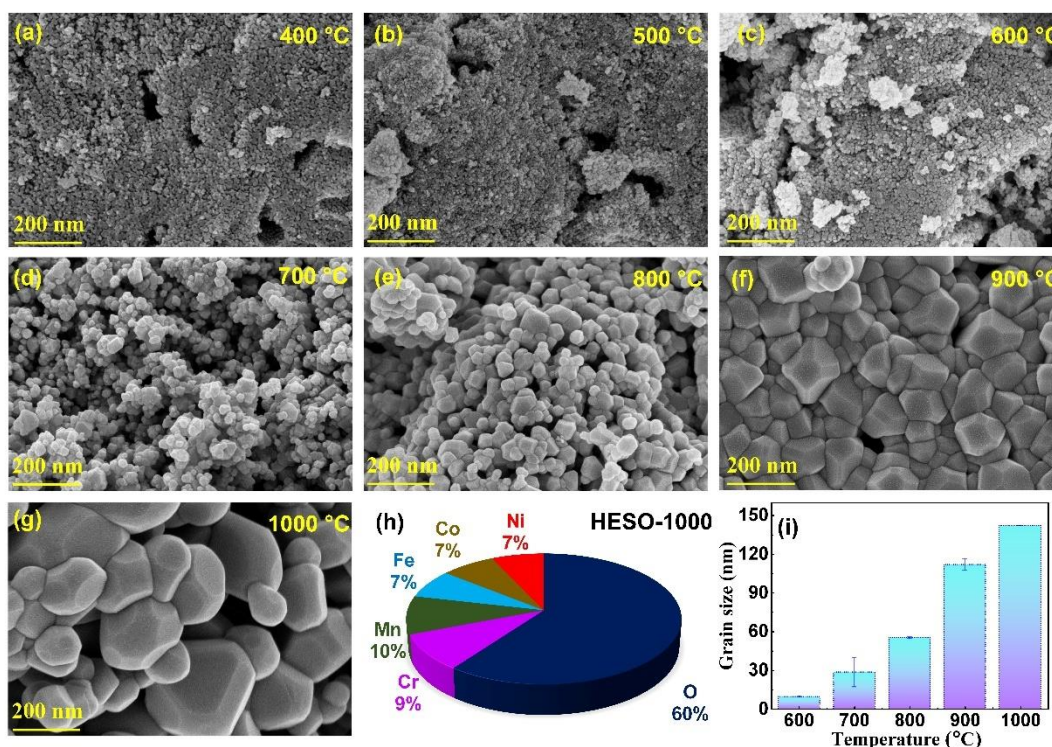


Fig. 5.7. (a-g) The surface morphology of HESO-400 to HESO-1000 displays a grain growth with temperature rise, (h) the pie chart indicating the elemental distribution of all five cations in HESO-1000 extracted from EDS, and (i) grain size distribution graph of particle diameter vs. temperature respectively.

To strengthen the analysis with regard to the impact of diverse oxidation states present in (CoMnNiFeCr)O, surface chemical compositions were analyzed using X-ray photoelectron spectroscopy (XPS) on HESO-1000. The five cations Co, Cr, Fe, Mn, and Ni, including other elements like C and O, were detected from the compositional analysis by XPS through a low-resolution survey scan in the range 0 – 1200 eV. The high-resolution spectra of all elements are displayed in Fig. 5.8; the spectra of HESO-1000 were calibrated using the carbon 1s (C 1s) spectrum positioned at 284.6 eV. The C 1s spectrum and the low-resolution survey scan are provided in Appendix III in Fig.

III (a and b). The fine scan of Co 2p XPS spectra of HESO-1000 is given in Fig. 5.8 (a), in which the peaks of Co 2p_{3/2} and Co 2p_{1/2} are located at around 778.9 eV and 794.6 eV and are ascribed to Co³⁺ respectively; a satellite peak centered at 787.67 eV is attributed to Co³⁺ oxidation state. The fitted peak for Co 2p_{3/2} and Co 2p_{1/2} at 783.87 eV and 800.97 eV is attributed to Co²⁺, respectively (Wang et al. 2019a). Nevertheless, according to the present multiple splitting, as shown in Fig. 5.8 (a), the Co ions were identified mainly as Co³⁺ by calculating the area of the synthetic peaks (Co²⁺/Co³⁺ = 0.53). The fine scan of Mn 2p XPS spectra, as shown in Fig. 5.8 (b), exhibits two main spin-orbit lines at binding energies of 639.94 eV and 651.66 eV, which correspond to Mn 2p_{3/2} and Mn 2p_{1/2}. The peaks centered at 639.94 eV, 643.22 eV (satellite peak of Mn 2p_{3/2}), and 651.66 eV are attributed to the Mn²⁺ (Biesinger et al. 2011; Wang et al. 2020f; Xiang et al. 2021c). As shown in Fig. 5.8 (c), the Ni 2p spectra were reasonably deconvoluted into six fitted peaks. The 853.02 eV and 870.62 eV peaks correspond to Ni²⁺ of Ni 2p_{3/2} and Ni 2p_{1/2} peaks. The fitted peak for Ni 2p_{3/2} and Ni 2p_{1/2} at 856.45 eV and 876.5 eV is attributed to Ni³⁺, respectively; two shake-up satellite peaks of Ni at 859.43 eV and 879.88 eV are attributed to Ni³⁺ oxidation state (Xiang et al. 2021c). According to the present multiple splitting, as shown in Fig. 5.8 (c), the Ni ions were recognized as Ni²⁺ in the majority by calculating the area of the synthetic peaks (Ni²⁺/Ni³⁺ = 6.94). In a fine scan of Fe 2p XPS spectra (Fig. 5.8 (d)), Fe 2p_{3/2} and Fe 2p_{1/2} peaks were centered at 709.01 eV and 721.9 eV, respectively, which was the feature of spin-orbit coupling. The Fe 2p spectra were deconvoluted, taking into account contributions from Fe²⁺, Fe³⁺, and satellite peaks. The Fe 2p peaks at binding energies 711.67 eV and 724.58 eV with a satellite signal at 717.43 eV were characteristic of Fe³⁺, while the peaks at 709.01 eV and 721.9 eV with a satellite signal at 714.54 eV were the characteristics of Fe²⁺ (Wang et al. 2019a). However, according to the present multiple splitting, as shown in Fig. 5.8 (d), by calculating the area of the synthetic peaks, the Fe²⁺ was in the majority (Fe²⁺/Fe³⁺ = 2.97). Interestingly in the fine scan Cr 2p XPS spectra (Fig. 5.8 (e)), a higher Cr 2p_{3/2} peak located at 574.93 eV and a separate Cr 2p_{1/2} peak at 584.05 eV was observed. The fitted peak for Cr 2p_{3/2} and Cr 2p_{1/2} is assigned to Cr³⁺ (574.39 eV, 576.6 eV, and 584.05 eV); while the peaks centered at 580 eV and 586.57 eV are ascribed to Cr⁶⁺ respectively (Biesinger et al. 2011)(Soe et al. 2020). However, the Cr ions were identified mainly as Cr³⁺ by calculating the area of

the synthetic peaks ($\text{Cr}^{3+}/\text{Cr}^{6+} = 10.56$). Fig. 5.8 (f) shows four oxygen peak contributions of the O 1s region of the (CoMnNiFeCr)O. The peak at 527.99 eV is typical for a metal-oxygen peak (lattice oxygen), the peak at 529.42 eV corresponds to O^{2-} (oxygen vacancy), the peak at 530.27 eV denotes surface metal hydroxide, the peak at 531.39 eV is the weakly bound adsorbed oxygen from the medium on the (CoMnNiFeCr)O surface respectively (Biesinger et al. 2011; Lou et al. 2020). The contribution of oxygen vacancy is 20.8 % by calculating the area of the synthetic peaks. According to the XPS results, the Co^{3+} , Mn^{2+} , Ni^{2+} , Fe^{2+} , and Cr^{3+} ions are the dominating states in the system, respectively, as tabulated in table 5.6.

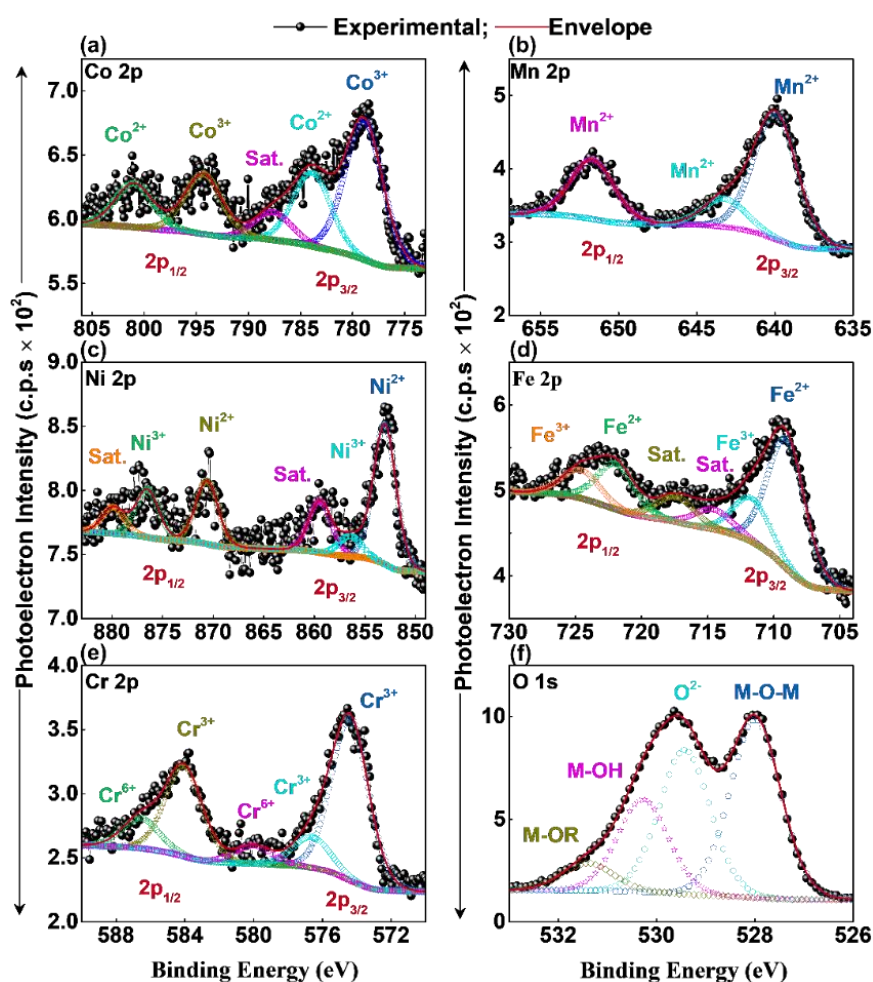


Fig. 5.8. Analysis of the chemical composition of the HESO-1000 using X-ray photoelectron spectroscopy. High-resolution deconvoluted spectra of core level (a) Co 2p, (b) Mn 2p, (c) Ni 2p, (d) Fe 2p, (e) Cr 2p and (f) O 1s depicting their respective oxidation states.

Table 5.6. Summary of the percentage area contribution of deconvoluted peaks in cations.

Deconvoluted peak ratio	Area ratio
Co ²⁺ /Co ³⁺	0.53
Mn ²⁺ /Mn ³⁺	1
Ni ²⁺ /Ni ³⁺	6.94
Fe ²⁺ /Fe ³⁺	2.97
Cr ³⁺ /Cr ⁶⁺	10.56

5.3.3 Dielectric constant of sintered (CoMnNiFeCr)O capacitor

The dielectric study is performed on the capacitor developed using the (CoCrFeMnNi)O pellet, as shown in Fig. 5.9 (a). The pellet is sintered at 1000 °C and displays excellent sinterability with no pores, as observed in Fig. 5.9 (b). To further confirm the constituent elemental distribution in the (CoMnNiFeCr)O pellet, an EDS was performed, as shown in Fig. 5.9 (c), which displayed the homogenous distribution of all five cations with the atomic percentage of the five elements being very nearby (Co – 0.7 %; Mn – 0.7 %, Ni – 0.8 %; Fe – 0.7 %; Cr – 0.8 %) as observed in HESO-1000. As mentioned earlier, the (CoMnNiFeCr)O pellet may result in good dielectric performance due to the entropy-driven stabilization effect of (CoMnNiFeCr)O, large grain surface area, and low leakage current attributed to good sintering and negligible pores. Fig. 5.9 (d) depicts the room temperature measured dielectric constant (κ) and dielectric loss ($\tan \delta$) of the sample as a function of frequency. The κ measured with an impedance analyzer at room temperature at a very low-frequency 20 Hz reaches its maximum value close to 3×10^3 . Besides, κ at a frequency range of 1 kHz – 100 kHz is $\approx 10^2$, which is of high dielectric constant value compared to other metal oxides applicable as a gate oxide in transistors or capacitors (Young and Frederikse 1973). Therefore, the impact of the entropy-driven stabilization effect of HEO is clearly observed. The $\tan \delta$ remains very small, as low as 0.002 at 20 Hz, signifies the use of HESO in energy storage applications, but the same $\tan \delta$ gradually increases up to 0.6 at 1 MHz. Simultaneously, impedance analysis is helpful to comprehend the dielectric behavior of the HESO-1000 (Ali et al. 2015). Fig. 5.9 (e) shows a plot of the real (Z') and imaginary (Z'') parts of complex impedance (Z) as a function of frequency measured at room temperature. A monotonic decrease in Z' and an increase in Z'' with

the rise in frequency attributed to the presence of the space charge effect at low frequency and less relaxation time for the space charge at high frequency (Ali et al. 2015). In addition, the magnitude of Z' decreases due to the reduced density of trapped charges and the improvement of immobile species at low frequencies (Sujatha et al. 2013). The complex electric modulus (M^*) which is considered as one of the most renowned and effective parameters, is used to study the electrical response and electrical relaxation in dielectric material. The real (M') and imaginary (M'') part of the electric modulus as a function of frequency at room temperature is showcased in Fig. 5.9 (f), where both display similar behavior. The near-zero value at low frequency and a rise to the maximum value at a higher frequency range in M' plot signifies that the contribution of space charge polarization is maximum at low frequency (Padmasree et al. 2006).

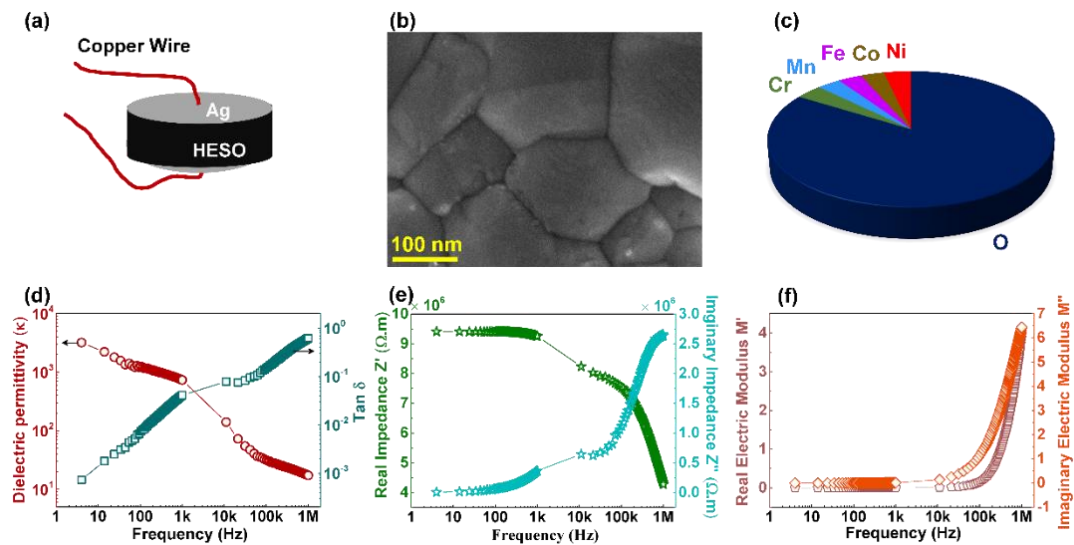


Fig. 5.9. (a) Schematic of the capacitor developed using (CoMnNiFeCr)O pellet sintered at 1000 °C, (b) the surface morphology of the (CoMnNiFeCr)O pellet sintered at 1000 °C and used for the development of capacitor, with admirable sinterability of the grain, and (c) the pie chart indicating the elemental distribution of all five cations in (CoMnNiFeCr)O pellet extracted from EDS, frequency dependence plots of the (d) dielectric constant (κ) and dielectric loss ($\tan \delta$), (e) real and imaginary part of the impedance (Z), (f) real and imaginary part of the electric modulus (M) measured at room temperature.

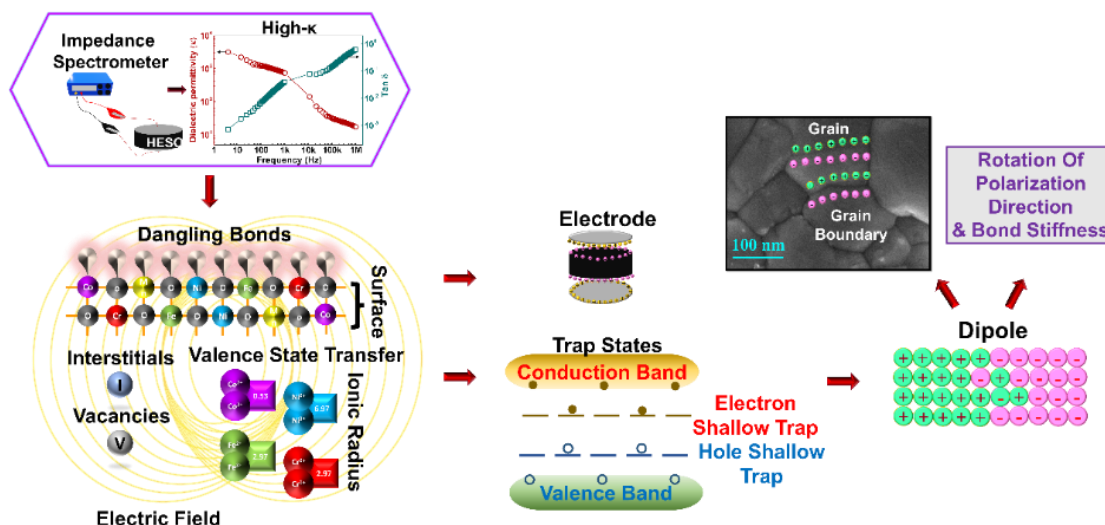


Fig. 5.10. Schematic depicting the interfacial polarization which occurs due to various reasons such as vacancies, interstitials, dangling bonds, grain, grain boundaries, rotation of vacancy, electrodes, valence state transfer, the capture of space charge by the trap states, and dipole formation when an electric field is applied in (CoMnNiFeCr)O resulting in high dielectric constant.

The display of high- κ in (CoMnNiFeCr)O as a function of frequency is observed, and Fig. 5.10 depicts the schematic which explains various reasons for high- κ . As observed in Fig. 5.9 (d), a decrease in the κ and an increase in $\tan \delta$ with an increase in frequency can be attributed to the reduction of space charge or interfacial polarization effect with a change in the electric field during the increase of frequency (Du et al. 2020). At low frequencies, large κ is governed mainly by electrode polarization. The high number of space charges tends to accumulate at the (CoMnNiFeCr)O-electrode interface and leads to large polarization, as depicted in Fig. 5.10 (Bérardan et al. 2016b). In addition, the structural inhomogeneity formed due to the large surface-to-volume ratio of grains, as shown in Fig. 5.9 (b), and point imperfections like vacancies, dangling bonds, and micropores at the grain boundaries allows the accumulation of charges at interfaces to result in interfacial polarization as shown in schematic representation Fig. 5.10 (Bérardan et al. 2016b; Du et al. 2020). On the other hand, when an electric field is enforced, the space charge moves, and the defects trap them, which ensures the formation of a dipole moment. As HESO-1000 possess oxygen ion vacancies, as seen in the XPS result, they may form dipoles as they are equivalent to positive charges. When exposed to an electric field, the dipole created by the oxygen vacancies may

rotate, which gives a resultant dipole moment in the direction of the applied electric field, as shown in Fig. 5.10. Furthermore, as the frequency is increased, interfacial polarization gets relaxed due to high energy electrons, less relaxation time, and faster recombination of the space charge, and then the electronic and ionic polarization becomes dominant (Raymond et al. 2006b). Thus, the reason for large κ at higher frequencies is due to combined effects from electronic and ionic polarizations; the larger radii cations in (CoMnNiFeCr)O (Co: 79 pm (+2) and 68.5 pm (+3), Mn: 81 pm (+2), Ni: 83 pm (+2) and 70 pm (+3), Fe: 75 pm (+2) and 69 pm (+3), Cr: 75.5 pm (+3) and 58 pm (+6) and O: 126pm) can be electronically polarized easily compared to the small radii ions (Bérardan et al. 2016b). However, the bond stiffness of M-O, where M represents cations of (CoMnNiFeCr)O, promotes ionic polarizability. Five distinct cations offer a large spectrum of bond stiffnesses, thus promotes ionic polarization. These parameters are considered effective at higher frequencies; therefore, a large κ has been observed. Hence, the high- κ value of (CoMnNiFeCr)O can be attributed to the entropy stabilization effect of (CoMnNiFeCr)O and the combination of interfacial, ionic, and electronic polarization with the rise in frequency.

5.4 Conclusion

The dielectric constant of the sintered (CoMnNiFeCr)O capacitor made of Co, Cr, Fe, Mn, and Ni (i.e., (CoCrFeMnNi)O) and produced via solution combustion synthesis was examined. Phase stabilization in HESO is crucial since it directly affects the characteristics. In-depth investigations of thermal, structural, morphological, and compositional analyses are conducted to investigate phase stability. Thermal analysis displayed combustion of the precursor gel at 240 °C with urea served as fuel. The XRD patterns of the (CoMnNiFeCr)O exhibited a single-phase, fcc spinel structure with an *Fd-3m* space group, and 500 °C was considered to be the phase stabilization temperature of the synthesized (CoMnNiFeCr)O. A non-significant increase in the lattice parameter with an increase in temperature (up to 1000 °C) was attributed to cationic disorder, variation of ionic radius and electronegativity of elements present, and interaction between various defect-related dipoles. An increase in the crystallite size was observed with an increase in temperature due to improved atomic diffusion. (CoMnNiFeCr)O displayed one of its parent oxide Co-O structural properties as both belong to the cubic

spinel family, and the change of solvent did not hamper the phase stabilization of (CoMnNiFeCr)O. The XRD results of lower cation systems exhibited a spinel structure with the presence of secondary phases and confirmed the effect of configurational entropy on phase stabilization. Simultaneously, the increment in the lattice parameter could be attributed to the addition of cations with varied ionic radius and the electronegativity of elements present in the high-entropy spinel system. (CoMnNiFeCr)O powder formed a pentagon-hexagonal shaped morphology, and with temperature, the average grain size increased from 9.25 ± 0.24 nm to 142 ± 0.17 nm. The dielectric measurements showed high dielectric constant (κ) $\sim 1.2 \times 10^3$, 7.3×10^2 , and 3.1×10^1 at 100, 1k, and 100k Hz at room temperature. The high- κ was attributed to the combined effect of entropy-driven stabilization effect, accumulation of space charge at the interface, structural inhomogeneity, accumulation of charge at grain boundaries due to point imperfections, rotation of oxygen vacancy, the difference in the ion radii and variation in the bond stiffness between the metal and oxygen.



CHAPTER 6

APPLICATION OF LOW-TEMPERATURE SOLUTION COMBUSTION PROCESSED HIGH ENTROPY SPINEL OXIDE (CoMnNiFeCr)O IN THIN FILM TRANSISTORS

The contents of this chapter have been published in the article:

Ashritha Salian, Pavan Pujar, Robbi Vivek Vardhan, Haewon Cho, Sunkook Kim, Saumen Mandal, **ACS Appl. Electron. Mater.**, 5(5), 2608-2623, (2023).

Page left intentionally blank

CHAPTER 6

APPLICATION OF LOW-TEMPERATURE SOLUTION COMBUSTION PROCESSED HIGH ENTROPY SPINEL OXIDE (CoMnNiFeCr)O IN THIN FILM TRANSISTORS

6.1 Introduction

The bulk and thin films have a distinct mechanism of combustion. In bulk, combustion occurs in all directions; hence, more mass is combusted every time. However, on the contrary, in the case of thin films, combustion movement is not yet visually experienced. The kinetics of combustion is different in both cases because of high surface-to-volume ratio in bulk results in the easy removal of gases produced during combustion at the nanoscale level (Pujar et al. 2020; Varma et al. 2016). Hence, it is important to investigate the phase stabilization of HEO in both architecture, bulk as well as thin film. Bulk is explored in previous chapters, and $(\text{Co}_{0.2}\text{Mn}_{0.2}\text{Ni}_{0.2}\text{Fe}_{0.2}\text{Cr}_{0.2})\text{O}_{1.2-\delta}$ was found to have low phase stabilization temperature and good dielectric properties. In this chapter, the optimized parameters of bulk- $(\text{CoCrFeMnNi})\text{O}$ powder and sintered $(\text{CoCrFeMnNi})\text{O}$ capacitor, as discussed in Chapter 5, are now implemented on solution combustion processed $(\text{CoCrFeMnNi})\text{O}$ thin film and are integrated into thin film transistors (TFTs) with molybdenum disulfide (MoS_2) channel for the first time, which bridges the gap between the HEO and electronics. A systematic derivation of the stoichiometric combustion reaction from sub-reactions of oxidation and reduction is depicted. In-depth thermal, structural, microstructural, and elemental analysis was made, which helped to draw a correlation between phase stabilization and transistor performances.

6.2 Experimental procedure

6.2.1 Formulation of combustible precursor

All reagents were of analytical-reagent grade and used as received without purification. The respective metal nitrates, namely, cobalt nitrate $[\text{Co}(\text{NO}_3)_2 \cdot 6\text{H}_2\text{O}]$; (99

% purity)], ferric nitrate [$\text{Fe}(\text{NO}_3)_3 \cdot 9\text{H}_2\text{O}$; (99 % purity)], nickel nitrate [$\text{Ni}(\text{NO}_3)_2 \cdot 6\text{H}_2\text{O}$; (98 % purity)], and urea [$\text{CH}_4\text{N}_2\text{O}$; (99.5 % purity)] were purchased from Molychem, India; chromium nitrate [$\text{Cr}(\text{NO}_3)_3 \cdot 9\text{H}_2\text{O}$; (99 % purity)] from Kemphasol, India; and manganese nitrate [$\text{Mn}(\text{NO}_3)_2 \cdot 4\text{H}_2\text{O}$; (99 % purity)] was obtained from Sigma Aldrich, India. All the metal nitrates and urea were individually dissolved in an organic solvent, 2-methoxy ethanol ($\text{C}_3\text{H}_8\text{O}_2$, 2-ME) separately, and kept in an airtight glass container at room temperature. All resulting solutions were mixed with maintained molarity of 0.2, under stirring to obtain a clear aqueous combustible precursor. The constant stirring at room temperature resulted in clear and homogeneous solutions. An organic solvent 2-ME is chosen for the thin film due to its high viscosity ($\eta = 1.375 \text{ mPa}\cdot\text{s}$ at 30°C) in comparison to water ($\eta = 0.7975 \text{ mPa}\cdot\text{s}$ at 30°C), which result in the thicker film. (Branquinho et al. 2014)

6.2.2 Deposition of HEO thin film and characterizations

To deposit a HESO film, the Si (p++) substrates were primarily sonicated with acetone, isopropyl alcohol, and D.I. water. The substrates were further subjected to UV-Ozonisation for 30 min, respectively. The synthesized combustible precursor with 2-ME as solvent was spin-coated at 3000 rpm for 30s onto the substrate, as shown in Fig. 6.1. Various spinning cycles were carried out (5, 10, and 15 times) with intermediate annealing. The final annealing of the film stack was carried out at 300, 400, and 500 °C for 2h. The resulting films were further used to fabricate thin film transistors (TFTs). The HESO thin film (HESOTF) spun 5, 10, and 15 times and annealed at different temperatures (300, 400, and 500 °C) will be symbolically represented as HESOTF-5-300/400/500, HESOTF-10-300/400/500, and HESOTF-15-300/400/500, respectively.

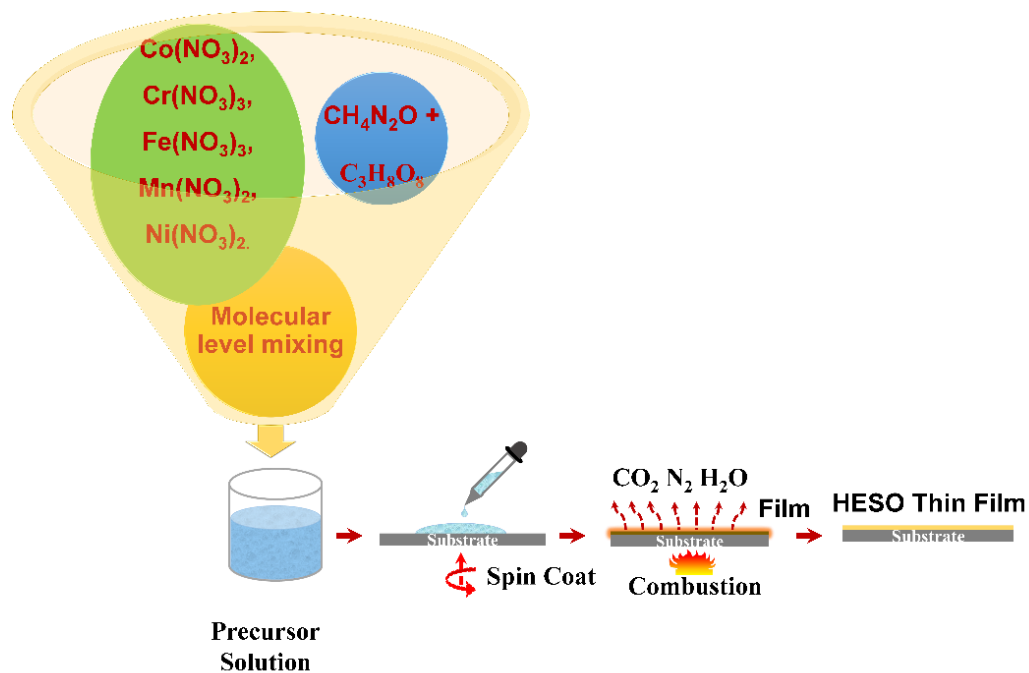


Fig. 6.1. Schematic of the synthesis process of (CoMnNiFeCr)O powder.

To understand the combustion behavior, precursor gel was collected during combustion and was subjected to thermal analysis using TGA (PerkinElmer, TGA 4000) and DSC (NETZSCH DSC 404 F1) with a heating rate of $10\text{ }^\circ\text{Cmin}^{-1}$. The phase structure of the HESOTF was characterized by grazing incidence X-ray diffraction (GIXRD- PANalytical multipurpose high-resolution XRD) at a grazing angle of 0.5° and scanning rate of $2^\circ/\text{min}$ with $\text{Cu K}\alpha$ (1.54 \AA) X-ray source. To study the morphology and elemental distribution, FE-SEM (Carl Zeiss AG model: GeminiSEM 300; JEOL: 7610FPLUS Japan) coupled with EDS at an accelerating voltage of 20 kV was used. The Raman spectra were recorded using the compact Raman spectrometer (Renishaw, UK) consists of a laser which was operated at 532 nm. Non-contact mode atomic force microscopy (AFM-Innova SPM) was used to find the surface roughness of the HEOTF. Surface chemical compositions for HEOSTF-15-500 were analyzed using XPS (Kratos Axis Ultra DLD). The monochromatic $\text{Al K}\alpha$ was used as the X-ray source for XPS. An ultra-vacuum system with a base pressure of $\sim 10^{-10}$ Torr is maintained. There could be contamination on surface of the film; hence, the interior of the film was analyzed after sputtering by the argon (Ar) bombardment for the 20s. The binding energy scale is mentioned in 'eV'. The received spectra were calibrated using the C-H peak of the

adventitious carbon positioned at 284.6 eV and the peak fit analysis of all five cations (Co 2p, Mn 2p, Ni 2p, Fe 2p, and Cr 2p) and oxygen 1s (O 1s) peaks were carried out using the product of Gaussian and Lorentzian functions with fixed G/L (30 %) ratio and FWHM of synthetic peaks fitted by the software. The FWHM of the synthetic peaks in the spectra of five metal cations and oxygen was constrained to be the same to avoid inconsistency in peak fitting. The peak fit analysis was performed using the CASAXPS 2.3.22PR1.0 software package.

6.2.3 Fabrication of HESO thin film MIM capacitor and thin film transistor

The HESOTF-15-500 was utilized for the fabrication of TFTs. Bottom gate top contact (BGTC) TFTs were fabricated. The semiconducting channel used in the present case was n-type MoS₂. MoS₂ is a transitional metal chalcogenide (TMC). This 2D semiconductor was mechanically exfoliated from the bulk crystal and carefully transformed into the Si/HESOTF samples. The process of mechanical exfoliation yields a few layers of MoS₂, and the randomly deposited flakes of MoS₂ are then subjected to the deposition of top electrodes. 20 nm of titanium (Ti) and 100 nm of gold (Au) were deposited and patterned using photolithography.

6.3 Results and discussion

6.3.1 Thermal decomposition analysis

The transformation of the precursor into a useful HEO product requires the initiation of the combustion reaction. The temperature at which the combustible precursors undergo exothermic reaction and yield HEO is termed combustion temperature. Fig. 6.2 depicts the TGA, DTG, and DSC thermal traces of precursor gel with 2-ME as solvent. In Fig. 6.2, at zone I, up to 175 °C, there is an initial weight loss profile of $\approx 42\%$ in TGA, and the corresponding exothermic peak at 145 °C in DSC is dedicated to the removal of bound water and decomposition of urea with the release of CO₂. Accordingly, two considerable weight loss profiles of $\approx 17\%$ and 13% , from 175 °C – 300 °C in TGA and the small exothermic peak at 220 °C in DSC, can be ascribed to destruction, ignition, and combustion of precursor gel and loss of (OH)⁻. In Zone II, weight loss of $\approx 7\%$ and exothermic peak in DSC at 376 °C indicates the removal of residual carbon remnant (Carp et al. 2003). The summary of all the thermal events in

the precursor gel with an increase in temperature from TGA and DSC is summarised in table 6.1.

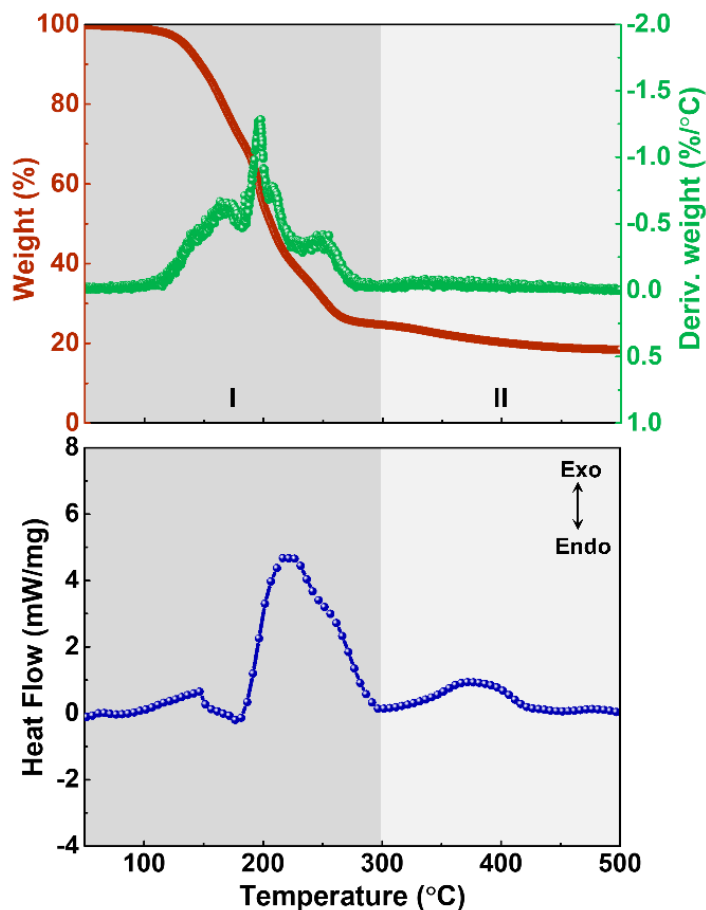


Fig. 6.2. The thermal traces represent the weight loss (TGA and DTG) and heat flow (DSC) of HEO precursors.

Table 6.1. Summary of thermal events in the (CoMnNiFeCr)O precursor gel with an increase in temperature from TGA and DSC.

Materials	Zones	Temperature interval (°C)	Weight loss (%)	Reason
Precursor gel	I	30 – 300	72	Evaporation of solvent, removal of bound water, destruction, ignition, and combustion of precursor gel, loss of (OH) ⁻ .
	II	300 – 500	7	Removal of residual carbon remnant

6.3.2 Structural, compositional, and morphological analysis

Although 500 °C has been considered to be the phase stabilization temperature in bulk-(CoCrFeMnNi)O powder, the combustion mechanism is different in the thin film. Hence, systematic structural compositional and morphological analysis is performed to characterize the efficiency of combustion in the thin film compared to the bulk. The thermal analysis of the precursor solution used in the development of thin film revealed the combustion temperature to be 220 °C, as shown in Fig. 6.2. Thus, 300 °C was selected as the thin film deposition temperature. As in the case of thin films, combustion movement is not yet visually experienced; hence it is important to investigate the phase stabilization of HEO thin film (Pujar et al. 2020). In order to study the phase stabilization, HESOTF-5 (300, 400, 500), HESOTF-10 (300, 400, 500), and HESOTF-15 (300, 400, 500) were subjected to GI-XRD characterization. The GI-XRD patterns of the HESOTF-5, 10, and 15 annealed at 300, 400, and 500 °C are presented in Fig. 6.3. It is noticeable that the HESOTF-5-300 and HESOTF-5-400 display amorphous nature, and crystallization with diffraction peak of the plane (311) is observed for HESOTF-5-500, as shown in Fig. 6.3 (a). Meanwhile, as depicted in Fig. 6.3 (b), the HESOTF-10-300 is also amorphous in nature, similar to HESOTF-5-300, but a display of crystallization with a weak diffraction peak of the plane (311) is observed in HESOTF-10-400. In contrast, a complete crystallization with more planes (111), (220), (311), (400), and (440) is observed HESOTF-10-500. In addition, unlike HESOTF-5-300 and HESOTF-10-300, the HESOTF-15-300 begins to crystallize, and the crystallinity increases furthermore in HESOTF-15-400 and HESOTF-15-500, with peaks of planes (111), (220), (311), (400), and (440) as displayed in Fig. 6.3 (c). The diffraction peaks in the XRD pattern correspond to the standard ICDD file of FeCr₂O₄ (ICDD: 00-034-0140). HESOTF exhibits a single-phase, fcc spinel structure with an *Fd-3m* space group. The display of amorphous nature and poor crystallinity can be ascribed to less thickness of the film and the deficiency of adequate thermal energy to crystallize at below 400 °C. Subsequently, with an increase in annealing temperature, diffraction peaks evolve to become narrower and more intense, which signifies an increase in crystallinity. Thus, an increase in the thickness of the film reduces the crystalline temperature. In addition, although the combustion mechanism is different in

both bulk and thin film, it is found that at 500 °C, the stabilization of phase pure spinel is observed in both bulk and thin film. This may be due to the higher thickness of the film, which acts similarly to the bulk system. Diffraction peaks that correspond to impurities or other phases, were not detectable except for the substrate, which indicates the high purity of the (CoCrFeMnNi)O thin film. As phase stabilization was observed in HESOTF-10-500 and HESOTF-15-500, it was subjected to further characterization.

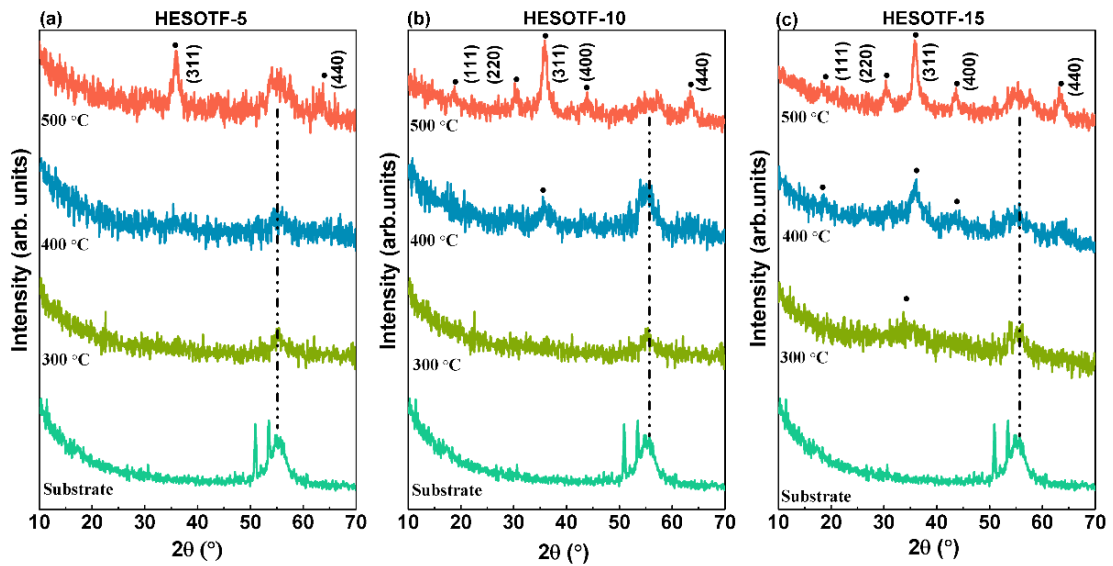


Fig. 6.3. GIXRD pattern with an increase in temperature of (a) HESOTF-5, (b) HESOTF-10, and (c) HESOTF-15 depicting the formation of a single-phase, face-centered cubic spinel structure with an $Fd-3m$ space group. With an increase in temperature, diffraction peaks started evolving, being narrower and more intense, signifying an increase in crystallinity.

To understand the molecular vibration happening within the (CoCrFeMnNi)O thin film, Raman spectroscopy was used. The Raman spectra of HESOTF-15 are shown in Fig. 6.4 (a). The spectrum reveals six main bands at 232, 302, 436, 616, 670, and 824 cm^{-1} . A similar spectrum is observed as that of bulk-(CoCrFeMnNi)O powder (Fig. 5.6 (a)). The bands at 232, 302, 436, 616, 670, and 824 cm^{-1} are attributed to Raman active modes of F_{2g} (1), E_g , F_{2g} (2), F_{2g} (3), and two A_{1g} , respectively. Similar to bulk-(CoCrFeMnNi)O powder, the F_{2g} (1) active mode at 232 cm^{-1} appears due to the translation movement of the tetrahedral metal-oxygen bond, and the F_{2g} (2) at 436 cm^{-1} is ascribed to the stretching vibration of octahedral sublattice (M^{3+} -O) and asymmetric

stretching of octahedral metal-oxygen bond, whereas the F_{2g} (3) at 616 cm^{-1} is due to the symmetric bending of metal-oxygen bond in the tetrahedral site which gets vanished with an increase in temperature. The E_g active mode at 302 cm^{-1} is attributed to the symmetric bending of oxygen in tetrahedral coordination with the metal ion. Finally, in spinel, the A_{1g} active mode at 670 and 824 cm^{-1} is ascribed to the local lattice effect observed in the sublattice of the tetrahedral site and symmetric stretching vibration of metal-oxygen bond in tetrahedral coordination ($M^{2+}\text{-O}$), which confirms a full occupancy of various metal cations in a disordered manner on the tetrahedral site (D'Ippolito et al. 2015; Phakatkar et al. 2021). The E_g and the A_{1g} active mode peaks are sharper at $500\text{ }^\circ\text{C}$, reveals the stabilization of the phase with the rise in temperature similar to that of XRD results. The proof of occupancy of multiple cations (Co, Mn, Ni, Cr, Fe, and Cr) in a disordered manner on tetrahedral and octahedral sites of spinel structure attributed to the configurational mixing entropy is confirmed by the Raman spectroscopy results.

Meanwhile, the topographical characteristics of HESOTF-15 on Si substrate annealed at 300 , 400 , and $500\text{ }^\circ\text{C}$ through AFM (3D micrographs of $5\times 5\text{ }\mu\text{m}^2$) are shown in Fig. 6.4 (b-d). The film displayed root mean square (RMS) surface roughness of 3.33 , 1.35 , and 1.35 nm and growth of particles over the Si substrate. The annealing process at higher temperatures makes the film denser and smoother. It provides adequate energy to the film, which allows the atoms to rearrange their positions, results in more closely packed and crystalline films as confirmed by XRD (Fig. 6.3 (c)) (Raymond et al. 2006a). Simultaneously, surface morphology and the thickness of the 15-layer film annealed at $500\text{ }^\circ\text{C}$ were revealed through cross-sectional FE-SEM, as shown in Fig. 6.4 (e and f). The thickness was found to be 233 nm . To further assess the constituent elemental distribution, an EDS was performed. The elemental distribution and EDS mapping, as shown in Fig. 6.4 (g), display a homogenous distribution of all five cations, with the atomic ratios of the five elements being very close (Co - 0.7% ; Mn - 0.9% , Ni - 0.8% ; Fe - 0.8% ; Cr - 0.8%). The mapping of all the elements of HESOTF-15-500 displays the distribution of elements without any segregation and is provided in Appendix IV as Fig. I.

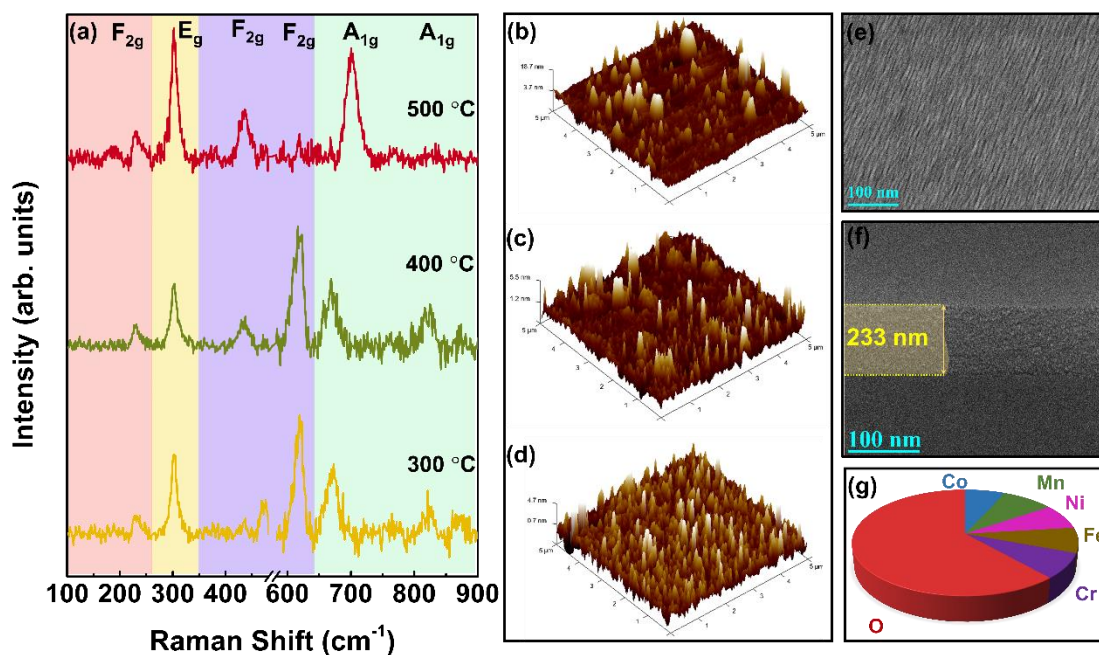


Fig. 6.4. (a) Raman spectrum of HESOTF-15 annealed at 300, 400, and 500 °C, (b-d) AFM image of HESOTF-15 annealed at 300, 400, and 500 °C, (e) surface morphology and (f) cross-sectional micrograph of HESOTF-15-500, and (g) pie chart displaying the elemental distribution respectively.

To strengthen the analysis, surface chemical compositions were analyzed using XPS on HESOTF-15-500. The five cations Co, Cr, Fe, Mn, and Ni, including other elements like C and O, were detected from the compositional analysis by XPS through a low-resolution survey scan in the range 0-1200 eV. The spectra of the film were calibrated using the carbon 1s (C 1s) spectrum positioned at 284.6 eV. The low-resolution survey scan and the C 1s spectrum are provided in Appendix IV in Fig. II (a and b). The deconvoluted high-resolution spectra of all elements are displayed in Fig. 6.5, respectively. The fine scan of Co 2p XPS spectra of HESOTF-15-500 is given in Fig. 6.5 (a), in which the peaks of Co 2p_{3/2} and Co 2p_{1/2} are located at around 780.03 eV and 795.72 eV is ascribed to Co³⁺ respectively; the satellite peaks centered at 787.49 eV and 802.06 eV is attributed to Co³⁺ oxidation state. The fitted peak for Co 2p_{3/2} and Co 2p_{1/2} at 782.48 eV, 790.25 eV, and 798.14 eV is attributed to Co²⁺, respectively; the satellite peaks centered at 785.3 eV and 804.42 eV are attributed to Co²⁺ oxidation state. Nevertheless, according to the present multiple splitting, as shown in Fig. 6.5 (a), the Co ions were identified mainly as Co³⁺ by calculating the area of the synthetic peaks.

The ratio $\text{Co}^{2+}/\text{Co}^{3+}$ is 0.72, which confirms the higher contribution of Co^{3+} than Co^{2+} . The fine scan of Mn 2p XPS spectra, as shown in Fig. 6.5 (b), exhibits two main spin-orbit lines at binding energies of 639.75 eV and 651.15 eV, which correspond to Mn 2p_{3/2} and Mn 2p_{1/2} peaks. The peaks centered at 639.75 eV, 642.68 eV, 646.07 eV, and 651.66 eV are attributed to the Mn^{2+} . The peaks centered at 641.2 eV and 652.65 eV are attributed to the Mn^{3+} , whereas the peaks centered at 644.35 eV, 647.83 eV, and 654.3 eV are attributed to the Mn^{4+} . The Mn ions were identified mainly as Mn^{2+} by calculating the area of the synthetic peaks. Therefore, the ratio $\text{Mn}^{2+}/\text{Mn}^{3+}$ of 1.89 confirms the higher contribution of Mn^{2+} than Mn^{3+} and Mn^{4+} . As shown in Fig. 6.5 (c), the Ni 2p spectra were reasonably deconvoluted into six fitted peaks. The peaks centered at 855.01 eV and 872.76 eV correspond to Ni^{2+} of Ni 2p_{3/2} and Ni 2p_{1/2} peaks. The fitted peak for Ni 2p_{3/2} and Ni 2p_{1/2} is attributed to Ni^{3+} (857.94 eV and 877.9 eV), respectively; two shake-up satellite peaks of Ni at 861.32 eV and 880.81 eV are attributed to Ni^{3+} oxidation state. According to the present multiple splitting, as shown in Fig. 6.5 (c), the Ni ions were identified mainly as Ni^{2+} by calculating the area of the synthetic peaks. The ratio $\text{Ni}^{2+}/\text{Ni}^{3+}$ is 7.67, thus confirms the higher contribution of Ni^{2+} than Ni^{3+} . In a fine scan of Fe 2p XPS spectra (Fig. 6.5 (d)), Fe 2p_{3/2} and Fe 2p_{1/2} peaks centered at 710.08 eV and 723.11 eV, respectively, is the feature of spin-orbit coupling. The Fe 2p spectra were deconvoluted, taking into account contributions from Fe^{2+} , Fe^{3+} , and satellite peaks. The Fe 2p peaks at binding energies 712.99 eV and 725.97 eV with a satellite signal at 719.05 eV were characteristic of Fe^{3+} , while the peaks at 710.18 eV and 723.11 eV with a satellite signal at 716.14 eV were the characteristics of Fe^{2+} . However, according to the present multiple splitting, as shown in Fig. 6.5 (d), the Fe ions were identified mainly as Fe^{2+} by calculating the area of the synthetic peaks. The ratio $\text{Fe}^{2+}/\text{Fe}^{3+}$ is 1.9, thus confirming the higher contribution of Fe^{2+} than Fe^{3+} . Interestingly, in the fine scan Cr 2p XPS spectra (Fig. 6.5 (e)), a higher Cr 2p_{3/2} peak located at 575.41 eV and a separated Co 2p_{1/2} peak at 584.86 eV was observed. The fitted peak for Cr 2p_{3/2} and Cr 2p_{1/2} at 575.41 eV, 576.63 eV, 578.15 eV, 584.86 eV, 585.91 eV, and 587.22 eV are assigned to Cr^{3+} ; while the peaks centered at 588.61 eV and 590.33 are ascribed to Cr^{6+} and satellite peak respectively. However, the Cr ions were identified mainly as Cr^{3+} by calculating the area of the synthetic peaks.

The ratio of $\text{Cr}^{3+}/\text{Cr}^{6+}$ is 8.35, thus confirms the higher contribution of Cr^{3+} than of Cr^{6+} . Fig. 6.5 (f) shows four oxygen peak contributions of the O 1s region of the (CoCrFeMnNi)O thin film. The peak at 529.62 eV is typical for metal-oxygen peak (lattice oxygen), the peak at 531.19 eV denotes surface metal hydroxide, and the peak at 532.25 eV is the weakly bound oxygen adsorbed onto the (CoCrFeMnNi)O thin film surface respectively. According to the results of XPS, it is found that the Co^{3+} , Mn^{2+} , Ni^{2+} , Fe^{2+} , and Cr^{3+} ions are the dominating states in the system, respectively, as tabulated in table 6.2, the same as that of the bulk (CoCrFeMnNi)O powder (Fig. 5.8).

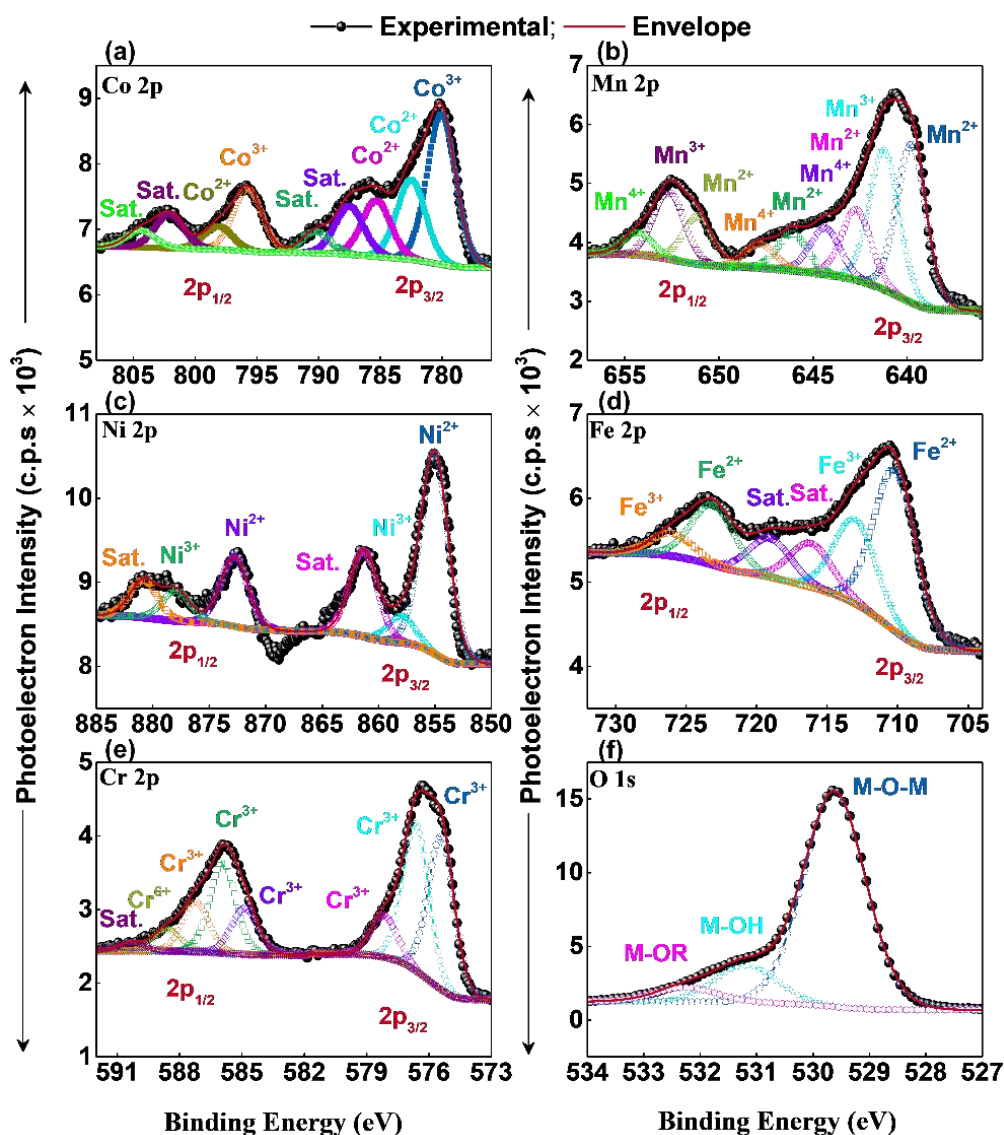


Fig. 6.5. XPS analysis of HESOTF-15-500 with a corresponding high-resolution spectrum of (a) Co 2p, (b) Mn 2p, (c) Ni 2p, (d) Fe 2p, (e) Cr 2p, and (f) O 1s.

Table 6.2. Summary of the percentage area contribution of deconvoluted peaks in cations.

Deconvoluted peak ratio	Area ratio
Co ²⁺ /Co ³⁺	0.72
Mn ²⁺ /Mn ³⁺	1.89
Ni ²⁺ /Ni ³⁺	7.67
Fe ²⁺ /Fe ³⁺	1.9
Cr ³⁺ /Cr ⁶⁺	8.35

6.3.3 Performance of HESO thin film MIM capacitor and transistor

The competence of large-area HESOTF-15-500 was evaluated by investigating the performance of TFTs. Subsequently, to understand the dielectric response of (CoCrFeMnNi)O, a MIM capacitor with HESOTF-15-500 as an insulating layer was employed. Fig. 6.6 (a) shows the architecture of the MIM capacitor, where Ti (20nm) /Au (100 nm) is used as electrodes, Si substrate as the bottom electrode, and HESOTF-15-500 is used as the passive-dielectric layer. Fig. 6.6 (b) depicts the κ as a function of frequency measured at room temperature. At lower frequencies (100 Hz), the magnitude of κ is of the order 1.4×10^2 . However, with an increase in the frequency, the reduction in the magnitude of κ has been observed with magnitudes 5.5×10^1 (at 1 kHz) and 3.1×10^1 (at 10 kHz). These values are relatively high compared to other oxide-dielectrics (Table 6.3) (Liu et al. 2018). Fig. 6.7 shows the C-V response of the capacitor at 100, 1 k, and 10 kHz with κ 1.4×10^2 , 5.5×10^1 , 3.1×10^1 . As mentioned above, the dielectric response of the HESOTF-15-500 can be attributed to the reduction of space charge or interfacial polarization effect at low frequency and combined effects from electronic and ionic polarizations at the higher frequency range with a change in the electric field. In order to measure transistor characteristics, a non-frequency-dependent current (i.e., leakage current) is important. Additionally, the high thickness of the film is very important to suppress the leakage current, which is traditionally suppressed using amorphous metal oxides as dielectrics (Liu et al. 2018). As we have developed a polycrystalline HESOTF-15-500 is developed, owing to the large fraction of grain boundary, it may contribute to the leakage current because of the segregation of oxygen vacancies at the grain boundaries (McKenna et al. 2011). The high film thickness of

HESOTF-15-500 may suppress the leakage current, and the leakage current characteristics of HESOTF-15-500 is shown in Fig. 6.6 (c). A low leakage current of $\sim 10^{-8}$ A.cm⁻¹ was obtained, an indication of stable TFT performance and characteristics (Fortunato et al. 2012; Liu et al. 2018).

The TFT composed of a (CoCrFeMnNi)O dielectric and an n-type 2D MoS₂ semiconductor was characterized under ambient conditions. The architecture of TFT is shown in Fig. 6.6 (d). The output characteristics of the TFT in different gate-voltage (V_{gs}), range from 1 to 5 V with the 1 V step, were recorded and presented in Fig. 6.6 (e). The initial linearity at smaller drain-voltage (V_{ds}) suggests good ohmic contact between the channel and electrodes. The saturation in the curve with an increase in the V_{ds} indicates stable performance at the larger applied electric field. Fig. 6.6 (f) shows the transfer characteristics of the HESO-based TFT in a log scale at a fixed V_{ds} of 1 V and sweeping V_{gs} ranges from -6 V to 6 V. The drain-current (I_{ds}) depicts saturation at around 5 V; this shows the low-operating voltage range of these TFTs. Owing to the large dielectric constant of HEO (5.5×10^1 at 1 kHz), the TFTs are found to operate within a small voltage range. The static performance characters such as field effect mobility, on-off ratio, transconductance, and threshold voltage are found to be of the order 8.79 cm² V⁻¹ s⁻¹, $\sim 10^5$, 5 μ s, and -1.5 V, respectively. Additionally, the TFTs have depicted an acceptable subthreshold swing (SS) of 0.38 V.dec⁻¹, and the extracted trap state density is 1.2×10^{12} cm⁻².eV⁻¹ suggests the presence of trap states, which indicates an acceptable HEO-MoS₂ interface quality. The subthreshold swing was calculated using

$$SS = \frac{dV_{gs}}{d \log I_D} \quad (6.1)$$

Where V_{gs} is the voltage between the gate and source and I_D is the drain current. The transconductance is measured using the following

$$g_m = \frac{\Delta I_D}{\Delta V_{gs}} \quad (6.2)$$

The maximum field effect mobility (μ) of $8.79 \text{ cm}^2 \text{ V}^{-1} \text{ s}^{-1}$ was estimated from the mathematical relation

$$\mu = \frac{g_m}{(W/L)C_i V_{ds}} \quad (6.3)$$

Where W is the width and L is the length of the channel and was maintained to be $44 \text{ }\mu\text{m}$ and $15 \text{ }\mu\text{m}$, respectively. C_i is the capacitance per unit area equal to $2.11 \times 10^{-7} \text{ F.cm}^{-2}$. The estimation of interfacial trap density was done using

$$N_i = \frac{C_i}{q^2} \left[\frac{SS}{\frac{kT \ln 10}{q}} - 1 \right] \quad (6.4)$$

Where q is the Coulomb's charge. These parameters make HESO a potential high dielectric constant dielectric for low voltage operation of the TFTs in devices like display back panels, inverters, logic devices, electronic circuits, and many more (Fortunato et al. 2012).

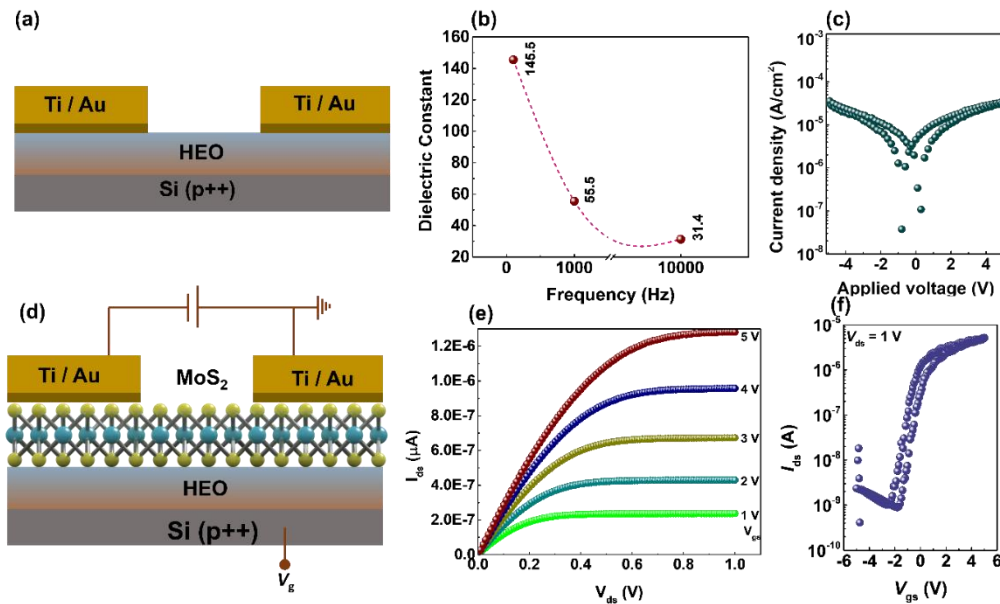


Fig. 6.6. (a) The schematic architecture of metal insulator metal (MIM) capacitor with (CoCrFeMnNi)O acting as an insulating layer, (b) dielectric constant-frequency plot, (c) Plot of current density vs. applied voltage utilized in estimating the leakage current in HESOTF-15-500, (d) schematic architecture of bottom gate HEO based TFT, (e) I_{ds} - V_{ds} curves (output curves) of the (CoCrFeMnNi)O based TFT in the V_{gs} range from $1\text{V} - 5\text{V}$, (f) transfer curve of (CoCrFeMnNi)O based TFT in the log scale.

Table 6.3. TFT Performance of oxide dielectrics.

Materials	Dielectric constant (κ)	Leakage current	Field effect mobility (μ) ($\text{cm}^2 \text{V}^{-1} \text{s}^{-1}$)	$I_{\text{on}}/I_{\text{off}}$ current ratio	Ref.
ZrO ₂	22	$10^{-2} \text{ A.cm}^{-2}$	12	$\approx 10^7$	(Hu et al. 2018)
AlN/Al ₂ O ₃	9	$0.1^{-12} \text{ A.}\mu\text{m}^{-2}$	3.3	$\approx 10^6$	(Qian et al. 2016)
Al ₂ O ₃	9	-	10	$\approx 10^6$	(Cho et al. 2014)
h-BN	3	-	6.2	-	(Dev et al. 2018)
HfO ₂	19	$10^{-3} \text{ A.cm}^{-2}$	55	$\approx 10^8$	(Zou et al. 2014)
Ta ₂ O ₅	15.5	-	60	$\approx 10^6$	(Chamlagain et al. 2017)
HEO	30	$10^{-8} \text{ A.cm}^{-2}$	8.8	10^5	Present

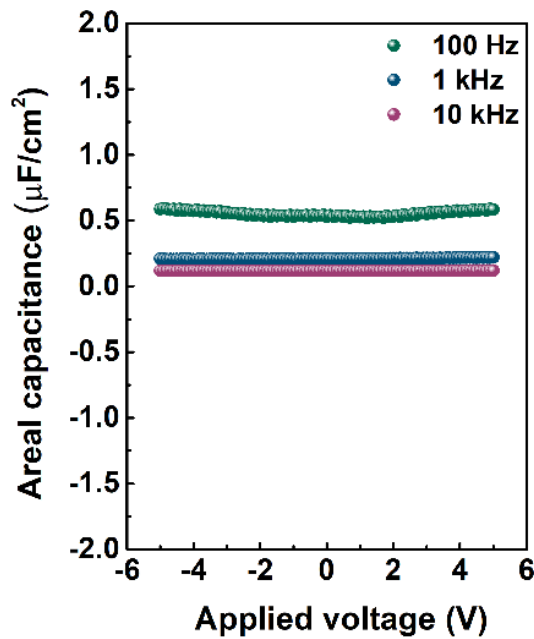


Fig. 6.7. The C-V response of the capacitor at 100, 1 k, and 10 kHz.

6.4 Conclusions

The bulk and thin films have distinct mechanisms of combustion. Hence, investigation was carried out on (CoCrFeMnNi)O thin film to understand the kinetics

of combustion and the phase stabilization. Thermal analysis displayed combustion of the precursor gel at 220 °C with 2-ME as a solvent containing urea served as fuel in both cases. The GI-XRD patterns of the (CoCrFeMnNi)O thin film exhibited a single-phase, fcc spinel structure with an $Fd-3m$ space group, and 500 °C was considered to be the phase stabilization temperature of the synthesized HESOTF. Simultaneously, the thickness of the HESOTF-15-500 was 233 nm, and the topographical characteristics of HESOTF-15-300 to HESOTF-15-500 through AFM displayed RMS surface roughness of 3.33, 1.35, and 1.35 nm. High thickness in HESOTF-15-500 helps to suppress the leakage current, and its application in making a good transistor is also demonstrated with low leakage current. In HESOTF-15-500, the dielectric measurements showed high dielectric constant (κ) with magnitudes 1.4×10^2 , 5×10^1 , and 3×10^1 at 100, 1 k, and 10 kHz, which is of considerably high dielectric constant value in comparison to other metal oxide materials applicable as a gate oxide in transistors or capacitors. The TFTs operated within a small voltage range with static performance characters such as field effect mobility, on-off ratio, transconductance, threshold voltage, SS, and extracted trap state density were found to be $8.79 \text{ cm}^2 \text{ V}^{-1} \text{ s}^{-1}$, $\sim 10^5$, $5 \text{ } \mu\text{s}$, -1.5 V , 0.38 V.dec^{-1} and $1.2 \times 10^{12} \text{ cm}^{-2} \cdot \text{eV}^{-1}$ respectively.



CHAPTER 7

CONCLUSIONS

Page left intentionally blank

CHAPTER 7

CONCLUSIONS

In the present dissertation, HEO is developed via solution combustion processing and employed as a functional dielectric. Three systems of HEO (CoCuMgZnNi)O, (CeLaPrSmY)O, and (CoMnNiFeCr)O are investigated. Phase stabilization of the (CoCuMgZnNi)O, (CeLaPrSmY)O, and (CoMnNiFeCr)O with temperature is investigated. In addition, a systematic study of phase-stabilized (CoCuMgZnNi)O, (CeLaPrSmY)O, and (CoMnNiFeCr)O with individual parent metal oxide and a lesser-cation system are also provided. Further, a capacitor developed using solution combustion processed phase-stabilized (CoCuMgZnNi)O, (CeLaPrSmY)O, and (CoMnNiFeCr)O as a dielectric is demonstrated. The optimized parameters of bulk-(CoCrFeMnNi)O powder and sintered (CoCrFeMnNi)O capacitor are further implemented on solution combustion processed (CoCrFeMnNi)O thin film and are integrated into TFTs with MoS₂ channel for the first time, creating a new bridge between the HEO and electronics. In-depth thermal, structural, microstructural, and elemental analysis was made, which helped to draw a correlation between phase stabilization and transistor performances. Based on these experimental results and analysis, the following conclusions are extracted:

- ✦ The precursor gel used in the development of (CoCuMgZnNi)O powder showed their combustion temperature at 270 °C. The (CoCuMgZnNi)O got fully stabilized at 1000 °C with a single-phase, fcc rocksalt structure with an *Fm-3m* space group. The (CoCuMgZnNi)O displays one of its parent oxide Mg-O structural properties as both belong to the cubic family and has lattice parameters very close to each other. The lower cation systems exhibited a transition from spinel to rocksalt structure with the addition of Mg-O. Dielectric measurements at room temperature showed high dielectric constant (κ) $\approx 1.9 \times 10^3$, 4.7×10^1 , and 0.9×10^1 at 100, 1 k, and 100 kHz, which is attributed to the combination of interface, orientation, ionic, and electronic polarization at low frequency, while at high frequency, a combination of ionic and electronic polarization.

- ✦ The precursor gel used in the development of (CeLaPrSmY)O powder showed their combustion temperature at 320 °C. The (CeLaPrSmY)O got fully stabilized at 1000 °C with a single-phase, fcc fluorite structure with an *Fm-3m* space group. (CeLaPrSmY)O displayed one of its parent oxide Ce-O structural properties as both belong to the fluorite family and had lattice parameters very close to each other. The presence of a secondary phase in the 2 and 3-cation systems and the display of a single phase in the 4 and 5-cation systems specified the role of configurational entropy in phase stabilization. The dielectric measurements showed good dielectric constant $\kappa \approx 29 - 5.7$ from 100 Hz – 1 MHz at room temperature, attributed to the combination of different polarization like space charge, ionic and electronic, and flake morphology and the porous structure.
- ✦ The precursor gel used in the development of (CoCrFeMnNi)O powder showed their combustion temperature at 250 °C. The (CoCrFeMnNi)O powder exhibited a single-phase, fcc spinel structure with an *Fd-3m* space group, and 500 °C was considered to be the phase stabilization temperature. (CoCrFeMnNi)O displays one of its parent oxide Co-O structural properties as both belong to the cubic spinel family, and solvent changes do not hamper the phase stabilization of (CoCrFeMnNi)O. The dielectric measurements showed high dielectric constant (κ) $\approx 1.2 \times 10^3$, 7.3×10^2 , and 3.1×10^1 at 100, 1k, and 100 kHz at room temperature, which is attributed to the combined effect of entropy-driven stabilization effect, accumulation of space charge at the interface, structural inhomogeneity, accumulation of charge at grain boundaries due to point imperfections, rotation of oxygen vacancy, difference in the ion radii and variation in the bond stiffness between the metal and oxygen.
- ✦ The precursor gel used in (CoCrFeMnNi)O thin film fabrication showed their combustion temperature at 220 °C. The (CoCrFeMnNi)O thin film exhibited a single-phase, fcc spinel structure with an *Fd-3m* space group, and 500 °C was considered to be the phase stabilization temperature. Simultaneously, high thickness in (CoCrFeMnNi)O thin film helped to suppress the leakage current and its application in making a suitable transistor. In (CoCrFeMnNi)O thin film, the dielectric measurements showed high dielectric constant (κ) with magnitudes \approx

1.4×10^2 , 5×10^1 , and 3×10^1 at 100, 1 k, and 10 kHz, and the TFTs operated within a small voltage range with static performance characters such as field effect mobility, on-off ratio, transconductance, threshold voltage, SS, and extracted trap state density were found to be $8.79 \text{ cm}^2 \text{ V}^{-1} \text{ s}^{-1}$, $\sim 10^5$, $5 \text{ } \mu\text{s}$, -1.5 V , 0.38 V.dec^{-1} and $1.2 \times 10^{12} \text{ cm}^{-2} \cdot \text{eV}^{-1}$. The low voltage operation ($< 5 \text{ V}$) of these TFTs makes solution combustion-derived HEO (CoMnNiFeCr)O a potential candidate in microelectronics and optoelectronics applications.

To sum up, HEO systems are highly versatile, enabling rapid synthesis and scalability. Additionally, they provide a significant level of influence over their composition, structure, and properties, making them a promising area of research for the development of future materials which can be applicable in devices like display back panels, inverters, integrated sensors, logic devices, electronic circuits, and many more.

7.1 Scope for future work

The present work has directed the facile, low-cost solution combustion method for synthesizing high entropy oxides (bulk and thin film). The current work aimed to develop three types of high entropy oxides with rocksalt, fluorite, and spinel crystal structures having compositions (CoCuMgZnNi)O, (CeLaPrSmY)O, and (CoCrFeMnNi)O and explored kinetics of combustion, the phase stabilization and dielectric performance. The present study provides the following scope for future work:

- ✦ Usage of different other compositions results in different crystal structures such as perovskite, magnetoplumbite, pyrochlore, and many more can be synthesized using solution combustion processing technique, and the kinetics of combustion, phase stabilization, and dielectric performance can be investigated.
- ✦ Employing a higher number of cations (>5) can be analyzed, and in-depth thermal, structural, and morphological analyses could be performed to view the effect of entropy on higher cation systems.
- ✦ In the present study, n-type TFT is demonstrated, similarly p-type TFT can be fabricated. Further, using the combination of n-type and p-type TFT, inverters and ring oscillators, RFID tags, and sensors can be developed.

- ✦ The effect of doping on HEO and their properties can be explored, mainly the phase stabilization and dielectric properties. The system can be further expanded to its application in batteries as anodes or cathodes.
- ✦ HEOs are anticipated to perform better in catalytic performance due to their increased surface area and active sites. Sluggish diffusion can also improve the catalyst's long-term catalytic stability of catalyst. As a result, they make an excellent choice for usage in processes including selective oxidation reactions, electrocatalysts, and fuel cells.
- ✦ The utilization of HEO in solar cells offers considerable potential for future research in renewable energy. This is primarily due to the fact that HEOs can be modified through compositional diversity to adjust their charge transfer mechanism and light absorption capabilities. Furthermore, HEO systems can also provide affordable and effective solutions for modern energy production. As a result, researchers may thus make use of the distinctive qualities of HEOs to develop effective and affordable solutions to the energy catastrophe.

APPENDIX

APPENDIX I

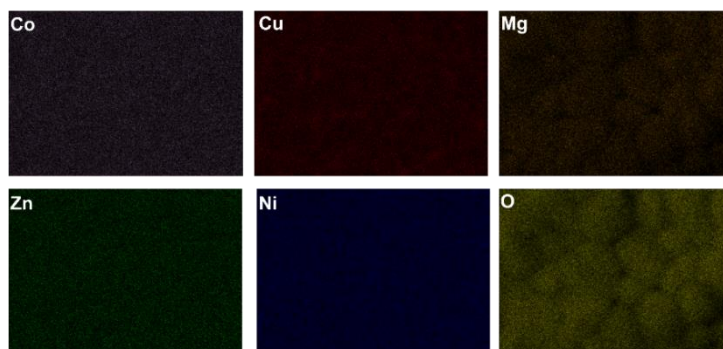


Fig. I. EDS element mapping of HERO-1000 of individual cations showcasing homogenous distribution of all five cations in near-atomic ratios without segregation.

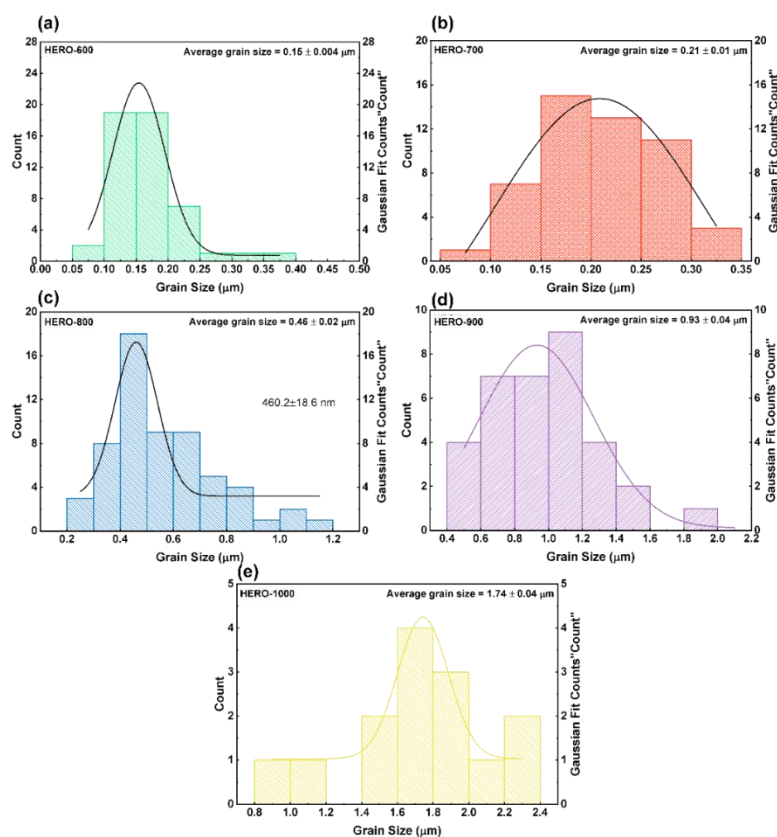


Fig. II. Grain size distribution of HERO powder heat treated at (a) 600 °C, (b) 700 °C, (c) 800 °C, (d) 900 °C, (e) 1000 °C.

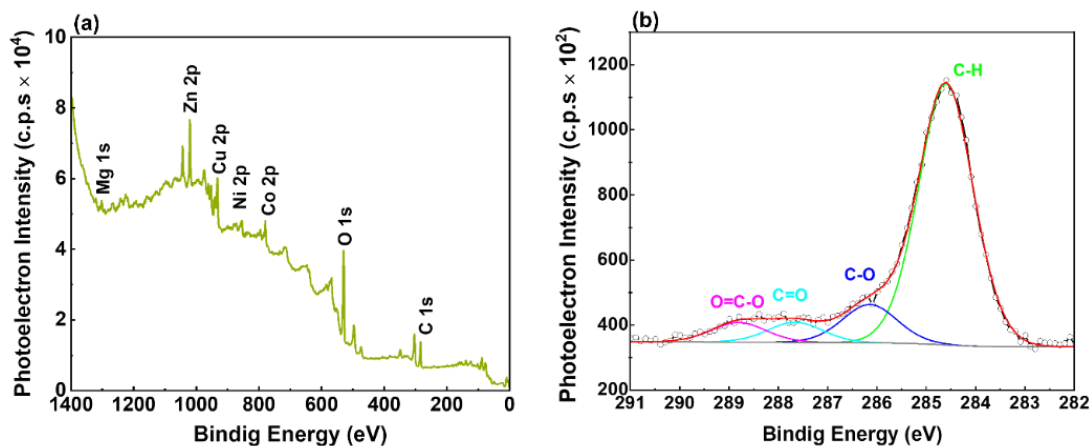


Fig. III. (a) Low-resolution survey XPS spectrum and (b) XPS peak fitting of C 1s of HERO-1000, respectively.

Details of C 1s XPS peak fitting parameters:

Fig. III (b) shows the C 1s XPS peak fitting of HERO-1000. The Carbon 1s (C 1s) peak centered at 284.6 eV is used to calibrate the XPS spectra. The peak fitting of the C 1s peak is performed in order to determine the position of the C-H peak for the charge correction. C 1s spectra were fit with four synthetic peaks centered at 284.6 eV (C-H, Peak I), 286.14 eV (C-O, Peak II), 287.66 eV (C=O, Peak III), and 288.81 (O=C-O, Peak IV). The Gaussian/Lorentz (G/L) ratio and FWHM of all the peaks in C 1s spectra were fit by the Casa XPS software and were constrained to be the same values. Table I provides the peak position constraints and parameters of C1s deconvoluted peaks of HERO-1000, respectively.

Table I. Peak position constraints and parameters of C1s deconvoluted peaks of HERO-1000.

Element	Peak position	Peak	G/L ratio	FWHM	Area
C 1s	284.6	C-H	30	1.30	1138.10
C 1s	286.14	C-O	30	1.30	166.77
C 1s	287.66	C=O	30	1.30	87.62
C 1s	288.81	O=C-O	30	1.30	85.34

APPENDIX II

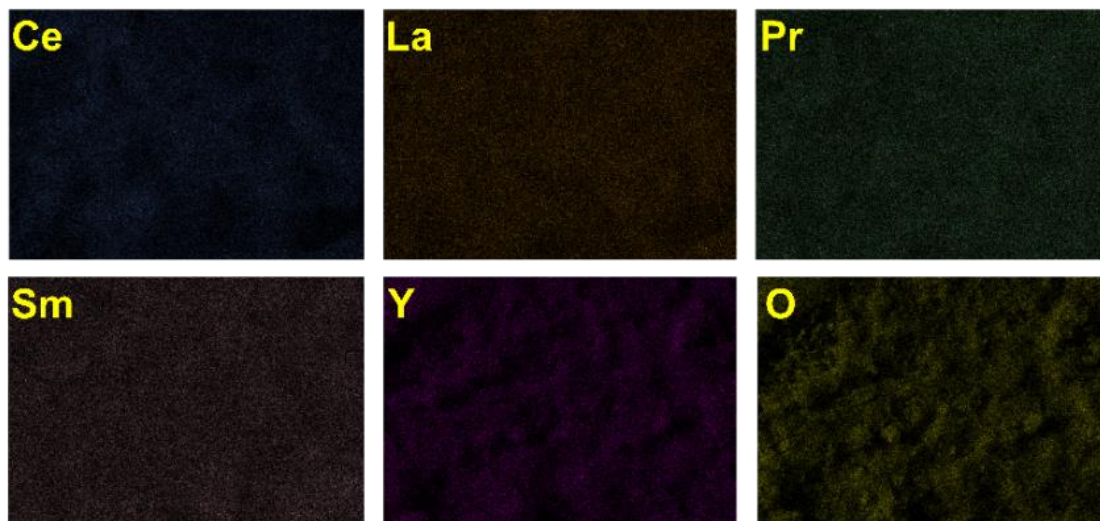


Fig. I. Element mapping of HEFO-1000 of individual cations showcasing homogenous distribution of all five cations in near-atomic ratios.

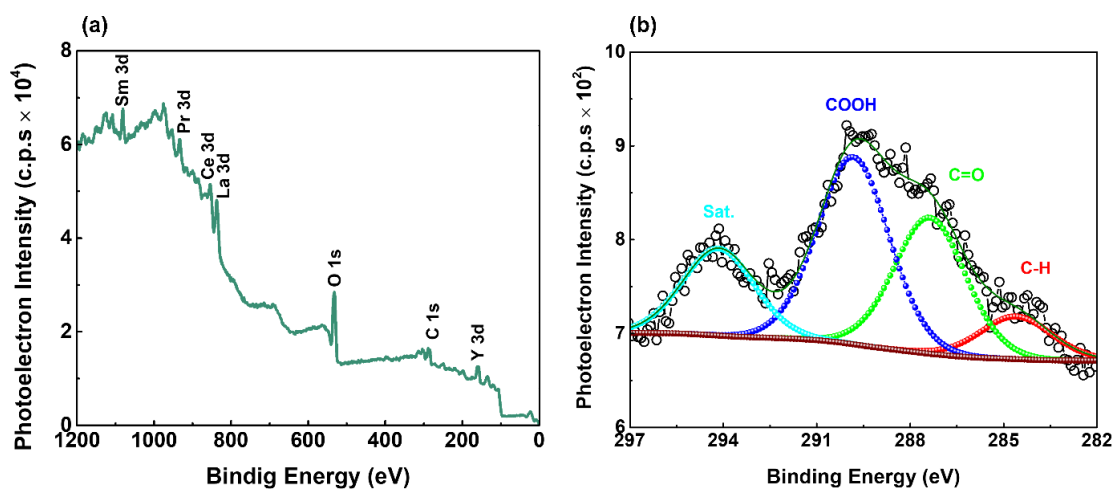


Fig. II. (a) Low-resolution survey XPS spectrum and (b) XPS peak fitting of C 1s of HEFO-1000, respectively.

Details of C 1s XPS peak fitting parameters:

Fig. II (b) shows the C 1s XPS peak fitting of HEFO-1000. The Carbon 1s (C 1s) peak centered at 284.6 eV is used to calibrate the XPS spectra. The peak fitting of the C 1s peak is performed in order to determine the position of the C-H peak for the charge correction. C 1s spectra were fit with four synthetic peaks centered at 284.6 eV (C-H,

Peak I), 287.37 eV (C=O, Peak II), 289.83 eV (COOH, Peak III), and 294.16 eV (carbonyl shake-up satellite, Peak IV). The Gaussian/Lorentz (G/L) ratio and FWHM of all the peaks in C 1s spectra were fit by the Casa XPS software and were constrained to be the same values. Table I provides the peak position constraints and parameters of C1s deconvoluted peaks of HEFO-1000, respectively.

Table I. Peak position constraints and parameters of C1s deconvoluted peaks of HEFO-1000.

Element	Peak position	Peak	G/L ratio	FWHM	Area
C 1s	284.6	C-H	30	2.71	133.60
C 1s	287.37	C=O	30	2.71	425.73
C 1s	289.83	COOH	30	2.71	585.62
C 1s	294.16	Carbonyl shake-up	30	2.71	272.5

APPENDIX III

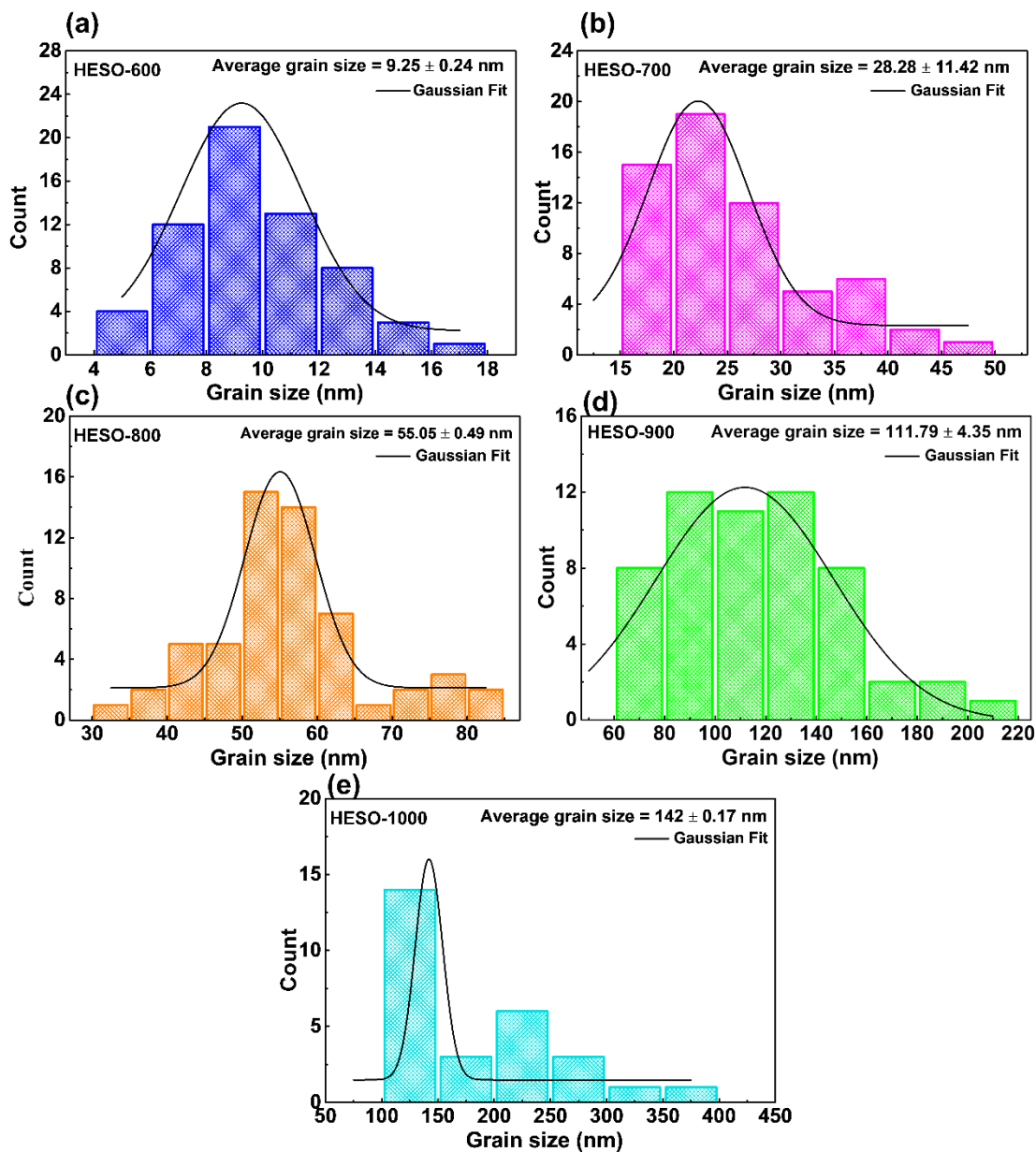


Fig. I. Grain size distribution of HESO powder heat treated at (a) 600 °C, (b) 700 °C, (c) 800 °C, (d) 900 °C, (e) 1000 °C.

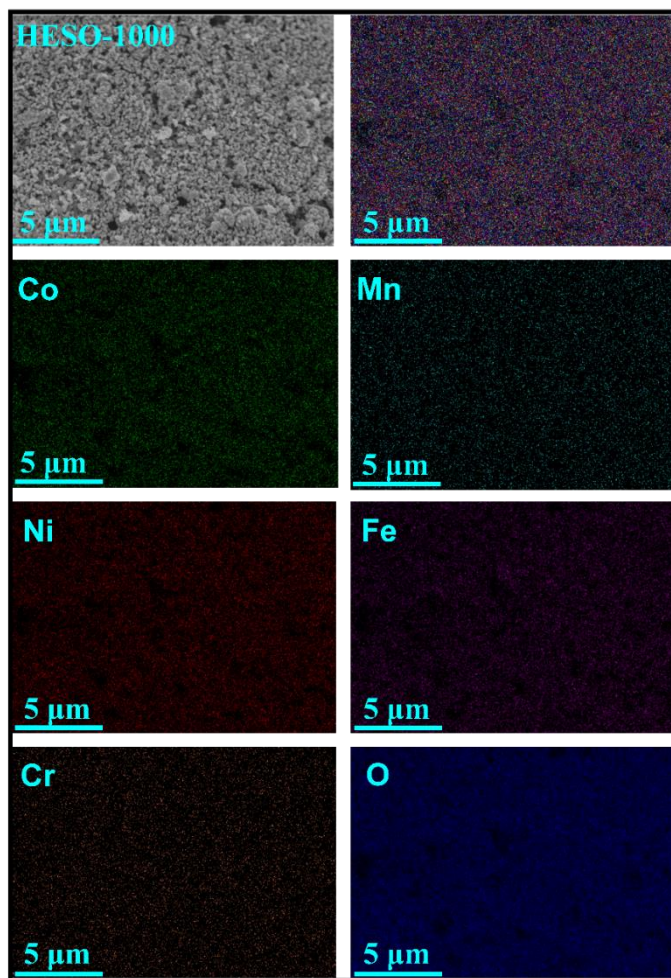


Fig. II. EDS element mapping of HESO-1000 with the surface image, element overlay, and surface mapping of individual cations showcasing homogenous distribution of all five cations in near-atomic ratios without any segregation

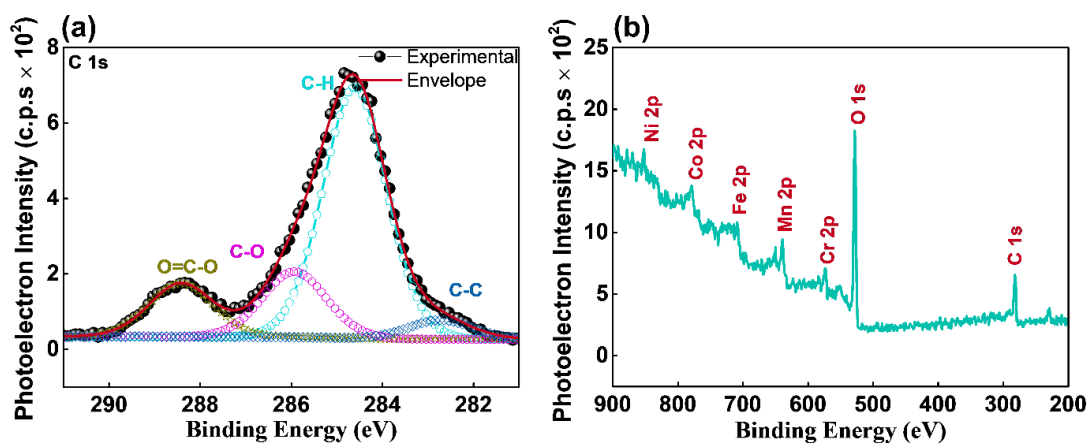


Fig. III. (a) XPS peak fitting of C 1s and (b) low-resolution survey XPS spectrum of HESO-1000, respectively.

Details of C 1s XPS peak fitting parameters:

Fig. III (a) shows the C 1s XPS peak fitting of HESO-1000, respectively. The Carbon 1s (C 1s) peak centered at 284.6 eV is used to calibrate the XPS spectra. The peak fitting of the C 1s peak is performed in order to determine the position of the C-H peak for the charge correction. C 1s spectra were fit with four synthetic peaks centered at 282.72 eV (C-C, Peak I), 284.6 eV (C-H, Peak II), 285.93 eV (C-O, Peak III), and 288.42 eV (O=C-O, Peak IV). The Gaussian/Lorentz (G/L) ratio and FWHM of all the peaks in C 1s spectra were fit by the Casa XPS software and were constrained to be the same values. Table I provides the peak position constraints and parameters of C1s deconvoluted peaks of HESO-1000, respectively.

Table I. Peak position constraints and parameters of C1s deconvoluted peaks of HESO-1000.

Element	Peak position	Peak	G/L ratio	FWHM	Area
C 1s	282.72	C=C	30	1.65	90.91
C 1s	284.6	C-H	30	1.65	1188.67
C 1s	285.93	C-O	30	1.65	310.88
C 1s	288.42	O=C-O	30	1.65	253.12

APPENDIX IV

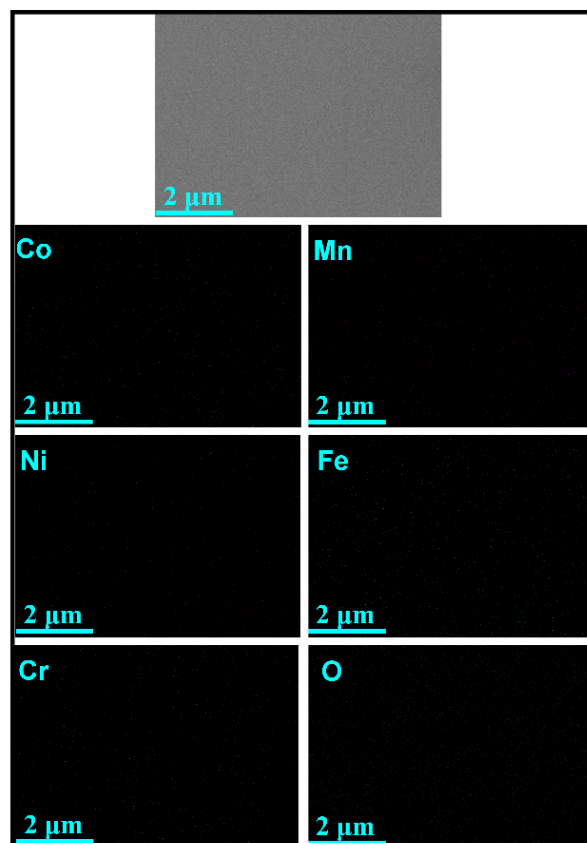


Fig. I. EDS element mapping of HESOTF-15-500 with the surface image and surface mapping of individual cations showcasing homogenous distribution of all five cations in near-atomic ratios without segregation.

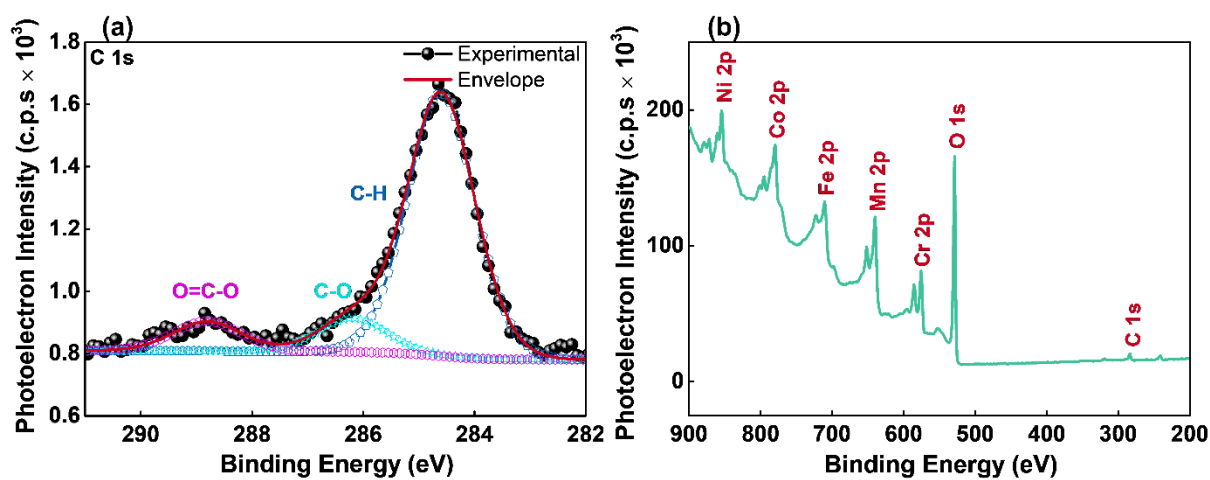


Fig. II. (a) Low-resolution survey XPS spectrum and (b) XPS peak fitting of C 1s of 15-Layer HESOTF annealed at 500 °C, respectively.

Details of C 1s XPS peak fitting parameters:

Fig. III (a) shows the C 1s XPS peak fitting of 15-Layer HESOTF annealed at 500 °C, respectively. The Carbon 1s (C 1s) peak centered at 284.6 eV is used to calibrate the XPS spectra. The peak fitting of the C 1s peak is performed in order to determine the position of the C-H peak for the charge correction. C 1s spectra were fit with four synthetic peaks centered at 284.6 eV (C-H, Peak I), 286.19 eV (C-O, Peak II), and 288.81 eV (O=C-O, Peak III). The Gaussian/Lorentz (G/L) ratio and FWHM of all the peaks in C 1s spectra were fit by the Casa XPS software and were constrained to be the same values. Table I provides the peak position constraints and parameters of C1s deconvoluted peaks of 15-Layer HESOTF annealed at 500 °C, respectively.

Table I. Peak position constraints and parameters of C1s deconvoluted peaks of HESOTF-500.

Element	Peak position	Peak	G/L ratio	FWHM	Area
C 1s	284.6	C-H	30	1.43	1308.18
C 1s	286.19	C-O	30	1.43	167.8
C 1s	288.15	O=C-O	30	1.43	148.12

Page left intentionally blank

REFERENCES

- Aamlid, S. S., Oudah, M., Rottler, J., and Hallas, A. M. (2022). “Understanding the role of entropy in high entropy oxides.” *J. Am. Chem. Soc.*, 145(11), 5991–6006.
- Abbas, H., Nadeem, K., Hafeez, A., Hassan, A., Saeed, N., and Krenn, H. (2019). “A comparative study of magnetic, photocatalytic and dielectric properties of NiO nanoparticles synthesized by sol-gel and composite hydroxide mediated method.” *Ceram. Int.*, 45(14), 17289–17297.
- Abrar, S., Ma, Z., Liu, L., Nazeer, F., and Malik, A. (2023). “Ultra-low thermal conductivity and excellent high temperature resistance against calcium-magnesium-alumina-silicate of a novel β -type pyrosilicates.” *J. Alloys Compd.*, 942, 169001.
- Adamopoulos, G., Bashir, A., Wöbkenberg, P. H., Bradley, D. D. C., and Anthopoulos, T. D. (2009). “Electronic properties of ZnO field-effect transistors fabricated by spray pyrolysis in ambient air.” *Appl. Phys. Lett.*, 95(13), 13350.
- Adamopoulos, G., Thomas, S., Wöbkenberg, P. H., Bradley, D. D. C., McLachlan, M. A., and Anthopoulos, T. D. (2011). “High-mobility low-voltage ZnO and Li-doped ZnO transistors based on ZrO₂ high- κ dielectric grown by spray pyrolysis in ambient air.” *Adv. Mater.*, 23(16), 1894–1898.
- Ahn, M., Park, Y., Lee, S. H., Chae, S., Lee, J., Heron, J. T., Kioupakis, E., Lu, W. D., and Phillips, J. D. (2021). “Memristors based on (Zr, Hf, Nb, Ta, Mo, W) high-entropy oxides.” *Adv. Electron. Mater.*, 7(5), 2001258.
- Ai, L. H., and Jiang, J. (2009). “Rapid synthesis of nanocrystalline Co₃O₄ by a microwave-assisted combustion method.” *Powder Technol.*, 195(1), 11–14.
- Akgul, F. A., Akgul, G., Yildirim, N., Unalan, H. E., and Turan, R. (2014). “Influence of thermal annealing on microstructural, morphological, optical properties and surface electronic structure of copper oxide thin films.” *Mater. Chem. Phys.*, 147(3), 987–995.
- Akopov, G., Pangilinan, L. E., Mohammadi, R., and Kaner, R. B. (2018). “Perspective:

Superhard metal borides: A look forward.” *APL Mater.*, 6(7), 70901.

Aksoy, S., Caglar, Y., Ilican, S., and Caglar, M. (2012). “Sol-gel derived Li-Mg co-doped ZnO films: Preparation and characterization via XRD, XPS, FESEM.” *J. Alloys Compd.*, 512(1), 171–178.

Ali, M. A., Khan, M. N. I., Chowdhury, F.-U.-Z., Akhter, S., and Uddin, M. M. (2015). “Structural properties, impedance spectroscopy and dielectric spin relaxation of Ni-Zn ferrite synthesized by double sintering technique.” *J. Sci. Res.*, 7(3), 65–75.

Anandkumar, M., and Trofimov, E. (2023). “Synthesis, properties, and applications of high-entropy oxide ceramics: Current progress and future perspectives.” *J. Alloys Compd.*, 960, 170690.

Anderson, J. T., Munsee, C. L., Hung, C. M., Phung, T. M., Herman, G. S., Johnson, D. C., Wager, J. F., and Keszler, D. A. (2007). “Solution-processed HafSO_x and ZircSO_x inorganic thin-film dielectrics and nanolaminates.” *Adv. Funct. Mater.*, 17(13), 2117–2124.

Asif, M., Khan, M. A., Atiq, S., Alshahrani, T., Mahmood, Q., Kattan, N. A., and Manzoor, A. (2021). “Evolution of structure and improvement in dielectric properties of praseodymium substituted YFeO_3 nanomaterials synthesized via a sol-gel auto-combustion method.” *Ceram. Int.*, 47(5), 6663–6674.

Banerjee, R., Chatterjee, S., Ranjan, M., Bhattacharya, T., Mukherjee, S., Jana, S. S., Dwivedi, A., and Maiti, T. (2020). “High-entropy perovskites: An emergent class of oxide thermoelectrics with ultralow thermal conductivity.” *ACS Sustain. Chem. Eng.*, 8(46), 17022–17032.

Baqer, A. A., Matori, K. A., Al-Hada, N. M., Shaari, A. H., Kamari, H. M., Saion, E., Chyi, J. L. Y., and Abdullah, C. A. C. (2018). “Synthesis and characterization of binary $(\text{CuO})_{0.6}(\text{CeO}_2)_{0.4}$ nanoparticles via a simple heat treatment method.” *Results Phys.*, 9, 471–478.

Bashir, A., Wöbkenberg, P. H., Smith, J., Ball, J. M., Adamopoulos, G., Bradley, D. D.

C., and Anthopoulos, T. D. (2009). “High-performance zinc oxide transistors and circuits fabricated by spray pyrolysis in ambient atmosphere.” *Adv. Mater.*, 21(21), 2226–2231.

Bécu, S., Crémer, S., and Autran, J. L. (2006). “Capacitance non-linearity study in Al₂O₃ MIM capacitors using an ionic polarization model.” *Microelectron. Eng.*, 83(11–12), 2422–2426.

Bell, A. T. (2003). “The impact of nanoscience on heterogeneous catalysis.” *Science*, 299(5613), 1688–91.

Bérardan, D., Franger, S., Dragoe, D., Meena, A. K., and Dragoe, N. (2016a). “Colossal dielectric constant in high entropy oxides.” *Phys. Status Solidi - Rapid Res. Lett.*, 10(4), 328–333.

Bérardan, D., Franger, S., Meena, A. K., and Dragoe, N. (2016b). “Room temperature lithium superionic conductivity in high entropy oxides.” *J. Mater. Chem. A*, 4(24), 9536–9541.

Berardan, D., Meena, A. K., Franger, S., Herrero, C., and Dragoe, N. (2017). “Controlled Jahn-Teller distortion in (MgCoNiCuZn)O-based high entropy oxides.” *J. Alloys Compd.*, 704, 693–700.

Berlijn, T., Alvarez, G., Parker, D. S., Hermann, R. P., and Fishman, R. S. (2020). “Simulating spin waves in entropy stabilized oxides.” *Phys. Rev. Res.*, 3(3), 033273.

Bhardwaj, P., Singh, J., Kumar, R., Kumar, D., Verma, V., and Kumar, R. (2022). “Oxygen defects induced tailored optical and magnetic properties of Fe_xCr_{2-x}O₃ (0 ≤ x ≤ 0.1) nanoparticles.” *Appl. Phys. A Mater. Sci. Process.*, 128(2), 1–14.

Bi, L., Li, X., Li, Z., Hu, Y., Zhang, J., Wang, Q., Dong, C., Zheng, Y., and Liaw, P. K. (2020). “Performance and local structure evolution of NbMoTaWV entropy-stabilized oxide thin films with variable oxygen content.” *Surf. Coatings Technol.*, 402, 126326.

Biesinger, M. C., Payne, B. P., Grosvenor, A. P., Lau, L. W. M., Gerson, A. R., and

Smart, R. S. C. (2011). “Resolving surface chemical states in XPS analysis of first row transition metals, oxides and hydroxides: Cr, Mn, Fe, Co and Ni.” *Appl. Surf. Sci.*, 257(7), 2717–2730.

Biesuz, M., Fu, S., Dong, J., Jiang, A., Ke, D., Xu, Q., Zhu, D., Bortolotti, M., Reece, M. J., Hu, C., and Grasso, S. (2019). “High entropy $\text{Sr}((\text{Zr}_{0.94}\text{Y}_{0.06})_{0.2}\text{Sn}_{0.2}\text{Ti}_{0.2}\text{Hf}_{0.2}\text{Mn}_{0.2})\text{O}_{3-x}$ perovskite synthesis by reactive spark plasma sintering.” *J. Asian Ceram. Soc.*, 7(2), 127–132.

Biesuz, M., Spiridigliozzi, L., Dell’Agli, G., Bortolotti, M., and Sglavo, V. M. (2018). “Synthesis and sintering of (Mg, Co, Ni, Cu, Zn)O entropy-stabilized oxides obtained by wet chemical methods.” *J. Mater. Sci.*, 53(11), 8074–8085.

Bong, H., Lee, W. H., Lee, D. Y., Kim, B. J., Cho, J. H., and Cho, K. (2010). “High-mobility low-temperature ZnO transistors with low-voltage operation.” *Appl. Phys. Lett.*, 96(19), 192115.

Bordi, F., Cametti, C., and Colby, R. H. (2004). “Dielectric spectroscopy and conductivity of polyelectrolyte solutions.” *J. Phys. Condens. Matter*, 16, R1423.

Bortamuly, R., Konwar, G., Boruah, P. K., Das, M. R., Mahanta, D., and Saikia, P. (2020). “ CeO_2 -PANI-HCl and CeO_2 -PANI-PTSA composites: synthesis, characterization, and utilization as supercapacitor electrode materials.” *Ionics*, 26(11), 5747–5756.

Bragg, W. H., Bragg Apr, W. L., H Bragg, B. W., and Professor of Physics, C. (1913). “The reflection of X-rays by crystals.” *Proc. R. Soc. London. Ser. A, Contain. Pap. a Math. Phys. Character*, 88(605), 428–438.

Branquinho, R., Salgueiro, D., Santos, L., Barquinha, P., Pereira, L., Martins, R., and Fortunato, E. (2014). “Aqueous combustion synthesis of aluminum oxide thin films and application as gate dielectric in GZTO solution-based TFTs.” *ACS Appl. Mater. Interfaces*, 6(22), 19592–19599.

Braun, J. L., Rost, C. M., Lim, M., Giri, A., Olson, D. H., Kotsonis, G. N., Stan, G.,

- Brenner, D. W., Maria, J. P., and Hopkins, P. E. (2018). "Charge-induced disorder controls the thermal conductivity of entropy-stabilized oxides." *Adv. Mater.*, 30(51), 1805004.
- Breitung, B., Wang, Q., Schiele, A., Tripković, Đ., Sarkar, A., Velasco, L., Wang, D., Bhattacharya, S. S., Hahn, H., and Brezesinski, T. (2020). "Gassing behavior of high-entropy oxide anode and oxyfluoride cathode probed using differential electrochemical mass spectrometry." *Batter. Supercaps*, 3(4), 361–369.
- Brezinsky, K. (1996). "Gas-phase combustion synthesis of materials." *Symp. Combust.*, 26(2), 1805–1816.
- Cabana, J., Monconduit, L., Larcher, D., and Palacín, M. R. (2010). "Beyond intercalation-based Li-ion batteries: The state of the art and challenges of electrode materials reacting through conversion reactions." *Adv. Mater.*, 22(35), E170–E192.
- Cantor, B., Chang, I. T. H., Knight, P., and Vincent, A. J. B. (2004). "Microstructural development in equiatomic multicomponent alloys." *Mater. Sci. Eng. A*, 375–377, 213–218.
- Cao, G., Ouyang, J. H., Li, Y., Liu, Z. G., Ding, Z. Y., Wang, Y. H., Jin, Y. J., Wang, Y. M., and Wang, Y. J. (2021). "Improved thermophysical properties of rare-earth monosilicates applied as environmental barrier coatings by adjusting structural distortion with RE-doping." *J. Eur. Ceram. Soc.*, 41(14), 7222–7232.
- Cardoso, A. L. F., Perdomo, C. P. F., Kiminami, R. H. G. A., and Gunnewiek, R. F. K. (2021). "Enhancing the stabilization of nanostructured rocksalt-like high entropy oxide by Gd addition." *Mater. Lett.*, 285, 129175.
- Carlos, E., Martins, R., Fortunato, E., and Branquinho, R. (2020). "Solution combustion synthesis: Towards a sustainable approach for metal oxides." *Chem. – A Eur. J.*, 26(42), 9099–9125.
- Carp, O., Patron, L., and Reller, A. (2003). "Thermal behavior of the coordination compound $[\text{Co}(\text{urea})_6](\text{NO}_3)_2$." *J. Therm. Anal. Calorim.*, 73(3), 867–876.

Castle, E., Csanádi, T., Grasso, S., Dusza, J., and Reece, M. (2018). “Processing and properties of high-entropy ultra-high temperature carbides.” *Sci. Rep.*, 8(1), 8609.

Cavin, J., Ahmadiparidari, A., Majidi, L., Thind, A. S., Misal, S. N., Prajapati, A., Hemmat, Z., Rastegar, S., Beukelman, A., Singh, M. R., Unocic, K. A., Salehi-Khojin, A., and Mishra, R. (2021). “2D high-entropy transition metal dichalcogenides for carbon dioxide electrocatalysis.” *Adv. Mater.*, 33(31), 2100347.

Chamlagain, B., Cui, Q., Paudel, S., Cheng, M. M. C., Chen, P. Y., and Zhou, Z. (2017). “Thermally oxidized 2D TaS₂ as a high-κ gate dielectric for MoS₂ field-effect transistors.” *2D Mater.*, 4(3), 31002.

Chang, H. W., Huang, P.-K., Davison, A., Yeh, J. W., Tsau, C. H., and Yang, C. C. (2008a). “Nitride films deposited from an equimolar Al–Cr–Mo–Si–Ti alloy target by reactive direct current magnetron sputtering.” *Thin Solid Films*, 516(18), 6402–6408.

Chang, H. W., Huang, P. K., Yeh, J. W., Davison, A., Tsau, C. H., and Yang, C. C. (2008b). “Influence of substrate bias, deposition temperature and post-deposition annealing on the structure and properties of multi-principal-component (AlCrMoSiTi)N coatings.” *Surf. Coatings Technol.*, 202(14), 3360–3366.

Chauhan, K. V., and Rawal, S. K. (2014). “A review paper on tribological and mechanical properties of ternary nitride based coatings.” *Procedia Technol.*, 14, 430–437.

Chellali, M. R., Sarkar, A., Nandam, S. H., Bhattacharya, S. S., Breitung, B., Hahn, H., and Velasco, L. (2019). “On the homogeneity of high entropy oxides: An investigation at the atomic scale.” *Scr. Mater.*, 166, 58–63.

Chen, H., Fu, J., Zhang, P., Peng, H., Abney, C. W., Jie, K., Liu, X., Chi, M., and Dai, S. (2018a). “Entropy-stabilized metal oxide solid solutions as CO oxidation catalysts with high-temperature stability.” *J. Mater. Chem. A*, 6(24), 11129–11133.

Chen, K., Pei, X., Tang, L., Cheng, H., Li, Z., Li, C., Zhang, X., and An, L. (2018b). “A five-component entropy-stabilized fluorite oxide.” *J. Eur. Ceram. Soc.*, 38(11),

4161–4164.

Chen, H., Lin, W., Zhang, Z., Jie, K., Mullins, D. R., Sang, X., Yang, S.-Z., Jafta, C. J., Bridges, C. A., Hu, X., Unocic, R. R., Fu, J., Zhang, P., and Dai, S. (2019a). “Mechanochemical synthesis of high entropy oxide materials under ambient conditions: dispersion of catalysis via entropy maximization.” *ACS Mater. Lett.*, 1(1), 83–88.

Chen, H., Qiu, N., Wu, B., Yang, Z., Sun, S., and Wang, Y. (2019b). “Tunable pseudocapacitive contribution by dimension control in nanocrystalline-constructed (Mg_{0.2}Co_{0.2}Ni_{0.2}Cu_{0.2}Zn_{0.2})O solid solutions to achieve superior lithium-storage properties.” *RSC Adv.*, 9(50), 28908–28915.

Chen, J., Liu, W., Liu, J., Zhang, X., Yuan, M., Zhao, Y., Yan, J., Hou, M., Yan, J., Kunz, M., Tamura, N., Zhang, H., and Yin, Z. (2019c). “stability and compressibility of cation-doped high-entropy oxide MgCoNiCuZnO₅.” *J. Phys. Chem. C*, 123(29), 17735–17744.

Chen, H., Jie, K., Jafta, C. J., Yang, Z., Yao, S., Liu, M., Zhang, Z., Liu, J., Chi, M., Fu, J., and Dai, S. (2020a). “An ultrastable heterostructured oxide catalyst based on high-entropy materials: A new strategy toward catalyst stabilization via synergistic interfacial interaction.” *Appl. Catal. B Environ.*, 276, 119155.

Chen, H., Sun, Y., Yang, S., Wang, H., Dmowski, W., Egami, T., and Dai, S. (2020b). “Self-regenerative noble metal catalysts supported on high-entropy oxides.” *Chem. Commun.*, 56(95), 15056-1505.

Chen, H., Zhao, Z., Xiang, H., Dai, F. Z., Xu, W., Sun, K., Liu, J., and Zhou, Y. (2020c). “High entropy (Y_{0.2}Yb_{0.2}Lu_{0.2}Eu_{0.2}Er_{0.2})₃Al₅O₁₂: A novel high temperature stable thermal barrier material.” *J. Mater. Sci. Technol.*, 48, 57–62.

Chen, T. Y., Wang, S. Y., Kuo, C. H., Huang, S. C., Lin, M. H., Li, C. H., Chen, H. Y. T., Wang, C. C., Liao, Y. F., Lin, C. C., Chang, Y. M., Yeh, J. W., Lin, S. J., Chen, T. Y., and Chen, H. Y. (2020d). “In operando synchrotron X-ray studies of a novel spinel (Ni_{0.2}Co_{0.2}Mn_{0.2}Fe_{0.2}Ti_{0.2})₃O₄ high-entropy oxide for energy storage applications.” *J.*

Mater. Chem. A, 8(41), 21756–21770.

Chen, Z., Lin, C., Zheng, W., Jiang, C., Song, X., and Zeng, Y. (2022). “A high-entropy $(\text{Yb}_{0.2}\text{Y}_{0.2}\text{Lu}_{0.2}\text{Ho}_{0.2}\text{Er}_{0.2})_2\text{Si}_2\text{O}_7$ environmental barrier coating prepared by atmospheric plasma-spray.” *Ceram. Int.*, 49(7), 11323–11333.

Cheng, K. H., Lai, C. H., Lin, S.-J., and Yeh, J. W. (2011). “Structural and mechanical properties of multi-element $(\text{AlCrMoTaTiZr})\text{N}_x$ coatings by reactive magnetron sputtering.” *Thin Solid Films*, 519(10), 3185–3190.

Chernyak, Y. (2006). “Dielectric constant, dipole moment, and solubility parameters of some cyclic acid esters.” *J. Chem. Eng. Data*, 51(2), 416–418.

Chhowalla, M., Shin, H. S., Eda, G., Li, L.-J., Loh, K. P., and Zhang, H. (2013). “The chemistry of two-dimensional layered transition metal dichalcogenide nanosheets.” *Nat. Chem.*, 5(4), 263–275.

Chick, L. A., Pederson, L. R., Maupin, G. D., Bates, J. L., Thomas, L. E., and Exarhos, G. J. (1990). “Glycine-nitrate combustion synthesis of oxide ceramic powders.” *Mater. Lett.*, 10(1–2), 6–12.

Cho, A. J., Yang, S., Park, K., Namgung, S. D., Kim, H., and Kwon, J. Y. (2014). “Multi-layer MoS_2 FET with small hysteresis by using atomic layer deposition Al_2O_3 as gate insulator.” *ECS Solid State Lett.*, 3(10), Q67.

Choudhary, A., Sahu, B. S., Mazumder, R., Bhattacharyya, S., and Chaudhuri, P. (2014). “Synthesis and sintering of Li_4SiO_4 powder from rice husk ash by solution combustion method and its comparison with solid state method.” *J. Alloys Compd.*, 590, 440–445.

Chu, B., Zhou, X., Ren, K., Neese, B., Lin, M., Wang, Q., Bauer, F., and Zhang, Q. M. (2006). “A dielectric polymer with high electric energy density and fast discharge speed.” *Science*, 313(5785), 334–336.

Coates, J. (2006). “Interpretation of infrared spectra, a practical approach.” *Encycl. Anal. Chem.*, John Wiley & Sons, Ltd, 10815–10837.

- Coşkun, M., Polat, A. O., Coşkun, F. M., Durmuş, Z., Caglar, C. M., and Türüt, A. (2018). “The electrical modulus and other dielectric properties by the impedance spectroscopy of LaCrO_3 and $\text{LaCr}_{0.90}\text{Ir}_{0.10}\text{O}_3$ perovskites.” *RSC Adv.*, 8(9), 4634–4648.
- D’Ippolito, V., Andreozzi, G. B., Bersani, D., and Lottici, P. P. (2015). “Raman fingerprint of chromate, aluminate and ferrite spinels.” *J. Raman Spectrosc.*, 46(12), 1255–1264.
- Dąbrowa, J., Stygar, M., Mikuła, A., Knapik, A., Mroczka, K., Tejchman, W., Danielewski, M., and Martin, M. (2018). “Synthesis and microstructure of the $(\text{Co,Cr,Fe,Mn,Ni})_3\text{O}_4$ high entropy oxide characterized by spinel structure.” *Mater. Lett.*, 216, 32–36.
- Dang, Z. M., Yuan, J. K., Yao, S. H., and Liao, R. J. (2013). “Flexible nanodielectric materials with high permittivity for power energy storage.” *Adv. Mater.*, 25(44), 6334–6365
- Deshpande, K., Nersesyan, M., Mukasyan, A., and Varma, A. (2005). “Novel ferrimagnetic iron oxide nanopowders.” *Ind. Eng. Chem. Res.*, 44(16), 6196–6199.
- Deshpande, P. A., Poliseti, S., and Madras, G. (2011). “Rapid synthesis of ultrahigh adsorption capacity zirconia by a solution combustion technique.” *Langmuir*, 27(7), 3578–3587.
- Dev, D., Krishnaprasad, A., Kalita, H., Das, S., Rodriguez, V., Calderon Flores, J., Zhai, L., and Roy, T. (2018). “High quality gate dielectric/ MoS_2 interfaces probed by the conductance method.” *Appl. Phys. Lett.*, 112(23), 232101.
- Diallo, A., Beye, A. C., Doyle, T. B., Park, E., and Maaza, M. (2015). “Green synthesis of Co_3O_4 nanoparticles via *Aspalathus linearis*: Physical properties.” *Green Chem. Lett. Rev.*, 8(3–4), 30–36.
- Ding, H. Y., and Yao, K. F. (2013). “High entropy $\text{Ti}_{20}\text{Zr}_{20}\text{Cu}_{20}\text{Ni}_{20}\text{Be}_{20}$ bulk metallic glass.” *J. Non. Cryst. Solids*, 364, 9–12.
- Djenadic, R., Sarkar, A., Clemens, O., Loho, C., Botros, M., Chakravadhanula, V. S.

- K., Kübel, C., Bhattacharya, S. S., Gandhi, A. S., and Hahn, H. (2017). “Multicomponent equiatomic rare earth oxides.” *Mater. Res. Lett.*, 5(2), 102–109.
- Dmitrienko, M. A., Legros, J. C., and Strizhak, P. A. (2018). “Experimental evaluation of main emissions during coal processing waste combustion.” *Environ. Pollut.*, 233, 299–305.
- Du, Q., Yan, J., Zhang, X., Li, J., Liu, X., Zhang, J., and Qi, X. (2020). “Phase evolution and dielectric properties of $\text{Ba}(\text{Ti}_{1/6}\text{Sn}_{1/6}\text{Zr}_{1/6}\text{Hf}_{1/6}\text{Nb}_{1/6}\text{Ga}_{1/6})\text{O}_3$ high-entropy perovskite ceramics.” *J. Mater. Sci. Mater. Electron.*, 31(10), 7760–7765.
- Dupuy, A. D., Wang, X., and Schoenung, J. M. (2019). “Entropic phase transformation in nanocrystalline high entropy oxides.” *Mater. Res. Lett.*, 7(2), 60–67.
- Eason, R. W. (2006). *Pulsed laser deposition of thin films: applications-led growth of functional materials*. (R. Eason, ed.), Hoboken, NJ, USA: John Wiley & Sons, Inc.
- Ekambaram, S., Iikubo, Y., and Kudo, A. (2007). “Combustion synthesis and photocatalytic properties of transition metal-incorporated ZnO.” *J. Alloys Compd.*, 433(1–2), 237–240.
- Ellmer, K. (2000). “Magnetron sputtering of transparent conductive zinc oxide: relation between the sputtering parameters and the electronic properties.” *J. Phys. D Appl. Phys.*, 33(4), R17.
- Erri, P., Pranda, P., and Varma, A. (2004). “Oxidizer-fuel interactions in aqueous combustion synthesis. 1. Iron(III) nitrate-model fuels.” *Ind. Eng. Chem. Res.*, 43(12), 3092–3096.
- Fahrenholtz, W. G., and Wuchina, E. J. (2014). *Ultra-high temperature ceramics : materials for extreme environment applications*. (W. G. Fahrenholtz, E. J. Wuchina, W. E. Lee, and Y. Zhou, eds.), Hoboken, NJ: John Wiley & Sons, Inc.
- Fauchais, P. (2004). “Understanding plasma spraying.” *J. Phys. D. Appl. Phys.*, 37, R86.

Fauchais, P., Vardelle, A., and Dussoubs, B. (2001). “Quo Vadis thermal spraying?” *J. Therm. Spray Technol.*, 10, 44–66.

Feng, D., Dong, Y., Zhang, L., Ge, X., Zhang, W., Dai, S., and Qiao, Z. A. (2020). “Holey lamellar high-entropy oxide as an ultra-high-activity heterogeneous catalyst for solvent-free aerobic oxidation of benzyl alcohol.” *Angew. Chemie.*, 132(44), 19503–19509.

Feuerbacher, M., Heidelmann, M., and Thomas, C. (2015). “Hexagonal high-entropy alloys.” *Mater. Res. Lett.*, 3(1), 1–6.

Fortunato, E., Barquinha, P., and Martins, R. (2012). “Oxide semiconductor thin-film transistors: A review of recent advances.” *Adv. Mater.*, 24(22), 2945–2986.

Fracchia, M., Ghigna, P., Pozzi, T., Anselmi Tamburini, U., Colombo, V., Braglia, L., and Torelli, P. (2020). “Stabilization by configurational entropy of the Cu(II) active site during CO Oxidation on $\text{Mg}_{0.2}\text{Co}_{0.2}\text{Ni}_{0.2}\text{Cu}_{0.2}\text{Zn}_{0.2}\text{O}$.” *J. Phys. Chem. Lett.*, 11(9), 3589–3593.

Fraigi, L. B., Lamas, D. G., and Walsøe De Reça, N. E. (2001). “Comparison between two combustion routes for the synthesis of nanocrystalline SnO_2 powders.” *Mater. Lett.*, 47(4–5), 262–266.

Frandsen, B. A., Petersen, K. A., Ducharme, N. A., Shaw, A. G., Gibson, E. J., Winn, B., Yan, J., Zhang, J., Manley, M. E., and Hermann, R. P. (2020). “Spin dynamics and a nearly continuous magnetic phase transition in an entropy-stabilized oxide antiferromagnet.” *Phys. Rev. Mater.*, 4(7), 74405.

Franklin, A. D. (2015). “Nanomaterials in transistors: From high-performance to thin-film applications.” *Science.*, 349(6249), aab2750.

Furukawa, H., Ko, N., Go, Y. B., Aratani, N., Choi, S. B., Choi, E., Yazaydin, A. O., Snurr, R. Q., O’Keeffe, M., Kim, J., and Yaghi, O. M. (2010). “Ultrahigh porosity in metal-organic frameworks.” *Science*, 329(5990), 424–8.

Gajula, G. R., Buddiga, L. R., Chidambara Kumar, K. N., Vattikunta, N., T, S. K.,

Nethala, G. P., and K, V. P. (2020). “An investigation on the conductivity, electric modulus and scaling behavior of electric modulus of barium titanate-lithium ferrite composite doped with Nb, Gd and Sm.” *Mater. Chem. Phys.*, 241, 122347.

Gao, X. Q., Zhao, K., Ke, H. B., Ding, D. W., Wang, W. H., and Bai, H. Y. (2011). “High mixing entropy bulk metallic glasses.” *J. Non. Cryst. Solids*, 357(21), 3557–3560.

Gazda, M., Miruszewski, T., Jaworski, D., Mielewczyk-Gryń, A., Skubida, W., Wachowski, S., Winiarz, P., Dzierzgowski, K., Łapiński, M., Szpunar, I., and Dzik, E. (2020). “Novel class of proton conducting materials - High entropy oxides.” *ACS Mater. Lett.*, 2(10), 1315–1321.

Gearhart, C. A. (1990). “Einstein before 1905: The early papers on statistical mechanics.” *Am. J. Phys.*, 58(5), 468–480.

Geng, G. Z., Liu, G. X., Shan, F. K., Liu, A., Zhang, Q., Lee, W. J., Shin, B. C., and Wu, H. Z. (2014). “Improved performance of InGaZnO thin-film transistors with Ta₂O₅/Al₂O₃ stack deposited using pulsed laser deposition.” *Curr. Appl. Phys.*, 14, S2–S6.

George, E. P., Raabe, D., and Ritchie, R. O. (2019). “High-entropy alloys.” *Nat. Rev. Mater.*, 4(8), 515–534.

Ghalmi, Y., Habelhames, F., Sayah, A., Bahloul, A., Nessark, B., Shalabi, M., and Nunzi, J. M. (2019a). “Capacitance performance of NiO thin films synthesized by direct and pulse potentiostatic methods.” *Ionics.*, 25(12), 6025–6033.

Ghigna, P., Airoidi, L., Fracchia, M., Callegari, D., Anselmi-Tamburini, U., D’Angelo, P., Pianta, N., Ruffo, R., Cibir, G., Souza, D. O. de, and Quartarone, E. (2020). “Lithiation mechanism in high-entropy oxides as anode materials for Li-ion batteries: An operando XAS study.” *ACS Appl. Mater. Interfaces*, 12(45), 50344–50354.

Gild, J., Braun, J., Kaufmann, K., Marin, E., Harrington, T., Hopkins, P., Vecchio, K., and Luo, J. (2019). “A high-entropy silicide: (Mo_{0.2}Nb_{0.2}Ta_{0.2}Ti_{0.2}W_{0.2})Si₂.” *J. Mater.*,

5(3), 337–343.

Gild, J., Samiee, M., Braun, J. L., Harrington, T., Vega, H., Hopkins, P. E., Vecchio, K., and Luo, J. (2018). “High-entropy fluorite oxides.” *J. Eur. Ceram. Soc.*, 38(10), 3578–3584.

Gild, J., Zhang, Y., Harrington, T., Jiang, S., Hu, T., Quinn, M. C., Mellor, W. M., Zhou, N., Vecchio, K., and Luo, J. (2016). “High-entropy metal diborides: A new class of high-entropy materials and a new type of ultrahigh temperature ceramics.” *Sci. Rep.*, 6(1), 1–10.

Gludovatz, B., Hohenwarter, A., Catoor, D., Chang, E. H., George, E. P., and Ritchie, R. O. (2014). “A fracture-resistant high-entropy alloy for cryogenic applications.” *Science*, 345(6201), 1153–1158.

Gorban', V. F., Andreyev, A. A., Kartmazov, G. N., Chikryzhov, A. M., Karpets, M. V., Dolomanov, A. V., Ostroverkh, A. A., and Kantsyr, E. V. (2017). “Production and mechanical properties of high-entropic carbide based on the TiZrHfVNbTa multicomponent alloy.” *J. Superhard Mater.*, 39(3), 166–171.

Gordon, L. (1952). “Precipitation from homogeneous solution.” *Anal. Chem.*, 24(3), 459–462.

Grzesik, Z., Smoła, G., Stygar, M., Dąbrowa, J., Zajusz, M., Mroczka, K., and Danielewski, M. (2019). “Defect structure and transport properties in (Co,Cu,Mg,Ni,Zn)O high entropy oxide.” *J. Eur. Ceram. Soc.*, 39(14), 4292–4298.

Guo, M., Lu, J., Wu, Y., Wang, Y., and Luo, M. (2011). “UV and visible Raman studies of oxygen vacancies in rare-earth-doped ceria.” *Langmuir*, 27(7), 3872–3877.

Guo, S., Hu, Q., Ng, C., and Liu, C. T. (2013). “More than entropy in high-entropy alloys: Forming solid solutions or amorphous phase.” *Intermetallics*, 41, 96–103.

Guo, T., Du, J., and Li, J. (2016). “The effects of ceria morphology on the properties of Pd/ceria catalyst for catalytic oxidation of low-concentration methane.” *J. Mater. Sci.*, 51(24), 10917–10925.

Hajra, S., Sahu, M., Purohit, V., and Choudhary, R. N. P. (2019). “Dielectric, conductivity and ferroelectric properties of lead-free electronic ceramic: $0.6\text{Bi}(\text{Fe}_{0.98}\text{Ga}_{0.02})\text{O}_3 - 0.4\text{BaTiO}_3$.” *Heliyon*, 5(5), e01654.

Harrington, T. J., Gild, J., Sarker, P., Toher, C., Rost, C. M., Dippo, O. F., McElfresh, C., Kaufmann, K., Marin, E., Borowski, L., Hopkins, P. E., Luo, J., Curtarolo, S., Brenner, D. W., and Vecchio, K. S. (2019). “Phase stability and mechanical properties of novel high entropy transition metal carbides.” *Acta Mater.*, 166, 271–280.

He, Y., Day, T., Zhang, T., Liu, H., Shi, X., Chen, L., and Snyder, G. J. (2014). “High thermoelectric performance in non-toxic earth-abundant copper sulfide.” *Adv. Mater.*, 26(23), 3974–3978.

He, Y., Wang, X., Wang, C., Liu, S., Li, L., Wu, Y., and Wang, Z. (2023). “Significantly improved corrosion resistance of high-entropy rare-earth silicate multiphase ceramics against molten CMAS.” *J. Am. Ceram. Soc.*, 106(5), 2744–2751.

Hemphill, M. A., Yuan, T., Wang, G. Y., Yeh, J. W., Tsai, C. W., Chuang, A., and Liaw, P. K. (2012). “Fatigue behavior of $\text{Al}_{0.5}\text{CoCrCuFeNi}$ high entropy alloys.” *Acta Mater.*, 60(16), 5723–5734.

Hirakawa, T., Shimokawa, Y., Tokuzumi, W., Sato, T., Tsushida, M., Yoshida, H., Hinokuma, S., Ohyama, J., and MacHida, M. (2019). “Multicomponent spinel oxide solid solutions: A possible alternative to platinum group metal three-way catalysts.” *ACS Catal.*, 9(12), 11763–11773.

Holleck, H. (1986). “Material selection for hard coatings.” *J. Vac. Sci. Technol. A Vacuum, Surfaces, Film.*, 4(6), 2661–2669.

Hong, W., Chen, F., Shen, Q., Han, Y. H., Fahrenholtz, W. G., and Zhang, L. (2019). “Microstructural evolution and mechanical properties of $(\text{Mg},\text{Co},\text{Ni},\text{Cu},\text{Zn})\text{O}$ high-entropy ceramics.” *J. Am. Ceram. Soc.*, 102(4), 2228–2237.

Hong, X., and Liao, L. (2020). “Metal oxide dielectrics.” *Solut. Process. Met. Oxide Thin Film. Electron. Appl.*, Elsevier, 31–39.

Hossain, M. K., Sotelo, P., Sarker, H. P., Galante, M. T., Kormányos, A., Longo, C., Macaluso, R. T., Huda, M. N., Janáky, C., and Rajeshwar, K. (2019). “Rapid one-pot synthesis and photoelectrochemical properties of copper vanadates.” *ACS Appl. Energy Mater.*, 2(4), 2837–2847.

Hsieh, M.-H., Tsai, M.-H., Shen, W.-J., and Yeh, J.-W. (2013). “Structure and properties of two Al–Cr–Nb–Si–Ti high-entropy nitride coatings.” *Surf. Coatings Technol.*, 221, 118–123.

Hu, Y., Jiang, H., Lau, K. M., and Li, Q. (2018). “Chemical vapor deposited monolayer MoS₂ top-gate MOSFET with atomic-layer-deposited ZrO₂ as gate dielectric.” *Semicond. Sci. Technol.*, 33(4), 45004.

Huang, P. K., and Yeh, J. W. (2010). “Inhibition of grain coarsening up to 1000 °C in (AlCrNbSiTiV)N superhard coatings.” *Scr. Mater.*, 62(2), 105–108.

Ishai, P. Ben, Talary, M. S., Caduff, A., Levy, E., and Feldman, Y. (2013). “Electrode polarization in dielectric measurements: A review.” *Meas. Sci. Technol.*, 24(10), 102001.

Jacobson, V., Diercks, D., To, B., Zakutayev, A., and Brennecke, G. (2021). “Thin film growth effects on electrical conductivity in entropy stabilized oxides.” *J. Eur. Ceram. Soc.*, 41(4), 2617–2624.

Jain, S. R., Adiga, K. C., and Pai Verneker, V. R. (1981). “A new approach to thermochemical calculations of condensed fuel-oxidizer mixtures.” *Combust. Flame*, 40, 71–79.

James, S. L. (2003). “Metal-organic frameworks.” *Chem. Soc. Rev.*, 32, 276–288.

Jeng, Y. L., and Lavernia, E. J. (1994). “Processing of molybdenum disilicide.” *J. Mater. Sci.*, 29(10), 2557–2571.

Jiang, H. qing, Endo, H., Natori, H., Nagai, M., and Kobayashi, K. (2008). “Fabrication and photoactivities of spherical-shaped BiVO₄ photocatalysts through solution combustion synthesis method.” *J. Eur. Ceram. Soc.*, 28(15), 2955–2962.

Jiang, N., Zhou, X., Jiang, Y. F., Zhao, Z. W., Ma, L. B., Shen, C. C., Liu, Y. N., Yuan, C. Z., Sahar, S., and Xu, A. W. (2018a). “Oxygen deficient Pr₆O₁₁ nanorod supported palladium nanoparticles: Highly active nanocatalysts for styrene and 4-nitrophenol hydrogenation reactions.” *RSC Adv.*, 8(31), 17504–17510.

Jiang, S., Hu, T., Gild, J., Zhou, N., Nie, J., Qin, M., Harrington, T., Vecchio, K., and Luo, J. (2018b). “A new class of high-entropy perovskite oxides.” *Scr. Mater.*, 142, 116–120.

Jimenez-Segura, M. P., Takayama, T., Bérardan, D., Hoser, A., Reehuis, M., Takagi, H., and Dragoë, N. (2019). “Long-range magnetic ordering in rocksalt-type high-entropy oxides.” *Appl. Phys. Lett.*, 114(12).

Jin, T., Sang, X., Unocic, R. R., Kinch, R. T., Liu, X., Hu, J., Liu, H., and Dai, S. (2018). “Mechanochemical-assisted synthesis of high-entropy metal nitride via a soft urea strategy.” *Adv. Mater.*, 30(23), 1707512.

Juan, C. C., Tsai, M. H., Tsai, C. W., Lin, C. M., Wang, W. R., Yang, C. C., Chen, S. K., Lin, S. J., and Yeh, J. W. (2015). “Enhanced mechanical properties of HfMoTaTiZr and HfMoNbTaTiZr refractory high-entropy alloys.” *Intermetallics*, 62, 76–83.

Kaltenbrunner, M., Sekitani, T., Reeder, J., Yokota, T., Kuribara, K., Tokuhara, T., Drack, M., Schwödiauer, R., Graz, I., Bauer-Gogonea, S., Bauer, S., and Someya, T. (2013). “An ultra-lightweight design for imperceptible plastic electronics.” *Nature*, 499(7459), 458–463.

Kaminaga, K., Sei, R., Hayashi, K., Happo, N., Tajiri, H., Oka, D., Fukumura, T., and Hasegawa, T. (2016). “A divalent rare earth oxide semiconductor: Yttrium monoxide.” *Appl. Phys. Lett.*, 108(12), 122102.

Kang, W., Ozgur, D. O., and Varma, A. (2018). “Solution combustion synthesis of high surface area CeO₂ nanopowders for catalytic applications: reaction mechanism and properties.” *ACS Appl. Nano Mater.*, 1(2), 675–685.

Kikuchi, Y., Bouyrie, Y., Ohta, M., Suekuni, K., Aihara, M., and Takabatake, T. (2016).

“Vanadium-free colusites $\text{Cu}_{26}\text{A}_2\text{Sn}_6\text{S}_{32}$ ($\text{A} = \text{Nb}, \text{Ta}$) for environmentally friendly thermoelectrics.” *J. Mater. Chem. A*, 4(39), 15207–15214.

Kim, B., Jang, S., Prabhumirashi, P. L., Geier, M. L., Hersam, M. C., and Dodabalapur, A. (2013a). “Low voltage, high performance inkjet printed carbon nanotube transistors with solution processed ZrO_2 gate insulator.” *Appl. Phys. Lett.*, 103(8), 082119.

Kim, C. H., Castro-Carranza, A., Estrada, M., Estrada, A., Horowitz, Y., Horowitz, G., and Iniguez, B. (2013b). “A compact model for organic field-effect transistors with improved output asymptotic behaviors.” *IEEE Trans. Electron Devices*, 60(3), 1136–1141.

Kim, B., Jang, S., Geier, M. L., Prabhumirashi, P. L., Hersam, M. C., and Dodabalapur, A. (2014a). “High-speed, inkjet-printed carbon nanotube/zinc tin oxide hybrid complementary ring oscillators.” *Nano Lett.*, 14(6), 3683–3687.

Kim, C. H., Bonnassieux, Y., and Horowitz, G. (2014b). “Compact DC modeling of organic field-effect transistors: Review and perspectives.” *IEEE Trans. Electron Devices*, 61(2), 278–287.

Kim, M. G., Kanatzidis, M. G., Facchetti, A., and Marks, T. J. (2011). “Low-temperature fabrication of high-performance metal oxide thin-film electronics via combustion processing.” *Nat. Mater.*, 10(5), 382–388.

Kim, M. G., Hennek, J. W., Kim, H. S., Kanatzidis, M. G., Facchetti, A., and Marks, T. J. (2012). “Delayed ignition of autocatalytic combustion precursors: Low-temperature nanomaterial binder approach to electronically functional oxide films.” *J. Am. Chem. Soc.*, 134(28), 11583–11593.

Kim, Y., Park, K. H., Chung, T. H., Bark, H. J., Yi, J. Y., Choi, W. C., Kim, E. K., Lee, J. W., and Lee, J. Y. (2001). “Ultralarge capacitance-voltage hysteresis and charge retention characteristics in metal oxide semiconductor structure containing nanocrystals deposited by ion-beam-assisted electron beam deposition.” *Appl. Phys. Lett.*, 78(7), 934–936.

Kingsley, J. J., and Patil, K. C. (1988). "A novel combustion process for the synthesis of fine particle α -alumina and related oxide materials." *Mater. Lett.*, 6(11–12), 427–432.

Kirnbauer, A., Spadt, C., Koller, C. M., Kolozsvári, S., and Mayrhofer, P. H. (2019). "High-entropy oxide thin films based on Al–Cr–Nb–Ta–Ti." *Vacuum*, 168, 108850.

Kolthoff, I. M. (1932). "Theory of coprecipitation. the formation and properties of crystalline precipitates." *J. Phys. Chem.*, 36(3), 860–881.

Kotsonis, G. N., Meisenheimer, P. B., Miao, L., Roth, J., Wang, B., Shafer, P., Engel-Herbert, R., Alem, N., Heron, J. T., Rost, C. M., and Maria, J. P. (2020). "Property and cation valence engineering in entropy-stabilized oxide thin films." *Phys. Rev. Mater.*, 4(10), 100401.

Kotsonis, G. N., Rost, C. M., Harris, D. T., and Maria, J. P. (2018). "Epitaxial entropy-stabilized oxides: growth of chemically diverse phases via kinetic bombardment." *MRS Commun.*, 8(3), 1371–1377.

Krawczyk, P. A., Jurczyszyn, M., Pawlak, J., Salamon, W., Baran, P., Kmita, A., Gondek, Ł., Sikora, M., Kapusta, C., Strączek, T., Wyrwa, J., and Żywczak, A. (2020). "High-entropy perovskites as multifunctional metal oxide semiconductors: synthesis and characterization of $(\text{Gd}_{0.2}\text{Nd}_{0.2}\text{La}_{0.2}\text{Sm}_{0.2}\text{Y}_{0.2})\text{CoO}_3$." *ACS Appl. Electron. Mater.*, 2(10), 3211–3220.

Kumar, P. R., Jung, Y. H., Bharathi, K. K., Lim, C. H., and Kim, D. K. (2014). "High capacity and low cost spinel Fe_3O_4 for the Na-ion battery negative electrode materials." *Electrochim. Acta*, 146, 503–510.

Kumari, N., Kumar, V., and Singh, S. K. (2014). "Synthesis, structural and dielectric properties of Cr^{3+} substituted Fe_3O_4 nano-particles." *Ceram. Int.*, 40, 12199–12205.

Kwon, H. J., Jang, J., and Grigoropoulos, C. P. (2016). "Laser direct writing process for making electrodes and high- κ Sol-Gel ZrO_2 for boosting performances of MoS_2 transistors." *ACS Appl. Mater. Interfaces*, 8(14), 9314–9318.

- Lai, C. H., Lin, S. J., Yeh, J. W., and Chang, S. Y. (2006). "Preparation and characterization of AlCrTaTiZr multi-element nitride coatings." *Surf. Coatings Technol.*, 201(6), 3275–3280.
- Lai, W., Wang, Y., Morelli, D. T., and Lu, X. (2015). "From bonding asymmetry to anharmonic rattling in $\text{Cu}_{12}\text{Sb}_4\text{S}_{13}$ tetrahedrites: When lone-pair electrons are not so lonely." *Adv. Funct. Mater.*, 25(24), 3648–3657.
- Lei, L., Ohfuji, H., Irifune, T., Qin, J., Zhang, X., and Shinmei, T. (2012). "Disorder-activated Raman spectra of cubic rocksalt-type $\text{Li}_{(1-x)/2}\text{Ga}_{(1-x)/2}\text{M}_x\text{O}$ (M = Mg, Zn) alloys." *J. Appl. Phys.*, 112(4), 43501.
- Lei, Z., Liu, X., Wang, H., Wu, Y., Jiang, S., and Lu, Z. (2019). "Development of advanced materials via entropy engineering." *Scr. Mater.*, 165, 164–169.
- Li, Z., Pradeep, K. G., Deng, Y., Raabe, D., and Tasan, C. C. (2016). "Metastable high-entropy dual-phase alloys overcome the strength–ductility trade-off." *Nature*, 534(7606), 227–230.
- Li, F., Zhou, L., Liu, J. X., Liang, Y., and Zhang, G. J. (2019). "High-entropy pyrochlores with low thermal conductivity for thermal barrier coating materials." *J. Adv. Ceram.*, 8(4), 576–582.
- Li, H., Zhu, H., Zhang, S., Zhang, N., Du, M., and Chai, Y. (2020a). "Nano high-entropy materials: Synthesis strategies and catalytic applications." *Small Struct.*, 1(2), 2000033.
- Li, J., Shen, Z., Chen, X., Yang, S., Zhou, W., Wang, M., Wang, L., Kou, Q., Liu, Y., Li, Q., Xu, Z., Chang, Y., Zhang, S., and Li, F. (2020b). "Grain-orientation-engineered multilayer ceramic capacitors for energy storage applications." *Nat. Mater.*, 19(9), 999–1005.
- Lim, K. R. G., Handoko, A. D., Nemani, S. K., Wyatt, B., Jiang, H. Y., Tang, J., Anasori, B., and Seh, Z. W. (2020). "Rational design of two-dimensional transition metal carbide/nitride (MXene) hybrids and nanocomposites for catalytic energy storage

and conversion.” *ACS Nano*, American Chemical Society.

Lin, M. I., Tsai, M. H., Shen, W. J., and Yeh, J. W. (2010). “Evolution of structure and properties of multi-component (AlCrTaTiZr)O_x films.” *Thin Solid Films*, 518(10), 2732–2737.

Lipatov, A., Alhabeab, M., Lu, H., Zhao, S., Loes, M. J., Vorobeva, N. S., Dall’Agnese, Y., Gao, Y., Gruverman, A., Gogotsi, Y., and Sinitskii, A. (2020). “Electrical and elastic properties of individual single-layer Nb₄C₃T_x MXene Flakes.” *Adv. Electron. Mater.*, 6(4), 1901382.

Liu, Z. G., Ouyang, J. H., and Zhou, Y. (2009). “Structural evolution and thermophysical properties of (Sm_xGd_{1-x})₂Zr₂O₇ (0 ≤ x ≤ 1.0) ceramics.” *J. Alloys Compd.*, 472(1–2), 319–324.

Liu, G. X., Liu, A., Shan, F. K., Meng, Y., Shin, B. C., Fortunato, E., and Martins, R. (2014). “High-performance fully amorphous bilayer metal-oxide thin film transistors using ultra-thin solution-processed ZrO_x dielectric.” *Appl. Phys. Lett.*, 105(11), 113509.

Liu, A., Zhu, H., Sun, H., Xu, Y., and Noh, Y. Y. (2018). “Solution processed metal oxide high-κ dielectrics for emerging transistors and circuits.” *Adv. Mater.*, 30(33), 1706364.

Liu, D., Wen, T., Ye, B., and Chu, Y. (2019). “Synthesis of superfine high-entropy metal diboride powders.” *Scr. Mater.*, 167, 110–114.

Liu, H., and Ning, S. (2020). “Fabrication of high-entropy disilicide nanopowders via molten salt-assisted magnesium thermal reduction.” *Res. Sq. Rapid Commun.*, 1–9.

Liu, D., Huang, Y., Liu, L., and Zhang, L. (2020a). “A novel of MSi₂ high-entropy silicide: Be expected to improve mechanical properties of MoSi₂.” *Mater. Lett.*, 268, 127629.

Liu, D., Peng, X., Liu, J., Chen, L., Yang, Y., and An, L. (2020b). “Ultrafast synthesis of entropy-stabilized oxide at room temperature.” *J. Eur. Ceram. Soc.*, 40(6), 2504–2508.

- Liu, J., Ren, K., Ma, C., Du, H., and Wang, Y. (2020c). “Dielectric and energy storage properties of flash-sintered high-entropy $(\text{Bi}_{0.2}\text{Na}_{0.2}\text{K}_{0.2}\text{Ba}_{0.2}\text{Ca}_{0.2})\text{TiO}_3$ ceramic.” *Ceram. Int.*, 46(12), 20576–20581.
- Liu, J., Shao, G., Liu, D., Chen, K., Wang, K., Ma, B., Ren, K., and Wang, Y. (2020d). “Design and synthesis of chemically complex ceramics from the perspective of entropy.” *Mater. Today Adv.*, 100114.
- Liu, L., Zhang, L., and Liu, D. (2020e). “Complete elimination of pest oxidation by high entropy refractory metallic silicide $(\text{Mo}_{0.2}\text{W}_{0.2}\text{Cr}_{0.2}\text{Ta}_{0.2}\text{Nb}_{0.2})\text{Si}_2$.” *Scr. Mater.*, 189, 25–29.
- Liu, Y., Jia, D., Zhou, Y., Zhou, Y., Zhao, J., Nian, H., and Liu, B. (2020f). “ $\text{Zn}_{0.1}\text{Ca}_{0.1}\text{Sr}_{0.4}\text{Ba}_{0.4}\text{ZrO}_3$: A non-equimolar multicomponent perovskite ceramic with low thermal conductivity.” *J. Eur. Ceram. Soc.*, 40(15), 6272–6277.
- Lo, S. H., Buchanan, D. A., Taur, Y., and Wang, W. (1997). “Quantum-mechanical modeling of electron tunneling current from the inversion layer of ultra-thin-oxide nMOSFET’s.” *IEEE Electron Device Lett.*, 18(5), 209–211.
- Lökçü, E., Toparli, Ç., and Anik, M. (2020). “Electrochemical performance of $(\text{MgCoNiZn})_{1-x}\text{Li}_x\text{O}$ high-entropy oxides in lithium-ion batteries.” *ACS Appl. Mater. Interfaces*, 12(21), 23860–23866.
- Lou, Y., Dai, C., Chang, W., Qian, H., Huang, L., Du, C., and Zhang, D. (2020). “Microbiologically influenced corrosion of $\text{FeCoCrNiMo}_{0.1}$ high-entropy alloys by marine *Pseudomonas aeruginosa*.” *Corros. Sci.*, 165, 108390.
- Lou, Y., Guan, L., Wang, Y., Zhou, X., Li, M., Zhao, B., Gao, Q., Zhang, X., Wang, H., and Zhang, R. (2023). “Synthesis of $(\text{MgCoNiCuZn})\text{O}$ high-entropy oxide composites by microwave heating.” *J. Mater. Sci. Mater. Electron.*, 34(2), 1–9.
- Lowndes, D. H., Geohegan, D. B., Puretzky, A. A., Norton, D. P., and Rouleau, C. M. (1996). “Synthesis of novel thin-film materials by pulsed laser deposition.” *Science.*, 273(5277), 898–903.

Lundin, D., Minea, T., and Gudmundsson, J. T. (2019). "Introduction to magnetron sputtering." *High Power Impuls. Magnetron Sputtering Fundam. Technol. Challenges Appl.*, Elsevier, 1–48.

Lunkenheimer, P., Bobnar, V., Pronin, A. V., Ritus, A. I., Volkov, A. A., and Loidl, A. (2002). "Origin of apparent colossal dielectric constants." *Phys. Rev. B*, 66(5), 52105.

Lunkenheimer, P., Krohns, S., Riegg, S., Ebbinghaus, S. G., Reller, A., and Loidl, A. (2009). "Colossal dielectric constants in transition-metal oxides." *Eur. Phys. J. Spec. Top.*, 180(1), 61–89.

Lv, R., Robinson, J. A., Schaak, R. E., Sun, D., Sun, Y., Mallouk, T. E., and Terrones, M. (2015). "Transition metal dichalcogenides and beyond: Synthesis, properties, and applications of single- and few-layer nanosheets." *Acc. Chem. Res.*, 48(1), 56–64.

Ma, L., Wang, L., Zhang, T., and Inoue, A. (2002). "Bulk glass formation of Ti-Zr-Hf-Cu-M (M=Fe, Co, Ni) Alloys." *Mater. Trans.*, 43(2), 277–280.

Maier, J., Prill, S., and Reichert, B. (1988). "Space charge effects in polycrystalline, micropolycrystalline and thin film samples: Application to AgCl and AgBr." *Solid State Ionics*, 28, 1465–1469.

Maiyalagan, T., Jarvis, K. A., Therese, S., Ferreira, P. J., and Manthiram, A. (2014). "Spinel-type lithium cobalt oxide as a bifunctional electrocatalyst for the oxygen evolution and oxygen reduction reactions." *Nat. Commun.*, 5(1), 1–8.

Manikandan, A., Kennedy, L. J., Bououdina, M., and Vijaya, J. J. (2014). "Synthesis, optical and magnetic properties of pure and Co-doped ZnFe₂O₄ nanoparticles by microwave combustion method." *J. Magn. Magn. Mater.*, 349, 249–258.

Manikandan, P., Ananth, M. V., Prem Kumar, T., Raju, M., Periasamy, P., and Manimaran, K. (2011). "Solution combustion synthesis of layered LiNi_{0.5}Mn_{0.5}O₂ and its characterization as cathode material for lithium-ion cells." *J. Power Sources*, 196(23), 10148–10155.

Manoharan, S. S., and Patil, K. C. (1993). "Combustion route to fine particle perovskite

oxides.” *J. Solid State Chem.*, 102(1), 267–276.

Mao, A., Quan, F., Xiang, H. Z., Zhang, Z.-G., Kuramoto, K., and Xia, A. L. (2019a). “Facile synthesis and ferrimagnetic property of spinel (CoCrFeMnNi)₃O₄ high-entropy oxide nanocrystalline powder.” *J. Mol. Struct.*, 1194, 11–18.

Mao, A., Xiang, H. Z., Zhang, Z. G., Kuramoto, K., Yu, H., and Ran, S. (2019b). “Solution combustion synthesis and magnetic property of rock-salt (Co_{0.2}Cu_{0.2}Mg_{0.2}Ni_{0.2}Zn_{0.2})O high-entropy oxide nanocrystalline powder.” *J. Magn. Mater.*, 484, 245–252.

Mao, A., Xie, H. X., Xiang, H. Z., Zhang, Z. G., Zhang, H., and Ran, S. (2020). “A novel six-component spinel-structure high-entropy oxide with ferrimagnetic property.” *J. Magn. Mater.*, 503, 166594.

Marik, S., Singh, D., Gonano, B., Veillon, F., Pelloquin, D., and Bréard, Y. (2020a). “Long range magnetic ordering and magneto-(di) electric effect in a new class of high entropy spinel oxide.” *Scr. Mater.*, 183, 107–110.

Marik, S., Singh, D., Gonano, B., Veillon, F., Pelloquin, D., and Bréard, Y. (2020b). “Enhanced magnetic frustration in a new high entropy diamond lattice spinel oxide.” *Scr. Mater.*, 186, 366–369.

Mathis, T. S., Maleski, K., Goad, A., Sarycheva, A., Anayee, M., Foucher, A. C., Hantanasirisakul, K., Shuck, C. E., Stach, E. A., and Gogotsi, Y. (2021). “Modified MAX phase synthesis for environmentally stable and highly conductive Ti₃C₂ MXene.” *ACS Nano*, 15(4), 6420–6429.

Matkovich, V. I. (Ed.). (1977). *Boron and refractory borides*. Berlin, Heidelberg: Springer.

Mattox, D. M. (2007). *Handbook of physical vapor deposition (PVD) processing*. *Handb. Phys. Vap. Depos. Process.*, Burlington, USA: Elsevier Inc.

Mayrhofer, P. H., Kirnbauer, A., Ertelthaler, P., and Koller, C. M. (2018). “High-entropy ceramic thin films; A case study on transition metal diborides.” *Scr. Mater.*,

149, 93–97.

Mazza, A. R., Skoropata, E., Sharma, Y., Lapano, J., Heitmann, T. W., Musico, B. L., Keppens, V., Gai, Z., Freeland, J. W., Charlton, T. R., Brahlek, M. J., Moreo, A., Dagotto, E., and Ward, T. Z. (2021). “Designer magnetism in high entropy oxides.” *Adv. Sci.*, 9, 2200391

McCormack, S. J., and Navrotsky, A. (2021). “Thermodynamics of high entropy oxides.” *Acta Mater.*, 202, 1–21.

McKamey, C. G., Tortorelli, P. F., DeVan, J. H., and Carmichael, C. A. (1992). “A study of pest oxidation in polycrystalline MoSi₂.” *J. Mater. Res.*, 7(10), 2747–2755.

McKenna, K., Shluger, A., Iglesias, V., Porti, M., Nafría, M., Lanza, M., and Bersuker, G. (2011). “Grain boundary mediated leakage current in polycrystalline HfO₂ films.” *Microelectron. Eng.*, 88(7), 1272–1275.

Meisenheimer, P. B., Kratofil, T. J., and Heron, J. T. (2017). “Giant enhancement of exchange coupling in entropy-stabilized oxide heterostructures.” *Sci. Rep.*, 7(1), 13344.

Mekhmer, G. A. H., and Balboul, B. A. A. (2001). “Thermal genesis course and characterization of lanthanum oxide.” *Colloids Surfaces A Physicochem. Eng. Asp.*, 181(1–3), 19–29.

Melnikov, P., Arkhangelsky, I. V., Nascimento, V. A., Oliveira, L. C. S. de, Rodrigues Guimarães, W., and Zanon, L. Z. (2018). “Thermal decomposition of praseodymium nitrate hexahydrate Pr(NO₃)₃·6H₂O.” *J. Therm. Anal. Calorim.*, 133(2), 929–934.

Melnikov, P., Arkhangelsky, I. V., Nascimento, V. A., Silva, A. F., and Zanon, L. Z. (2014). “Thermolysis mechanism of samarium nitrate hexahydrate.” *J. Therm. Anal. Calorim.*, 118(3), 1537–1541.

Melnikov, P., Nascimento, V. A., Zanon, L. Z., and Silva, A. F. (2013). “Mechanism of thermal decomposition of yttrium nitrate hexahydrate, Y(NO₃)₃·6H₂O and modeling of intermediate oxynitrates.” *J. Therm. Anal. Calorim.*, 111(1), 115–119.

Merzhanov, A. G. (2004). "The chemistry of self-propagating high-temperature synthesis." *J. Mater. Chem.*, 14(12), 1779-1786.

Messing, G. L., Zhang, S. C., and Jayanthi, G. V. (1993). "Ceramic Powder Synthesis by Spray Pyrolysis." *J. Am. Ceram. Soc.*, 76(11), 2707–2726.

Mihaylov, M. Y., Zdravkova, V. R., Ivanova, E. Z., Aleksandrov, H. A., Petkov, P. S., Vayssilov, G. N., and Hadjiivanov, K. I. (2021). "Infrared spectra of surface nitrates: Revision of the current opinions based on the case study of ceria." *J. Catal.*, 394, 245–258.

Miracle, D. B., and Senkov, O. N. (2017). "A critical review of high entropy alloys and related concepts." *Acta Mater.*, 122, 448–511.

Miranda L. Cheney, Gregory J. McManus, Jason A. Perman, Zhenqiang Wang, A., Zaworotko, M. J., Cheney, M. L., McManus, G. J., Perman, J. A., Zhenqiang, W., and Zaworotko, M. J. (2007). "The role of cocrystals in solid-state synthesis: Cocrystal-controlled solid-state synthesis of imides." *Cryst. Growth Des.*, 7(4), 616–617.

Mizushima, K., Jones, P. C., Wiseman, P. J., and Goodenough, J. B. (1980). "Li_xCoO₂ (0 < x < 1): A new cathode material for batteries of high energy density." *Mater. Res. Bull.*, 15(6), 783–789.

Moore, G. E. (1998). "Cramming more components onto integrated circuits." *Proc. IEEE*, 86(1), 82–85.

Moraes, V., Riedl, H., Fuger, C., Polcik, P., Bolvardi, H., Holec, D., and Mayrhofer, P. H. (2018). "Ab initio inspired design of ternary boride thin films christian doppler laboratory for application oriented coating development at the open." *Sci. Rep.*, 8(1), 9288.

Morales, W., Cason, M., Aina, O., Tacconi, N. R. De, and Rajeshwar, K. (2008). "Combustion synthesis and characterization of nanocrystalline WO₃." *J. Am. Chem. Soc.*, 130(20), 6318–6319.

Mukasyan, A. S., and Dinka, P. (2007). "Novel approaches to solution-combustion

synthesis of nanomaterials.” *Int. J. Self-Propagating High-Temperature Synth.*, 16(1), 23–35.

Murty, B. S., Yeh, J. W., Ranganathan, S., and Bhattacharjee, P. P. (2019). *High-Entropy Alloys*. Cambridge, USA; Elsevier.

Musicó, B. L., Gilbert, D., Ward, T. Z., Page, K., George, E., Yan, J., Mandrus, D., and Keppens, V. (2020). “The emergent field of high entropy oxides: Design, prospects, challenges, and opportunities for tailoring material properties.” *APL Mater.*, 8(4), 040912.

Nagaraja, R., Girija, C. R., Nagabhushana, B. M., Donappa, N., and Manjunatha Sastry, K. (2011). “Solution combustion synthesis, characterization and photocatalytic activity of nanosized ZnO catalyst for textile industrial dye effluents degradation.” *Asian J. Chem.*, 23(11), 5040–5044.

Nagasubramanian, G., and Doughty, D. H. (2004). “Electrical characterization of all-solid-state thin film batteries.” *J. Power Sources*, 136, 395–400.

Nemani, S. K., Zhang, B., Wyatt, B. C., Hood, Z. D., Manna, S., Khaledialidusti, R., Hong, W., Sternberg, M. G., Sankaranarayanan, S. K. R. S., and Anasori, B. (2021). “High-entropy 2D carbide MXenes: TiVNbMoC₃ and TiVCrMoC₃.” *ACS Nano*, 15(8), 12815–12825.

Nguyen, T. X., Patra, J., Chang, J. K., and Ting, J. M. (2020a). “High entropy spinel oxide nanoparticles for superior lithiation-delithiation performance.” *J. Mater. Chem. A*, 8(36), 18963–18973.

Nguyen, T. X., Su, Y.-H., Hatrick-Simpers, J., Joress, H., Nagata, T., Chang, K.-S., Sarker, S., Mehta, A., and Ting, J.-M. (2020b). “Exploring the first high-entropy thin film libraries: Composition spread-controlled crystalline structure.” *ACS Comb. Sci.*, 22(12), 858–866.

Ni, Y., Zhu, Y., and Ma, X. (2011). “A simple solution combustion route for the preparation of metal-doped TiO₂ nanoparticles and their photocatalytic degradation

properties.” *Dalt. Trans.*, 40(14), 3689–3694.

Nitta, N., Wu, F., Lee, J. T., and Yushin, G. (2015). “Li-ion battery materials: Present and future.” *Mater. Today*, Elsevier B.V.

Nketia-Yawson, B., Kang, S. J., Tabi, G. D., Perinot, A., Caironi, M., Facchetti, A., and Noh, Y. Y. (2017). “Ultrahigh mobility in solution-processed solid-state electrolyte-gated transistors.” *Adv. Mater.*, 29(16), 1605685.

Okejiri, F., Zhang, Z., Liu, J., Liu, M., Yang, S., and Dai, S. (2020). “Room-temperature synthesis of high-entropy perovskite oxide nanoparticle catalysts through ultrasonication-based method.” *ChemSusChem*, 13(1), 111–115.

Oliveira, M. A., Peterson, M. L., and Davey, R. J. (2011). “Relative enthalpy of formation for co-crystals of small organic molecules.” *Cryst. Growth Des.*, 11(2), 449–457.

Omri, A., Dhahri, E., Costa, B. F. O., and Valente, M. A. (2020). “Structural, electric and dielectric properties of $\text{Ni}_{0.5}\text{Zn}_{0.5}\text{FeCoO}_4$ ferrite prepared by sol-gel.” *J. Magn. Magn. Mater.*, 499, 166243.

Osada, M., and Sasaki, T. (2012). “Two-dimensional dielectric nanosheets: Novel nanoelectronics from nanocrystal building blocks.” *Adv. Mater.*, 24(2), 210–228.

Osenciat, N., Bérardan, D., Dragoe, D., Léridon, B., Holé, S., Meena, A. K., Franger, S., and Dragoe, N. (2019). “Charge compensation mechanisms in Li-substituted high-entropy oxides and influence on Li superionic conductivity.” *J. Am. Ceram. Soc.*, 102(10), 6156–6162.

Otto, F., Yang, Y., Bei, H., and George, E. P. (2013). “Relative effects of enthalpy and entropy on the phase stability of equiatomic high-entropy alloys.” *Acta Mater.*, 61(7), 2628–2638.

Özgür, Ü., Alivov, Y. I., Liu, C., Teke, A., Reshchikov, M. A., Doğan, S., Avrutin, V., Cho, S. J., and Morkoç, H. (2005). “A comprehensive review of ZnO materials and devices.” *J. Appl. Phys.*, 98(4), 041301.

Padmasree, K. P., Kanchan, D. K., and Kulkarni, A. R. (2006). "Impedance and modulus studies of the solid electrolyte system $20\text{CdI}_2-80[\text{xAg}_2\text{O}-\text{y}(0.7\text{V}_2\text{O}_5-0.3\text{B}_2\text{O}_3)]$, where $1 \leq \text{x/y} \leq 3$." *Solid State Ionics*, 177, 475–482.

Pasquarelli, R. M., Ginley, D. S., and O'hayre, R. (2011). "Solution processing of transparent conductors: From flask to film." *Chem. Soc. Rev.*, 40(11), 5406–5441.

Patel, R. K., Ojha, S. K., Kumar, S., Saha, A., Mandal, P., Freeland, J. W., and Middey, S. (2020). "Epitaxial stabilization of ultra thin films of high entropy perovskite." *Appl. Phys. Lett.*, 116(7), 71601.

Patil, K. C., Aruna, S. T., and Mimani, T. (2002). "Combustion synthesis: An update." *Curr. Opin. Solid State Mater. Sci.*, 6(6), 507–512.

Patil, K. C., Hegde, M. S., Rattan, T., and Aruna, S. T. (2008). *Chemistry of Nanocrystalline Oxide Materials. Chem. Nanocrystalline Oxide Mater.*, Singapore: World Scientific.

Pawłowski, L. (2008). *The science and engineering of thermal spray coatings.*, England; John Wiley & Sons.

Pązik, R., Zięcina, A., Zachanowicz, E., Małecka, M., Poźniak, B., Miller, J., Ćniadecki, Z., Pierunek, N., Idzikowski, B., Mrówczyńska, L., Ekner-Grzyb, A., and Wigłusz, R. J. (2015). "Synthesis, structural features, cytotoxicity, and magnetic properties of colloidal ferrite spinel $\text{Co}_{1-x}\text{Ni}_x\text{Fe}_2\text{O}_4$ ($0.1 \leq \text{x} \leq 0.9$) Nanoparticles." *Eur. J. Inorg. Chem.*, 2015(28), 4750–4760.

Pechini P. Maggio. (1967). "Method of preparing ideal and alkaline earth titanates and niobates and coating method using the same." *U.S. Pat. No. 3,330,697*, United States.

Petrovic, J. J., and Vasudevan, A. K. (1999). "Key developments in high temperature structural silicides." *Mater. Sci. Eng. A*, 261(1–2), 1–5.

Phakatkar, A. H., Saray, M. T., Rasul, M. G., Sorokina, L. V., Ritter, T. G., Shokuhfar, T., and Shahbazian-Yassar, R. (2021). "Ultrafast synthesis of high entropy oxide nanoparticles by flame spray pyrolysis." *Langmuir*, 37(30), 9059–9068.

Phillips, J. C. (1968). “Dielectric definition of electronegativity.” *Phys. Rev. Lett.*, 20(11), 550–553.

Pikalova, E. Y., Kalinina, E. G., Pikalova, N. S., and Filonova, E. A. (2022). “High-entropy materials in SOFC technology: Theoretical foundations for their creation, features of synthesis, and recent achievements.” *Materials.*, 15(24), 8783.

Pitike, K. C., Marquez-Rossy, A. E., Flores-Betancourt, A., Chen, D. X., Santosh, K. C., Cooper, V. R., and Lara-Curzio, E. (2020). “On the elastic anisotropy of the entropy-stabilized oxide (Mg, Co, Ni, Cu, Zn)O compound.” *J. Appl. Phys.*, 128(1), 15101.

Pogrebnyak, A. D., Yakushchenko, I. V., Bagdasaryan, A. A., Bondar, O. V., Krause-Rehberg, R., Abadias, G., Chartier, P., Oyoshi, K., Takeda, Y., Beresnev, V. M., and Sobol, O. V. (2014). “Microstructure, physical and chemical properties of nanostructured (Ti-Hf-Zr-V-Nb)N coatings under different deposition conditions.” *Mater. Chem. Phys.*, 147(3), 1079–1091.

Pogrebnyak, A. D., Yakushchenko, I. V., Bondar, O. V., Beresnev, V. M., Oyoshi, K., Ivasishin, O. M., Amekura, H., Takeda, Y., Opielak, M., and Kozak, C. (2016). “Irradiation resistance, microstructure and mechanical properties of nanostructured (TiZrHfVNbTa)N coatings.” *J. Alloys Compd.*, 679, 155–163.

Prado-Gonjal, J., Heuguet, R., Marinel, S., Morán, E., and Schmidt, R. (2017). “Chapter 2: Novel synthetic techniques for nanomaterials.” *Adv. Environ. Anal. Appl. Nanomater.*, B. K. Chaudhery Mustansar Hussain, ed., Royal Society of Chemistry, 35–57.

Pratsinis, S. E., and Vemury, S. (1996). “Particle formation in gases: A review.” *Powder Technol.*, 88(3), 267–273.

Pu, Y., Zhang, Q., Li, R., Chen, M., Du, X., and Zhou, S. (2019). “Dielectric properties and electrocaloric effect of high-entropy (Na_{0.2}Bi_{0.2}Ba_{0.2}Sr_{0.2}Ca_{0.2})TiO₃ ceramic.” *Appl. Phys. Lett.*, 115(22), 223901.

Pujar, M. S., Hunagund, S. M., Desai, V. R., Patil, S., and Sidarai, A. H. (2018). “One-

step synthesis and characterizations of cerium oxide nanoparticles in an ambient temperature via Co-precipitation method.” *AIP Conf. Proc.*, 1942, 050026.

Pujar, P., Gandla, S., Gupta, D., Kim, S., and Kim, M. G. (2020). “Trends in low-temperature combustion derived thin films for solution-processed electronics.” *Adv. Electron. Mater.*, 6(10), 2000464.

Qian, Q., Li, B., Hua, M., Zhang, Z., Lan, F., Xu, Y., Yan, R., and Chen, K. J. (2016). “Improved gate dielectric deposition and enhanced electrical stability for single-layer MoS₂ MOSFET with an AlN interfacial layer.” *Sci. Rep.*, 6(1), 1–9.

Qin, Y., Liu, J. X., Li, F., Wei, X., Wu, H., and Zhang, G. J. (2019). “A high entropy silicide by reactive spark plasma sintering.” *J. Adv. Ceram.*, 8(1), 148–152.

Qin, Y., Wang, J. C., Liu, J. X., Wei, X. F., Li, F., Zhang, G. J., Jing, C., Zhao, J., and Wu, H. (2020). “High-entropy silicide ceramics developed from (TiZrNbMoW)Si₂ formulation doped with aluminum.” *J. Eur. Ceram. Soc.*, 40(8), 2752–2759.

Qiu, N., Chen, H., Yang, Z., Sun, S., Wang, Y., and Cui, Y. (2019). “A high entropy oxide (Mg_{0.2}Co_{0.2}Ni_{0.2}Cu_{0.2}Zn_{0.2}O) with superior lithium storage performance.” *J. Alloys Compd.*, 777, 767–774.

Rajith Kumar, C. R., Betageri, V. S., Nagaraju, G., Pujar, G. H., Suma, B. P., and Latha, M. S. (2020). “Photocatalytic, nitrite sensing and antibacterial studies of facile bio-synthesized nickel oxide nanoparticles.” *J. Sci. Adv. Mater. Devices*, 5(1), 48–55.

Rák, Z., and Brenner, D. W. (2020). “Exchange interactions and long-range magnetic order in the (Mg,Co,Cu,Ni,Zn)O entropy-stabilized oxide: A theoretical investigation.” *J. Appl. Phys.*, 127(18), 185108.

Rak, Z., Rost, C. M., Lim, M., Sarker, P., Toher, C., Curtarolo, S., Maria, J. P., and Brenner, D. W. (2016). “Charge compensation and electrostatic transferability in three entropy-stabilized oxides: Results from density functional theory calculations.” *J. Appl. Phys.*, 120(9), 95105.

Ravindra, A. V., Behera, B. C., and Padhan, P. (2014). “Laser induced structural phase

transformation of cobalt oxides nanostructures.” *J. Nanosci. Nanotechnol.*, 14(7), 5591–5595.

Raymond, O., Font, R., Portelles, J., Suárez-Almodovar, N., and Siqueiros, J. M. (2006a). “Frequency-temperature response of ferroelectromagnetic $\text{Pb}(\text{Fe}_{12}\text{Nb}_{12})\text{O}_3$ ceramics obtained by different precursors. III. Dielectric relaxation near the transition temperature.” *J. Appl. Phys.*, 99(12), 124101.

Raza, H., Cheng, J., Lin, | Cong, Majumder, S., Zheng, G., Chen, | Guohua, and Chen, G. (2023). “High-entropy stabilized oxides derived via a low-temperature template route for high-performance lithium-sulfur batteries.” *EcoMat*, e12324.

Ren, X., Tian, Z., Zhang, J., and Wang, J. (2019). “Equiatomic quaternary $(\text{Y}_{1/4}\text{Ho}_{1/4}\text{Er}_{1/4}\text{Yb}_{1/4})_2\text{SiO}_5$ silicate: A perspective multifunctional thermal and environmental barrier coating material.” *Scr. Mater.*, 168, 47–50.

Ridley, M., Gaskins, J., Hopkins, P., and Opila, E. (2020). “Tailoring thermal properties of multi-component rare earth monosilicates.” *Acta Mater.*, 195, 698–707.

Rim, Y. S., Chen, H., Song, T. Bin, Bae, S. H., and Yang, Y. (2015). “Hexaaqua metal complexes for low-temperature formation of fully metal oxide thin-film transistors.” *Chem. Mater.*, 27(16), 5808–5812.

Rivas-Murias, B., and Salgueiriño, V. (2017). “Thermodynamic $\text{CoO}-\text{Co}_3\text{O}_4$ crossover using Raman spectroscopy in magnetic octahedron-shaped nanocrystals.” *J. Raman Spectrosc.*, 48(6), 837–841.

Robertson, J. (2004). “High dielectric constant oxides.” *EPJ Appl. Phys.*, 28(3), 265–291.

Robertson, J. (2006). “High dielectric constant gate oxides for metal oxide Si transistors.” *Reports Prog. Phys.*, 69(2), 327–396.

Robertson, J., and Wallace, R. M. (2015). “High- κ materials and metal gates for CMOS applications.” *Mater. Sci. Eng. R Reports*, 88, 1–41.

Rojas, J. V., Toro-Gonzalez, M., Molina-Higgins, M. C., and Castano, C. E. (2016). “Facile radiolytic synthesis of ruthenium nanoparticles on graphene oxide and carbon nanotubes.” *Mater. Sci. Eng. B Solid-State Mater. Adv. Technol.*, 205, 28–35.

Rost, C. M., Sachet, E., Borman, T., Moballegh, A., Dickey, E. C., Hou, D., Jones, J. L., Curtarolo, S., and Maria, J. P. (2015). “Entropy-stabilized oxides.” *Nat. Commun.*, 6(1), 8485.

Rost, C. M. (2016). “Entropy-stabilized oxides: Explorations of a novel class of multicomponent materials by.” *North Carolina State Univ.*, North Carolina State University.

Rowsell, J. L. C., and Yaghi, O. M. (2004). “Metal-organic frameworks: A new class of porous materials.” *Microporous Mesoporous Mater.*, 73(1–2), 3-14.

Roy, P., and Srivastava, S. K. (2015). “Nanostructured anode materials for lithium ion batteries.” *J. Mater. Chem. A*, 3, 2454-2484.

Ruffa, A. R. (1982). “Thermal potential, mechanical instability, and melting entropy.” *Phys. Rev. B*, 25(9), 5895–5900.

Safat, S., Buazar, F., Albukhaty, S., and Matroodi, S. (2021). “Enhanced sunlight photocatalytic activity and biosafety of marine-driven synthesized cerium oxide nanoparticles.” *Sci. Rep.*, 11(1), 1–11.

Safi, I. (2000). “Recent aspects concerning DC reactive magnetron sputtering of thin films: a review.” *Surf. Coatings Technol.*, 127(2–3), 203–218.

Saha, D., Madras, G., and Guru Row, T. N. (2012). “Synthesis and structure of $\text{Bi}_2\text{Ce}_2\text{O}_7$: A new compound exhibiting high solar photocatalytic activity.” *Dalt. Trans.*, 41(32), 9598–9600.

Salian, A., Pujar, P., and Mandal, S. (2019). “Facile in situ formation of high conductive Ag and Cu_xO_y composite films: A role of aqueous spray combustion.” *J. Mater. Sci. Mater. Electron.*, 30(3), 2888–2897.

Salian, A., and Mandal, S. (2022a). “Review on the deposition, structure and properties of high entropy oxide films: current and future perspectives.” *Bull. Mater. Sci.*, 45(49), 1–21.

Salian, A., and Mandal, S. (2022b). “Entropy stabilized multicomponent oxides with diverse functionality—a review.” *Crit. Rev. Solid State Mater. Sci.*, 47(2), 142–193.

Salian, A., Pujar, P., Vardhan, R. V., Cho, H., Kim, S., and Mandal, S. (2023a). “Evolution of high dielectric permittivity in low-temperature solution combustion-processed phase-pure high entropy oxide (CoMnNiFeCr)O for thin film transistors.” *ACS Appl. Electron. Mater.* 5(5), 2608–2623.

Salian, A., Sengupta, P., Vishalakshi Aswath, I., Gowda, A., and Mandal, S. (2023b). “A review on high entropy silicides and silicates: Fundamental aspects, synthesis, properties.” *Int. J. Appl. Ceram. Technol.*, 20(5), 2635–2660.

Sanchez-Rodriguez, D., Farjas, J., Roura, P., Ricart, S., Mestres, N., Obradors, X., and Puig, T. (2013). “Thermal analysis for low temperature synthesis of oxide thin films from chemical solutions.” *J. Phys. Chem. C*, 117(39), 20133–20138.

Sang, W., Zhang, H., Zhang, H., Liu, X., Chen, X., Xie, W., Hou, R., Ma, H., Li, S., Wang, N., and Li, X. (2023). “Novel (Sm_{0.2}Lu_{0.2}Yb_{0.2}Y_{0.2}Dy_{0.2})₃TaO₇ high-entropy ceramic for thermal barrier coatings.” *Ceram. Int.*, 49(6), 9052–9059.

S Ranganathan. (2003). “Alloyed pleasures: Multimetallic cocktails.” *Curr. Sci.*, 85(10), 1404–1406.

Sarkar, A., Djenadic, R., Usharani, N. J., Sanghvi, K. P., Chakravadhanula, V. S. K., Gandhi, A. S., Hahn, H., and Bhattacharya, S. S. (2017a). “Nanocrystalline multicomponent entropy stabilised transition metal oxides.” *J. Eur. Ceram. Soc.*, 37(2), 747–754.

Sarkar, A., Loho, C., Velasco, L., Thomas, T., Bhattacharya, S. S., Hahn, H., and Djenadic, R. (2017b). “Multicomponent equiatomic rare earth oxides with a narrow band gap and associated praseodymium multivalency.” *Dalt. Trans.*, 46(36), 12167–

12176.

Sarkar, A., Djenadic, R., Wang, D., Hein, C., Kautenburger, R., Clemens, O., and Hahn, H. (2018a). "Rare earth and transition metal based entropy stabilised perovskite type oxides." *J. Eur. Ceram. Soc.*, 38(5), 2318–2327.

Sarkar, A., Velasco, L., Wang, D., Wang, Q., Talasila, G., Biasi, L. de, Kübel, C., Brezesinski, T., Bhattacharya, S. S., Hahn, H., and Breitung, B. (2018b). "High entropy oxides for reversible energy storage." *Nat. Commun.*, 9(1), 3400.

Sarkar, A., Wang, Q., Schiele, A., Chellali, M. R., Bhattacharya, S. S., Wang, D., Brezesinski, T., Hahn, H., Velasco, L., and Breitung, B. (2019). "High-entropy oxides: Fundamental aspects and electrochemical properties." *Adv. Mater.*, 31(26), 1806236.

Sarkar, A., Breitung, B., and Hahn, H. (2020a). "High entropy oxides: The role of entropy, enthalpy and synergy." *Scr. Mater.*, 187, 43–48.

Sarkar, A., Eggert, B., Velasco, L., Mu, X., Lill, J., Ollefs, K., Bhattacharya, S. S., Wende, H., Kruk, R., Brand, R. A., and Hahn, H. (2020b). "Role of intermediate 4f states in tuning the band structure of high entropy oxides." *APL Mater.*, 8(5), 51111.

Sekar, M. M. A., and Patil, K. C. (1993). "Hydrazine carboxylate precursors to fine particle titania, zirconia and zirconium titanate." *Mater. Res. Bull.*, 28(5), 485–492.

Sen, S., Choudhary, R. N. P., and Pramanik, P. (2013). "Impedance spectroscopy of $Ba_{1-x}Sr_xSn_{0.15}Ti_{0.85}O_3$ ceramics." *Br. Ceram. Trans.*, 103(6), 250–256.

Senkov, O. N., Scott, J. M., Senkova, S. V., Miracle, D. B., and Woodward, C. F. (2011a). "Microstructure and room temperature properties of a high-entropy TaNbHfZrTi alloy." *J. Alloys Compd.*, 509(20), 6043–6048.

Senkov, O. N., Wilks, G. B., Scott, J. M., and Miracle, D. B. (2011b). "Mechanical properties of $Nb_{25}Mo_{25}Ta_{25}W_{25}$ and $V_{20}Nb_{20}Mo_{20}Ta_{20}W_{20}$ refractory high entropy alloys." *Intermetallics*, 19(5), 698–706.

Senkov, O. N., and Woodward, C. F. (2011). "Microstructure and properties of a

refractory NbCrMo_{0.5}Ta_{0.5}TiZr alloy.” *Mater. Sci. Eng. A*, 529, 311–320.

Sharma, Y., Musico, B. L., Gao, X., Hua, C., May, A. F., Herklotz, A., Rastogi, A., Mandrus, D., Yan, J., Lee, H. N., Chisholm, M. F., Keppens, V., and Ward, T. Z. (2018). “Single-crystal high entropy perovskite oxide epitaxial films.” *Phys. Rev. Mater.*, 2(6), 60404.

Sharma, Y., Zheng, Q., Mazza, A. R., Skoropata, E., Heitmann, T., Gai, Z., Musico, B., Miceli, P. F., Sales, B. C., Keppens, V., Brahlek, M., and Ward, T. Z. (2020). “Magnetic anisotropy in single-crystal high-entropy perovskite oxide La(Cr_{0.2}Mn_{0.2}Fe_{0.2}Co_{0.2}Ni_{0.2})O₃ films.” *Phys. Rev. Mater.*, 4(1), 14404.

Shi, Y., Yang, B., Liaw, P., Shi, Y., Yang, B., and Liaw, P. K. (2017). “Corrosion-resistant high-entropy alloys: A review.” *Metals.*, 7(2), 43.

Shu, Y., Bao, J., Yang, S., Duan, X., and Zhang, P. (2020). “Entropy-stabilized metal-CeO_x solid solutions for catalytic combustion of volatile organic compounds.” *AIChE J.*, 67(1), e17046.

Soe, T., Jityen, A., Kongkaew, T., Subannajui, K., Sinsarp, A., and Osotchan, T. (2020). “X-ray photoelectron spectroscopy study of chromium and magnesium doped copper ferrite thin film.” *AIP Conf. Proc.*, 2279, 140002.

Sotnikov, A. V., Bakovets, V. V., and Plyusnin, P. E. (2021). “Kinetics of thermal decomposition of yttrium and samarium hydroxides and Sm(OH)₃@Y(OH)₃ compound with a core-shell nanostructure.” *Russ. J. Gen. Chem.*, 91(7), 1368–1378.

Stygar, M., Dąbrowa, J., Moździerz, M., Zajusz, M., Skubida, W., Mroczka, K., Berent, K., Świerczek, K., and Danielewski, M. (2020). “Formation and properties of high entropy oxides in Co-Cr-Fe-Mg-Mn-Ni-O system: Novel (Cr,Fe,Mg,Mn,Ni)₃O₄ and (Co,Cr,Fe,Mg,Mn)₃O₄ high entropy spinels.” *J. Eur. Ceram. Soc.*, 40(4), 1644–1650.

Subohi, O., Kumar, G. S., Malik, M. M., and Kurchania, R. (2012). “Dielectric properties of Bismuth Titanate (Bi₄Ti₃O₁₂) synthesized using solution combustion route.” *Phys. B Condens. Matter*, 407(18), 3813–3817.

Sujatha, C., Reddy, K. V., Babu, K. S., Reddy, A. R. C., Suresh, M. B., and Rao, K. H. (2013). “Effect of co substitution of Mg and Zn on electromagnetic properties of NiCuZn ferrites.” *J. Phys. Chem. Solids*, 74(7), 917–923.

Suman, C. K., Prasad, K., and Choudhary, R. N. P. (2006). “Complex impedance studies on tungsten-bronze electroceramic: $\text{Pb}_2\text{Bi}_3\text{LaTi}_5\text{O}_{18}$.” *J. Mater. Sci.*, 41(2), 369–375.

Sun, L., Luo, Y., Ren, X., Gao, Z., Du, T., Wu, Z., and Wang, J. (2020). “A multicomponent γ -type $(\text{Gd}_{1/6}\text{Tb}_{1/6}\text{Dy}_{1/6}\text{Tm}_{1/6}\text{Yb}_{1/6}\text{Lu}_{1/6})_2\text{Si}_2\text{O}_7$ disilicate with outstanding thermal stability.” *Mater. Res. Lett.*, 8(11), 424–430.

Sure, J., Sri Maha Vishnu, D., Kim, H., and Schwandt, C. (2020). “Facile electrochemical synthesis of nanoscale $(\text{TiNbTaZrHf})\text{C}$ high-entropy carbide powder.” *Angew. Chemie.*, 59(29), 11830–11835.

Suresh, K., and Patil, K. C. (1993). “A combustion process for the instant synthesis of γ -iron oxide.” *J. Mater. Sci. Lett.*, 12(8), 572–574.

Takeuchi, A., Chen, N., Wada, T., Yokoyama, Y., Kato, H., Inoue, A., and Yeh, J. W. (2011). “ $\text{Pd}_{20}\text{Pt}_{20}\text{Cu}_{20}\text{Ni}_{20}\text{P}_{20}$ high-entropy alloy as a bulk metallic glass in the centimeter.” *Intermetallics*, 19(10), 1546–1554.

Takeuchi, A., Amiya, K., Wada, T., Yubuta, K., Zhang, W., and Makino, A. (2013). “Entropies in alloy design for high-entropy and bulk glassy alloys.” *Entropy*, 15(12), 3810–3821.

Takeuchi, A., Amiya, K., Wada, T., Yubuta, K., and Zhang, W. (2014). “High-entropy alloys with a hexagonal close-packed structure designed by equi-atomic alloy strategy and binary phase diagrams.” *JOM*, 66(10), 1984–1992.

Takeuchi, A., Gao, M. C., Qiao, J., and Widom, M. (2016). “High-entropy metallic glasses.” *High-Entropy Alloy. Fundam. Appl.*, M. C. Gao, J. W. Yeh, P. K. Liaw, and Y. Zhang, eds., Cham: Springer International Publishing, 445–468.

Talapin, D. V., Lee, J. S., Kovalenko, M. V., and Shevchenko, E. V. (2010). “Prospects

of colloidal nanocrystals for electronic and optoelectronic applications.” *Chem. Rev.*, 110(1), 389–458.

Tallarita, G., Licheri, R., Garroni, S., Orrù, R., and Cao, G. (2019). “Novel processing route for the fabrication of bulk high-entropy metal diborides.” *Scr. Mater.*, 158, 100–104.

Talluri, B., Yoo, K., and Kim, J. (2022). “High entropy spinel metal oxide (CoCrFeMnNi)₃O₄ nanoparticles as novel efficient electrocatalyst for methanol oxidation and oxygen evolution reactions.” *J. Environ. Chem. Eng.*, 10(1), 106932.

Tang, C. W., Wang, C. Bin, and Chien, S. H. (2008). “Characterization of cobalt oxides studied by FT-IR, Raman, TPR and TG-MS.” *Thermochim. Acta*, 473(1–2), 68–73.

Tang, P., Cao, Y., Hao li, Lu, M., and Qiu, W. (2022). “The preparation of high-performance aqueous supercapacitor with high-entropy pyrochlore-type electrode and super-concentrated electrolyte.” *Ceram. Int.*, 48(2), 2660–2669.

Teng, Z., Tan, Y., Zeng, S., Meng, Y., Chen, C., Han, X., and Zhang, H. (2021). “Preparation and phase evolution of high-entropy oxides A₂B₂O₇ with multiple elements at A and B sites.” *J. Eur. Ceram. Soc.*, 41(6), 3614–3620.

Teng, Z., Zhu, L., Tan, Y., Zeng, S., Xia, Y., Wang, Y., and Zhang, H. (2020). “Synthesis and structures of high-entropy pyrochlore oxides.” *J. Eur. Ceram. Soc.*, 40(4), 1639–1643.

Theiss, F. L., Couperthwaite, S. J., Ayoko, G. A., and Frost, R. L. (2014). “A review of the removal of anions and oxyanions of the halogen elements from aqueous solution by layered double hydroxides.” *J. Colloid Interface Sci.*, 417, 356–368.

Tian, Z., Zhu, C., Wang, J., Xia, Z., Liu, Y., and Yuan, S. (2015). “Size dependence of structure and magnetic properties of CoCr₂O₄ nanoparticles synthesized by hydrothermal technique.” *J. Magn. Magn. Mater.*, 377, 176–182.

Tomiyasu, K., Fukunaga, J., and Suzuki, H. (2004). “Magnetic short-range order and reentrant-spin-glass-like behavior in CoCr₂O₄ and MnCr₂O₄ by means of neutron

scattering and magnetization measurements.” *Phys. Rev. B - Condens. Matter Mater. Phys.*, 70(21), 1–12.

Tsai, M. H., Wang, C.-W., Lai, C. H., Yeh, J.-W., and Gan, J. Y. (2008). “Thermally stable amorphous (AlMoNbSiTaTiVZr)₅₀N₅₀ nitride film as diffusion barrier in copper metallization.” *Appl. Phys. Lett.*, 92(5), 52109.

Tsau, C. H., Hwang, Z. Y., and Chen, S. K. (2015). “The microstructures and electrical resistivity of (Al, Cr, Ti)FeCoNiO_x high-entropy alloy oxide thin films.” *Adv. Mater. Sci. Eng.*, 2015.

Tsau, C. H., Yang, Y. C., Lee, C. C., Wu, L. Y., and Huang, H. J. (2012). “The low electrical resistivity of the high-entropy alloy oxide thin films.” *Procedia Eng.*, Elsevier Ltd, 246–252.

Tudose, I. V., Comanescu, F., Pascariu, P., Bucur, S., Rusen, L., Iacomi, F., Koudoumas, E., and Sucheai, M. P. (2019). “Chemical and physical methods for multifunctional nanostructured interface fabrication.” *Funct. Nanostructured Interfaces Environ. Biomed. Appl.*, Elsevier, 15–26.

Turcer, L. R., and Padture, N. P. (2018). “Towards multifunctional thermal environmental barrier coatings (TEBCs) based on rare-earth pyrosilicate solid-solution ceramics.” *Scr. Mater.*, 154, 111–117.

Usharani, N. J., Bhandarkar, A., Subramanian, S., and Bhattacharya, S. S. (2020a). “Antiferromagnetism in a nanocrystalline high entropy oxide (Co,Cu,Mg,Ni,Zn)O: Magnetic constituents and surface anisotropy leading to lattice distortion.” *Acta Materialia.*, 200, 526-536

Usharani, N. J., Shringi, R., Sanghavi, H., Subramanian, S., and Bhattacharya, S. S. (2020b). “Role of size, alio-/multi-valency and non-stoichiometry in the synthesis of phase-pure high entropy oxide (Co,Cu,Mg,Na,Ni,Zn)O.” *Dalt. Trans.*, 49(21), 7123–7132.

Uwamino, Y., Ishizuka, T., and Yamatera, H. (1984). “X-ray photoelectron

spectroscopy of rare-earth compounds.” *J. Electron Spectros. Relat. Phenomena*, 34(1), 67–78.

Vaqueiro, P., Orabi, R. A. R. Al, Luu, S. D. N., Guélou, G., Powell, A. V., Smith, R. I., Song, J.-P., Wee, D., and Fornari, M. (2015). “The role of copper in the thermal conductivity of thermoelectric oxychalcogenides: do lone pairs matter?” *Phys. Chem. Chem. Phys.*, 17(47), 31735–31740.

Varma, A., Mukasyan, A. S., Rogachev, A. S., and Manukyan, K. V. (2016). “Solution Combustion Synthesis of Nanoscale Materials.” *Chem. Rev.*, 116(23), 14493–14586.

Vescio, G., Crespo-Yepes, A., Alonso, D., Claramunt, S., Porti, M., Rodriguez, R., Cornet, A., Cirera, A., Nafria, M., and Aymerich, X. (2017). “Inkjet printed HfO₂-based ReRAMs: First demonstration and performance characterization.” *IEEE Electron Device Lett.*, 38(4), 457–460.

Vinnik, D. A., Trofimov, E. A., Zhivulin, V. E., Zaitseva, O. V., Gudkova, S. A., Starikov, A. Y., Zherebtsov, D. A., Kirsanova, A. A., Häßner, M., and Niewa, R. (2019). “High-entropy oxide phases with magnetoplumbite structure.” *Ceram. Int.*, 45(10), 12942–12948.

Vinnik, D. A., Trofimov, E. A., Zhivulin, V. E., Zaitseva, O. V., Zherebtsov, D. A., Starikov, A. Y., Sherstyuk, D. P., Gudkova, S. A., and Taskaev, S. V. (2020). “The new extremely substituted high entropy (Ba,Sr,Ca,La)Fe_{6-x}(Al,Ti,Cr,Ga,In,Cu,W)_xO₁₉ microcrystals with magnetoplumbite structure.” *Ceram. Int.*, 46(7), 9656–9660.

Vinothkumar, G., Arunkumar, P., Mahesh, A., Dhayalan, A., and Suresh Babu, K. (2018). “Size- and defect-controlled anti-oxidant enzyme mimetic and radical scavenging properties of cerium oxide nanoparticles.” *New J. Chem.*, 42(23), 18810–18823.

Vladescu, A., Titorencu, I., Dekhtyar, Y., Jinga, V., Pruna, V., Balaceanu, M., Dinu, M., Pana, I., Vendina, V., and Braic, M. (2016). “In Vitro Biocompatibility of Si Alloyed Multi-Principal Element Carbide Coatings.” *PLoS One*, (A. Mukherjee, ed.), 11(8), e0161151.

- Waits, R. K. (1978). "Planar magnetron sputtering." *J Vac Sci Technol*, 15(2), 179–187.
- Wan, C., Qu, Z., Du, A., and Pan, W. (2009). "Influence of B site substituent Ti on the structure and thermophysical properties of $A_2B_2O_7$ -type pyrochlore $Gd_2Zr_2O_7$." *Acta Mater.*, 57(16), 4782–4789.
- Wan, C., Zhang, W., Wang, Y., Qu, Z., Du, A., Wu, R., and Pan, W. (2010). "Glass-like thermal conductivity in ytterbium-doped lanthanum zirconate pyrochlore." *Acta Mater.*, 58(18), 6166–6172.
- Wang, Q. H., Kalantar-Zadeh, K., Kis, A., Coleman, J. N., and Strano, M. S. (2012). "Electronics and optoelectronics of two-dimensional transition metal dichalcogenides." *Nat. Nanotechnol.*, 7(11), 699–712.
- Wang, Q., and O'Hare, D. (2012). "Recent advances in the synthesis and application of layered double hydroxide (LDH) nanosheets." *Chem. Rev.*, 112(7), 4124–4155.
- Wang, B., Qin, D., Liang, G., Gu, A., Liu, L., and Yuan, L. (2013a). "High- κ materials with low dielectric loss based on two superposed gradient carbon nanotube/cyanate ester composites." *J. Phys. Chem. C*, 117(30), 15487–15495.
- Wang, Y., Yang, F., and Xiao, P. (2013b). "Rattlers or oxygen vacancies: Determinant of high temperature plateau thermal conductivity in doped pyrochlores." *Appl. Phys. Lett.*, 102(14).
- Wang, W. H. (2014). "High-entropy metallic glasses." *JOM*, 66(10), 2067–2077.
- Wang, B., Jiao, Y., Gu, A., Liang, G., and Yuan, L. (2014a). "Dielectric properties and mechanism of composites by superposing expanded graphite/cyanate ester layer with carbon nanotube/cyanate ester layer." *Compos. Sci. Technol.*, 91, 8–15.
- Wang, J., Zheng, Z., Xu, J., and Wang, Y. (2014b). "Microstructure and magnetic properties of mechanically alloyed FeSiBAlNi (Nb) high entropy alloys." *J. Magn. Mater.*, 355, 58–64.

Wang, B., Liu, L., Huang, L., Chi, L., Liang, G., Yuan, L., and Gu, A. (2015a). “Fabrication and origin of high- κ carbon nanotube/epoxy composites with low dielectric loss through layer-by-layer casting technique.” *Carbon N. Y.*, 85, 28–37.

Wang, Y., Lü, Y., Zhan, W., Xie, Z., Kuang, Q., and Zheng, L. (2015b). “Synthesis of porous Cu₂O/CuO cages using Cu-based metal-organic frameworks as templates and their gas-sensing properties.” *J. Mater. Chem. A*, 3(24), 12796–12803.

Wang, B., Yu, X., Guo, P., Huang, W., Zeng, L., Zhou, N., Chi, L., Bedzyk, M. J., Chang, R. P. H., Marks, T. J., and Facchetti, A. (2016a). “Solution-processed all-oxide transparent high-performance transistors fabricated by spray-combustion synthesis.” *Adv. Electron. Mater.*, 2(4), 1500427.

Wang, J., Li, Y., Yaer, X., Qiqige, A., Fang, C., Miao, L., and Liu, C. (2016b). “Improvement of thermoelectric power of n-type earth-abundant iron rich alloy by microstructure engineering.” *J. Alloys Compd.*, 665, 7–12.

Wang, B., Huang, W., Chi, L., Al-Hashimi, M., Marks, T. J., and Facchetti, A. (2018a). “High- κ Gate dielectrics for emerging flexible and stretchable electronics.” *Chem. Rev.*, 118(11), 5690–5754.

Wang, Y. P., Gan, G.-Y., Wang, W., Yang, Y., and Tang, B.-Y. (2018b). “Ab Initio prediction of mechanical and electronic properties of ultrahigh temperature high-entropy ceramics (Hf_{0.2}Zr_{0.2}Ta_{0.2}Mo_{0.2}Ti_{0.2})B₂ (M = Nb, Mo, Cr).” *Phys. status solidi*, 255(8), 1800011.

Wang, D., Liu, Z., Du, S., Zhang, Y., Li, H., Xiao, Z., Chen, W., Chen, R., Wang, Y., Zou, Y., and Wang, S. (2019a). “Low-temperature synthesis of small-sized high-entropy oxides for water oxidation.” *J. Mater. Chem. A*, 7(42), 24211–24216.

Wang, Q., Sarkar, A., Li, Z., Lu, Y., Velasco, L., Bhattacharya, S. S., Brezesinski, T., Hahn, H., and Breitung, B. (2019b). “High entropy oxides as anode material for Li-ion battery applications: A practical approach.” *Electrochem. commun.*, 100, 121–125.

Wang, Q., Sarkar, A., Wang, D., Velasco, L., Azmi, R., Bhattacharya, S. S., Bergfeldt,

T., Düvel, A., Heitjans, P., Brezesinski, T., Hahn, H., and Breitung, B. (2019c). “Multi-anionic and -cationic compounds: New high entropy materials for advanced Li-ion batteries.” *Energy Environ. Sci.*, 12(8), 2433–2442.

Wang, Q., Xue, K., Fu, P., Du, F., Lin, Z., Chen, Z., Wang, S., and Wang, G. (2019d). “Tunable dielectric properties of porous ZnAl_2O_4 ceramics for wave-transmitting devices.” *J. Mater. Sci. Mater. Electron.*, 30(7), 6475–6481.

Wang, Y., Jie, W., Yang, C., Wei, X., and Hao, J. (2019e). “Colossal permittivity materials as superior dielectrics for diverse applications.” *Adv. Funct. Mater.*, John Wiley & Sons, Ltd.

Wang, D., Jiang, S., Duan, C., Mao, J., Dong, Y., Dong, K., Wang, Z., Luo, S., Liu, Y., and Qi, X. (2020a). “Spinel-structured high entropy oxide $(\text{FeCoNiCrMn})_3\text{O}_4$ as anode towards superior lithium storage performance.” *J. Alloys Compd.*, 844, 156158.

Wang, G., Qin, J., Feng, Y., Feng, B., Yang, S., Wang, Z., Zhao, Y., and Wei, J. (2020b). “Sol-gel synthesis of spherical mesoporous high-entropy oxides.” *ACS Appl. Mater. Interfaces*, 12(40), 45155–45164.

Wang, J., Cui, Y., Wang, Q., Wang, K., Huang, X., Stenzel, D., Sarkar, A., Azmi, R., Bergfeldt, T., Bhattacharya, S. S., Kruk, R., Hahn, H., Schweidler, S., Brezesinski, T., and Breitung, B. (2020c). “Lithium containing layered high entropy oxide structures.” *Sci. Rep.*, 10(1), 1–13.

Wang, J., Stenzel, D., Azmi, R., Najib, S., Wang, K., Jeong, J., Sarkar, A., Wang, Q., Sukkurji, P. A., Bergfeldt, T., Botros, M., Maibach, J., Hahn, H., Brezesinski, T., and Breitung, B. (2020d). “Spinel to rock-salt transformation in high entropy oxides with Li incorporation.” *Electrochem*, 1(1), 60–74.

Wang, Q., Hou, M., Huang, Y., Li, J., Zhou, X., Ma, G., and Ren, S. (2020e). “One-pot synthesis of NiCoP/CNTs composites for lithium ion batteries and hydrogen evolution reaction.” *Ionics*, 26(4), 1771–1778.

Wang, Y., Hao, J., Li, W., Zuo, X., Xiang, B., Qiang, Y., Zou, X., Tan, B., Hu, Q., and

- Chen, F. (2020f). “Mn₃O₄/Co(OH)₂ cactus-type nanoarrays for high-energy-density asymmetric supercapacitors.” *J. Mater. Sci.*, 55(2), 724–737.
- Wang, G., Lu, Z., Li, Y., Li, L., Ji, H., Feteira, A., Zhou, D., Wang, D., Zhang, S., and Reaney, I. M. (2021a). “Electroceramics for high-energy density capacitors: Current status and future perspectives.” *Chem. Rev.*, 121(10), 6124–6172.
- Wang, T.-H., Kuo, C. T., Chung, P. H., Liu, C. I., Lu, Y. Y., Lee, Y. T., and Yew, T. R. (2021b). “Novel Cu–Mg–Ni–Zn–Mn oxide thin film electrodes for NIR photodetector applications.” *J. Mater. Chem. C*, 9(14), 4961–4970.
- Wei, Z., Qiao, H., Yang, H., Zhang, C., and Yan, X. (2009). “Characterization of NiO nanoparticles by anodic arc plasma method.” *J. Alloys Compd.*, 479(1–2), 855–858.
- Wen, T., Liu, H., Ye, B., Liu, D., and Chu, Y. (2020). “High-entropy alumino-silicides: A novel class of high-entropy ceramics.” *Sci. China Mater.*, 63(2), 300–306.
- Wen, Y., and Liu, Y. (2023). “Evolution behaviour of the lattice and thermal expansion of a high-entropy fluorite oxide (Zr_{0.2}Ce_{0.2}Hf_{0.2}Y_{0.2}Al_{0.2})O_{2-δ} during heating and cooling in an inert atmosphere.” *Ceram. Int.*, 15-26.
- Williams, W. S. (1971). “Transition-metal carbides.” *Prog. Solid State Chem.*, 6, 57–118.
- Witte, R., Sarkar, A., Kruk, R., Eggert, B., Brand, R. A., Wende, H., and Hahn, H. (2019). “High-entropy oxides: An emerging prospect for magnetic rare-earth transition metal perovskites.” *Phys. Rev. Mater.*, 3(3), 34406.
- Witte, R., Sarkar, A., Velasco, L., Kruk, R., Brand, R. A., Eggert, B., Ollefs, K., Weschke, E., Wende, H., and Hahn, H. (2020). “Magnetic properties of rare earth and transition metal based perovskite type high entropy oxides.” *J. Appl. Phys.*, 127, 185109.
- Wong, H. (2011). *Nano-CMOS: Gate dielectric engineering. NANO-CMOS Gate Dielectr. Eng.*, CRC Press.

Worku, A. K., Ayele, D. W., Habtu, N. G., and Yemata, T. A. (2021). “Engineering $\text{Co}_3\text{O}_4/\text{MnO}_2$ nanocomposite materials for oxygen reduction electrocatalysis.” *Heliyon*, 7(9), e08076.

Wright, A. J., Huang, C., Walock, M. J., Ghoshal, A., Murugan, M., and Luo, J. (2021). “Sand corrosion, thermal expansion, and ablation of medium- and high-entropy compositionally complex fluorite oxides.” *J. Am. Ceram. Soc.*, 104(1), 448–462.

Wright, A. J., Wang, Q., Huang, C., Nieto, A., Chen, R., and Luo, J. (2020). “From high-entropy ceramics to compositionally-complex ceramics: A case study of fluorite oxides.” *J. Eur. Ceram. Soc.*, 40(5), 2120–2129.

Wu, C. F., Arifin, D. E. S., Wang, C. A., and Ruan, J. (2018). “Coalescence and split of high-entropy polymer lamellar cocrystals.” *Polymer*, 138, 188–202.

Xiang, H., Xie, H., Chen, Y., Zhang, H., and Mao, A. (2021a). “materials entropy oxide as a novel high-performance anode material for lithium-ion batteries.” *J. Mater. Sci.*, 56(13), 8127–8142.

Xiang, H., Xing, Y., Dai, F., Wang, H., Su, L., Miao, L., Zhang, G., Wang, Y., Qi, X., Yao, L., Wang, H., Zhao, B., Li, J., and Zhou, Y. (2021b). “High-entropy ceramics: Present status, challenges, and a look forward.” *J. Adv. Ceram.*, 10(3), 385–441.

Xiang, H. Z., Xie, H. X., Chen, Y. X., Zhang, H., Mao, A., and Zheng, C. H. (2021c). “Porous spinel-type $(\text{Al}_{0.2}\text{CoCrFeMnNi})_{0.58}\text{O}_{4-\delta}$ high-entropy oxide as a novel high-performance anode material for lithium-ion batteries.” *J. Mater. Sci.*, 56(13), 8127–8142.

Xing, Y., Dan, W., Fan, Y., and Li, X. (2022). “Low temperature synthesis of high-entropy $(\text{Y}_{0.2}\text{Yb}_{0.2}\text{Sm}_{0.2}\text{Eu}_{0.2}\text{Er}_{0.2})_2\text{O}_3$ nanofibers by a novel electrospinning method.” *J. Mater. Sci. Technol.*, 103, 215–220.

Xu, H., Zhang, Z., Liu, J., Do-Thanh, C. L., Chen, H., Xu, S., Lin, Q., Jiao, Y., Wang, J., Wang, Y., Chen, Y., and Dai, S. (2020). “Entropy-stabilized single-atom Pd catalysts via high-entropy fluorite oxide supports.” *Nat. Commun.*, 11(1), 1–9.

- Yager, W. A. (1936). "The distribution of relaxation times in typical dielectrics." *J. Appl. Phys.*, 7(12), 434–450.
- Yang, Z.-M., Zhang, K., Qiu, N., Zhang, H.-B., Wang, Y., and Chen, J. (2019). "Effects of helium implantation on mechanical properties of $(\text{Al}_{0.31}\text{Cr}_{0.20}\text{Fe}_{0.14}\text{Ni}_{0.35})\text{O}$ high entropy oxide films." *Chinese Phys. B*, 28(4), 46201.
- Ye, B., Wen, T., Nguyen, M. C., Hao, L., Wang, C.-Z., and Chu, Y. (2019). "First-principles study, fabrication and characterization of $(\text{Zr}_{0.25}\text{Nb}_{0.25}\text{Ti}_{0.25}\text{V}_{0.25})\text{C}$ high-entropy ceramics." *Acta Mater.*, 170, 15–23.
- Ye, Y. F., Wang, Q., Lu, J., Liu, C. T., and Yang, Y. (2015). "The generalized thermodynamic rule for phase selection in multicomponent alloys." *Intermetallics*, 59, 75–80.
- Ye, Y. F., Wang, Q., Lu, J., Liu, C. T., and Yang, Y. (2016). "High-entropy alloy: challenges and prospects." *Mater. Today*, 19(6), 349–362.
- Yeh, J.-W., Chen, S.-K., Lin, S.-J., Gan, J.-Y., Chin, T.-S., Shun, T.-T., Tsau, C.-H., and Chang, S.-Y. (2004a). "Nanostructured high-entropy alloys with multiple principal elements: Novel alloy design concepts and outcomes." *Adv. Eng. Mater.*, 6(5), 299–303.
- Yeh, J. W., Chen, S. K., Lin, S. J., Gan, J. Y., Chin, T. S., Shun, T. T., Tsau, C. H., and Chang, S. Y. (2004b). "Nanostructured high-entropy alloys with multiple principal elements: Novel alloy design concepts and outcomes." *Adv. Eng. Mater.*, 6(5), 299–303.
- Yin, S., Zhang, W., Xue, L., and Yan, Y. (2013). "Effects of reaction parameters on solution combustion synthesis of lepidocrocite-like $\text{K}_{0.80}\text{Ti}_{1.733}\text{Li}_{0.267}\text{O}_4$: Phase formation and morphology evolution." *J. Mater. Sci.*, 48(4), 1533–1542.
- Yoon, B., Avila, V., Raj, R., and Jesus, L. M. (2020). "Reactive flash sintering of the entropy-stabilized oxide $\text{Mg}_{0.2}\text{Ni}_{0.2}\text{Co}_{0.2}\text{Cu}_{0.2}\text{Zn}_{0.2}\text{O}$." *Scr. Mater.*, 181, 48–52.
- Young, K. F., and Frederikse, H. P. R. (1973). "Compilation of the static dielectric

constant of inorganic solids.” *J. Phys. Chem. Ref. Data*, 2(2), 313–410.

Yv, L., Wang, J., Shi, J., Shi, Z., and Dai, L. (2022). “Preparation of high-entropy ceramic powder ($\text{Mg}_{0.2}\text{Co}_{0.2}\text{Ni}_{0.2}\text{Cu}_{0.2}\text{Zn}_{0.2}\text{O}$) by a precipitation method and kinetic analysis of the synthesis process.” *Ceram. Int.*, 48(2), 2138–2147.

Zhang, S. L., and Östling, M. (2003). “Metal silicides in CMOS technology: Past, present, and future trends.” *Crit. Rev. Solid State Mater. Sci.*, 28(1), 1-129.

Zhang, Z., Wang, W., Shang, M., and Yin, W. (2010). “Low-temperature combustion synthesis of Bi_2WO_6 nanoparticles as a visible-light-driven photocatalyst.” *J. Hazard. Mater.*, 177(1–3), 1013–1018.

Zhang, Y., Zuo, T. T., Tang, Z., Gao, M. C., Dahmen, K. A., Liaw, P. K., and Lu, Z. P. (2014). “Microstructures and properties of high-entropy alloys.” *Prog. Mater. Sci.*, 61, 1–93.

Zhang, R. Z., Gucci, F., Zhu, H., Chen, K., and Reece, M. J. (2018). “Data-driven design of ecofriendly thermoelectric high-entropy sulfides.” *Inorg. Chem.*, 57(20), 13027–13033.

Zhang, J., Yan, J., Calder, S., Zheng, Q., McGuire, M. A., Abernathy, D. L., Ren, Y., Lapidus, S. H., Page, K., Zheng, H., Freeland, J. W., Budai, J. D., and Hermann, R. P. (2019a). “Long-range antiferromagnetic order in a rocksalt high entropy oxide.” *Chem. Mater.*, 31(10), 3705–3711.

Zhang, J., Zhang, X., Li, Y., Du, Q., Liu, X., and Qi, X. (2019b). “High-entropy oxides $10\text{La}_2\text{O}_3\text{-}20\text{TiO}_2\text{-}10\text{Nb}_2\text{O}_5\text{-}20\text{WO}_3\text{-}20\text{ZrO}_2$ amorphous spheres prepared by containerless solidification.” *Mater. Lett.*, 244, 167–170.

Zhang, Y., Guo, W.-M., Jiang, Z. B., Zhu, Q.-Q., Sun, S.-K., You, Y., Plucknett, K., and Lin, H.-T. (2019c). “Dense high-entropy boride ceramics with ultra-high hardness.” *Scr. Mater.*, 164, 135–139.

Zhang, J. C., Sun, S., Yang, Z. M., Qiu, N., and Wang, Y. (2020a). “Extended damage range of $(\text{Al}_{0.3}\text{Cr}_{0.2}\text{Fe}_{0.2}\text{Ni}_{0.3})_3\text{O}_4$ high entropy oxide films induced by surface

irradiation.” *Chinese Phys. B*, 29(6), 66104.

Zhang, K., Li, W., Zeng, J., Deng, T., Luo, B., Zhang, H., and Huang, X. (2020b). “Preparation of $(\text{La}_{0.2}\text{Nd}_{0.2}\text{Sm}_{0.2}\text{Gd}_{0.2}\text{Yb}_{0.2})_2\text{Zr}_2\text{O}_7$ high-entropy transparent ceramic using combustion synthesized nanopowder.” *J. Alloys Compd.*, 817, 153328.

Zhao, Y., Kita, K., and Toriumi, A. (2010). “Thermodynamic analysis of moisture absorption phenomena in high-permittivity oxides as gate dielectrics of advanced complementary-metal-oxide-semiconductor devices.” *Appl. Phys. Lett.*, 96(24), 242901.

Zhao, K., Xia, X. X., Bai, H. Y., Zhao, D. Q., and Wang, W. H. (2011). “Room temperature homogeneous flow in a bulk metallic glass with low glass transition temperature.” *Appl. Phys. Lett.*, 98(14), 141913.

Zhao, X., Xue, Z., Chen, W., Bai, X., Shi, R., and Mu, T. (2019a). “Ambient fast, large-scale synthesis of entropy-stabilized metal-organic framework nanosheets for electrocatalytic oxygen evolution.” *J. Mater. Chem. A*, 7(46), 26238–26242.

Zhao, Z., Chen, H., Xiang, H., Dai, F. Z., Wang, X., Peng, Z., and Zhou, Y. (2019b). “ $(\text{La}_{0.2}\text{Ce}_{0.2}\text{Nd}_{0.2}\text{Sm}_{0.2}\text{Eu}_{0.2})\text{PO}_4$: A high-entropy rare-earth phosphate monazite ceramic with low thermal conductivity and good compatibility with Al_2O_3 .” *J. Mater. Sci. Technol.*, 35(12), 2892–2896.

Zhao, C., Ding, F., Lu, Y., Chen, L., and Hu, Y. (2020a). “High-entropy layered oxide cathodes for sodium-ion batteries.” *Angew. Chemie.*, 59(1), 264–269.

Zhao, Z., Chen, H., Xiang, H., Dai, F. Z., Wang, X., Xu, W., Sun, K., Peng, Z., and Zhou, Y. (2020b). “High entropy defective fluorite structured rare-earth niobates and tantalates for thermal barrier applications.” *J. Adv. Ceram.*, 9(3), 303–311.

Zhao, Z., Xiang, H., Chen, H., Dai, F., Wang, X., and Peng, Z. (2020c). “High-entropy $(\text{Nd}_{0.2}\text{Sm}_{0.2}\text{Eu}_{0.2}\text{Y}_{0.2}\text{Yb}_{0.2})_4\text{Al}_2\text{O}_9$ with good high temperature stability, low thermal conductivity and anisotropic thermal expansivity.” *J. Adv. Ceram.*, 9(5): 595–605.

Zhao, Z., Xiang, H., Chen, H., Dai, F. Z., Wang, X., Peng, Z., and Zhou, Y. (2020d).

“High-entropy $(\text{Nd}_{0.2}\text{Sm}_{0.2}\text{Eu}_{0.2}\text{Y}_{0.2}\text{Yb}_{0.2})_4\text{Al}_2\text{O}_9$ with good high temperature stability, low thermal conductivity, and anisotropic thermal expansivity.” *J. Adv. Ceram.*, 9(5), 595–605.

Zheng, Y., Yi, Y., Fan, M., Liu, H., Li, X., Zhang, R., Li, M., and Qiao, Z.-A. (2019). “A high-entropy metal oxide as chemical anchor of polysulfide for lithium-sulfur batteries.” *Energy Storage Mater.*, 23, 678–683.

Zhou, L., Li, F., Liu, J. X., Hu, Q., Bao, W., Wu, Y., Cao, X., Xu, F., and Zhang, G. J. (2020a). “High-entropy thermal barrier coating of rare-earth zirconate: A case study on $(\text{La}_{0.2}\text{Nd}_{0.2}\text{Sm}_{0.2}\text{Eu}_{0.2}\text{Gd}_{0.2})_2\text{Zr}_2\text{O}_7$ prepared by atmospheric plasma spraying.” *J. Eur. Ceram. Soc.*, 40(15), 5731–5739.

Zhou, S., Pu, Y., Zhang, Q., Shi, R., Guo, X., Wang, W., Ji, J., Wei, T., and Ouyang, T. (2020b). “Microstructure and dielectric properties of high entropy $\text{Ba}(\text{Zr}_{0.2}\text{Ti}_{0.2}\text{Sn}_{0.2}\text{Hf}_{0.2}\text{Me}_{0.2})\text{O}_3$ perovskite oxides.” *Ceram. Int.*, 46(6), 7430–7437.

Ziehl, T. J., Morris, D., and Zhang, P. (2023). “Detection and impact of short-range order in medium/high-entropy alloys.” *iScience.*, 26(3), 106209.

Zou, X., Wang, J., Chiu, C. H., Wu, Y., Xiao, X., Jiang, C., Wu, W. W., Mai, L., Chen, T., Li, J., Ho, J. C., and Liao, L. (2014). “Interface engineering for high-performance top-gated MoS_2 field-effect transistors.” *Adv. Mater.*, 26(36), 6255–6261.

Zou, Y., Ma, H., and Spolenak, R. (2015). “Ultrastrong ductile and stable high-entropy alloys at small scales.” *Nat. Commun.*, 6(1), 7748.

LIST OF PUBLICATIONS

PATENTS

Ashritha Salian, Saumen Mandal, “A method of preparing low temperature stabilized high entropy high-k oxides”, **Indian Patent**. Application Number: 202141035822, filed on 9th August 2021

PUBLICATIONS IN PEER-REVIEWED JOURNALS

RELATED TO THESIS

Ashritha Salian, Saumen Mandal, “Entropy stabilized multicomponent oxides with diverse functionality—a review”, Critical Reviews in Solid State and Materials Sciences, 47 (2), 142-193 (2021).

Ashritha Salian, Saumen Mandal, “Review on the deposition, structure and properties of high entropy oxide films: current and future perspectives”, Bulletin of Materials Science, 45 (1), 1-21 (2022).

Ashritha Salian, Pavan Pujar, Robbi Vivek Vardhan, Haewon Cho, Sunkook Kim, Saumen Mandal, “Evolution of high dielectric permittivity in low-temperature solution combustion processed phase-pure high entropy oxide (CoMnNiFeCr)O for thin film transistors”, ACS Applied Electronic Materials, 5 (5), 2608-2623 (2023).

Ashritha Salian, Pradyut Sengupta, Iteesha V A, Avinash Gowda, Saumen Mandal, “A review on the emergent field of high entropy silicides and silicates: Fundamental aspects, synthesis, properties.”, International Journal of Applied Ceramic Technology, 20 (5), 2635-2660 (2023).

Ashritha Salian, Lakkimsetti Lakshmi Praveen, Santhra Krishnan P, Saumen Mandal, “Role of Mg–O on phase stabilization in solution combustion processed rocksalt structured high entropy oxide (CoCuMgZnNi) O with high dielectric performance”, Ceramics International, 49 (19), 31131-31143 (2023).

Ashritha Salian, Akshay Prasad K, Saumen Mandal, “Phase stabilized solution combustion processed $(\text{Ce}_{0.2}\text{La}_{0.2}\text{Pr}_{0.2}\text{Sm}_{0.2}\text{Y}_{0.2})\text{O}_{1.6-\delta}$: An exploration of the dielectric properties”, Journal of Alloys and compounds, 960, 170786 (2023).

OTHERS

G Manjunath, Robbi Vivek Vardhan, **Ashritha Salian**, Rashi Jagannatha, Mayank Kedia, Saumen Mandal, “Effect of annealing-temperature-assisted phase evolution on conductivity of solution combustion processed calcium vanadium oxide films”, Bulletin of Materials Science, 41, 1-9 (2018).

Ashritha Salian, Pavan Pujar, and Saumen Mandal, “Facile in situ formation of high conductive Ag and Cu_xO_y composite films: a role of aqueous spray combustion”, Journal of Materials Science: Materials in Electronics, 30, 2888-2897 (2019).

Santhra Krishnan P, **Ashritha Salian**, Saikat Dutta and Saumen Mandal, “A roadmap to UV-protective natural resources: classification, characteristics, and applications”, Materials Chemistry Frontiers, 5 (21), 7696-7723 (2021). (Equal Contribution)

Perabathula Satish, **Ashritha Salian**, Komalakrushna Hadagalli, Saumen Mandal, “Preparation and structural characteristics of biphasic calcium phosphates from prawn shell bio-waste”, Advances in Applied Ceramics: Structural, Functional and Bioceramics, 1-10 (2023).

LIST OF CONFERENCE PRESENTATIONS

RELATED TO THESIS

Ashritha Salian, Amal Mohan, Yukti Gupte, Saumen Mandal, “Formulation of Spinel - Type High Entropy Oxide by Solution Combustion Technique”, 3rd International Workshop on high entropy materials (IWHEM 2020), March 7-8, IIT Kanpur, Kanpur, India. (Poster)

Ashritha Salian, Robbi Vivek Vardhan, Lakkimsetti Lakshmi Praveen, Santhra Krishnan P, Pavan Pujar, Saumen Mandal, “Development of low temperature processed high dielectric constant high entropy oxide for electronic applications”, XXI International Workshop on Physics of Semiconductor Devices (IWPSD 2021), December 14-17, IIT Delhi, India. (Poster)

Ashritha Salian, Saumen Mandal, “ Examination of phase stabilization, microstructural, optical, and dielectric properties on solution combustion processed high entropy fluorite oxide (CeLaPrSmY)O”, International Conference on Nanoscience and Technology (ICONSAT 2023), March 27-29, SRM Institute of Science and Technology, Chennai, India. (Oral)

Ashritha Salian, Saumen Mandal, “Investigation of phase stabilization, microstructural, optical, and dielectric properties in solution combustion processed high entropy oxide (CoCuMgZnNi)O: A potential anode material of Li-ion batteries”, International Conference on Women in Electrochemistry (ICWEC 2023), April 7-8, IISc Bengaluru, India. (Poster) (Best Paper Award)

OTHERS

Pavan Pujar, Manjunath G, **Ashritha Salian**, Anusha P, Bikesh Gupta, Saumen Mandal, “Distinct technologies featuring nanoparticles and molecular precursors of silver to deposit electrodes for optoelectronic devices”, Fourth International Conference on Nanomaterials: Synthesis, Characterization and Applications (ICN 2019), April 12-14, Mahatma Gandhi University, Kottayam, Kerala, India. (Oral)

G Manjunath, **Ashritha Salian**, Pavan Pujar, P Nagraju, Saumen Mandal, “Solution combustion derived metal & metal oxides for thin film transistors and gas sensing applications”, 12th Indo-German Frontiers of Engineering Symposium (INDOGFOE - 2022), September 9-October 2, Department of Science and Technology (DST), India and the Alexander von Humboldt Foundation, Bremen, Germany. (Poster)

Lakkimsetti Lakshmi Praveen, **Ashritha Salian**, Saumen Mandal, “Precise estimation of lattice parameter and optical bandgap of cobalt oxide synthesized via hydrothermal and solution combustion process: A comparative study towards gas sensing application”, International school and conference on Evolution of Electronic Structure Theory and Experimental Realization (EESTER 2023), January 4-12, SRM Institute of Science and Technology KTR and Indian Institute of Technology Madras, Chennai, India. (Poster)

BIODATA

Name : Ashritha Salian

Father's name : Vasanth Salian

Mother's name : Parvathi Salian

Date of birth : 04th October 1993

Permanent Address : 3-118-4, Shri Datta Sai Nivasa,
Near railway over bridge,
Padil, Kannur Post,
Dakshina Kannada District, Mangaluru
Karnataka, India – 575007.

Mobile : +91-9113911605

E-mail : ashrithasalian18@gmail.com

Academic qualification:

Bachelor of Technology (B.Tech.) in Electronics and Communication Engineering from Bearys Institute of Technology, Mangaluru, Karnataka (74.1 % out of 100 %).

Master of Technology (M.Tech.) in Nanotechnology from National Institute of Technology Karnataka, Surathkal (CGPA: 8.75 out of 10).